Published by Empress Catherine II
Saint Petersburg Mining University

SINCE 1907

E-ISSN 2541-9404
ISSN 2411-3336

JOURNAL OF MINING INSTITUTE

ZAPISKI GORNOGO INSTITUTA

SCIENTIFIC JOURNAL

Volume 266

№ 2 • 2024

INDEXING IN
SCOPUS (Q1)
WEB OF SCIENCE (ESCI)

WWW.PMI.SPMI.RU

Journal of Mining Institute

Empress Catherine II Saint Petersburg Mining University

The International Competence Center for Mining Engineering Education under the auspices of UNESCO

The scientific periodical “Journal of Mining Institute” is published since 1907 by Empress Catherine II Saint Petersburg Mining University – the first higher technical educational institution in Russia, founded in 1773 by the decree of Catherine II as the embodiment of the ideas of Peter I and M.V. Lomonosov on the training of engineers for the development of mining business.

The International Competence Center for Mining Engineering Education under the auspices of UNESCO operates on the basis of Empress Catherine II Saint Petersburg Mining University and contributes to active interaction of the Journal with the international scientific community.

The purpose of the Journal is to create an information space in which Russian and foreign scientists can present results of their theoretical and empirical research on the problems of the mining sector.

Published articles cover the issues of geology, geotechnical engineering and engineering geology, mining and petroleum engineering, mineral processing, energy, geoecology and life safety, economics of raw materials industries.

The Journal is indexed by Scopus (Q1), Web of Science Core Collection (ESCI), DOAJ Seal, RSCI, GeoRef, Google Scholar, RSCI. It is included in the White list of the Ministry of Education and Science of the Russian Federation.

The Journal is published six times a year. The average first decision time is one month.

Articles are published free of charge. Translation is provided by the author.

The cover shows an exhibit of the Mining Museum – malachite is a rich green mineral due to the presence of copper compounds. As A.E.Fersman put it, this is “a stone of bright, rich, cheerful and at the same time silky-tender green”. The main source of malachite are deposits of the Democratic Republic of the Congo, the USA and other countries, but in terms of color and beauty of patterns, malachite from foreign deposits cannot be compared with that from the Urals.

The Mining Museum is the world’s third largest natural-science exposition, it contains more than 230 thousand exhibits, including precious metals and stones, unique collections of minerals, ores, rocks, paleontological remains, meteorites, a collection of models and prototypes of mining equipment, pieces of stone-cutting and jewelry art.

JOURNAL OF MINING INSTITUTE

ZAPISKI GORNOGO INSTITUTA

PEER-REVIEWED SCIENTIFIC JOURNAL

Published since 1907

ISSN 2411-3336
e-ISSN 2541-9404

Volume 266

ST. PETERSBURG • 2024

Journal founder: Empress Catherine II Saint Petersburg Mining University

Sections

• Geology • Geotechnical Engineering and Engineering Geology • Economic Geology • Energy

Registration Certificate PI No. FS77-70453 dated 20.07.2017

PH License No. 06517 dated 09.01.02

Editorial staff: Head of the Editorial Center V.L.Lebedev; Editors: E.S.Dribinskaya, M.G.Khachirova, L.V.Nabieva
Computer Design: N.N.Sedykh, V.I.Kashirina, E.A.Golovinskaya

Passed for printing 25.04.2024. Format 60 × 84/8. Academic Publishing Division 41.
Circulation: 300 copies. Order 190. Printed by RIC of Empress Catherine II Saint Petersburg Mining University. Free sale price.

Mailing address of the Journal Founder and the Editorial Board
21st Linia V.O., No. 2, St. Petersburg, Russia, 199106
Phone: +7 (812) 328-8416; Fax +7 (812) 327-7359;
E-mail: pmi@spmi.ru Journal website: pmi.spmi.ru

CONTENTS

Geology

Geotechnical Engineering and Engineering Geology

ISSN 2411-3336; e-ISSN 2541-9404

JOURNAL OF MINING INSTITUTE
Zapiski Gornogo instituta
Journal homepage: pmi.spmi.ru

Research article

Assessment of rock massif sustainability in the area of the underground research laboratory (Nizhnekanskii Massif, Enisei site)

Dastan Zh. Akmatov[1,2], **Aleksandr I. Manevich**[1,2], **Viktor N. Tatarinov**[1,3]✉, **Roman V. Shevchuk**[1,2,3], **Sergei M. Zabrodin**[1]

[1] *Geophysical Center of the RAS, Moscow, Russia*
[2] *National University of Science and Technology "MISIS", Moscow, Russia*
[3] *Schmidt Institute of Physics of the Earth RAS, Moscow, Russia*

How to cite this article: Akmatov D.Zh., Manevich A.I., Tatarinov V.N., Shevchuk R.V., Zabrodin S.M. Assessment of rock massif sustainability in the area of the underground research laboratory (Nizhnekanskii Massif, Enisei site). Journal of Mining Institute. 2024. Vol. 266, p. 167-178.

Abstract. The study presents the results of the research on geodynamic and geological conditions of the Enisei site (Krasnoyarsk Krai), chosen for the construction of an underground research laboratory. The laboratory is being built at a depth of 500 m to assess the suitability of the rock mass for burying high-level radioactive waste. The rocks consist of weakly fractured gneisses, granites, and dikes of metadolerites. Field observations were conducted on bedrock outcrops. They included the determination of rock mass quality indicators, measurement of rock fracturing, and a rating classification of stability using N.Barton's method. GNSS observations were also made to monitor surface deformations. These data were used to develop a three-dimensional structural model, including lithology, fault disruptions, intrusive bodies, elastic-strength properties of rocks, and the sizes of zones influenced by faulting. It will serve as a basis for boundary conditions and the construction of three-dimensional variational models of stress-strain states, identifying zones of concentration of hazardous stresses, and planning in situ geomechanical experiments in underground mines of the laboratory. The obtained values of the modified Q^R index for the main types of rocks allowed their classification as stable and moderately stable, corresponding to strong and very strong rocks on Barton's scale and the massif rating according to geomechanical classification.

Keywords: geoecological safety; high-level radioactive waste; underground research laboratory; structural-tectonic model; tectonic block; fault; rating assessments of rock mass quality

Acknowledgment. This work was conducted in the framework of budgetary funding of the Geophysical Center of RAS, adopted by the Ministry of Science and Higher Education of the Russian Federation.

Received: 29.10.2022 ***Accepted: 25.10.2023*** ***Online: 26.02.2024*** ***Published: 25.04.2024***

Introduction. In Russia, a vast amount of radioactive waste (RAW) has been accumulated, and its surface storage poses an extraordinary danger to the population and the environment. The most hazardous are high-level RAW containing radionuclides with a half-life of more than 10,000 years. At the current level of scientific and technological progress, the most reliable method for removing them from the biosphere is the disposal of RAW in deep impermeable geological formations (crystalline rocks, salts, tuffs). The fundamental condition for ensuring the geoecological safety of RAW disposal is the isolation capabilities of the rock massif and a low-activity geodynamic regime of the area. The safety concept of geological repositories for RAW is based on the principle of multibarrier systems, where a complex of engineering and natural barriers ensures the isolation of RAW. Each barrier performs its functions for a specific period. Obviously, the most durable is the geological barrier. However, tectonic movements

Journal of Mining Institute. 2024. Vol. 266. P. 167-178

(slow creep and fast seismic) can lead to the destruction of the structurally-tectonic block (far zone) with the mines of the deep geological repository of RAW (DGR). Geomechanical processes, causing the formation of high-gradient stress zones or weakening the near-contour part (near zone) of the DGR mines, pose no less danger.

In 2022, the construction of an underground research laboratory (URL) began in the granitoid rocks of the Nizhnekanskii Massif, 20 km north of Krasnoyarsk, to make a final decision on the feasibility of building the deep geological repository for RAW [1, 2]. Research in URL is conducted in many developed countries that use nuclear technologies, including Sweden (Äspö), Finland (Onkalo), Switzerland (Grimsel), Germany (Gorleben) [3-5], Japan (Mizunami), China (Beishan), and others [6, 7]. In Russia, a research program is being developed for the URL of the Nizhnekanskii Massif. An important part of these studies is geomechanical experiments. Special chambers and deep boreholes are planned for their implementation [8-11]. Project decisions on the organization of monitoring systems include the justification of methods and measurement techniques, optimal locations for sensors, conducting field experiments, the selection of necessary equipment and technical means, interaction with other experiments, algorithms for processing observation results, etc. [12].

The article presents the results of developing a three-dimensional geomechanical model of the rock massif in the Enisei area as the initial stage of these works. It is assumed that based on this model, plans for the arrangement of chambers and boreholes for in-situ geomechanical experiments, the placement of sensors in the monitoring network, and the specification of boundary conditions for numerical modeling of the stress-strain state (SSS) of rocks within the area will be developed.

Methods. In Fig.1, a variant of the volumetric-planning solution for the location of research mines in the underground research laboratory at the end of 2018 is presented. The laboratory is situated at a depth of 500 m from the Earth's surface and includes three shafts (ventilation, operational for the descent of radioactive waste and personnel), a system of horizontal mines, research chambers, and boreholes. This scheme is preliminary and will be refined depending on the identification of geological structure features [1]. Before the excavation of mines, a classification of the stability of hosting rocks should be developed, and their critical properties influencing both the long-term stability of the URL and the provision of safe conditions for underground works at a depth of 500 m should be determined. The following main parameters should be taken into account [13-15].

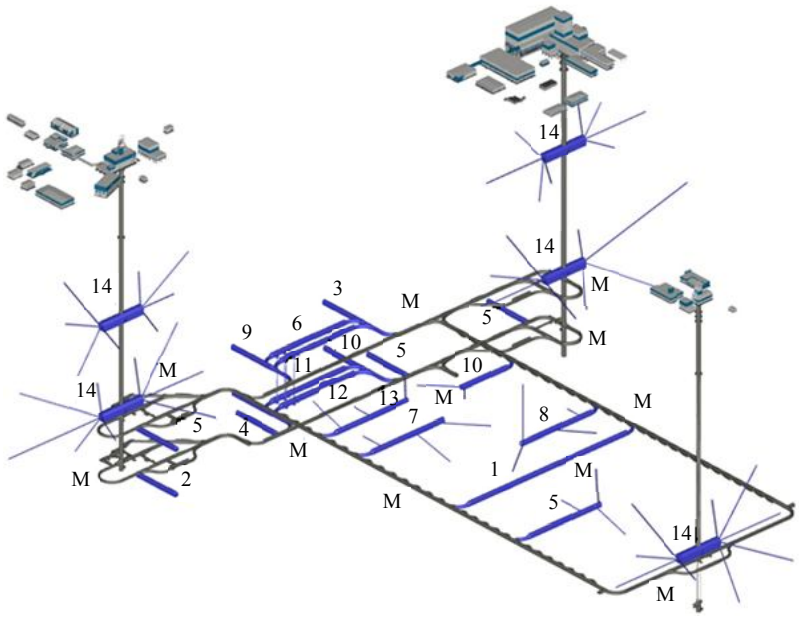

Fig.1. Schematic diagram of the URL (research mines are highlighted in blue), numbers indicate planned experiments on geomigration (1-3); geochemistry (4); geomechanics (5); engineering barriers (6-8); microbiology (9); gas release (10); RAW packaging technology development (11, 12); burial prototype (13); hydrogeology (14); M – monitoring stations

Fault influence zones. Fault zones are potential pathways for the migration of nuclides beyond the sanitary zone of the DRG [16-18]. Zones of dynamic influence of faults are rocks that are strongly disturbed compared to the internal parts of structural blocks. If they intersect the site, they can act as triggers for hazardous geomechanical

processes in the near-contour part of the mines and as channels for the infiltration of groundwater into the containers with RAW [19, 20].

Faults are classified into three categories depending on their length [13, 14]:

- class *A* – faults with a length ranging from several tens to several hundreds of kilometers;
- class *B* – faults with a length ranging from several kilometers to tens of kilometers;
- class *C* – faults with a length measured in meters or hundreds of meters.

The zone of dynamic influence of faults in this article is a rather general concept that includes all types of fractured zones. The width of the zone of dynamic influence for local and regional faults is calculated according to the formula provided in the article by G.G.Kocharyan [21],

$$F^W = kL, \tag{1}$$

where L – is the length of the fault, km; k – is a coefficient dependent on the scale and type of rock deformation. The range of variation for k is from 0.1 to 0.2 for local and regional faults, respectively [22]. Some authors suggest even smaller values for k (down to 10^{-4}).

Areas with class *A* faults are prohibited from encompassing the construction site of the radioactive waste disposal facility. The presence of class *B* faults is allowed, but they should not intersect with mines intended for the disposal of radioactive waste. Class *C* faults are permitted to intersect with mines, but a rating assessment of rock quality is necessary to take additional measures.

Chemical index of underground waters. Reflects the basic chemical properties of fluids – acidity, alkalinity, salt content, and other chemical elements that affect the corrosion resistance of engineering barriers. The chemical index C^R_{chm} includes three parameters: TDS – total dissolved solids content; pH – acidity/alkalinity; Cl – a parameter indicating the concentration of chloride ions in water. The value of the total chemical index is determined based on the composition of underground waters. With $6 < \text{pH} < 10$, TDS < 50 g/l, Cl < 20 g/l, the geochemical environment is quite favorable and does not reduce the "quality" of rocks. The value of the geochemical parameter is determined as 1.0. If any of these requirements is not met, the geochemical environment is considered generally favorable, and a value of 0.8 is assigned. Otherwise, the geochemical environment is considered "not very suitable", and it is assigned a relatively low value of 0.1.

Thermal effect. Due to the decay of radionuclides, the surrounding rocks will be exposed to elevated temperatures for an extended period (according to various estimates, around 120-150 °C for more than 150 years). Under the simultaneous influence of lithostatic pressure and tectonic stresses, this can significantly impact the stability of the rocks. The properties of rocks are considered in two aspects. The value of thermal conductivity can influence the layout decisions of the radioactive waste disposal facility. Another aspect is the alteration of the physical and mechanical properties under the influence of high temperatures. Experimental studies in [23] confirmed that high temperatures can lead to a significant decrease in the mechanical strength of geological formations. In this article, the thermal effect index $\sigma^{T_{\max}}_{cd}$ is defined as the ratio of the compressive strength at maximum temperature to the strength at room temperature C_{cd} :

$$C^R_T = \frac{\sigma^{T_{\max}}_{cd}}{C_{cd}}. \tag{2}$$

It is proposed to use the weighted average value of the thermal effect index in case there are several types of rocks in the studied area. For example, if granite and metamorphic rock (gneiss) are present in a ratio of 70 and 30 %, respectively, the index is calculated using the formula:

$$C^R_T = 0.7C^R_{T_{gran}} + 0.3C^R_{T_{metam}}. \tag{3}$$

Q-index according to N.Barton. According to the research conducted at the Äspö underground laboratory (Sweden) [6], it has been revealed that the parameters of the stress relaxation factor (SRF) and rock moisture content (J_w) are not suitable for assessing the stability of the rock mass during the underground isolation of radioactive waste [24, 25]. Therefore, in the system for assessing the suitability of the rock mass for the disposal of radioactive waste, it is accepted to use the product of four parameters:

$$Q' = \frac{\text{RQD}}{J_n}\frac{J_r}{J_a}, \tag{4}$$

where RQD – is the rock quality designation; J_n is the number of joint sets; J_r is the joint roughness coefficient (roughness of the most unfavorable joint); J_a is the alteration and condition of the joints.

The rock quality index, characterizing their structural disruption, is calculated using the formula [26-28]:

$$\text{RQD} = \frac{L_\Sigma}{L}\cdot 100\ \%, \tag{5}$$

where L_Σ – is the sum of the lengths of distances between natural cracks longer than 10 cm, m.

Hydraulic conductivity is the rate of fluid flow through pores and fractures. It plays a crucial role in determining the speed of radionuclide transport into the surrounding environment (in this case, the Yenisei River) in the event of the failure of engineered barriers. Hydraulic conductivity depends on permeability, saturation, fluid density, and viscosity. The index is determined as follows:

$$J_w^R = \begin{cases} 1.0, & \text{if } (K < 10^{-8}\ \text{m/day}) \geq 90\ \%; \\ 0.7, & 70\ \%\ \text{if } (K < 10^{-8}\ \text{m/day}) < 90\ \%; \\ 0.3, & 30\ \%\ \text{if } (K < 10^{-8}\ \text{m/day}) < 70\ \%; \\ 0.1, & 70\ \%\ \text{if } (K < 10^{-8}\ \text{m/day}) < 30\ \%, \end{cases} \tag{6}$$

where K – is the specific hydraulic conductivity (or permeability) of the rock formations.

The strength-to-stress ratio index. The mechanical stability of mines primarily depends on the relationship between strength and the acting stresses in the rock mass [26, 29]. Typically, this is assessed by the ratio of uniaxial compressive strength to the maximum principal stress. This ratio is used as a factor of safety [30]. According to Barton's stability classification, it is determined by the formula:

$$\text{SRF}^R = \begin{cases} 0.5, & \text{if } (\sigma_c/\sigma_1 > 5) \geq 90\ \%; \\ 1.0, & 70\ \%\ \text{if } (\sigma_c/\sigma_1 > 5) < 90\ \%; \\ 5.0, & 40\ \%\ \text{if } (\sigma_c/\sigma_1 > 5) < 70\ \%; \\ 20, & \text{if } (\sigma_c/\sigma_1 > 5) < 40\ \%, \end{cases} \tag{7}$$

where σ_c – is the rock strength under uniaxial compression; σ_1 – is the maximum stress in the rock mass; $\sigma_c/\sigma_1 > 5$ – indicates a percentage of data related to the strength-stress ratio.

The paper [31] presents a rock classification system based on the Q-index by N.Barton, adapted to the specific features of underground radioactive waste isolation. The suitability index of host rocks includes factors such as thermal impact, chemical composition of groundwater, and permeability of the hosting massif. The modified index is determined by the formula:

$$Q^R = C_{chm}^R C_T^R Q' \frac{J_w^R}{\text{SRF}^R}. \tag{8}$$

Classification of rock massif by stability class is given in Table 1.

Table 1

Categories of rock massif according to stability class

Q^R	Class	Degree of stability	Massif stability category
[40, 1000]	I	High	Resistant
[10, 40]	II	Medium	Medium resistant
[0, 10]	III	Low	Unstable

Description of the rock massif. The Nizhnekanskii Massif is located in the accretion zone, at the contact of two major geological structures – the Siberian Platform and the West Siberian Plate [32]. The chosen area for the construction of the URL is approximately 2 × 3 km in size and is located in the northwest of the granitoid Nizhnekanskii Massif. Fig.2 shows the main tectonic disturbances

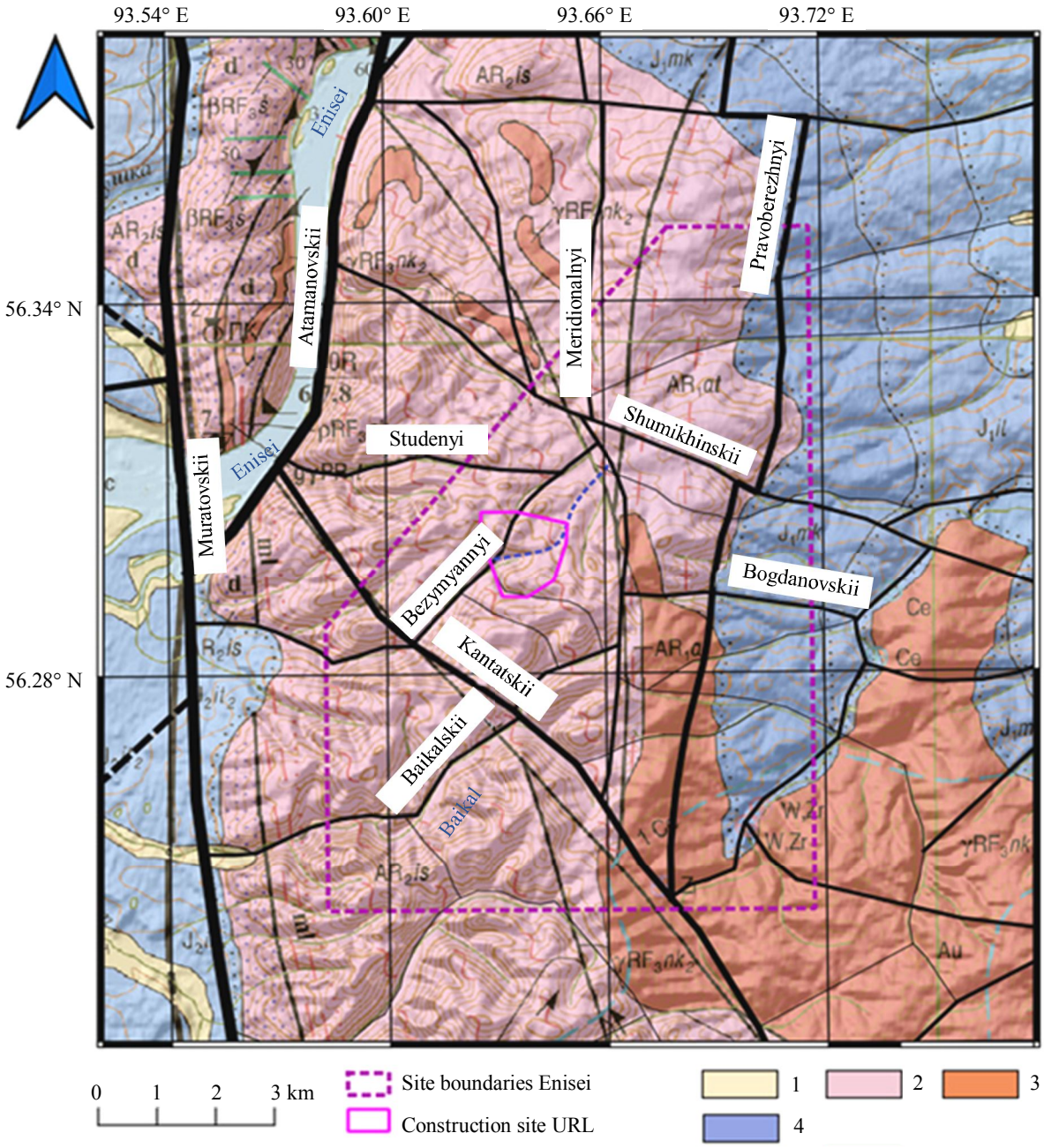

Fig.2. Structural-tectonic scheme of the area. Black lines represent faults: thick lines – major faults, medium-thick lines – regional faults, thin lines – local faults, dashed lines – presumed faults

1 – alluvial deposits (pebbles, sands); 2 – Jurassic deposits (sandstones, aleurolites, argillites); 3 – Early Archean gneisses, crystal schists of the Atamanovsk series; 4 – Late Devonian biotite granites [33]

Journal of Mining Institute. 2024. Vol. 266. P. 167-178

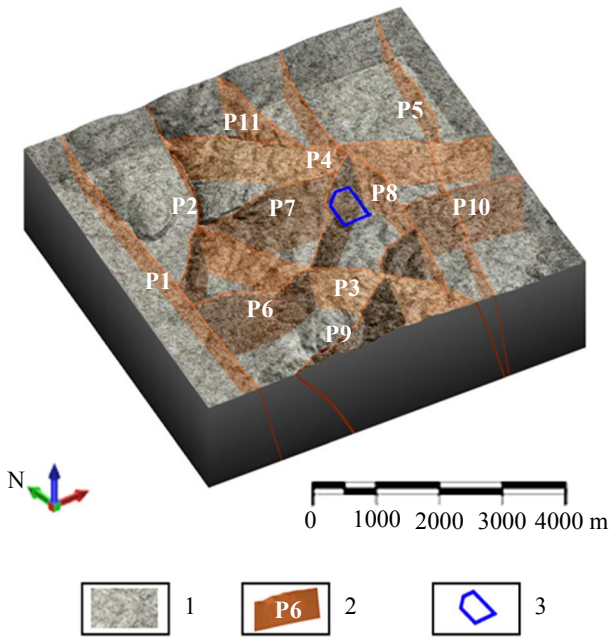

Fig.3. Three-dimensional model of major tectonic disruptions. Faults: P1 – Muratovskii; P2 – Atamanovskii; P3 – Kantatskii; P4 – Shumikhinskii; P5 – Pravoberezhnyi; P6 – Bezymyannyi; P7 – Studenyi; P8 – Meridionalnyi; P9 – Baikalskii; P10 – Bogdanovskii; P11 – N 1

1 – gneiss; 2 – faults; 3 – outline of the RAW disposal repository site

in the area [32]. A more detailed characterization of the tectonic and geological conditions is provided in [9, 30-32, 34]. The Pravoberezhnyi and Shumikhinskii faults divide the Enisei area into three structural blocks. According to geological data, the Right Bank fault is considered tectonically active. An analysis of the relief morphology reveals local faults and fractures. At a distance of 2-3 km to the west of the area's boundary, the active Muratov fault passes, which many geologists consider as the boundary between the Siberian Platform and the West Siberian Plate [8-9].

Based on the developed classification, a 3D model of the site was constructed, including 11 faults of various classes. The three-dimensional model is visually shown in Fig.3. Among the faults, two belong to class *A* and extend for more than 30 km. They are located in the western part of the studied area. Within the construction site of the underground laboratory, faults of class *C* with lengths ranging from 300 to 1000 m were identified. These local faults are oriented to the northeast, and their number exceeds 16. According to the suitability assessment classification, class *A* faults do not reach the construction site boundary. The class *B* fault (Bezymyannyi) intersects the construction site but does not reach the repositories of the RAW disposal facility. It can be concluded that the Enisei site is assessed as suitable for the construction of the URL.

On the Enisei site, 17 boreholes were drilled with core sampling, and the determination of the physico-mechanical properties of the rocks was performed (Table 2) [35]. Due to the lack of documentation for the core material to determine the stability categories of rock masses, geotechnical documentation of rock outcrops was carried out in 2021-2022 to assess the degree of rock disturbance and stability [33]. Statistical analysis of the results showed that fractures in the dynamic influence zone of the Muratovskii fault have a northeast direction (Fig.4, *c*), the Bezymyannyi fault has a northeast-southwest and southeast-northwest direction (azimuths of approximately 10° and 130°) (Fig.4, *d*). In contrast to the granite-gneiss rocks, the dike complexes of metadolerites are less fractured [35].

Table 2

Summary physical and mechanical properties of rocks at the Enisei site

Characteristic	Rocks	
	Gneisses	Metadolerites
Volume weight, t/m^3	2.75	2.91
Poisson's ratio	0.27	0.29
Modulus of elasticity, MPa	(7.0-7.7)·10^4	9.15·10^4
Modulus of deformation, MPa	5.9·10^4	7.09·10^4
Uniaxial compression strength, MPa	131.0	143.9
Tensile strength, MPa	12.89	12.41
Shear strength, MPa	57.15	99.6

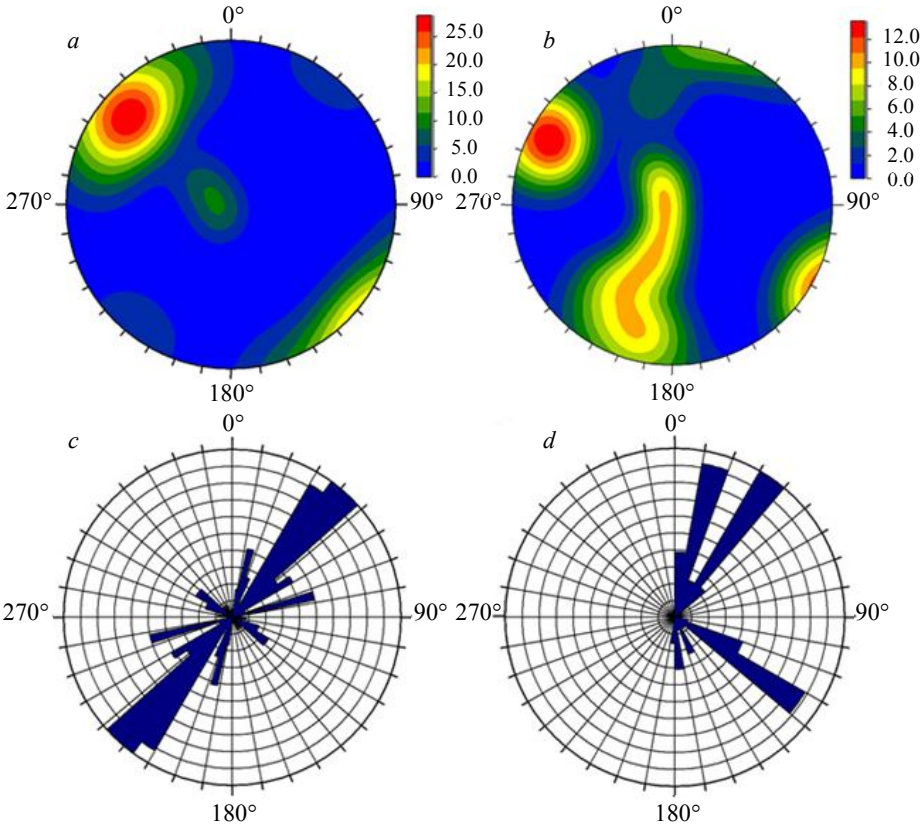

Fig.4. Stereograms of rock fracturing in the Lower Jurassic formation in the zones of dynamic influence of the Muratovskii (*a*) and Bezymyannyi (*b*) faults; rose diagram of fracturing in the zones of dynamic influence of the Muratovskii (*c*) and Bezymyannyi (*d*) faults

When specifying boundary conditions for modeling stress fields, it is crucial to accurately consider the direction of external tectonic forces [36-39]. The results of geological-geophysical studies indicate that the stress field in the region is characterized by dominant sub-horizontal compression with azimuths around 40°. A more detailed examination of the contemporary stress field in the Lower Cretaceous complex is presented in [8]. Analysis of the orientation of axes and deformation rates obtained through GNSS (Global Navigation Satellite System) reveals a mosaic-like pattern of deformation (Fig.5). The northern and eastern boundaries of the area west of the Pravoberezhnyi fault are predominantly characterized by sub-meridional extension. The western boundary of the area, corresponding to the axis of the Pravoberezhnyi fault, experiences sub-meridional compression and sub-latitudinal extension. The zone north of the Bezymyannyi fault undergoes extension, while the block bounded by the Merkurevskii and Verkhneshumikhinskii faults experiences compression.

At a distance of 3 km from the Enisei site, previous stress assessment work was conducted using the hydraulic fracturing method. The results showed horizontal stresses $\sigma_{xx} = \sigma_{yy} = 13.5$ MPa, and vertical stress $\sigma_{zz} = 12$ MPa. In other studies [33, 40], it is noted that stresses in the rock massif reach 21.4 MPa. As can be seen, the data are quite contradictory. During the geotechnical documentation of rock outcrops on the site, samples were uniformly selected in various geological conditions. The zone of dynamic influence of the Muratovskii fault was thoroughly studied, and measurements were taken at four geological sites at a distance of up to 1 km from it.Three additional sites were chosen away from local tectonic disturbances, in the masses not affected by intrusive dike bodies. Five research sites corresponded to local-scale fault disruptions – Baikalskii, Kantatskii, Bezymyannyi, Verkhneshumikhinskii, and Merkurevskii faults. Another four sites were described during reconnaissance routes,

Journal of Mining Institute. 2024. Vol. 266. P. 167-178

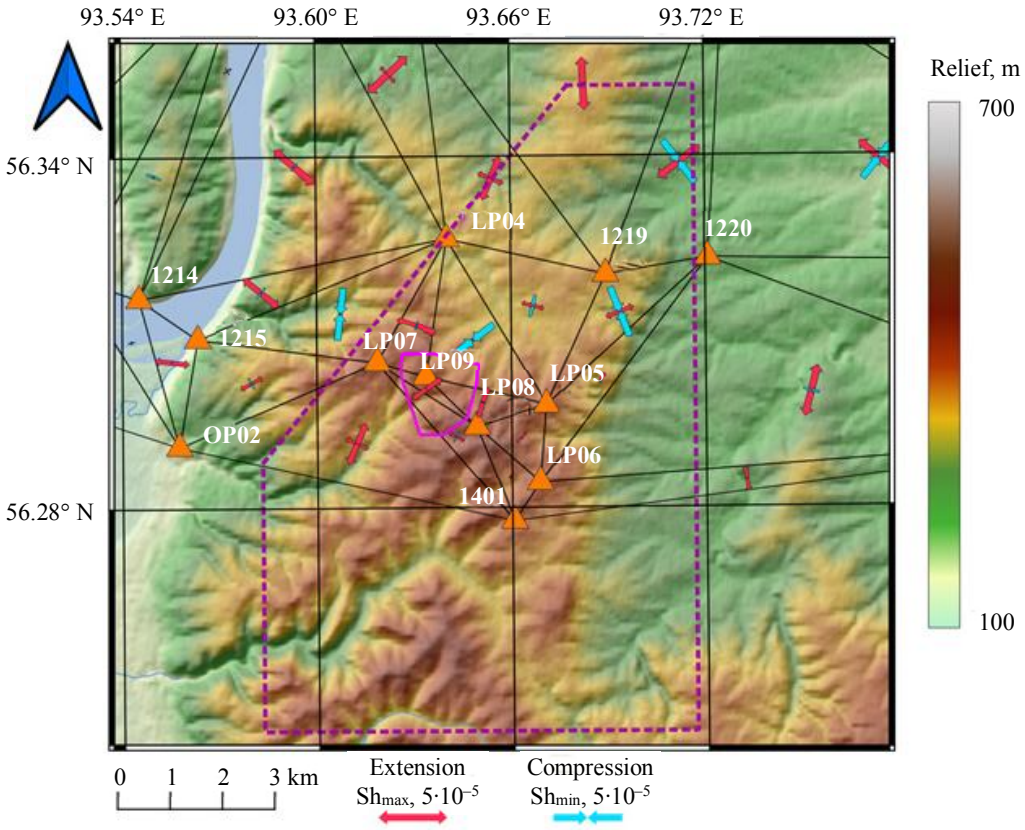

Fig.5. Principal axes and velocities of horizontal deformations determined from GNSS observations during the period from 2012 to 2021 [8]

where intrusive dike complexes of metadolérites were identified. All the data were summarized based on the rock stability categories according to the Q^R value and systematized in Table 3:

• category 1 – 500-meter zone of dynamic influence of the Muratovskii fault. The rocks mainly consist of granites and gneisses with veins of quartz and thin dikes of metadolerites;

• category 2 – zones of dynamic influence of local-scale fault disruptions. The rocks are predominantly granites and gneisses with veins of quartz and thin dikes of metadolerites;

• category 3 – intrusive complexes represented by thicker dikes of metadolerites, with a thickness of up to 10-20 m;

• category 4 – outside the zone of dynamic influence of fault disruptions. The rocks are mainly expressed as granites and gneisses.

Table 3

Rock stability classes

Category	Q'	C^R_{chm}	C^R_T	J^R_w	SRF	Q^R	Class
1	13	1.0	0.80	1.0	0.5	20.8	II
2	86	1.0	0.88	1.0	0.5	151.4	I
3	22	1.0	0.87	0.8	0.5	30.6	II
4	68	1.0	0.85	0.7	0.5	80.9	I

Hydrochemical studies have shown that the overall mineralization ranges from 50 to 450 mg/l, and the water is hydrocarbonate-calcium [41]. The average pH value is 8.1, and the total hardness does not exceed 6.25 °F. The nitrate ion content is below 3.76 mg/l, and chloride levels range from 0.9 to 7.5 mg/l. Therefore, the requirements for geochemical parameters are met, and the geochemical

parameter can be accepted as 1.0. The thermal effect index C_T^R is assumed 0.88 based on the analysis of the results of physical-mechanical studies and experiments in China [13]. According to studies [32, 42], the coefficient of permeability for granite-gneiss rocks of the Nizhnekanskii Massif varies in the range of 10^{-9} to 10^{-10} m/day. This means that they have low permeability. Following the equation (6), the value of J_W^R is taken as 1.0. The specific value of the strength-to-major stress ratio, according to equation (7), is 6.2; therefore, the value of SRF^R is 0.5. Thus, the stability assessment of the rock mass (8) indicates that the site is characterized by good quality ratings and is suitable for the construction of the radioactive waste repository.

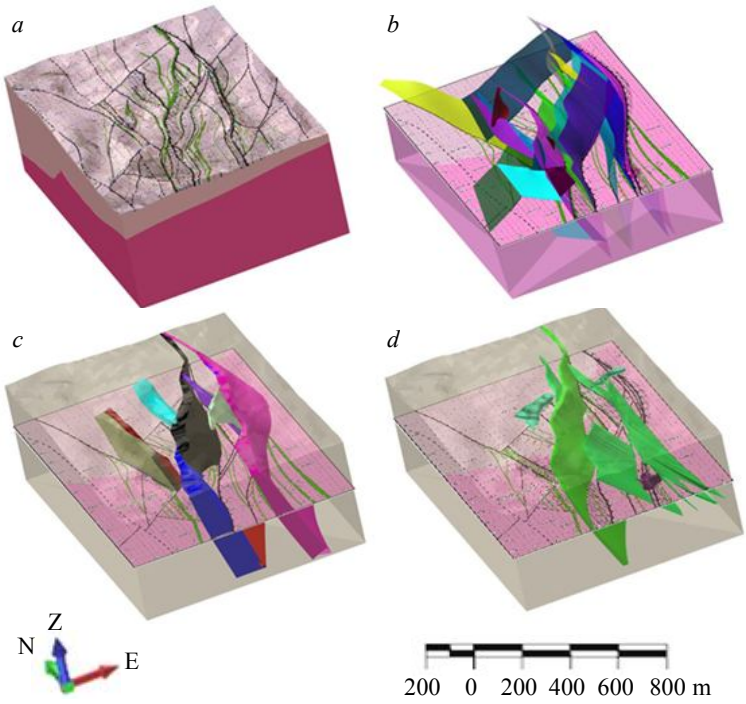

Fig.6. Three-dimensional representation of the main geological structures in the 3D model of the Enisei site: *a* – lithological model; *b* – model of discontinuous faults; *c* – zones of fracturing, increased fissility, and brecciation; *d* – intrusive and dyke complexes

The next stage of the work involved creating a three-dimensional geological model based on the analysis of archival geological-geophysical data [42-44]. Using geological cross-sections and diagrams of various horizons, a framework and block geological-structural model of the Enisei site were developed [33]. The lithological model includes three layers of rocks: Quaternary deposits and weathering crust formations with a thickness of up to 20 m. The upper layer consists of plagiogneisses and biotite gneisses with layers of crystalline schists. The lower layer consists of cordierite-biotite gneisses with layers of biotite and garnet-bearing gneisses (Fig.6, *a*). Disruptive disturbances on the site are represented by zones of crushing, mylonitization, tectonic breccias, and fractures without displacement (Fig.6, *b*, *c*) [33, 35]. The tectonic faults in the model are classified into major and minor disruptions. Intrusive and ultrametamorphic formations are represented by a dense network of steeply dipping metadolerite dikes with a thickness of up to 30 m (Fig.6, *d*). Disruptive disturbances on local and regional scales are detailed in the study [33]. Additionally, zones of crushing and deformation, based on geological cross-section data, were incorporated into the model. These zones closely correlate with the major faults of the site, extending to depths of up to 700 m.

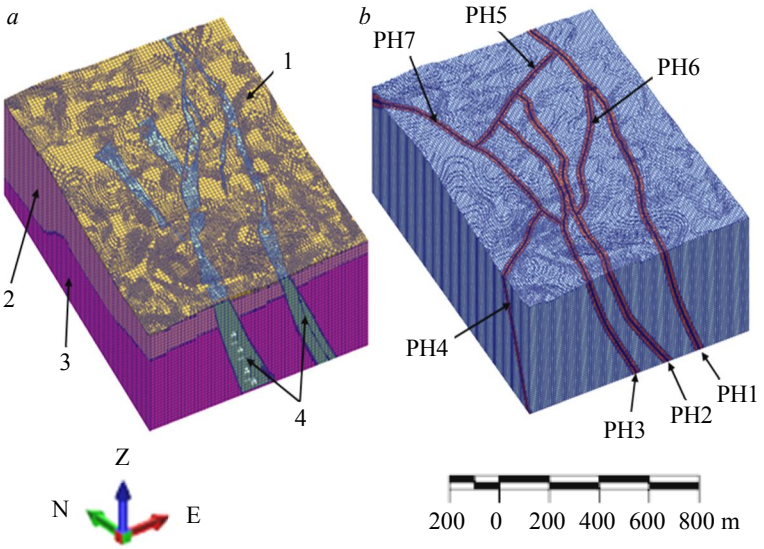

Fig.7. Structural block model and zones of dynamic influence of major fault disruptions

1 – Quaternary deposits; 2 – upper layer; 3 – lower layer; 4 – zones of increased fracturing; faults: PH1 – Verkhneshumikhinskii; PH2 – Verkhnemerkurevskii; PH3 – Merkurevskii; PH4 – Bezymyannyi; PH5 – N 5; PH6 – N 6; PH7 – N 7

The block model, constructed based on the framework model (Fig.6, *a*, *c*), represents geological structural features in the form of blocks with specific physical and mechanical properties (Fig.7, *a*). This model is used for a more detailed and accurate description of the geological structure and behavior of the rock mass.

In the framework model (see Fig.6, *b*), fault disruptions were represented as surfaces (dislocations) with zero width due to a lack of information about the thickness of the faults [33]. Using empirical relationships, the dimensions of the zones of dynamic influence of fault disruptions were determined, and based on this information, a block model was constructed (Fig.7, *b*).

Building a block model of faults with zones of dynamic influence is an important tool for variational modeling of stress-strain states, analysis, and assessment of geodynamic processes occurring in the rock mass.

Conclusion. For the safe disposal of high-level RAW, it is crucial to determine the critical properties of rock formations that influence both the long-term stability of the geological repository for RAW and the provision of safe conditions for underground mining operations. Global experience analysis has shown that empirical rating classifications are effectively used for this purpose. To assess the stability of the rock mass surrounding the underground openings of the geological repository for RAW, existing classifications have been modernized.

The modernized Q^R index incorporates parameters that consider fault zones, the strength-to-stress factor (SRF), the Q index, and others. Preliminary results of the rock mass stability assessment have indicated that the selected site is suitable for the construction of the RAW repository. It has been determined that rock mass areas within the dynamic influence zones of major tectonic faults in the region are less stable, while intrusive rocks represented by dike complexes are more stable.

A three-dimensional structural-tectonic model of the Enisei site has been developed, which will subsequently serve as the basis for numerical variational modeling of the stress-strain state of the rock mass and the creation of a comprehensive geomechanical model of the site. Building a block model with zones of dynamic influence of fault disruptions is the first step toward a deeper understanding of fault behavior and their impact on the stability and safety of rock masses. The model will help identify zones of dangerous stress concentration and plan in-situ geomechanical experiments in the underground mines of the URL.

REFERENCES

1. Dorofeev A.N., Bolshov L.A., Linge I.I. et al. Strategic Master Plan for R&D Demonstrating the Safety of Construction, Operation and Closure of a Deep Geological Disposal Facility for Radioactive Waste. *Radioactive Waste*. 2017. N 1, p. 41-42.

2. Abramov A.A., Bolshov L.A., Dorofeev A.N. et al. Underground Research Laboratory in the Nizhnekanskiy Massif: Evolutionary Design Study. *Radioactive Waste*. 2020. N 1 (10), p. 7-16. DOI: 10.25283/2587-9707-2020-1-9-21

3. Joutsenvaara J., Holma M., Kotavaara O. et al. Callio Lab – the deep underground research centre in Finland, Europe. 17th International Conference on Topics in Astroparticle and Underground Physics, 26 August – 3 September 2021, Valencia, Spain. Journal of Physics Conference Series, 2022. Vol. 2156. N 012166. DOI: 10.1088/1742-6596/2156/1/012166

4. Qiangyong Zhang, Chuancheng Liu, Kang Duan et al. True Three-Dimensional Geomechanical Model Tests for Stability Analysis of Surrounding Rock During the Excavation of a Deep Underground Laboratory. *Rock Mechanics and Rock Engineering*. 2020. Vol. 53, p. 517-537. DOI: 10.1007/s00603-019-01927-0

5. Tsebakovskaya N.S., Utkin S.S., Kapyrin I.V. et al. Obzor zarubezhnykh praktik zakhoroneniya OYaT i RAO. Moscow: Komtekhprint, 2015, p. 208 (in Russian).

6. Koyama T., Chijimatsu M., Shimizu H. et al. Numerical modeling for the coupled thermo-mechanical processes and spalling phenomena in Äspö Pillar Stability Experiment (APSE). *Journal of Rock Mechanics and Geotechnical Engineering*. 2013. Vol. 5. Iss. 1, p. 58-72. DOI: 10.1016/j.jrmge.2013.01.001

7. Saceanu M.C., Paluszny A., Zimmerman R.W., Ivars D.M. Fracture growth leading to mechanical spalling around deposition boreholes of an underground nuclear waste repository. *International Journal of Rock Mechanics and Mining Sciences*. 2022. Vol. 152. N 105038. DOI: 10.1016/j.ijrmms.2022.105038

8. Tatarinov V.N., Morozov V.N., Kaftan V.I., Manevich A.I. Modern geodynamics of the southern of the Yenisei ridge derived from the results of satellite observations. *Geophysical research*. 2018. Vol. 19. N 4, p. 64-79 (in Russian). DOI: 10.21455/gr2018.4-5

9. Kaftan V.I., Gvishiani A.D., Morozov V.N., Tatarinov V.N. Methods and results of determination of movements and deformations of the Earth's crust according to GNSS data at the Nizhne-Kansk geodynamic test network in the area of radioactive waste disposal. *Sovremennye problemy distantsionnogo zondirovaniya Zemli iz kosmosa*. 2019. Vol. 16. N 1, p. 83-94 (in Russian). DOI: 10.21046/2070-7401-2019-16-1-83-94

10. Manevich A.I., Tatarinov V.N., Kolikov K.S. Detection of crustal deformation anomalies with regard to spatial scale effect. *Eurasian mining*. 2019. N 2, p. 19-22. DOI: 10.17580/em.2019.02.04

11. Gupalo V.S. Priority parameters of physical processes in a rock mass when determining the safety of radioactive waste disposal. *Journal of Mining Institute.* 2020. Vol. 241, p. 118-124. DOI: 10.31897/PMI.2020.1.118

12. Demenkov P.A., Karasev M.A., Petrov D.N. Predicting Land-Surface Deformations During The Construction of Underground Facilities of Complex Spatial Configuration. *International Journal of Civil Engineering and Technology*. 2017. Vol. 8. Iss. 11, p. 1161-1171.

13. Liang Chen, Ju Wang, Zihua Zong et al. A new rock mass classification system QHLW for high-level radioactive waste disposal. *Engineering Geology*. 2015. Vol. 190, p. 33-51. DOI: 10.1016/j.enggeo.2015.02.006

14. Ju Wang, Liang Chen, Rui Su, Xingguang Zhao. The Beishan underground research laboratory for geological disposal of high-level radioactive waste in China: Planning, site selection, site characterization and in situ tests. *Journal of Rock Mechanics and Geotechnical Engineering*. 2018. Vol. 10. Iss. 3, p. 411-435. DOI: 10.1016/j.jrmge.2018.03.002

15. Tong Y., Yue Y., Huang Z. et al. Modified *RMR* Rock Mass Classification System for Preliminary Selection of Potential Sites of High-Level Radioactive Waste Disposal Engineering. *Sustainability*. 2022. Vol. 14 (23), p. 1-17. DOI: 10.3390/su142315596

16. Zhang Q., Liu C., Duan K. et al. True Three-Dimensional Geomechanical Model Tests for Stability Analysis of Surrounding Rock During the Excavation of a Deep Underground Laboratory. *Rock Mechanics and Rock Engineering*. 2020. Vol. 53, p. 517-537. DOI: 10.1007/s00603-019-01927-0

17. Protosenya A.G., Karasev M.A., Belyakov N.A. Numerical simulation of rock mass limit state using Stavrogin's strength criterion. *Journal of Mining Science.* 2015. Vol. 51. N 1, p. 31-37. DOI: 10.1134/S1062739115010056

18. Kovalev O.V. Engineering and geomechanical forecast for waste disposal in underground caverns including earthquake-prone zones. *Journal of Mining Institute.* 2016. Vol. 217, p. 61-71 (in Russian).

19. León Vargas R.P., Friedel M., Hassanzadegan A. et al. BARIK: an extended Hoek–Brown-based anisotropic constitutive model for fractured crystalline rock. *Safety of Nuclear Waste Disposal*. 2023. Vol. 2, p. 119-120. DOI: 10.5194/sand-2-119-2023

20. Xie He-ping, Gao Feng, Ju Yang et al. Quantitative definition and investigation of deep mining. *Journal of the China Coal Society*. 2015. Vol. 40. N 1, p. 1-10. DOI: 10.13225/j.cnki.jccs.2014.1690

21. Kocharyan G.G. Geomechanics of Faults. Moscow: GEOS, 2016, p. 424.

22. Sherman S.I., Bornyakov S.A., Buddo V.Yu. Areas of Dynamic Influence of Faults (modeling results). Novosibirsk: Nauka, Sibirskoe otdelenie, 1983, p. 112 (in Russian).

23. Wang F., Konietzky H. Thermo-Mechanical Properties of Granite at Elevated Temperatures and Numerical Simulation of Thermal Cracking. *Rock Mechanics and Rock Engineering*. 2019. Vol. 52. Iss. 10, p. 3737-3755. DOI: 10.1007/s00603-019-01837-1

24. Barton N. A review of mechanical over-closure and thermal over-closure of rock joints: Potential consequences for coupled modelling of nuclear waste disposal and geothermal energy development. *Tunnelling and Underground Space Technology*. 2020. Vol. 99. N 103379. DOI: 10.1016/j.tust.2020.103379

25. Barton N. Shear strength criteria for rock, rock joints, rockfill and rock masses: Problems and some solutions. *Journal of Rock Mechanics and Geotechnical Engineering*. 2013. Vol. 5. Iss. 4, p. 249-261. DOI: 10.1016/j.jrmge.2013.05.008

26. Eremenko V.A., Ainbinder I.I., Marsyuk V.P., Nagovitsyn Y.N. Guidelines for selecting ground support system for the Talnakh operations based on the rock mass quality assessment. *Gornyi Zhurnal.* 2018. N 10, p. 101-106 (in Russian). DOI: 10.17580/gzh.2018.10.18

27. Shaposhnik Y.N., Uskov V.A. Definitions qualitive characteristic (RQD) and rating (RMR) ore mass in the underground drive of the Skalisty mine. XIII Mezhdunarodnyi nauchnyi kongress i vystavka "Interekspo GEO-Sibir", 19-21 April 2017, Novosibirsk, Russia. Interekspo GEO-Sibir, 2017. Vol. 2. N 2, p. 99-107 (in Russian).

28. Protosenya A.G., Verbilo P.E. Research of Compression Strength of Fissured Rock Mass. *Journal of Mining Institute.* 2017. Vol. 223, p. 51-57. DOI: 10.18454/PMI.2017.1.51

29. Anderson E.B., Savonenkov V.G., Lyubtseva E.F. et al. Results of survey and research works on site selection for underground disposal of HLW and SNF in Nizhnekansk granitoid massif (South Enisei Ridge). Trudy Radievogo instituta im. V.G.Khlopina. 2006. Vol. XI, p. 8-64 (in Russian).

30. Kovalenko A.A., Zakharov N.E., Pul E.K., Zolotin V.G. Geomechanical aspects of the Internatsionalnaya kimberlite pipe mining. *Gornyi Zhurnal*. 2019. N 2, p. 27-31 (in Russian). DOI: 10.17580/gzh.2019.02.05

31. Yong Ye, Liang Chen, Jian Liu. Study on Rock Mass Classification Methods Used in the Geological Disposal of High-level Radioactive Waste. 11th Conference of Asian Rock Mechanics Society, 21-25 October 2021, Beijing, China. IOP Conference Series: Earth and Environmental Science, 2021. Vol. 861. N 4. N 042118. DOI: 10.1088/1755-1315/861/4/042118

32. Kochkin B.T., Malkovskiy V.I., Yudintsev S.V. Scientific basis for the safety assessment of long-lived radioactive waste geological disposal (the Eniseyskiy project). Moscow: IGEM RAS, 2017, p. 384 (in Russian).

33. Akmatov D.Z., Manevich A.I., Tatarinov V.N., Shevchuk R.V. 3D structure tectonics model of Yenisei site of the Nizhnekansk Massif. *Gornyi Zhurnal*. 2023. N 1, p. 69-74 (in Russian). DOI: 10.17580/gzh.2023.01.11

34. Kochkin B.T. Investigating the Geological Environment at the Yeniseisky Site: Tasks for the Current Stage of the Disposal Project. *Radioactive Waste.* 2019. N 2 (7), p. 76-91 (in Russian). DOI: 10.25283/2587-9707-2019-2-76-91

35. Morozov O.A., Rastorguev A.V., Neuvazhaev G.D. Assessing the State of the Geological Environment at the Yeniseyskiy Site (Krasnoyarsk Region). *Radioactive Waste.* 2019. N 4 (9), p. 46-62. DOI: 10.25283/2587-9707-2019-4-46-62

36. Tarasov B.G. Fan mechanism of dynamic shear fractures as a source of strength and brittleness paradoxes in rocks. *Gornyi Zhurnal.* 2020. N 1, p. 18-23 (in Russian). DOI: 10.17580/gzh.2020.01.03

37. Biryuchev I.V., Makarov A.B., Usov A.A. Geomechanical model of underground mine. Part I. Creation. *Gornyi Zhurnal.* 2020. N 1, p. 42-48 (in Russian). DOI: 10.17580/gzh.2020.01.08

38. Abdulla H. Al Nuaimi, Williams L.G. Sensitivity study of risk to future generations from geological disposal of radioactive waste in high strength rock in the UAE. *Journal of Radiation Research and Applied Sciences*. 2022. Vol. 15. Iss. 3, p. 218-231. DOI: 10.1016/j.jrras.2022.06.013

39. Gunzburger Y., Magnenet V. Stress inversion and basement-cover stress transmission across weak layers in the Paris basin, France. *Tectonophysics*. 2014. Vol. 617, p. 44-57. DOI: 10.1016/j.tecto.2014.01.016

40. Leontyev A.V., Rubtsova Y.V., Skulkin A.A. To the estimate of stress-strain state of the rock mass in the Nizhnekansky region. XVI Mezhdunarodnyi nauchnyi kongress i vystavka "Interekspo GEO-Sibir", 18 June – 8 July 2020, Novosibirsk, Russia. Interekspo GEO-Sibir, 2020. Vol. 2, p. 109-116 (in Russian). DOI: 10.33764/2618-981X-2020-2-109-116

41. Eremenko V.A., Vinnikov V.A., Kosyreva M.A., Lagutin D.V. Identification of rock jointing parameters by borehole imaging and interval geotechnical documentation of non-oriented drill cores. *Gornyi Zhurnal*. 2022. N 1, p. 21-26. DOI: 10.17580/gzh.2022.01.04

42. Xuechao Wu, Gang Liu, Zhengping Weng et al. Constructing 3D geological models based on large-scale geological maps. *Open Geosciences*. 2021. Vol. 13. Iss. 1, p. 851-866. DOI: 10.1515/geo-2020-0270

43. Biryuchev I.V., Makarov A.B., Usov A.A. Geomechanical model of underground mine. Part II. Application. *Gornyi Zhurnal*. 2020. N 2, p. 35-44 (in Russian). DOI: 10.17580/gzh.2020.02.04

44. Kurtsev B.V., Fedotov G.S. MICROMINE-based geomechanical supervision of mining. *Gornyi Zhurnal*. 2022. N 1, p. 45-50 (in Russian). DOI: 10.17580/gzh.2022.01.08

***Authors*: Dastan Zh. Akmatov,** *Junior Researcher, Postgraduate Student, https://orcid.org/0000-0001-6435-464X* (*Geophysical Center of the RAS*, *Moscow*, *Russia*; *National University of Science and Technology "MISIS"*, *Moscow*, *Russia*), **Aleksandr I. Manevich,** *Researcher, Senior Lecturer, https://orcid.org/0000-0001-7486-6104* (*Geophysical Center of the RAS*, *Moscow*, *Russia*; *National University of Science and Technology "MISIS"*, *Moscow*, *Russia*), **Viktor N. Tatarinov,** *Corresponding Member RAS*, *Doctor of Engineering Sciences*, *Head of Laboratory, Leading Researcher, victat@wdcb.ru*, *https://orcid.org/0000-0001-7546-2072* (*Geophysical Center of the RAS*, *Moscow*, *Russia*; *Schmidt Institute of Physics of the Earth RAS*, *Moscow*, *Russia*), **Roman V. Shevchuk,** *Junior Researcher, Postgraduate Student*, *Junior Researcher, https://orcid.org/0000-0003-3461-6383* (*Geophysical Center of the RAS*, *Moscow*, *Russia*; *National University of Science and Technology "MISIS"*, *Moscow*, *Russia*; *Schmidt Institute of Physics of the Earth RAS*, *Moscow*, *Russia*), **Sergei M. Zabrodin,** *Chief Specialist, https://orcid.org/0000-0003-2834-9311* (*Geophysical Center of the RAS*, *Moscow*, *Russia*).

The authors declare no conflict of interests.

ISSN 2411-3336; e-ISSN 2541-9404

JOURNAL OF MINING INSTITUTE
Zapiski Gornogo instituta
Journal homepage: pmi.spmi.ru

Research article

Depth distribution of radiation defects in irradiated diamonds by confocal Raman spectroscopy

Rajendra M. Ardalkar, Yogesh D. Salunkhe, Mahesh P. Gaonkar, Sandesh N. Mane, Omkar A. Ghaisas, Shripalkumar N. Desai, Annareddy V.R. Reddy✉
Gemmological Institute of India, Mumbai, India

***How to cite this article*:** Ardalkar R.M., Salunkhe Y.D., Gaonkar M.P., Mane S.N., Ghaisas O.A., Desai S.N., Reddy A.V.R. Depth distribution of radiation defects in irradiated diamonds by confocal Raman spectroscopy. Journal of Mining Institute. 2024. Vol. 266, p. 179-187.

Abstract. Five colored diamonds were investigated. According to the results of the study by FTIR, UV-Vis-NIR and Photolumines-cence spectroscopy, they are natural type Ia diamonds. The depth distribution of the color intensity was carried out by meas-uring the intensity of the PL peak at 741 nm (GR1 center) upon excitation by a laser with a wave-length of 633 nm of Raman Confocal microscope. To minimise the perturbation due to geometrical effects, defect distribution profiles were normalised with respect to diamond Raman peak intensity (691 nm) point by point. For two diamonds, the intensity of the GR1 peak (741 nm) sharply decreased to a depth of 10 μm, and then became equal to the background level, which is typical for irradia-tion with alpha particles from natural sources like uranium. In other diamonds, the profiles vary slightly with depth, and the color intensity is close to uniform, which is for irradiation with accelerated electrons or neutrons. The source of radiation has not been determined. However, long duration radioacti-vity measurements of the diamonds suggested that neutrons were not used for colour centers production in the diamonds studied.

***Keywords*:** confocal Raman microscopy; coloured diamond; depth profile; ionising radiation; irradiation; photolumines-cence; normalization; GR1

Received: 10.02.2023 ***Accepted: 20.09.2023*** ***Online: 10.01.2024*** ***Published: 25.04.2024***

Introduction. Defects of intrinsic or impurity nature are known to impart color in many diamonds [1]. Colorless diamonds are the most expensive, but some fancy color diamonds are also in demand [2]. Research on bleaching of diamonds or enhancing the intensity of fancy colors remains relevant. The two most common methods used for this purpose are high-pressure high temperature (HPHT) treatment [3] and exposing diamonds to controlled doses of high energy ionizing radiations, often followed by HPHT treatment. Irradiation of diamonds with neutrons, energetic electrons, or α-particles creates radiation defects (vacancies and interstitial atoms) in the diamond, which absorb part of the visible spectrum. This leads to a change in the color of the diamond crystal from blue-green to brown [4]. A diamond would receive a radiation dose in natural conditions by contacting with natural radioactive substances, for example, uranium and its decay products [5]. The depth of penetration of α-particles into diamond does not exceed 30 μm. Thus during the contact irradiation with α-particles around the contact point, so-called pigmentation spots-colored areas would be formed.

To improve color of diamonds in the laboratory, they are exposed to high-energy electrons or γ-rays [6]. Energy of the radiation is so chosen such that exposure does not cause nuclear reactions to form residual radioactivity* [7-11]. Range and energy of the radiation** are crucial for choosing it for irradiation of diamonds. Color centers and their distribution in the bulk of crystals are usually

* Regulation for the Safe Transport of Radioactive Material. 2018 Ed. Specific Safety Requirements. IAEA Safety Standards Series N SRR-6 (Rev. 1).

** Knoll G.F. Radiation Detection and Measurements. New York: John Wiley & Sons Inc., 1999, p. 802.

investigated by spectroscopy. Typically, photoluminescence (PL) spectra of diamonds are obtained by excitation with a suitable laser. When using a laser with a wavelength of 633 nm, a noticeable observed feature in the PL spectrum of diamond exposed to ionizing radiation is a peak at 741 nm, corresponding to the center of the GR1 – neutral vacancy [12].

Confocal Raman spectroscopy with a spatial resolution of about 0.1 μm [13] is one of the universal tools for measuring the depth distribution of defects in thin films, polymer composites, solids, including diamonds, etc. Compared to other methods [14-16], confocal Raman microscopy gives poorer resolution, but other advantages make it very suitable for measuring the depth distribution of defects, especially for solids such as diamonds.

In this work, the depth distribution of defects in five colored diamonds was studied, and the characteristics of the IR and UV-visible regions were measured by spectroscopy. The aim of the work is to determine whether these crystals were exposed to ionising radiation.

Methods. Physical properties of the five samples investigated are given in Table.

Diamonds description

Name *	Weight, carats**	Colour	Cut	Type ***
S.G.1	3.12	Tinted Green	Rough	Ia
S.G.2	4.83	Tinted Green	Rough	Ia
T.B.1	0.015	Blue	R.B.C.	IaA
T.B.2	3.23	Blue	Rough	IaAB
T.B.3	12.13	Bluish Green	Rough	Ia

* Names of the samples are given, after initial investigations, as T.B. for treated diamonds and S.G. for diamonds exposed to short range radiation in the earth crust or in the lab.

** 1 carat = 200 mg.

*** Types of the diamonds are identified by FTIR spectral measurements.

Images of the diamonds. The optical images of the five diamonds were captured under white light by using Canon EOS 90D Digital SLR Camera with 18-135 IS USM Lens. Luminescence (fluorescence and phosphorescence) images for all the diamonds were obtained using the De Beers Diamond View which has an UV excitation source (≤ 230 nm). These images were used to examine the growth patterns.

Spectroscopic measurements. IR absorption measurements were made using Thermo Nicolet iS50 FTIR with DRIFT accessory and DLaTGS (deuterated L-alanine doped triglycine sulphate) detector. Spectra were recorded with 100 scans in the range of 8,000 to 400 cm^{-1} with a resolution of 4 cm^{-1} at room temperature.

UV-Vis absorption spectra were recorded in the range of 200 to 800 nm, with Cary Varian 5000 UV-Vis-NIR spectrometer having sources of Deuterium lamp for UV region and Tungsten Halogen for Visible and IR regions. This system has a PMT (photo multiplier tube) as the detector for UV-Visible region and polycrystalline lead sulfide (PbS) detector for IR region. Measurements were made at liquid nitrogen temperature, 77 K.

Photoluminescence spectra were measured with the Renishaw InVia Reflex Raman Spectrometer having confocal optics and CCD (charge coupled device) detector. We chose 100× objective lens that has a laser working distance of 0.33 mm between the lens and the sample. We used only two laser sources, 405 nm (for spectral range of 407 to 743 nm) and 633 nm (for spectral range 637 to 991 nm) for spectral studies. 633 nm laser source was chosen for defect distribution measurements. Spectral measurements were made at 77 K temperature. On the other hand, depth profile measurements were carried out at room temperature with an interval of 4 μm in air by tagging 741 nm peak

(GR1 centre) using 633 nm laser. Measurements were carried out through an inbuilt software controlled programme.

The distribution of GR1 centre as a function of depth. Our confocal Raman spectrometer has a spatial resolution of 0.1 μm and higher. *Z* distance was changed stepwise using a motorised *X-Y* plane platform of the object (diamond sample) and *Z* movement was software controlled. A provision is available to acquire spectra up to 200 μm. Prolonged measurements at liquid nitrogen temperature result in precipitation of fog on the surface of the diamond and could affect PL signal. Hence, these measurements were carried out at room temperature. From the analysis of GR1 data as a function of depth on one diamond, showed that required information was obtained from the profiles in the depth range starting from 0 to 60 μm and therefore we collected data for all other diamonds from 0 to 60 μm.

Peak area analysis. Our confocal Raman spectrometer has an inbuilt Spectrum analysis programme. After acquiring the spectrum, the displayed spectrum was taken into analysis mode. This inbuilt programme has a provision in the tools "curve fit" which identifies peak position, calculates peak intensity (peak areas) and peak (centroid) counts, and the results for all the peaks are displayed. They contain both gross and background subtracted data. This inbuilt programme identifies both the minima counts on the left side and right side of a chosen peak (*L* and *R*), through an inbuilt software in which successive differentiation is used. Background counts corresponding to *L* and *R* channels are taken as a five point average around minima. Counts in the small interval between *L* and *R* is assumed to vary linearly. Thus the background for each peak is calculated by trapezium rule, peak area is computed by subtracting background from integrated area. In the case of peak counts, software recognizes the channel corresponding to that peak (centroid) and peak count is obtained by subtracting background corresponding to centroid.

Spectrum analysis was also carried out by us as a crosscheck using origin software (Gaussian). The results obtained by both origin and inbuilt programmes were reproducible.

The range of peak areas is from 80,000 to background level whereas for peak count it is 10,000 to background level. In all the cases the reported peak areas are much above background level and thus are significant.

Results and discussion. All the five diamonds investigated in this work were characterised by examining the images obtained by Diamond View as well as by spectroscopic techniques.

Diamond images. The optical images of the five diamonds are given in Fig.1. Luminescence images obtained by Diamond View are shown in Fig.2. In the Diamond View, all the diamonds except T.B.1 showed blue fluorescence with no phosphorescence, where as T.B.1 showed Green fluorescence with blue patches. The observed growth patterns confirmed that the diamonds are natural. The observed blue fluorescence is because of the presence of N3 centre (415 nm). Interestingly E.Vasilev et al. observed heterogeneous distribution of optical centres in a diamond along with blue fluorescence which was attributed to N3 centre [17].

Fig.1. Optical images of diamonds investigated

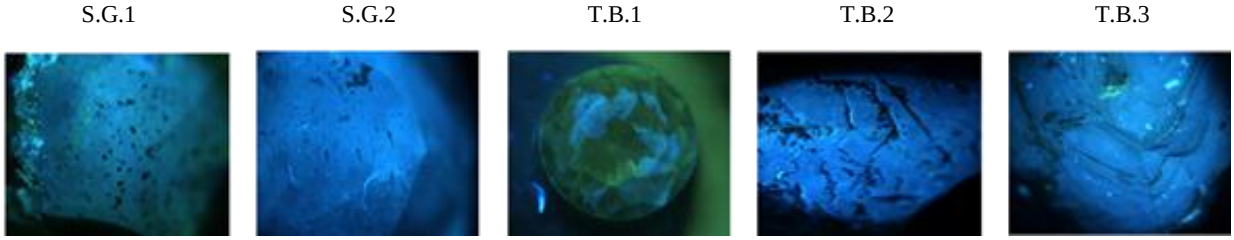

Fig.2. Luminescence images of diamonds under Diamond View (UV < 230 nm)

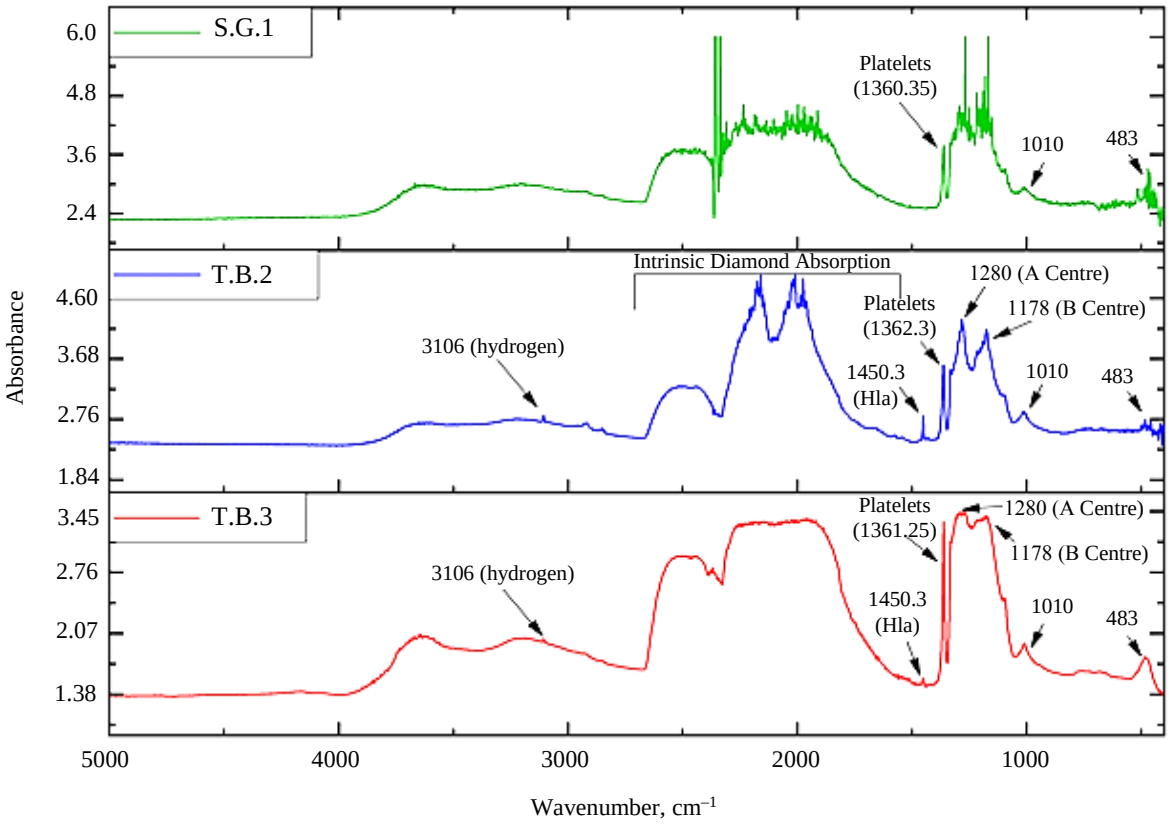

Fig.3. FT-IR Spectra of S.G.1, T.B.2 and T.B.3

FTIR spectra. IR absorption spectra were recorded to characterise diamonds and many investigators used FTIR to obtain absorption spectra for identifying and characterising the types of centres present in the diamonds [18, 19]. FTIR spectra of all the five diamonds showed signature peaks of type Ia natural diamonds corresponding to A (1282 cm^{-1}) and B (1178 cm^{-1}) centres which are due to nitrogen aggregation in diamonds. IR spectra of S.G.1, T.B.2 & T.B.3 are given in Fig.3 for spectral comparison. All the prominent absorption peaks in the spectra are labelled.

A broad band was observed around 482.33 cm^{-1} which is attributed to A centre. A sharp platelet peak was observed in the range of 1360 cm^{-1} to 1370 cm^{-1} and it is commonly associated with type Ia natural diamonds. Peaks at 3106 cm^{-1} and 1010.36 cm^{-1} were seen, as expected, generally in hydrogen containing diamonds which are due to carbon hydrogen (C–H) bond vibration. A weak peak at 1450.30 cm^{-1} (H1a centre) was present in T.B.2 and T.B.3, but absent in S.G.1. The observed H1a centre is due to electron beam irradiation and annealing [20]. The absence of H1a peak in the IR spectrum of S.G.1 could be that the diamond might not have been annealed after irradiation.

UV-Vis NIR spectra. The absorption spectra of the five diamonds were measured at 77 K temperature. Two spectra corresponding to S.G.1 and T.B.1 are given in Fig.4.

Spectra of S.G.1 & S.G.2 diamonds showed an absorption peak at 415 nm (N3) which is the most common feature of type Ia natural diamonds [21]. A weak peak at 503 nm due to H3 centre was also observed. Spectrum of S.G.1 had an absorption peak at 496 nm due to H4 centre. Both H3 and H4 centres occur in diamonds that are exposed to natural or artificial radiations.

The absorption spectrum of T.B.3 has similar features like those observed in the spectrum of T.B.1 that showed a huge absorption in the region of 350-380 nm. It is observed that in the absorption spectra of diamonds T.B.1, T.B.2 and T.B.3, the most prominent peak was found at 741 nm which is due to GR1 centre. It is an artefact of exposure of diamonds to ionising radiation (natural or artificial) [12]. Peak at 394 nm (ND1 centre) was present in T.B.1 and T.B.3, and weak signals at 430, 503 and 723 nm were also seen. G.Davies and A.T.Collins [22] reported that more neutral vacancies V^0 (GR1 centre) were present than those of V^- (ND1 centre) in the diamonds exposed to electron beam irradiation followed by annealing. A peak at 595 nm was seen in the absorption spectra of T.B.1 and T.B.3

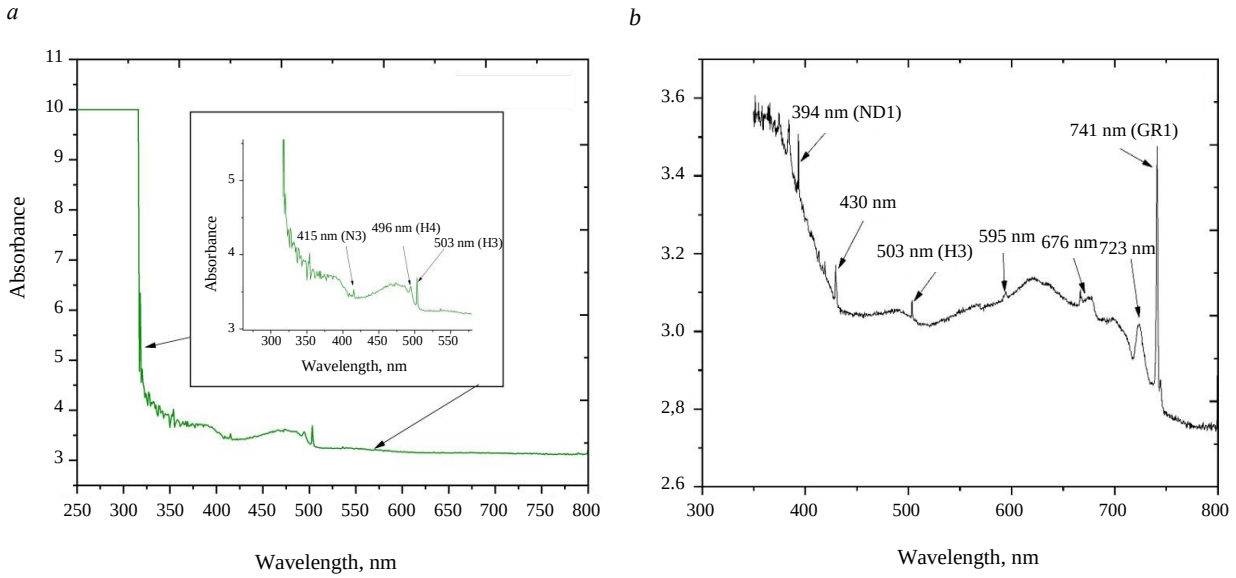

Fig.4. UV-Vis-NIR absorption spectra: *a* – S.G.1; *b* – T.B.1

which is attributed to primary radiation damage and annealing*. A similar observation was made by A.Osvet et al. and they reported that these defects were also created by neutron irradiation in type Ia natural diamonds [23]. Peaks at 676 and 723 nm were observed in T.B.1 and T.B.3 spectra which are due to exposure to high energy radiation and subsequent annealing at high temperature. However, it could not be seen in the absorption spectrum of intense blue coloured T.B.2 diamond. In this case absorption was saturated in the regions of 200 to 400 nm and 550 to 670 nm, and thus the peaks expected at 394, 595 and 676 nm were engulfed.

Photoluminescence spectra. Luminescence (photo-, cathodo-, thermo-luminescence etc.) spectra of diamond provide characteristic emission peaks for identification of colour centres and defects [24-28]. PL spectra of the five diamonds were measured at liquid nitrogen temperature (77 K) using 405 nm and 633 nm laser excitations and are given in Fig.5.

PL spectra of diamonds obtained with 405 nm laser excitation showed an intense peak at 415 nm, due to strong N3 centre. Presence of this peak in all the five spectra indicates that these diamonds are natural diamonds which is a corroboration to IR and UV spectral observations. Photoluminescence spectra of diamonds S.G.1 and S.G.2 showed peaks at 415 nm (N3) and 503 nm (H3). PL spectrum

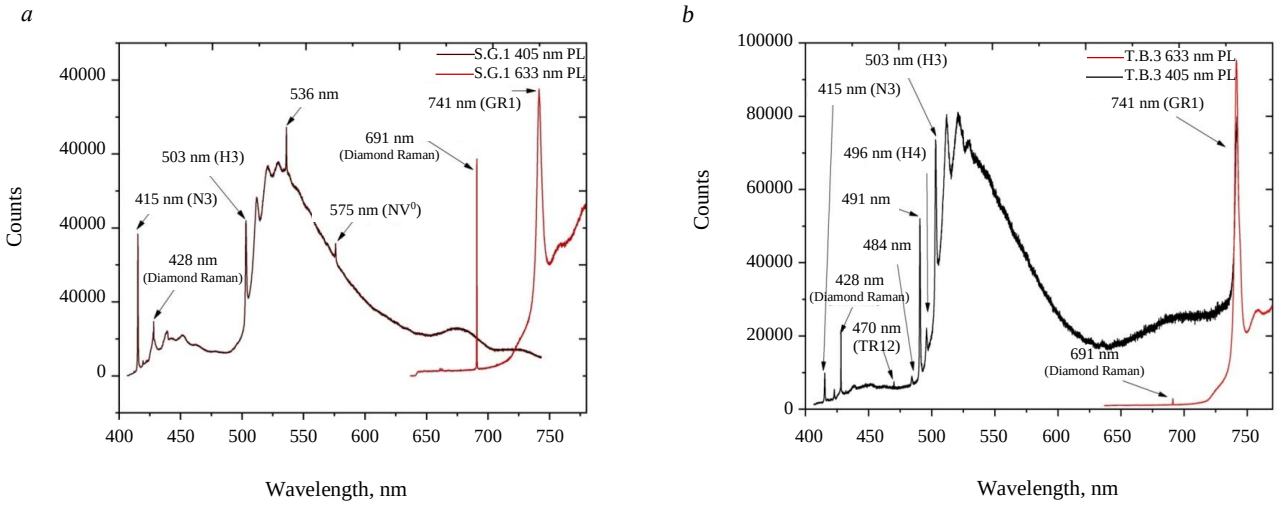

Fig.5. PL spectra of S.G.1 (*a*) and T.B.3 (*b*) with 405 and 633 nm laser excitations

* Zaitsev A.M. Optical Properties of Diamond. Berlin: Springer – Verlag, 2001, p. 213.

of S.G.1 also showed a peak at 536 nm which is present in natural diamonds. This is an indication of radiation damage*. A weak peak at 470 nm (TR12 centre) is also observed in the spectrum of T.B.3. It is reported that TR12 occurs due to high energy irradiation of both natural and synthetic diamonds [29]. The observed peak at 575 nm is due to the presence of NV^0 centre. This centre is reported to be present in the nitrogen-containing natural and synthetic diamonds. An intense PL Peak at 503 nm corresponding to H3 centre was present in the spectra of all the diamonds except that of S.G.2. A feeble peak at 503 nm could be observed for S.G.2 using a higher laser power of 10 % (36 mW) instead of 1 % (3.6 mW) used for other diamonds.

Distribution of GR1 centre as a function of depth. Methods for changing the colour of the diamond were evolved over the years and reviewed by various investigators [11, 30, 31]. Uniform surface coloration can be achieved if the diamond is completely covered by uranium mineral or with an alpha source in a laboratory. Such exposures resulting in uniform colouration of the diamond might rarely occur in the earth's crust. On the other hand, diamonds exposed to artificial ionising radiations like high energy electron beams produce colour centres throughout the bulk [4]. Exposure of diamonds to high energy neutrons or electrons cause changes in the diamonds and these changes were studied before and after annealing the diamonds [25]. Depth and intensity of the colour depends on the energy and exposure dose of the ionising radiation respectively. It is also possible that the irradiated diamonds might be subjected to HPHT to optimise colour intensity [30]. In the case of diamonds, GR1 centres are expected to be produced along the path of the interaction of ionising radiations. While treating with artificial irradiation, generally care is taken to expose diamonds from all the directions so that colour is imparted in the entire volume of the diamond. Therefore depth profiles in coloured diamonds in the present work were measured from different directions using confocal Raman microscope.

A series of spectra as a function of depth were acquired to visualise 3D picture of the defect distribution (Fig.6).

In all the spectra, peak areas and peak counts at the centroid corresponding to GR1 centre (741 nm) as well as diamond Raman line (691 nm) were computed. By examining the data, it is clear that qualitatively the distributions obtained using peak area and peak counts for a chosen diamond are similar, and nearly parallel. Therefore in further analysis, only peak counts as a function of depth were used.

N.J.Everall [13] and N.A.Freebody et al. [32] reported a detailed description to obtain precise depth profiles using confocal Raman microscopy and stated that the resolution obtained is inferior compared to other techniques. As the aim of the present investigation is to examine the GR1 defect distribution for the type of radiation used and not to determine the exact depth, quality of resolution was not an influencing factor in this study.

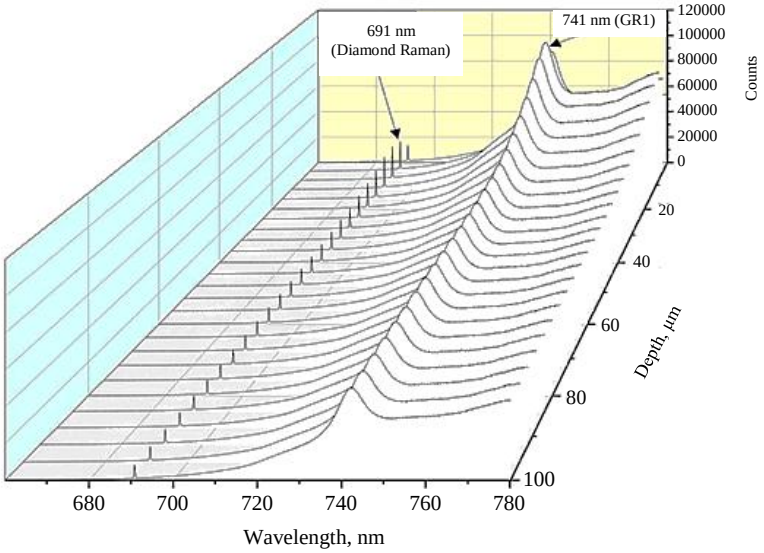

Fig.6. Spectra as a function of Depth of T.B.2 with 633 nm laser excitation

* Zaitsev A.M. Optical Properties of Diamond. Berlin: Springer – Verlag, 2001, p. 244, 285, 279, 290, 317.

Peak counts were normalised *in situ* with respect to intensity of one of the emission lines, which is present in the same spectrum. In a similar situation, pertaining to nuclear fission and nuclear reaction studies [33, 34] one of the authors used an internal normalisation method. Only condition was that the chosen emission line (in γ-spectrometry) should be present in every spectrum and has to have a correlation to the reaction under study. Similar treatment was applied in the present studies as each spectrum has a Raman diamond line, peak intensity of which depends on the laser intensity, diamond weight, detection efficiency etc. Therefore diamond line has been used for *in situ* normalising the intensity of 741 nm peak, point by point as a function of depth. On this premise, GR1 data were divided point by point by corresponding Raman peak areas that were normalised with respect to laser power. A similar normalisation procedure was used by S.C.Lawson et al [35] and E.A.Vasiliev et al. [36]. Normalised data were used to obtain defect distributions which are given in Fig.7.

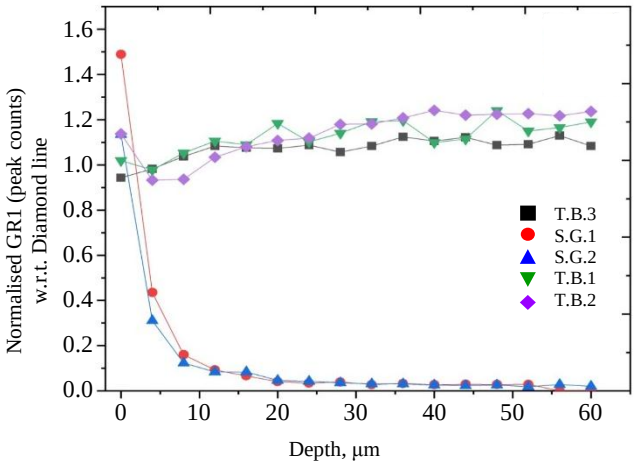

Fig.7. Depth profile of all diamonds using normalised GR1 peak counts

From Fig.7 it is clear that in the profiles of S.G.1 and S.G.2 intensity decreased drastically initially and later became nearly a parallel line to X-axis with slow (no change) in the peak counts as a function of depth. Thus both the curves showed two distinct slopes, a rapid reduction in the peak counts up to 10 μm and from there onwards with slow (no change). This indicates that the colour of the diamonds is only a few μm deep from the surface. This confirms that these two diamonds might have been exposed to short range α-radiations. Thus the presence of GR1 centre could be due to interaction of α-rays, with diamond, either produced from an α emitting source like Uranium in earth's crust or from an α emitting source in the laboratory. This also could be achieved in the laboratory by exposing diamonds to low energy heavy ion beams. Observed uniform colouration indicates that these diamonds could have been further treated.

Defect distribution profiles of other three diamonds are also given in Fig.7 with squares (T.B.3), inverted triangles (T.B.1) and rhombuses (T.B.2). In all the three profiles, an initial slow rise is observed up to around 10 μm and there onwards started decreasing slowly [37]. Initially the laser working distance is kept at maximum which corresponds to surface (zero depth) of the diamond. Thus the peak area and peak counts corresponding to GR1 are due to excitation by laser and emission of GR1 from the atoms on the surface of the sample. As the laser is brought closer to the diamond surface, laser beam penetrates more depth in the diamond and interacts with more GR1 centres resulting in an increase of intensity of GR1 peak. It is possible that some of the 741 nm photons, while penetrating through the diamond layers might get self-attenuated before coming out of the surface, that results in the reduction of intensity. It is also possible that other defects in the diamonds, if present in the path could also influence the intensity by absorbing emitted PL photons. Net result is an increase in the intensity of 741 nm PL peak.

After reaching a maximum intensity, rate of emission of 741 nm (GR1 centre) could become constant with the depth whereas self-attenuation of these photons and loss due to absorption by other defects will continue. This might result in a slow decrease in the intensity of 741 nm as a function of depth as shown in Fig.7.

From this, the depth of GR1 in S.G.1 and S.G.2 diamonds was estimated as about 10 μm. In the case of artificially irradiated diamonds the near parallel curves (lines) to X axis suggest that the radiation effect is nearly uniform. This could be due to the volumetric effect of artificial irradiation of diamonds and/or diamonds after exposure could have been further treated. It is possible that the observed decrease in the intensity (Fig.7) could be used to find out the range of the radiation used. However, no attempt is made to calculate the same, as it is not the main objective of these studies.

Conclusions. Five coloured diamonds were investigated to find out whether they were exposed to natural/artificial radiation. IR, UV-Vis and PL spectral studies were used to characterise these diamonds as type Ia natural diamonds. From UV-Vis and PL spectra, it was found that three diamonds were exposed to long range artificial radiation. This was further confirmed from the measured defect distribution profiles of all the five diamonds, measured by tagging PL peak at 741 nm (GR1 centre) using Confocal Raman Microscope with laser 633 nm as an excitation source. GR1 depth distributions of S.G.1 and S.G.2 diamonds showed two slopes, one corresponding to the contact of diamonds with materials like uranium and its daughter products in the earth's crust which emit short ranged ionising α particles as well as long ranged β and γ rays. Second slope is due to exposure to only long ranged β and γ rays. It is also possible that these diamonds might have been exposed to α-radiations from alpha sources like uranium, in the laboratory. As a function of depth, the second part of the curve became nearly parallel to X-axis. In the case of T.B.1, T.B.2 and T.B.3 diamonds, depth distribution profiles showed initial rise up to 10 μm and later a slow decrease was observed. When normalised with respect to diamond line intensity, the curves became nearly parallel to X-axis. This indicates that the GR1 centres are present uniformly throughout the volume of these diamonds. This could have been achieved by exposing to ionising radiations like long ranged electron beam followed by annealing.

Thanks are due to Dr. Anik Goswami for his help during the preparation of the manuscript.

REFERENCES

1. Magaña S.E., Ardon T., Smit K.V. et al. Natural-Color Pink, Purple, Red, and Brown Diamonds: Band of Many Colors. *Gems & Gemology*. 2018. Vol. 54. N 4, p. 352-377. DOI: 10.5741/GEMS.54.4.352

2. King J.M. Gems & Gemology in Review: Coloured Diamonds. Carlsband: The Gemological Institute of America, 2006. 317 p.

3. Fisher D. Brown diamonds and high pressure high temperature treatment. *Lithos*. 2009. Vol. 112. S. 2, p. 619-624. DOI: 10.1016/j.lithos.2009.03.005

4. Campbell B., Mainwood A. Radiation Damage of Diamond by Electron and Gamma Irradiation. *Physica status solidi (a)*. 2000. Vol. 181. Iss. 1, p. 99-107. DOI: 10.1002/1521-396X(200009)181:1<99::AID-PSSA99>3.0.CO;2-5

5. Vasilev E.A., Kozlov A.V., Petrovsky V.A. Volume and Surface Distribution of Radiation Defect in Natural Diamonds. *Journal of Mining Institute*. 2018. Vol. 230, p. 107-115. DOI: 10.25515/PMI.2018.2.107

6. Shigley J.E. Gems & Gemology in Review: Treated Diamonds. Carlsband: The Gemological Institute of America, 2005. 301 p.

7. Desai S.N. Radiation induced colour enhancement of diamonds. International conference on peaceful uses of atomic energy, 29 September – 1 October 2009, New Delhi, India. Proceedings of international conference on peaceful uses of atomic energy, 2009. Vol. 2, p. 589-590.

8. Sahavat S., Kornduangkaeo A., Thongcham K. et al. Color Enhancement of Natural Type Ia Diamond Using a Neutron-Irradiation and Annealing Method. *Kasetsart Journal (Natural Science)*. 2009. Vol. 43. Iss. 1, p. 216-229.

9. Crookes W. On the Action of Radium Emanations on Diamond. *Proceedings of the Royal Society of London*. 1904. Vol. 74. Iss. 497, p. 47-49. DOI: 10.1098/rspl.1904.0077

10. Jaewon Park, Jaehyung Lee, Changwon Sohn, Byungho Choi. Patent N 7604846 US. Manufacturing method of colored diamond by ion implantation and heat treatment. Publ. 20.10.2009.

11. Khmelnitsky R.A., Dravin V.A., Tal A.A. et al. Damage accumulation in diamond during ion implantation. *Journal of Materials Research*. 2015. Vol. 30. Iss. 9, p. 1583-1592. DOI: 10.1557/jmr.2015.21

12. Clark C.D., Norris C.A. Photoluminescence associated with the 1.673, 1.944 and 2.498 eV centres in diamond. *Journal of Physics C: Solid State Physics*. 1971. Vol. 4. N 14, p. 2223-2229. DOI: 10.1088/0022-3719/4/14/036

13. Everall N.J. Modelling and Measuring the Effect of Refraction on the Depth Resolution of Confocal Raman Microscopy. *Applied Spectroscopy*. 2000. Vol. 54. Iss. 6, p. 773-782. DOI: 10.1366/0003702001950382

14. Suzuki S., Kakita K. A Comparative Study of GDOES, SIMS and XPS Depth Profiling of Thin Layers on Metallic Materials. *Journal of Surface Analysis*. 2005. Vol. 12. Iss. 2, p. 174-177.

15. Babu S.R., Preisser N., Michelic S.K. Image Processing Procedure to Evaluate Inclusion Dissolution in a Slag Observed by High-Temperature Confocal Scanning Laser Microscopy. *Metals*. 2022. Vol. 12. Iss. 4. N 531. DOI: 10.3390/met12040531

16. Datta J., Biswas H.S., Rao P. et al. Study of depth profile of hydrogen in hydrogenated diamond like carbon thin film using ion beam analysis techniques. *Nuclear Instruments and Methods in Physics Research Section B: Beam Interactions with Materials and Atoms*. 2014. Vol. 328, p. 27-32. DOI: 10.1016/j.nimb.2014.02.127

17. Vasilev E., Petrovsky V., Kozlov A. et al. The story of one diamond: the heterogeneous distribution of the optical centres within a diamond crystal from the Ichetju placer, northern Urals. *Mineralogical Magazine*. 2019. Vol. 83. Iss. 4, p. 515-522. DOI: 10.1180/mgm.2019.32

18. Collins A.T., Spear P.M. Optically active nickel in synthetic diamond. *Journal of Physics D: Applied Physics*. 1982. Vol. 15. N 12, p. L183-L187. DOI: 10.1088/0022-3727/15/12/006

19. Collins A.T. Optical Centres Produced in Diamond by Radiation Damage. *New Diamond and Frontier Carbon Technology*. 2007. Vol. 17. N 2, p. 47-61.

20. Woods G.S., Collins A.T. The 1450 cm^{-1} infrared absorption in annealed, electron-irradiated type I diamonds. *Journal of Physics C: Solid State Physics*. 1982. Vol. 15. N 26, p. L949-L952. DOI: 10.1088/0022-3719/15/26/013

21. Yeliseyev A.P. Thermostimulated Luminescence and Delayed Luminescence of Natural Diamonds: Avtoref. dis. … kand. fiz.-mat. nauk. Sverdlovsk: Ural'skii politekhnicheskii institut im. S.M. Kirova, 1977, p. 20 (in Russian).

22. Davies G., Collins A.T. Vacancy complexes in diamond. *Diamond and Related Materials*. 1993. Vol. 2. Iss. 2-4, p. 80-86. DOI: 10.1016/0925-9635(93)90035-Z

23. Osvet A., Palm V., Sildos. I. Spectral hole burning and uniaxial stress study of radiation-induced defects in diamond. *Journal of Applied Physics*. 1996. Vol. 79. Iss. 11, p. 8290-8293. DOI: 10.1063/1.362469

24. Breeding C.M., Eaton-Magña S., Shigley J.E. Natural-Color Green Diamonds: A Beautiful Corundum. *Gems and Gemology*. 2018. Vol. 54. N 1, p. 2-27. DOI: 10.5741/GEMS.54.1.2

25. Hainschwang T., Respinger A., Notari F. et al. A comparison of diamonds irradiated by high fluence neutrons or electrons, before and after annealing. *Diamond and Related Materials*. 2009. Vol. 18. Iss. 10, p. 1223-1234. DOI: 10.1016/j.diamond.2009.04.011

26. Vasilev E., Kriulina G., Klepikov I. Luminescence of natural diamond in the NIR range. *Physics and Chemistry of Minerals*. 2020. Vol. 47. Iss. 7. N 31. DOI: 10.1007/s00269-020-01099-2

27. Sastry M.D., Gaonkar M.P., Nagar Y.C. et al. Optically stimulated luminescence (OSL) and laser excited photo luminescence of electron beam treated (EBT) diamonds: Radiation sensitization and potential for tissue equivalent dosimetry. *Diamond and Related Materials*. 2011. Vol. 20. Iss. 8, p. 1095-1102. DOI: 10.1016/j.diamond.2011.06.012

28. Vasilev E., Zedgenizov D., Zamyatin D. et al. Cathodoluminescence of Diamond: Features of Visualization. *Crystals*. 2021. Vol. 11. Iss. 12, p. 1522. DOI: 10.3390/cryst11121522

29. Davies G., Foy C., O'Donnell K. The TR12 vibronic band in diamond. *Journal of Physics C: Solid State Physics*. 1981. Vol. 14. N 28, p. 4153-4165. DOI: 10.1088/0022-3719/14/28/016

30. Collins A.T., Kanda H., Kitawaki H. Colour changes produced in natural brown diamonds by high-pressure, high-temperature treatment. *Diamond and Related Materials*. 2000. Vol. 9. Iss. 2, p. 113-122. DOI: 10.1016/S0925-9635(00)00249-1

31. Collins A.T. The colour of diamond and how it may be changed. *The Journal of Gemmology*. 2001. Vol. 27. Iss. 6, p. 341-359. DOI: 10.15506/jog.2001.27.6.341

32. Freebody N.A., Vaughan A.S., Macdonald A.M. On optical depth profiling using confocal Raman spectroscopy. *Analytical and Bioanalytical Chemistry*. 2010. Vol. 396. Iss. 8, p. 2813-2823. DOI: 10.1007/s00216-009-3272-0

33. Reddy A.V.R., Goswami A., Tomar D.S. et al. Charge Distribution in 96 MeV ^{16}O Induced Fission of ^{238}U. *Radiochimica. Acta*. 1994. Vol. 64, p. 149-154. DOI: 10.1524/ract.1994.64.34.149

34. Acharya R., Nair A.G.C., Reddy A.V.R., Goswami A. Standard-less analysis of Zircaloy clad samples by an instrumental neutron activation method. *Journal of Nuclear Materials*. 2004. Vol. 326. Iss. 2-3, p. 80-85. DOI: 10.1016/j.jnucmat.2003.12.013

35. Lawson S.C., Spear P.M., Martineau P.M. Patent N EP1430291B1. Examining a diamond. Publ. 14.02.2007.

36. Vasilev E.A., Ivanov-Omskii V.I., Pomazanskii B.S., Bogush I.N. The N3 center luminescence quenched by nitrogen impurity in natural diamond. *Technical Physics Letters*. 2004. Vol. 30. N 10, p. 802-803. DOI: 10.1134/1.1813714

37. Ardalkar R., Salunkhe Y., Gaonkar M. et al. Depth profile studies on natural and artificially irradiated diamonds. 71st Diamond conference (Poster-45) 6-10 July 2021, Warwick U.K, University of Warwick, Coventry.

Authors: **Rajendra M. Ardalkar,** *Masters in Physics, Research Assistant, https://orcid.org/0000-0002-5981-9972 (Gemmological Institute of India, Mumbai, India),* **Yogesh D. Salunkhe,** *Masters in Geophysics, Research Assistant, https://orcid.org/0000-0001-9256-6447 (Gemmological Institute of India, Mumbai, India),* **Mahesh P. Gaonkar,** *Masters in Chemistry, Research Associate, https://orcid.org/0000-0002-3053-7867 (Gemmological Institute of India, Mumbai, India),* **Sandesh N. Mane,** *Masters in Chemistry, Research Associate, https://orcid.org/0000-0002-0587-7923 (Gemmological Institute of India, Mumbai, India),* **Omkar A. Ghaisas,** *Masters in Physics, Research Assistant, https://orcid.org/0009-0002-5851-2909 (Gemmological Institute of India, Mumbai, India),* **Shripalkumar N. Desai,** *Bachelor of Engineering, Diamond Valuer and Trustee, https://orcid.org/0009-0000-0101-0102 (Gemmological Institute of India, Mumbai, India),* **Annareddy V.R. Reddy,** *Doctorate in Chemistry, Head of Department, avramanareddy1@gmail.com, https://orcid.org/0000-0002-3396-9606 (Gemmological Institute of India, Mumbai, India).*

The authors declare no conflict of interests.

ISSN 2411-3336; e-ISSN 2541-9404

JOURNAL OF MINING INSTITUTE

Zapiski Gornogo instituta

Journal homepage: pmi.spmi.ru

Research article

Velocity structure of the Earth's crust and upper mantle in the Pechenga ore region and adjacent areas in the northwestern part of the Lapland-Kola orogen by the receiver function technique

Andrei G. Goev
Sadovsky Institute of Geosphere Dynamics, RAS, Moscow, Russia

***How to cite this article*:** Goev A.G. Velocity structure of the Earth's crust and upper mantle in the Pechenga ore region and adjacent areas in the northwestern part of the Lapland-Kola orogen by the receiver function technique. Journal of Mining Institute. 2024. Vol. 266, p. 188-198.

Abstract. The article presents a study of the Earth's crust and upper mantle in the Pechenga ore region, as well as areas adjacent to it in the northwestern part of the Kola region. Applying the receiver function technique to data acquired by three broadband seismic stations, we obtained one-dimensional seismic velocity distribution models to a depth of 300 km. The stations are located in the northern parts of Finland and Norway, as well as in the Pechenga region of the Russian Federation. Despite the stations being in relatively close proximity (within 100 km of each other), the velocity models turned out to be significantly different, which indicates structural discontinuity within the lithosphere. Thus, Finland station data set revealed a gradient crust-mantle transition, which is not present in the other two models. At depths of about 150 km, a low-velocity zone was discovered, associated with mid-lithospheric discontinuity, which was not found beneath the Pechenga ore region. Furthermore, the crustal structure of the Pechenga region has an anomalously high *Vp/Vs* ratio to a depth of about 20 km. Considering the fact that the Pechenga (Nikel) seismic station was installed in close proximity to major copper-nickel deposits, this anomaly can be interpreted as a relic of Proterozoic plume activity.

***Keywords*:** Kola Peninsula; Lapland-Kola orogen; lithosphere; mantle; receiver function; ore deposits; plume

Acknowledgment. The work was supported by the Russian Science Foundation, grant N 21-17-00161, part of the review of the tectonic history of the entire Fennoscandian Shield carried out in accordance with topic 122040400015-5.

Received: 31.05.2023 ***Accepted: 27.12.2023*** ***Online: 09.04.2024*** ***Published: 25.04.2024***

Introduction. The Fennoscandian (Baltic) Shield is one of the most well-studied Precambrian regions on Earth. Its core area was formed in the Paleoproterozoic, and consists of the Svecofennian province (1.8-2.0 Ga) and the Transscandinavian Igneous Belt (1.6-1.8 Ga). In addition, at its southwestern end there is the Sveconorwegian belt with an age of 0.9-1.2 Ga [1]. The most ancient Archean rocks are exposed in the northeastern part of the Shield on the Kola Peninsula, which, in turn, consists of three major tectonic elements – the Murmansk, Kola, and Belomorian blocks (the Kola and Belomorian blocks are usually combined with smaller Umba-Terskii and Strelna terranes into the Lapland-Kola orogen [2]). The location of the major tectonic elements is shown in Fig.1. Thus, in the structure of the Fennoscandian Shield, the oldest formations are found in the east, while the more recent ones (from the perspective of geological time) are found towards the west, which, considering the absence of sedimentary sheath, makes it a convenient area for studying the evolution of the Earth.

The Lapland-Kola Orogen (LKO) in the central part of the Kola Peninsula is located between the Murmansk block in the north and the Karelian block in the south. It is a well-exposed part of the Shield, where all the most important tectonic elements are observable. Thereby, it provides an understanding

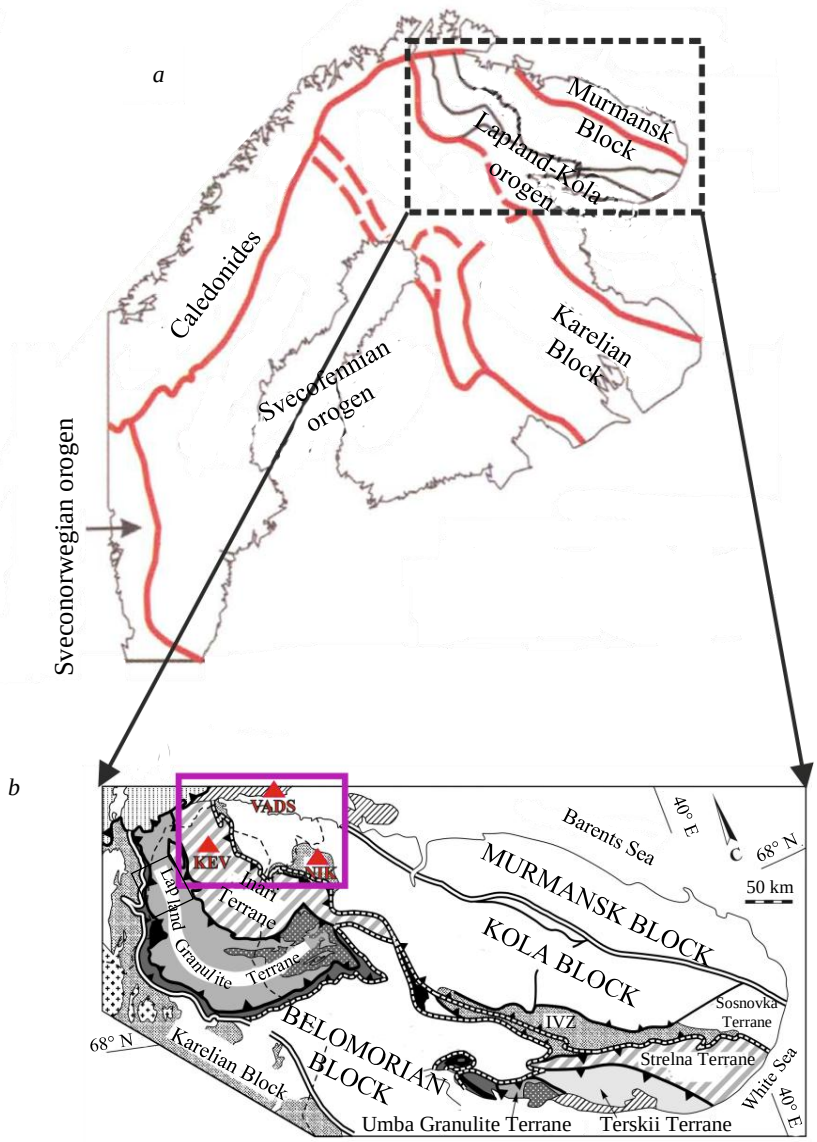

Fig.1. Tectonic sketch of the Fennoscandian Shield according to [3, 4] (*a*) and detailed tectonic map of the Kola region according to [4, 5] (*b*). Red triangles mark the positions of the seismic stations VADS, NIK, and KEV used in this work; the purple rectangle shows the study region

of the geodynamic process patterns of the Neo-Archean to Paleoproterozoic. The LKO was the centre of major plume processes in the Late Neoarchean and early Paleoproterozoic [6-8], which led to rifting and splitting of the Kenorland supercontinent [9-12]. Afterwards, it led to the formation of the oceanic crust, subduction zone, and generation of the Paleoproterozoic juvenile continental crust [13, 14]. In addition, LKO is known to be abundant with large deposits of nickel and iron ores, apatite, platinum, palladium, titanium, baddeleyite, etc.

The article presents the results of new seismological studies regarding the northwestern LKO lithosphere structure. The Pechenga ore region and "Nikel" (NIK) seismic station located within it deserved our special attention. Researching this region's structure may lead to solutions for a wide range of fundamental scientific issues. Additionally, Pechenga holds one of the largest sulphide copper-nickel deposits in the world, and its genesis is of major interest.

The initial studies of the Pechenga region's deep structure began in 1960-1963 under the leadership of I.V.Litvinenko of the Leningrad Mining Institute, and used the method of deep seismic sounding along its Barents Sea – Pechenga – Lovno profile, and were later continued by many other scientists [15]. In addition, within the Pechenga region, a unique experiment on superdeep drilling of the

SG-3 well (i.e. the Kola Superdeep Borehole) was carried out. The Earth's crust was penetrated to a depth of 12,262 m, which allowed scientists to verify the results of indirect geophysical research with direct observations. As new data accumulated and the general understanding of the Earth's evolution changed, the theories around the development of the Pechenga structure and the mineral deposits' genesis have changed as well. According to the current scientific consensus, their genesis is attributed to Paleoproterozoic plumes that contributed to the rise of primitive magmas and undepleted material to the surface. Traces of these plumes can still be detected today [16, 17].

Methodology. To obtain deep velocity sections, the receiver function (RF) technique was used. It is based on the use of the converted phases of teleseismic waves forming at contrast seismic boundaries in a close proximity beneath a seismic station. These converted waves characterize the part of the medium in which they were formed. Thus, RF results can be effectively localized and interpreted by estimating the depth the converted waves formed at (conversion points).

The method is divided into two parts according to the types of converted phases used – the *P*-receiver function (or PRF), analyses *P-S* (*Ps*) converted waves and their multiples, and, accordingly, the *S*-receiver function (or SRF) analyses *S-P* (*Sp*) converted waves and their multiples. Joint inversion of PRF and SRF allows us to obtain a stable one-dimensional velocity section of the Earth's crust and upper mantle [18, 19].

To obtain the receiver functions, we used a well-tested and reliable approach that is described in detail in [20]. Thus, we will discuss only the main aspects. The key elements of this methodology are as follows: at the first stage, we selected seismic events according to their epicentral distances; the criteria of epicentral distances for PRF analysis is 30-100°, while for SRF analysis it is 65-100°. The event parameters for this analysis (origin time, depth, and coordinates) were taken from the Global Centroid Moment Tensor Catalog (GCMT Catalog) [21, 22]. In addition, due to remote epicentral distances, earthquakes with a magnitude of less than 5.5 were not considered. We handpicked events with an impulse waveform of the first incident wave (*P* for PRF and *S* for SRF) and a high (more than 3) signal-to-noise ratio. The seismogram of each selected event was filtered (a second-order Butterworth filter with a corner period of 5 s was used to obtain PRF, and 8 s for SRF) and then their standard *ZNE* three-component coordinate system was rotated to a *LQT* ray coordinate system for PRF and *LAB* for SRF. In the *LQT* ray coordinate system, the *L* component coincides with the oscillation direction of the incident *P* wave, *Q* is perpendicular to *L* in the *P-SV* plane, and *T* is orthogonal to the *LQ* plane. In the LAB coordinate system, the *L* component corresponds to the direction of the movement of the incident wave, and *A* to the direction of polarization of the *S* wave. B is orthogonal to *L* and *A*. To standardize the recordings and minimize the influence of the focal mechanism, we applied deconvolution to each individual RF under the assumption that the *L* and *A* components in PRF and SRF are determined up to a normalizing factor by the shape of the incident wave and are near-independent of the medium parameters. During the deconvolution, we selected and applied to all components a filter that brings the observed waveforms on the *L* and *A* components closer to the gaussian shape.

To identify the converted phases that describe the seismic boundaries in the Earth's crust and upper mantle, the individual receiver functions we selected and prepared were stacked together. The stacking mechanisms for PRF and for SRF are different. For PRF, individual functions were stacked with adjustments that correspond to the beam parameter of a given incident wave and the depth of the conversion point. All events were reduced to the same beam parameter value – 6.4 s/deg. For each target depth and for each event, individual time corrections were estimated, by which the seismograms were shifted relative to each other before stacking. Stacked traces were estimated for multiple assumed conversion depths. The SRFs were stacked considering the weighting indices for the noise level on each of the traces and for the deviation of the incident *S*-wave polarization from the *P-SV* plane, as well as relative to the reference (usually average of all individual records') epicentral distance. The method for estimating these indices is given in detail in [23].

To obtain deep velocity models, we carried out the joint inversion of PRF and SRF. The search for optimal models (minimization) was conducted using the Levenberg – Marquardt algorithm [24]. A model of the medium consisting of laterally homogeneous layers was used. The forward modelling of estimating synthetic receiver functions was done using the Thomson – Haskell matrix algorithm [25]. To obtain the required velocity models, a probabilistic-statistical approach was used with the generation of multiple random trial a priori models. The main advantage of this approach is independence from any initial velocity model.

In the given research, the varied parameters for the individual models were: the shear wave velocity *Vs*, the ratio of the primary and shear wave velocities *Vp/Vs*, and the thickness of each layer; the medium was set to consist of 14 layers. For the data from each seismic station, 100,000 random initial models and synthetic PRF and SRF were calculated, which were then minimized. The final velocity model was built as the median of a sample of 2-3 % of the best solutions (those synthetic PRFs and SRFs that best correlate with observations). To stabilize the inversion and estimate the absolute velocities along the section with increased precision, the converted waves' travel time discrepancies from the boundaries of 410 and 660 km in the upper mantle relative to the IASP91 model (Δtp and Δts) [26] were also included in the inversion, which is demonstrated in [27]. To obtain the final distribution of varied parameters, the model parameter space was divided into cells. The solution is presented as a region saturated with minimized random initial models, where synthetic PRF and SRF best coincide with the observed data. The cells with the largest number of selected minimized trial models have been highlighted. The method used is described in detail in [28].

Data. As the data for this research, we used seismic recordings accumulated by the new NIK seismic station, which is located in the village of Nikel, Murmansk Region, near the largest copper-nickel deposits of the Pechenga region. The station was launched in 2020 and is equipped with a broadband velocimeter with a frequency range of 0.03-50 Hz and a RefTek 130 seismic recorder.

To assess the quality of the recordings obtained by the new NIK station, the levels of microseismic background noise were examined. To do this, we estimated the spectral noise power density SPM (Fig.2) based on the records of each of the components (*Z*, *N*, *E*) for the full set of continuous seismic data for the entire recording period; that data was compared to the permissible values for this parameter obtained

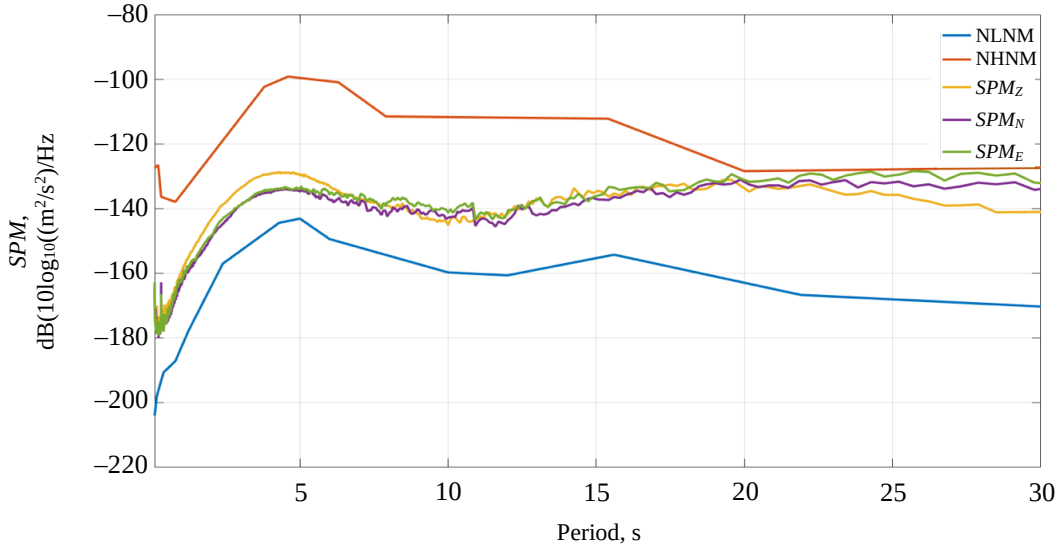

Fig.2. Noise power spectral density
for each of the component (SPM_Z, SPM_N, SPM_E) for the NIK station data.
NLNM and NHNM – minimum and maximum permissible values of this parameter

during the observations of 75 "reference" seismic stations of the global network*. The level of microseismic noise did not exceed the standard values in its entire registering range; moreover, the station can be classified as "quiet" when analyzing signals over up to 15 s periods.

In addition to the NIK station data, our research incorporates data from two other broadband seismic stations of the Global Network located in the northwestern part of the LKO – Vadso (VADS) and Kevo (KEV). Both stations are permanent and have been in operation for more than seven years. They are equipped with broadband velocimeters with a maximum recording period of at least 120 s, which ensures high quality of recorded seismic data. The main parameters of the seismic stations used are provided in the Table below.

Basic parameters of seismic stations and the number of estimated individual PRF and SRF receiver functions

Station code	Station name	Latitude	Longitude	Launch year	Sensor type	Bandwidth, Hz	PRF	SRF
NIK	Nikel	69.24	30.13	2020	RefTek 151-30	0.03-50	41	32
VADS	Vadso	70.12	29.36	2016	Trillium 120 PA	0.008-30	85	143
KEV	Kevo	69.75	27.00	1993	STS 1	0.002-10	247	200

Based on the analyzed seismic data, 143 individual SRFs and 85 individual PRFs were obtained from the VADS station; from the KEV station – 200 SRFs, 247 PRFs; from the NIK station – 32 SRFs, 41 PRFs. The distribution of epicentres for the selected events is shown in Fig.3. The distribution of the epicentres for the selected events makes it possible to avoid azimuthal dependence when obtaining velocity models after stacking individual PRFs and SRFs. That is also true for the NIK station, which has the lowest amount of accumulated data. The azimuth values in degrees are plotted along the perimeter of the grid, and the epicentral distances in degrees are plotted along the azimuthal directions.

Results. The receiver function method is characterised by high sensitivity to seismic velocity contrasts and relatively low accuracy when it comes to absolute velocity estimates. This issue can be resolved by using the values of the detected travel time discrepancies of the converted waves formed at the boundaries of the phase transition zone in the upper mantle at depths of about

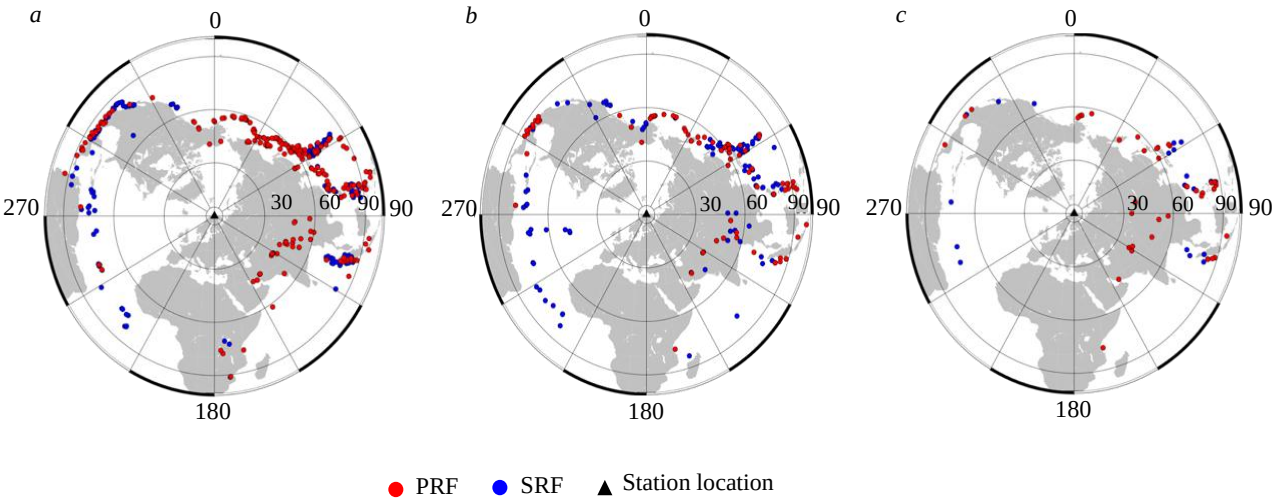

Fig.3. Epicenters of seismic events for PRF and SRF
for KEV (*a*), VADS (*b*) and NIK (*c*) stations

* *Peterson J.* Observation and modeling of seismic background noise: Open-File Report 93-322. Albuquerque: U.S. Department of Interior, Geological Survey, 1993, p. 94. DOI: 10.3133/ofr93322

410 and 660 km [27]. In addition, the presence of well-defined phases from these global boundaries in the recordings is an additional marker of high-quality experimental data. To determine the observed discrepancies using the PRF data for each station, we constructed stacks in accordance with the methodology described above (Fig.4).

The analyzed *Ps* converted waves from the P410s and P660s mantle transition zone boundaries are easily observable in the stacks. Moreover, these phases are "focusing" at appropriate depths, i.e. the maximum phase amplitude is observed on the stack corresponding to the expected depth (400 km stack for 410 km discontinuity and 640 km stack for 660 km discontinuity). For each individual station, consistent values (with approximately a 0.1 s margin of error) of the arrival times of these phases were obtained. According to the standard IASP91 Earth velocity model and a ray parameter of 6.4 s/deg, to which the selected recordings are reduced, P410s and P660s phases should be registered at 44 and 67.9 s. The resulting data, however, indicates consistent negative time discrepancies $t_{obs} - t_{std} = -1$ both for the P410s and P660s phases, which in turn indicates average increased velocities in the upper mantle.

Based on joint PRF and SRF modelling and observed discrepancies in the travel times of converted P410s and P660s waves, we obtained velocity models of the Earth's crust and upper mantle to a depth of about 300 km for each individual station (Fig.5). The most significant identified feature of the upper mantle structure is a layer of relatively low velocities for the VADS station at depths of 140-170 km. In the same interval, a low velocity layer is also observed at the KEV station, but it is significantly less pronounced. For the NIK station data, the low velocity layer is not observed.

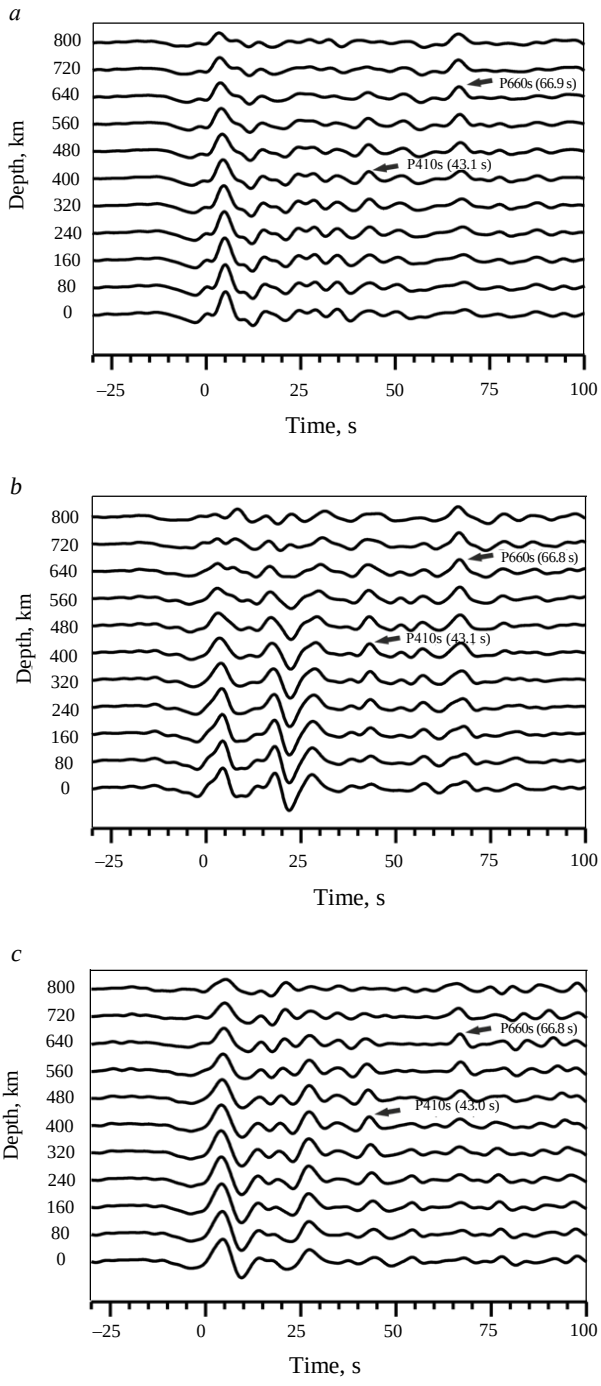

Fig.4. Stacks of PRF records for KEV (*a*), VADS (*b*), and NIK (*c*) stations (the observed delay times of the maximum amplitudes of converted waves relative to the arrival time of the first *P*-wave are indicated in parentheses; the target conversion depth is indicated for each trace)

The velocity structure of the Earth's crust within the research area does not reveal any common distinguishable features or seismic boundaries of high contrast (Fig.6). The average velocity values in the crust calculated using VADS station data are significantly higher than both the values of the standard IASP91 Earth velocity model and those observed at the KEV and NIK stations. However, a significant difference in the crust-mantle transition structure is apparent. According to the VADS station model, it appears as a well-defined boundary at a depth of about 46 km, while for KEV station

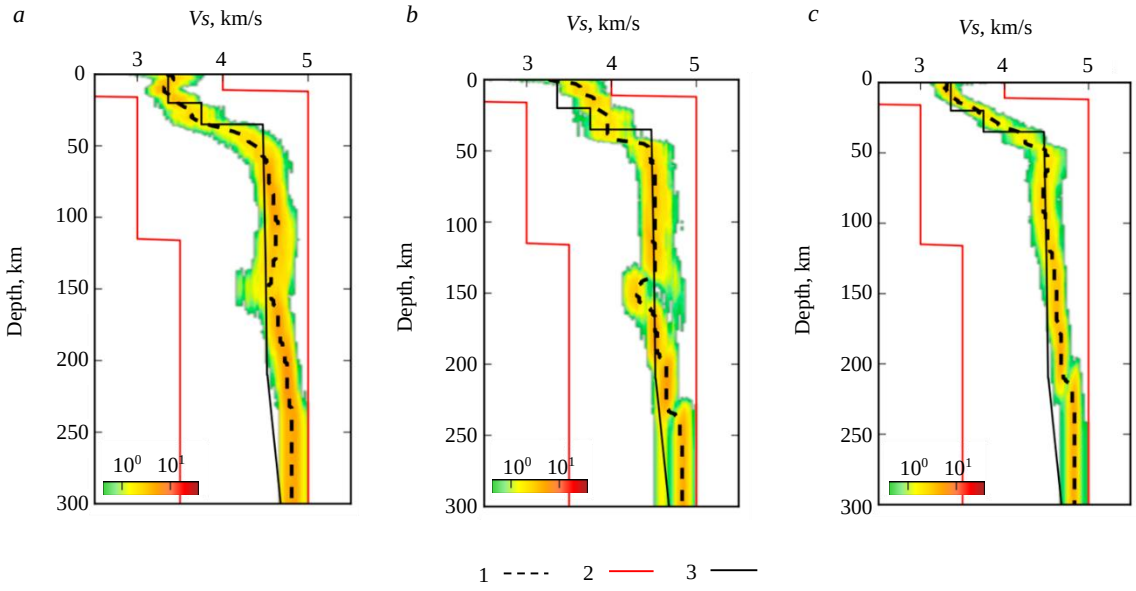

Fig.5. Shear wave velocity models to depths of about 300 km for KEV (*a*), VADS (*b*) and NIK (*c*) stations (conden-sation fields of individual minimized trial models)

1 – final median models; 2 – the boarders of the formation of trial initial models; 3 – IASP91 model

the model around this depth shows a relatively smooth velocity gradient and velocity values reaching standard values for the mantle at a depth of about 55 km. In the NIK model, two boundaries are identifiable in the lower crust at depths of 37 and 47 km; moreover, the modelled velocities match a standard mantle at a depth of about 47 km, which makes it preferable for determining the depth of the Moho.

Discussion. Despite the stations being in relatively close proximity, the obtained velocity models indicate that the lithosphere velocity structures in the northwestern part of the LKO vary significantly. Moreover, differences can be traced not only in the crustal structure, but in the upper mantle as well. The consistency of results across all stations is achieved using structural features analysis for the 410 and 660 km boundaries.

Based on the *Vs* distribution model, obtained for the VADS station, we observe a low-velocity layer in the upper mantle at depths of 140-170 km. The KEV station reveals a decrease in seismic

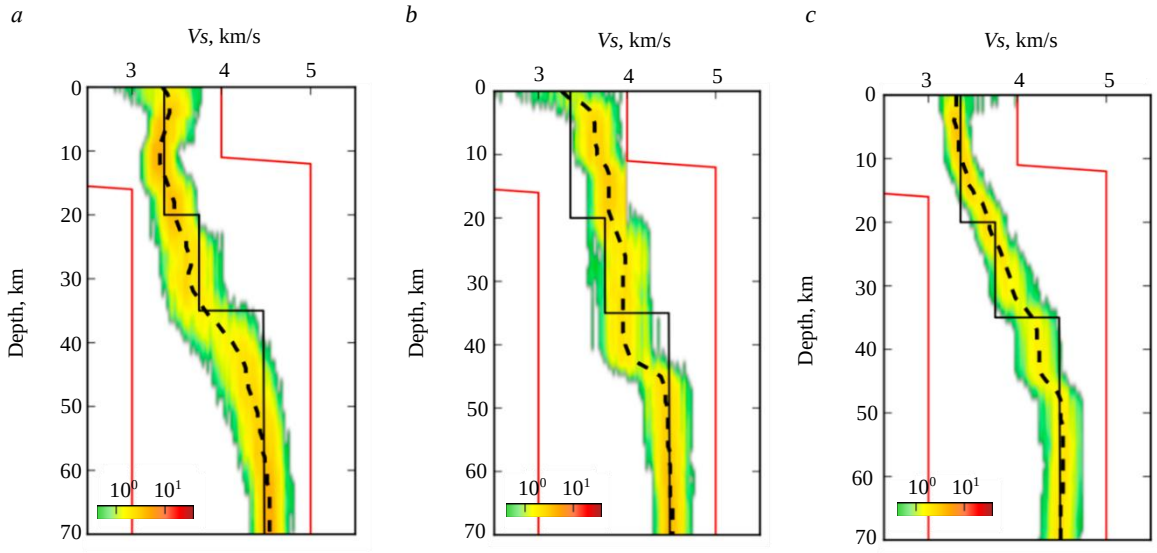

Fig.6. Shear wave velocity models to depths of about 70 km for KEV (*a*), VADS (*b*) and NIK (*c*) stations (for symbols, see Fig.5)

velocities at the indicated depths as well; however, it is not easily identifiable and it is impossible to reliably confirm or deny the presence of a low-velocity layer for this station. The relatively shallow depths (about 140-170 km) at which this layer was discovered do not allow us to associate it with the asthenosphere [29]. It is possible that our models marked the mid-lithosphere discontinuity or MLD. The presence of this layer in various regions of the Earth, including the Fennoscandian Shield, was first described using seismic data in [30]. This layer appears to be global, at least for craton areas. However, its depth, thickness, and seismic velocities vary within different tectonic structures and probably depend on local geological history [31-33]. It is worth noting that for most regions of the Earth, this layer is characteristically present at the depth range of 100-150 km, including for the central and eastern parts of the Kola region. Analyzing data obtained by the "Kvartz" superlong profile conducted using peaceful nuclear explosions, the presence of the low-velocity layer is shown at the depths of about 80-140 km [34]. For Finland, seismic tomography data has identified a low-velocity layer with parameters, which differ for the northern and southern parts of the territory. In particular, its depth was shown to increase in a northerly direction. [35]. In the area where the KEV station was installed, the low-velocity layer was observed at a depth of about 180 km, which does not contradict our estimates, considering the greater accuracy of RF at those depths.

At present, there is no model describing the formation mechanism and nature of mid-lithospheric discontinuity (MLD). Among the hypotheses expressed, the following can be distinguished: rheological – layering at a temperature close to the solidus point [36]; petrophysical – layering under conditions of either partial submergence of the substance [37] or in the presence of basaltic melts [36, 38]; change in *deformation* properties with depth [39].

Dissimilarities in the depth and character of the crust-mantle transition cannot be unambiguously interpreted using models obtained from the KEV, VADS, and NIK stations, as data from three seismic stations is not sufficient to provide a complete understanding on a regional level. In order to significantly alter the Moho structure, a large-scale tectonic process is required. It would be most logical to associate with Caledonian orogen formation artifacts, developed as a result of the collision of the Baltica-Avalonia-Laurentia microcontinents [40, 41]. The change in the sharpness of the Moho can be associated with reorganisation during deformation, which possibly led to dissolution of the high-velocity layer within the lower crust that is found in central and southern Sweden [42] (and which may have been metamorphosized into eclogites, locally found on the surface along the coast of Norway).

Of greatest interest is the deep structure model of the Pechenga region obtained using the new NIK seismic station data (Fig.7). It is located in close proximity to the major copper-nickel deposits of Kotselvaara-Kammikivi and the Zhdanovskii eastern ore cluster, and 42 km from the SG-3 Kola Superdeep Borehole.

In the resulting NIK Earth's crust velocity structure model, contrasting seismic boundaries are not detected. In the lower part of both the *Vp* and *Vs* velocity section, two seismic boundaries are observed at the depths of 37 and 47 km, respectively. The velocity values match the standard for the upper mantle at the depths of about 47 km. The complex two-stage structure of the crust-mantle transition with two boundaries – M1 and M2, is generally confirmed by other geophysical methods [43, 44]. Such "splitting" of the crust-mantle transition can be interpreted as a large-scale tectonic process relic, for example, a mantle diapir or plume, which is believed to have existed in the Pechenga region in the Proterozoic [16]. It should be noted that traces of mantle diapirs in the modern geological structure have been found in various regions of the Earth (for example, in the Russian Far East [45]).

Another distinct feature of the new depth models obtained is the anomalously high *Vp/Vs* parameter (~ 2) zone, which is observed from the surface to the depth of about 20 km. Velocity models obtained by the RF method can be spatially localized for a given depth. To determine a region that is characterized by velocity patterns, conversion points can be estimated, i.e. projections of converted wave

formation points onto the surface for a given depth. Fig.7 shows the conversion points for a depth of 20 km and outlines the area characterized by the resulting velocity models for the given depth. The presence of a zone with such a high *Vp*/*Vs* ratio within the Earth's crust may indicate not only a preserved intermediate magma chamber [46], which may contain ore mineralization, but also the preservation of a relict magma channel through which the material reached the surface.

Direct comparison between the velocity sections obtained in this research and the results of SG-3 studies is complicated for a number of reasons. This is primarily due to the long-period nature of the data used in the RF technique, which leads to significant lateral averaging, which does not allow us to distinguish layers several hundred metres thick, which were observed during the Kola superdeep well experiment [47]. In addition, the SG-3 research provided significantly more accurate *Vp* velocities, while the RF method is more focused on determining *Vs*. It should be noted that the seismic velocities obtained by the author are in qualitative agreement with the values shown in the SG-3 section and with modern spatial regional tomographic models of the Pechenga region [43, 47].

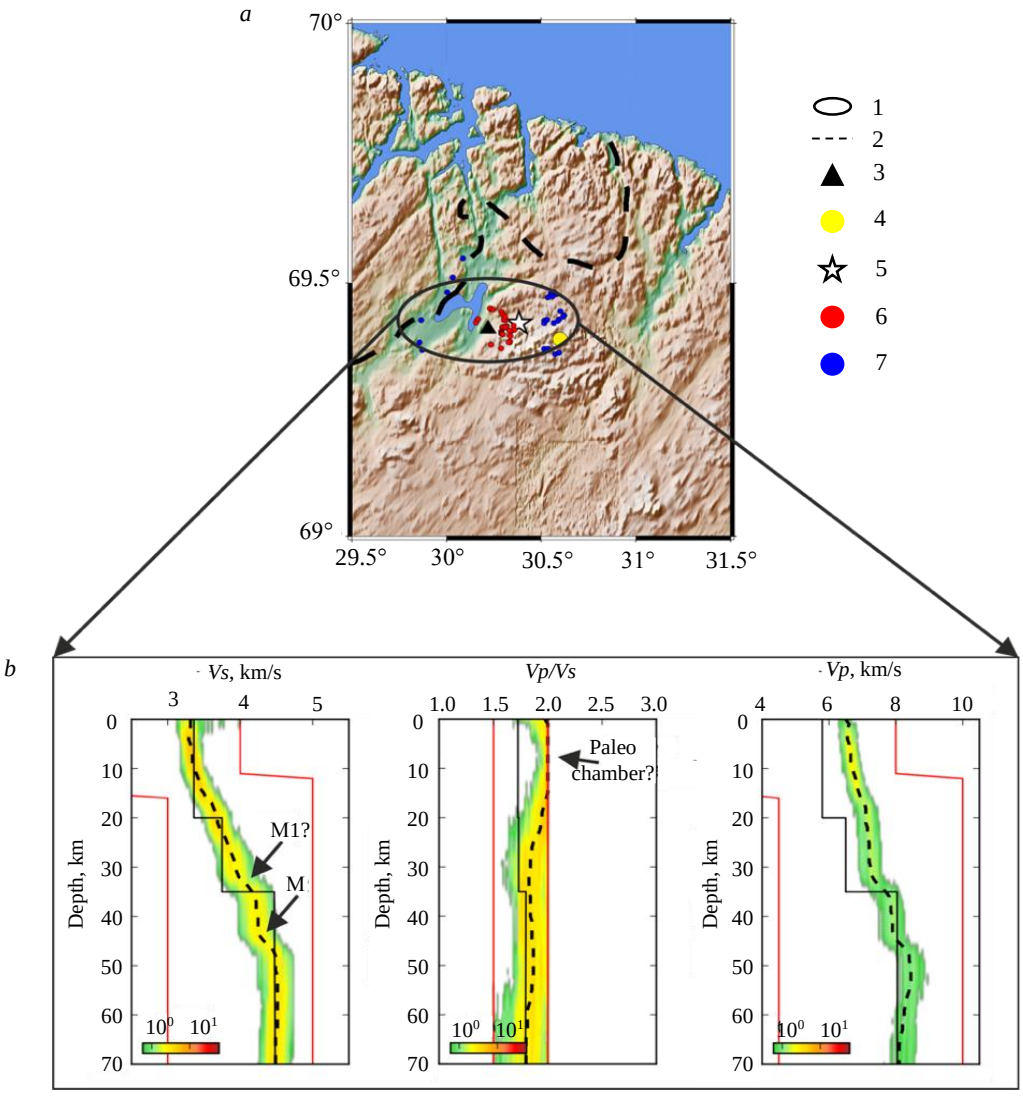

Fig.7. Map of the Pechenga region (*a*) and velocity models (*b*) of *Vs*, *Vp*/*Vs*, and *Vp* with depth (for symbols, see Fig.5)

1 – area characterized by velocity models at the depth of about 20 km; 2 – state border; 3 – NIK seismic station; 4 – Kola superdeep well; 5 – Kaula-Kotselvaara mine; 6 – PRF conversion points for a depth of 20 km; 7 – SRF conversion points for a depth of 20 km

Conclusion. Seismological data from three seismic stations located in the northwestern part of the Lapland-Kola orogen was analyzed. Two of these stations are well established, KEV in northern Finland and VADS in the northeastern part of the Norwegian Caledonides, joining them in 2020 was the NIK station, established in the Pechenga ore region. As part of the research, it was shown that the lithosphere in the research area has a heterogeneous velocity structure not only within the Earth's crust, but also in the upper mantle, to a depth of approximately 200 km. In the upper mantle structure, a zone of lower velocities can be traced at depths of about 150 km, most likely associated with mid-lithospheric discontinuity. MLD is most clearly manifested in northern Finland, hardly observable beneath the Norwegian Caledonides, and is not observed beneath the Pechenga region. Significant differences were revealed in the structure of the crust-mantle transition, represented by a single discontinuity at a depth of 46 km (VADS station), a gradient layer with seismic wave velocities reaching standard values for the mantle at a depth of about 55 km (KEV station), and a complex zone with two boundaries at the depths of about 37 and 47 km beneath the Pechenga region (NIK station). Considering the absolute values of velocities, the lower boundary detected at the NIK station looks preferable for detecting the Moho.

The Pechenga region model indicates the presence of anomalously high values of the *Vp*/*Vs* ratio (~ 2) from the surface to depths of about 20 km in the area of the major copper-nickel deposits of Kotselvaara-Kammikivi and the Zhdanovskii eastern ore cluster. Such high values are indicative, in particular, of undepleted mantle rocks, and may be associated with an intermediate magma chamber relic formed during the Proterozoic rifting.

The identified anomalies in the structure of the crust-mantle transition, *Vp/Vs* values, as well as the absence of MLD beneath the Pechenga region (its presence was shown in the neighbouring areas) can be jointly interpreted as artifacts of the Proterozoic plume magmatism stage, characteristic of the Pechenga region and confirmed by geological and geochemical research [16].

REFERENCES

1. Daly J.S., Balagansky V.V., Timmerman M.J., Whitehouse M.J. The Lapland–Kola orogen: Palaeoproterozoic collision and accretion of the northern Fennoscandian lithosphere. *European Lithosphere Dynamics: Geological Society Memoirs. London: Geological Society*. 2006. Vol. 32, p. 579-598. DOI: 10.1144/GSL.MEM.2006.032.01.35

2. Hjelt S.-E., Daly J.S. SVEKALAPKO colleagues. SVEKALAPKO: evolution of Palaeoproterozoic and Archaean Lithosphere. Lithosphere Dynamics: Origin and Evolution of Continents. Uppsala: EUROPROBE Secretariat, Uppsala University, 1996, p. 56-67.

3. Gorbatschev R., Bogdanova S. Frontiers in the Baltic Shield. *Precambrian Research*. 1993. Vol. 64. Iss. 1-4, p. 3-21. DOI: 10.1016/0301-9268(93)90066-B

4. Mudruk S.V., Balagansky V.V., Gorbunov I.A., Raevsky A.B. Alpine-type tectonics in the Paleoproterozoic Lapland-Kola Orogen. *Geotectonics*. 2013. Vol. 47. N 4, p. 251-265. DOI: 10.1134/S0016852113040055

5. Balagansky V.V., Glaznev V.N., Osipenko L.G. Early Proterozoic evolution of the northeastern Baltic Shield: terrane analysis. *Geotectonics*. 1998. Vol. 32. N 2, p. 81-93.

6. Amelin Y.V., Semenov V.S. Nd and Sr isotopic geochemistry of mafic layered intrusions in the eastern Baltic shield: implications for the evolution of Paleoproterozoic continental mafic magmas. *Contributions to Mineralogy and Petrology*. 1996. Vol. 124. Iss. 3-4, p. 255-272. DOI: 10.1007/s004100050190

7. Lobach-Zhuchenko S.B., Arestova N.A., Chekulaev V.P. et al. Geochemistry and petrology of 2.40-2.45 Ga magmatic rocks in the north-western Belomorian Belt, Fennoscandian Shield, Russia. *Precambrian Research*. 1998. Vol. 92. Iss. 3, p. 223-250. DOI: 10.1016/S0301-9268(98)00076-X

8. Sharkov E.V., Bogatikov O.A., Krasivskaya I.S. The Role of Mantle Plumes in the Early Precambrian Tectonics of the Eastern Baltic Shield. *Geotectonics*. 2000. Vol. 34. N 2, p. 85-105.

9. Williams H., Hoffman P.F., Lewry J.F. et al. Anatomy of North America: thematic geologic portrayals of the continent. *Tectonophysics*. 1991. Vol. 187. Iss. 1-3, p. 117-134. DOI: 10.1016/0040-1951(91)90416-P

10. Pesonen L.J., Elming S.-Å., Mertanen S. et al. Palaeomagnetic configuration of continents during the Proterozoic. *Tectonophysics*. 2003. Vol. 375. Iss. 1-4, p. 289-324. DOI: 10.1016/S0040-1951(03)00343-3

11. Mints M.V., Konilov A.N. Geodynamic crustal evolution and long-lived supercontinents during the Palaeoproterozoic: evidence from granulite-gneiss belts, collisional and accretionary orogens. The Precambrian Earth, Tempos and Events. Elsevier, 2004. Vol. 12. P. 223-239.

12. Balaganskii V.V., Mints M.V., Deili Dzh.S. Paleoproterozoic Lapland-Kola orogeny. Structure and dynamics of the lithosphere in Eastern Europe. Results of research under the EUROPROBE program. Moscow: GEOKART; GEOS, 2006. Vol. 2, p. 158-171 (in Russian).

13. Daly J.S., Balagansky V.V., Timmerman M.J. et al. Ion microprobe U–Pb zircon geochronology and isotopic evidence for a trans-crustal suture in the Lapland–Kola Orogen, northern Fennoscandian Shield. *Precambrian Research*. 2001. Vol. 105. Iss. 2-4, p. 289-314. DOI: 10.1016/S0301-9268(00)00116-9

14. Lahtinen R., Huhma H. A revised geodynamic model for the Lapland-Kola Orogen. *Precambrian Research*. 2019. Vol. 330, p. 1-19. DOI: 10.1016/j.precamres.2019.04.022

15. Sharov N.V. Lithosphere of Northern Europe: seismic data. Petrozavodsk: Karelian Research Centre, RAS, 2017, p. 173 (in Russian).

16. Skufin P.K., Bayanova T.B. Early Proterozoic central-type volcano in the Pechenga structure and its relation to the ore-bearing gabbro-wehrlite complex of the Kola Peninsula. *Petrology*. 2006. Vol. 14. N 6, p. 609-627. DOI: 10.1134/S0869591106060063
17. Arzamastsev A.A., Salnikova E.B., Stepanova A.V. et al. Mafic Magmatism of Northeastern Fennoscandia (2.06–1.86 Ga): Geochemistry of Volcanic Rocks and Correlation with Dike Complexes. *Stratigraphy and Geological Correlation*. 2020. Vol. 28. N 1, p. 3-40. DOI: 10.1134/S0869593820010025
18. Kosarev G.L., Oreshin S.I., Vinnik L.P. et al. Heterogeneous lithosphere and the underlying mantle of the Indian subcontinent. *Tectonophysics*. 2013. Vol. 592, p. 175-186. DOI: 10.1016/j.tecto.2013.02.023
19. Oreshin S., Kiselev S., Vinnik L. et al. Crust and mantle beneath western Himalaya, Ladakh and western Tibet from integrated seismic data. *Earth and Planetary Scientific Letters*. 2008. Vol. 271. Iss. 1-4, p. 75-87. DOI: 10.1016/j.epsl.2008.03.048
20. Vinnik L.P. Receiver Function Seismology. *Izvestiya, Physics of the Solid Earth*. 2019. Vol. 55. N 1, p. 12-21. DOI: 10.1134/S1069351319010130
21. Dziewonski A.M., Chou T.-A., Woodhouse J.H. Determination of earthquake source parameters from waveform data for studies of global and regional seismicity. *Journal of Geophysical Research: Solid Earth*. 1981. Vol. 86. Iss. B4, p. 2825-2852. DOI: 10.1029/JB086iB04p02825
22. Ekström G., Nettles M., Dziewonski A.M. The global CMT project 2004-2010: Centroid-moment tensors for 13,017 earthquakes. *Physics of the Earth and Planetary Interiors*. 2012. Vol. 200-201, p. 1-9. DOI: 10.1016/j.pepi.2012.04.002
23. Farra V., Vinnik L. Upper mantle stratification by P and S receiver functions. *Geophysical Journal International*. 2000. Vol. 141. Iss. 3, p. 699-712. DOI: 10.1046/j.1365-246x.2000.00118.x
24. Press W.H., Teukolsky S.A., Vetterling W.T., Flannery B.P. Numerical Recipes: The Art of Scientific Computing. New York: Cambridge University Press, 2007, p. 1256.
25. Haskell N.A. Crustal reflection of plane *P* and *SV* waves. *Journal of Geophysical Research*. 1962. Vol. 67. N 12, p. 4751-4768. DOI: 10.1029/JZ067i012p04751
26. Kennett B.L.N., Engdahl E.R. Traveltimes for global earthquake location and phase identification. *Geophysical Journal International*. 1991. Vol. 105. Iss. 2, p. 429-465. DOI: 10.1111/j.1365-246X.1991.tb06724.x
27. Vinnik L., Kozlovskaya E., Oreshin S. et al. The lithosphere, LAB, LVZ and Lehmann discontinuity under central Fennoscandia from receiver functions. *Tectonophysics*. 2016. Vol. 667, p. 189-198. DOI: 10.1016/j.tecto.2015.11.024
28. Aleshin I.M. The inverse problem solution with an ensemble of models: an example for receiver function inversion. *Doklady Earth Sciences*. 2021. Vol. 496. N 1, p. 63-66. DOI: 10.31857/S2686739721010047
29. Wang Z., Kusky T.M. The importance of a weak mid-lithospheric layer on the evolution of the cratonic lithosphere. *Earth-Science Reviews*. 2019. Vol. 190, p. 557-569. DOI: 10.1016/j.earscirev.2019.02.010
30. Thybo H., Perchuć E. The Seismic 8° Discontinuity and Partial Melting in Continental Mantle. *Science*. 1997. Vol. 275. Iss. 5306, p. 1626-1629. DOI: 10.1126/science.275.5306.1626
31. Yang H., Artemieva I.M., Thybo H. The Mid-Lithospheric Discontinuity Caused by Channel Flow in Proto-Cratonic Mantle. *Journal of Geophysical Research: Solid Earth*. 2023. Vol. 128. Iss. 4. N e2022JB026202. DOI: 10.1029/2022JB026202
32. Weijia Sun, Li-Yun Fu, Erdinc Saygin, Liang Zhao. Insights Into Layering in the Cratonic Lithosphere Beneath Western Australia. *Journal of Geophysical Research: Solid Earth*. 2018. Vol. 123. Iss. 2, p. 1405-1418. DOI: 10.1002/2017JB014904
33. Rychert C.A., Shearer P.M. A Global View of the Lithosphere-Asthenosphere Boundary. *Science*. 2009. Vol. 324. Iss. 5926, p. 495-498. DOI: 10.1126/science.1169754
34. Yegorova T.P., Pavlenkova G.A. Velocity–Density Models of the Earth's Crust and Upper Mantle from the Quartz, Craton, and Kimberlite Superlong Seismic Profiles. *Izvestiya, Physics of the Solid Earth*. 2015. Vol. 51. N 2, p. 250-267. DOI: 10.1134/S1069351315010048
35. Silvennoinen H., Kozlovskaya E., Kissling E. POLENET/LAPNET teleseismic P wave travel time tomography model of the upper mantle beneath northern Fennoscandia. *Solid Earth*. 2016. Vol. 7. Iss. 2, p. 425-439. DOI: 10.5194/se-7-425-2016
36. Thybo H. The heterogeneous upper mantle low velocity zone. *Tectonophysics*. 2006. Vol. 416. Iss. 1-4, p. 53-79. DOI: 10.1016/j.tecto.2005.11.021
37. Yuan H., Romanowicz B. Lithospheric layering in the North American craton. *Nature*. 2010. Vol. 466. Iss. 7310, p. 1063-1068. DOI: 10.1038/nature09332
38. Rader E., Emry E., Schmerr N. et al. Characterization and Petrological Constraints of the Midlithospheric Discontinuity. *Geochemistry, Geophysics, Geosystems*. 2015. Vol. 16. Iss. 10, p. 3484-3504. DOI: 10.1002/2015GC005943
39. Shun-ichiro Karato, Olugboji T., Park J. Mechanisms and geologic significance of the mid-lithosphere discontinuity in the continents. *Nature Geoscience*. 2015. Vol. 8. N 7, p. 509-514. DOI: 0.1038/ngeo2462
40. Corfu F., Gasser D., Chew D.M. New perspectives on the Caledonides of Scandinavia and related areas: introduction. New Perspectives on the Caledonides of Scandinavia and Related Areas. London: Geological Society, 2014. Special Publications. Vol. 390, p. 9-43. DOI: 10.1144/SP390.28
41. Egorov A.S., Vinokurov I.Yu., Telegin A.N. Scientific and Methodical Approaches to Increase Prospecting Efficiency of the Russian Arctic Shelf State Geological Mapping. *Journal of Mining Institute*. 2018. Vol. 233, p. 447-458. DOI: 10.31897/PMI.2018.5.447
42. Buntin S., Artemieva I.M., Malehmir A. et al. Long-lived Paleoproterozoic eclogitic lower crust. *Nature Communications*. 2021. Vol. 12. N 6553. DOI: 10.1038/s41467-021-26878-5
43. Isanina E.V. The receiver function method (from the earthquake – RFM) investigations on the SD-3 district. Apatity: Kola Science Centre Russian Academy of Science, 1997, p. 101-115 (in Russian).
44. Sharov N.V., Isanina E.V., Krupnova N.A. Deep structure of the Kola Superdeep Borehole area (from seismic data). *Vestnik of MSTU*. 2007. Vol. 10. N 2, p. 309-319 (in Russian).
45. Alekseev V.I. Deep structure and geodynamic conditions of granitoid magmatism in the Eastern Russia. *Journal of Mining Institute*. 2020. Vol. 243, p. 259-265. DOI: 10.31897/PMI.2020.3.259
46. Lobanov K.V., Chicherov M.V., Chizhova I.A. et al. Depth structure and ore-forming systems of the Pechenga ore region (Russian Arctic Zone). *Arctic: Ecology and Economy*. 2019. N 3 (35), p. 107-122 (in Russian). DOI: 10.25283/2223-4594-2019-3-107-122
47. Kola Superdeep. Scientific Results and Research Experience. Moscow: "TECHNONEFTEGAZ", 1998, p. 260 (in Russian).

***Author* Andrei G. Goev,** *Candidate of Physics and Mathematics, Leading Researcher, andr.goev@gmail.com, https://orcid.org/0000-0001-9477-5963 (Sadovsky Institute of Geosphere Dynamics, RAS, Moscow, Russia).*

The author declares no conflict of interests.

ISSN 2411-3336; e-ISSN 2541-9404

JOURNAL OF MINING INSTITUTE

Zapiski Gornogo instituta

Journal homepage: pmi.spmi.ru

Research article

Assessment of the contribution of Precambrian deposits in forming the petroleum potential of the eastern part of the Volga-Urals basin using results of modeling

Dmitrii D. Kozhanov✉, **Mariya A. Bolshakova**
Lomonosov State University, Moscow, Russia

***How to cite this article*:** Kozhanov D.D., Bolshakova M.A. Assessment of the contribution of Precambrian deposits in forming the petroleum potential of the eastern part of the Volga-Urals basin using results of modeling. Journal of Mining Institute. 2024. Vol. 266, p. 199-217.

Abstract. Consideration is given to results of geochemical analysis of organic matter and oils of the Proterozoic (the RF-V complex) and the Paleozoic (the pay intervals D_2, D_3, C_{1-2}) of the eastern part of the Volga-Urals petroleum basin. The obtained data is corroborated by results of 2D basin modeling along four regional profiles two of which are situated in the Kama and two in the Belaya parts of the Kama-Belaya aulacogen. An update is given to earlier data on degree of catagenetic alteration of oil/gas source rocks of the Riphean-Vendian play, maps of catagenesis are constructed. New evidence is provided concerning presence of Precambrian oils in the Paleozoic plays. The oils under investigation are mixed – those formed from generation products of the Precambrian (Riphean, Vendian) and Paleozoic (Devonian and Early Carboniferous) source rock intervals. The results of modeling have shown that the principal source rock intervals in the RF-V play of the Kama part of the Kama-Belaya aulacogen are deposits of the Kaltasy formation of the Lower Riphean and the Vereshchagino formation of the Upper Vendian, while in the Belaya part these are rocks of the Kaltasy, Kabakov, Olkhovo, Priyutovo, Shikhan and Leuza formations of the Riphean and the Staropetrovo formation of the Vendian. It is found that the interval of the main oil and gas window increases in the southeastward direction. In both depressions of the Kama-Belaya aulacogen, a single oil play is distinguished that functions within the stratigraphic interval from the Riphean to the Lower Carboniferous. As the principal petroleum source rock intervals within this play, Riphean-Vendian deposits are considered, reservoirs are confined to the Riphean carbonate complex, Upper Vendian and Middle Devonian clastic deposits, while the Upper Devonian – Tournaisian deposits serve as the upper seal.

Keywords: Volga-Urals basin; basin modeling; geochemistry; organic matter; Precambrian; oil play

Received: 28.02.2023 ***Accepted: 05.03.2024*** ***Online: 08.04.2024*** ***Published: 25.04.2024***

Introduction. Analysis of possible oil and gas sources in petroleum basins is one of the key objectives in search for hydrocarbon (HC) accumulations. Evaluation of possible HC sources is especially critical in such basins where presence of several source rock intervals is predicted. One of such objects is the Volga-Urals petroleum basin. The said region is situated in the east of the East European platform and is confined to the Volga-Urals anteclise. The basin's sedimentary cover is presented by Riphean, Vendian, Devonian, Carboniferous, and Permian deposits. Structurally, it is divided into two major complexes – the aulacogen (RF) and plate (V-P) ones. Stratigraphic scope of the Riphean complex of the lows within the Kama-Belaya aulacogen is different [1, 2], therefore in this work these deposits are analyzed separately – for its Kama and Belaya parts.

Commercial oil and gas presence of the Volga-Urals petroleum basin is mainly associated with petroleum plays of the clastic Devonian (the Ardatov, Mullino and Pashiya horizons), Upper Devonian (terrigenous-carbonate deposits of Frasnian and Famenniasn age), Lower (Tula and Bobriki horizons) and Middle Carboniferous (Bashkirian-Moskovian deposits), it is not unusual that Lower Permian (Asselian, Sakmarian and Artinskian) deposits demonstrate oil and gas presence. The underlying Vendian deposits include several small-size (Sokolovo, Siva, Sharkan, Debes) oil fields [1, 3, 4].

The cause for a practically total absence of HC accumulations in the Riphean-Vendian (RF-V) play is not completely clear up-to-date. This is possibly associated with destruction of previously formed accumulations or with availability of a merely insignificant amount of organic matter for hydrocarbon generation. Unavailability of an impervious top seal in the RF-V play is considered as the cause for such situation (D.I.Ivanov, 2008), due to which hydrocarbons generated by Riphean-Vendian rocks migrated and concentrated in the overlying Paleozoic sediments (Pz) [3].

Based on data of a literature review and own analytical research, analysis of accumulation and alteration of Riphean, Vendian and Upper Devonian-Tournaisian organic matter was conducted. Based on a limited set of biomarker parameters (distribution of normal alkanes, cheilanthanes and steranes) a genetic link of Paleozoic and Proterozoic oils with Precambrian organic matter was established*.

Results of the performed 2D basin modeling corroborated the data obtained earlier and also made it possible to reveal spatial and temporal peculiarities of development of the oil plays of the part of the basin under investigation.

The goal of this research was to analyze the influence of RF-V source rocks upon formation of hydrocarbon potential of the sedimentary cover of the eastern part of the Volga-Urals petroleum basin based on biomarker analysis and 2D basin modeling.

Objectives:

• Collect and analyze data on geological framework and hydrocarbon potential of Riphean-Vendian deposits of the eastern part of the Volga-Urals petroleum basin.

• Consider the available publications concerning composition (biomarkers including) of organic matter in Proterozoic source rock intervals in Russia and worldwide.

• Perform geochemical analysis of organic matter of Precambrian deposits and oils of the V_2, D_2, D_3, $C_{1\text{-}2}$ plays using methods of isotopic geochemistry and chromato-mass-spectrometry.

• Based on the thus obtained material, construct 2D basin models along regional profiles within the Kama and Belaya depressions of the Kama-Belaya aulacogen.

• Analyze performance of oil plays of the region, assess the role of source rock intervals of various ages in the formation of petroleum potential of the region, and present a model of petroleum plays non-contradictory to the available information.

Materials and methods. *Geochemical analysis.* There have been analyzed 12 oil samples and 8 samples of bitumoids extracted from Precambrian source rocks (V_2kc – Kocheshor formation). Oil samples were selected based on spatial closeness to near-flank zones of the Kama-Belaya aulacogen (proceeding from the recommendations suggested in the previous work [3]). Utilized were oil samples from pay intervals of the following areas: Debes (V_2kr), Sokolovo (V_2kr), Siva (D_3tm), Kudymkar (D_3tm), Krasnokamsk (D_3tm), Kuyeda (D_2ps), Kasib (D_2ps), Mishkino (D_3dm), Kuligino (D), Savino (C_1t) and Gozhan (C_1bb). Bitumoids were extracted from carbonaceous deposits of the Kocheshor formation (V_2kc) of the Efimovo area (Fig.1).

Separation of extracts and oils into groups was conducted on glass columns filled with АСКГ grade silver-impregnated silica gel with grain size of 0.1-0.2 mm. After drenching of silica gel with hexane, a sample weight of maltenes was transferred into the column. Thereafter, elution of the paraffin-naphthene HC fraction with hexane was conducted. The aromatic HC fraction was desorbed and eluted with toluene. Upon completion of separation, flasks with fractions were put under exhaust hood until complete evaporation of the solvent. Subsequent geochemical analysis of analytical groups in organic matter and oils was made by the chromato-mass-spectrometry method on the Agilent 6890B chromatograph furnished with Agilent 5977A MSD mass-spectrometer.

Basin modeling. Performing 2D basin modeling made it possible to reveal and illustrate spatial-temporal peculiarities of the development of petroleum plays in the part of the basin under investigation. In this work, four regional profiles were utilized – one near-east-west and one near-north-south ones for each of the Kama and Belaya depressions of the Kama-Belaya aulacogen correspondingly (Fig.1).

*The idea concerning possible presence of oils generated by Precambrian source rock intervals in the Paleozoic plays was suggested at various times by V.I.Kozlov, K.R.Chepikova, I.A.Larochkina, G.N.Gordadze, et al. However, no comprehensive argumentation in favor of this idea has been presented up till present.

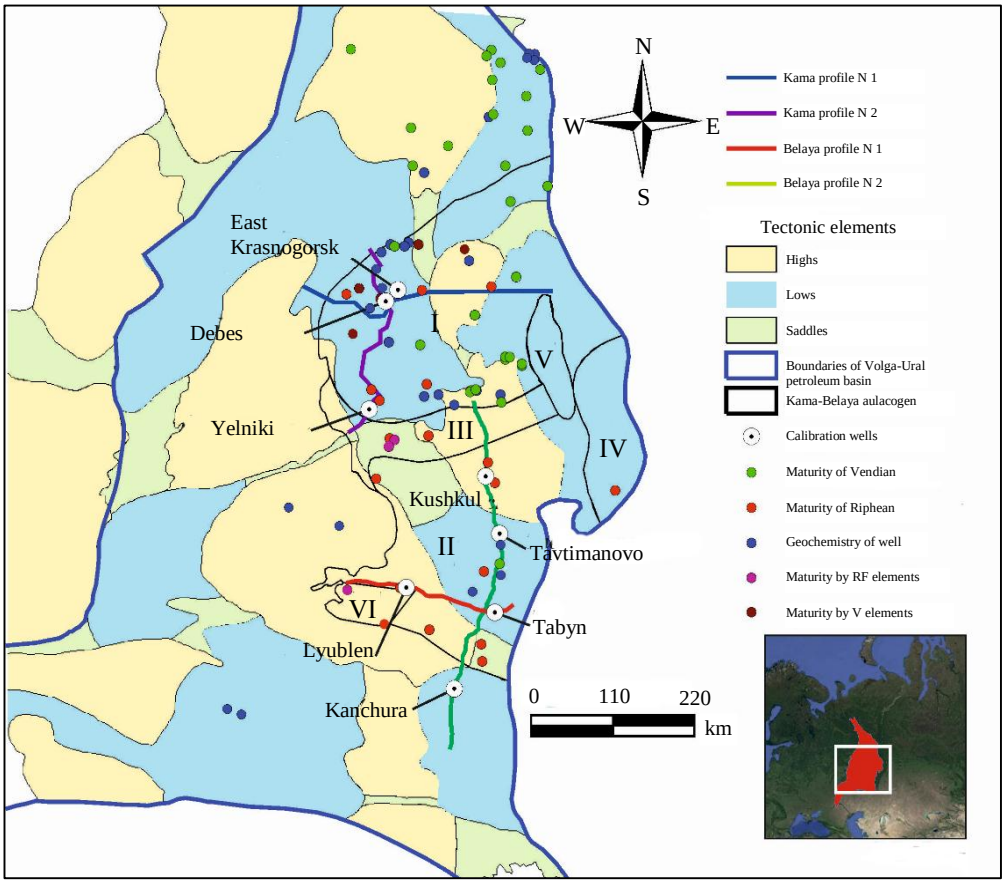

Fig.1. Factual basis map on tectonic base
Structures of the Kama-Belaya aulacogen:
I – Kama depression; II – Belaya depression;
III – Oriebash-Tatyshly-Chernushino uplifted zone; IV – Druzhinino bulge;
V – Osintsevo-Krasnoufimsk bulge; VI – Novotroitsk terrace

Source data were borrowed from field level reports of various years (2005-2009). Length of the profiles totals to more than 1450 km. Sections in the models were populated with stratigraphy and lithology in accordance with regional schemes, paleogeography reconstructions and well data [1]. Modeling was performed using several scenarios – with and without availability of source rock intervals in the RF-V play. The lithology characteristic was downloaded with due regard for various paleofacies maps and reconstructions (Fig.2).

The model takes in due account the *erosion events* that took place in the territory of the Volga-Urals petroleum basin. At the Riphean-Vendian boundary, thickness of deposits being eroded did not exceed 1500 m, at that a maximum thickness of eroded sediments is characteristic just of the northern regions [5, 6]. The beginning of the Early Paleozoic was also marked with a significant erosion event for the eastern margin of the East European platform. Up to 1000 m of Riphean-Vendian deposits were supposedly denudated at that time. At the end of Late Permian and beginning of Triassic, the territory again experienced upward movements, that having resulted in "cutting-off" of up to 250-300 m of rocks.

Fault tectonics. During the time of its formation, the territory of the basin under consideration has experienced rather a lot of alterations caused by the geology evolution of the region and to a greater extent by its geodynamic rearrangements. Manifestations of fault tectonics are traced at all structural stages. Within the eastern part of the Volga-Urals basin, principal zones of fault tectonics manifestation are confined to boundaries of various basement blocks (the Tatar, Bashkir and Perm arches), that having been caused by Archean-Early Proterozoic processes of formation of consolidation zones of protoplaforms. Northwestern (almost meridional) strike is typical of these faults. It is supposed that "opening" of the available faults took place in the time period of tectonic activation (at the end of Vendian and in the Late Permian-Triassic).

Journal of Mining Institute. 2024. Vol. 266. P. 199-217

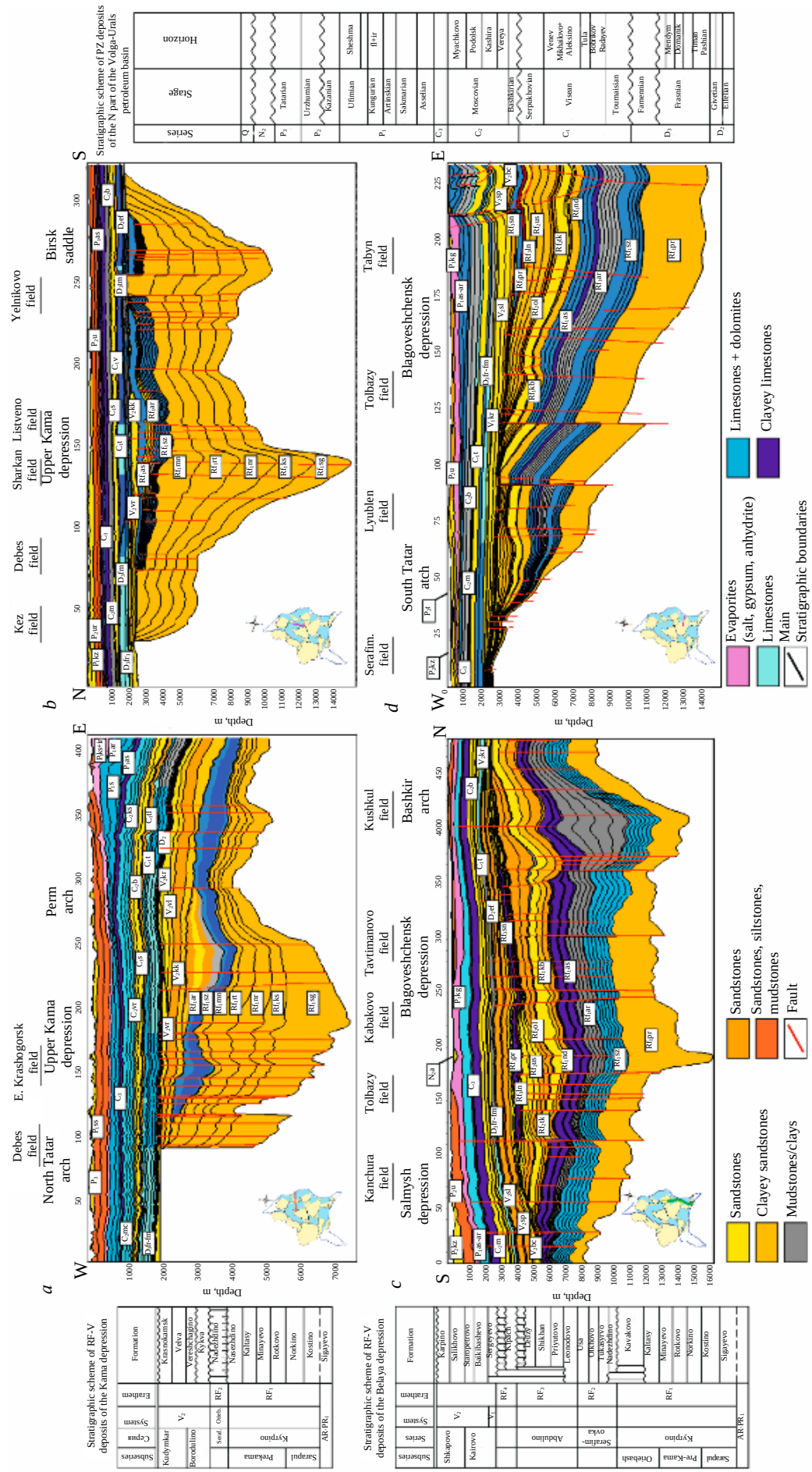

Fig.2. Lithology-stratigraphy profiles with position of the section line on structure map of the Volga-Ural petroleum basin and stratigraphic columns

Boundary conditions. Heat flux values versus time were matched in accordance with the geotectonic regime of the basin's evolution [7]. At the Riphean (aulacogen) stage in the zones of active rifting (the eastern part of the area) heat flux values reached 50-60 mW/m^2. The time of closure of the rift basin in RF_3-V_1 was characterized by a moderate heat flux of up to 50 mW/m^2. At the Vendian-Cambrian boundary heat flux could increase to values of 55 mW/m^2. Further on, up to the Permian-Triassic boundary heat flux was stable (at a level of 40-50 mW/m^2). Thereafter at the Meso-Cenozoic stage, heat flow values reduced, especially in the western parts of the study area (down to the level of 19 mW/m^2). Heat flux values were ranked area-wise and section-wise. Maximum values of the said parameter are observed in depression parts of the section. Data on values of present-time formation temperatures were taken from reference books and depository reports. The parameters introduced into the model are presented in Table 1.

Table 1

Characteristics of source rock intervals

Rocks	Lithology	Thickness, m	Organic matter type	TOC, %	HI_0, mgHC/gTOC
RF_1sz	Argillite	Up to 300 (cumulatively)	II	1.5	900
RF_1ar	Dolomitic marl	Up to 100	II	1.5	600
RF_2ol	Argillite	Up to 50	II	0.47	400
RF_3shn	Argillite	Up to 50	II	0.53	650
V_2vr (sp)	Argillite	Up to 100	II	5	710
D_2af	Argillite	30	II/III	1.0	250
D_3fr-fm	Siliceous argillite	Up to 60	II	2.0-10.7	600-710
C_2vr	Carbonaceous argillite	30	II/III	0.54	300

Characteristics of source rock intervals. As the input parameters, there were used analytical values of total organic carbon content (TOC_0) and hydrogen index (HI_0) recalculated to initial values. The detailed description of organic matter of source rock intervals was presented in the previous work [3] and is also shown in Table 1. In light of the fact that organic matter of various (in age, type and areal extension) source rock intervals has various individual characteristics, the kinetic models selected for modeling only partly reflect the character of realization of generation potential of the deposits under investigation.

The degree of catagenetic alteration of organic matter in various source rock intervals was assessed based on literary data [2, 8, 9]. Calibration of the models was made by data of present-time formation temperatures from wells located in the areas: Kanchura, Tavtimanovo, Kushkul, Lyublen, Tabyn, Debes, East Krasnogorsk, Lozolyuk, Yeseney, Baklanovo, Yelniki, and others (Table 2); by values of *Ro* ((Vitrinit) Reflection in oil) taken from maps, and by zones of catagenesis identified previously by the authors [4, 8, 9]; and by location of hydrocarbon fields area-wise and section-wise.

Geological characteristic. *Tectonics*. Tectonic appearance of the study area is presented by three structural stages. The lower – aulacogen stage is located within boundaries of the Kama-Belaya aulacogen – it comprises ancient-laid structures. It is divided into the Kama and Belaya depressions separated by the Oriebash-Talyshly-Chernushino uplifted zone. In the east, there are identified uplifted blocks of the crystalline basement – the Osintsevo-Krasnoufimsk and Druzhinino bulges (see Fig.1).

In the middle (syneclise) structural stage, two lows are identified – the northern (Upper Kama depression) and the southern (Shkapovo-Shikhany depression) separated by the Sarapul-Yanybayevo saddle. All structures are composed of Upper Vendian deposits. Stratigraphic fill of the depressions is similar to one another, though names of complexes are different. Brief description of the Riphean-Vendian stratigraphy is presented below separately for the northern and the southern depression parts of the study area.

Table 2

Main calibration parameters utilized in the model

HC field	Structure	Depth, m / *T*, °C	Depth, m / *Ro*, %	Catagenesis grade
Kanchura	Salmysh depression	25/4	25/0.5	–
Tavtimanovo	Blagoveshchensk depression	2067-2125/41	2067-2125/0.5	–
Kushkul	Bashkir arch	25/6	25/0.5	–
Lyublen	South Tatar arch	1413-1451/28	–	–
Tabyn	Blagoveshchensk depression	339/12 1585/31 1669/36	–	–
Debes	Upper Kama depression	1276/26 1760/36	–	1797/PC_3-MC_1
East Krasnogorsk	Upper Kama depression	1306/26 1580/28 1611/28	–	1705/PC_3
Lozolyuk	Upper Kama depression	1292/27 1383/28	–	1724/MC_1
Yeseney	Upper Kama depression	–	–	2011/PC_3
Baklanovo	Perm arch	1267/23 1276/24 1631/29	–	2446/MC_1
Yelniki	Birsk saddle	786/18.5 895/23 1410/28 1470/29	–	–

The third (present-time) structural stage within the study area is presented in the composition of the Upper Kama, Bym-Kungur, Yuryuzan-Sylva, Blagoveshchensk and Salmysh depressions, Perm, Bashkir and Tatar arches, and also the Birsk saddle. Similarity in stratigraphic and facies appearance of various parts of the said structural stage afforded the opportunity to consider Paleozoic deposits in concordance with the regional stratigraphic schemes (Fig.2).

Stratigraphy. Stratigraphic fill of depressions of the Kama-Belaya aulacogen is different – the northern (Kama) depression is composed of Lower and piecewise Middle Riphean deposits, the southern (Belaya) depression is composed of rocks of all the three series of the Rihean – Kyrpy (Lower), Serafimovka (Middle) and Abdulino (Upper) series. The composition of the Lower Riphean complex of the sedimentary cover of the northern (Kama) depression include clastic deposits of the Sarapul and Pre-Kama series and also clayey-carbonate sequences of the Kaltasy formation of Kyrpy series. The Upper Vendian part of the overlying Upper Kama depression is presented in the composition of the Kykva, Vereshchagino, Velva and Krasnokamsk formations [1]. The section of the Riphean-Vendian part of the Belaya depression of the Kama-Belaya aulacogen has a significantly wider span. In addition to Lower Riphean deposits, present are also mainly terrigenous rocks of the Middle Riphean and terrigenous-carbonate sequences of the Upper Riphean. The Upper Vendian terrigenous complex of the said part of the Volga-Urals region is presented practically in the same volume, though names of stratigraphic subdivisions are different: Baykibashevo, Staropetrovskoye, Salikhovo and Karlino formations (Fig.2).

Oil and gas presence. In the section of the basin's sedimentary cover, several oil plays and promising oil/gas plays are identified, each of which is characterized by similar conditions of oil/gas accumulation and types of HC deposits. Boundaries of plays are drawn along regionally persistent impervious seals. As source rocks of the Riphean-Vendian play, the deposits of the Lower Riphean Kaltasy formation, as well as clayey deposits of the Vereshchagino and Staropetrovo formations of the Upper Vendian are considered. In the Paleozoic part, as source rock intervals there serve deposits

of the Afonino horizon of Middle Devonian, Domanik high-carbonaceous formation of the Upper Devonian-Tournaisian, and coal-bearing rocks of the Vereya horizon of the Middle Carboniferous. In the Belaya part, in addition to the above-mentioned ones, there are also source rocks of the Kabakovo, Olkhovo and Shikhan formations of Riphean. Reservoirs are mainly presented by Upper Vendian, Middle Devonian clastic deposits, and also carbonate sequences of the Middle-Upper Carboniferous and Lower Permian. As impervious seals, there serve Upper Vendian argillites, Upper Devonian-Tournaisian clayey-carbonate-siliceous sequences, and also carbonate-evaporite deposits of the Kungurian stage of the Lower Permian.

Availability of a considerable number of source rock intervals in combination with favorable thermobaric conditions for generation of liquid and gaseous hydrocarbons, presence of reservoirs and impervious seals in the section caused appearance of a considerable amount of oil and gas fields in the territory of the basin. Most of them are confined to structures draping major projections of the basement: the South Tatar, North Tatar, Perm and Bashkir arches, Birsk and Kosva-Chusovaya saddles. The biggest number of HC accumulations are revealed in Middle Devonian and Lower-Middle Carboniferous deposits. In the overlying sequences, there are less HC deposits – from the Upper Devonian-Tournaisian play to the Lower Permian play the number of revealed accumulations gradually decreases. Apparently, the Upper Devonian-Tournaisian clayey-carbonate deposits present a seal impeding free movement of hydrocarbons.

Within the Kama depression of the Kama-Belaya aulacogen, oil and gas presence in Precambrian deposits of the Volga-Urals petroleum basin is associated with Kykva and Krasnokamsk formations of Upper Vendian (the Siva, Sokolovo, Sharkan, Debes fields and others). In the Riphean play, but insignificant oil and gas shows were observed in deposits of the Kaltasy formation [2, 4].

In the territory of the Belaya depression of the Kama-Belaya aulacogen, no Riphean-Vendian oil and gas fields have been found. However oil and gas shows are presented rather widely in deposits of the Kaltasy, Tukayevo, Olkhovo and Usa formations of the Riphean, as well as in the Baykibashevo, Salikhovo and Karlino formations of the Upper Vendian [2, 4].

Geochemical peculiarities of Precambrian organic matter and oils. It is known from the history of geologic evolution that biotic communities of the Archean-Proterozoic are presented mainly by bacteria and also primitive algae and protozoans (phyto- and zooplankton). This have reflected in all-round dominance of hopanes over steranes [10]. Organic matter accumulation was taking place exclusively in marine environments in conditions of arid and moderate climate (except the time of Laplandian glaciation) [11, 12]. This is also distinctly indicated by ratio of tricyclic terpanes t19/t23, whose values are usually less than 0.5 [13].

The initial kerogen type is determined as II – aquagenic (sapropelic) organic matter. At that, geochemical appearance of initial OM often might be distorted by alteration processes in source rock sequences that took place in the past [14]. That is why at present the appearance of type III and IV kerogens can be observed, that however contradicting the composition of the biosphere of that time [10, 15, 16]. Inconsistency in determining OM accumulation environments in the Precambrian also resulted in distribution of steranes C27:C28:C29. In particular, a peculiarity of Precambrian oils is dominance of ethylcholestane over cholestane proper and methylcholestane [17-19]. Usually such distribution is characteristic of humic OM. As one more detected geochemical peculiarity of ancient oils is presence of high concentrations of monomethylalkanes (12-, 13-monomethylalkanes, 2-, 3-monomethylalkanes [11, 20]) and dimethylalkanes (2.7-dimethylalkanes) [21]. The nature of this phenomenon is at present not clear until the end. Nonetheless, it is obvious that presence of such HC compounds is characteristic of just a narrow stratigraphic interval (Vendian) and a small number of petroleum basins worldwide (East Siberia and Oman) [10]. A specific marker of Precambrian OM is lightened isotopic composition of carbon. After the conducted analysis of numerous publications it was revealed that most oils have values of indicator $\delta^{13}C$ from –30 to –31 ‰. Such peculiarity is also explained by the nature of initial OM (aquagenic, bacteriogenic). Note that the ratio $\delta^{15}N$sed for most Precambrian oils varies within the range of 0 to +8 ‰ [22].

Apparently, the revealed geochemical peculiarities are indicative of high aggressiveness of the environment of that time [22-24], high water salinity [22], low diversity of living organisms [11, 22, 25], low-oxygen composition of the atmosphere [26] and lengthy epochs of earth glaciations (Greenlandian, Laplandian, etc.) [11, 27].

Discussion of results. *Geochemical analysis of PR_2 and Pz oils of the study area*. The authors conducted geochemical studies of organic matter and oils from Precambrian and Paleozoic deposits of the eastern part of the Volga-Urals petroleum basin (Table 3). The degrees of catagenetic alteration of source of oils of V_2-Pz plays were revealed, paleogeographic environments of initial OM accumulation were determined.

Table 3

Estimated coefficients obtained by results of cromato-mass-spectrometry of oils and extracts

Well, area	Fluid type	Stratigraphic interval	Environment								Maturity			
			Pr/Ph	Pr/n-C_{17}	Ph/n-C_{18}	t19/t23	C27/C29	C28ββ/C29ββ	ETR (4)	DBT/P	Ts/Tm	MPR (1)	MPI 1 (2)	MDR (3)
Debes, 600	E	V_2kr	0.3	0.66	0.48	0.06	0.1	0.14	0.6	0.04	0.4	1.0	0.4	0.3
Sokolovo, 52	O	V_2kr	1.13	0.86	0.85	0.1	0.1	0.15	0.7	0.08	0.4	0.8	0.7	2.8
Siva, 1	O	D_3tm	1.12	0.75	0.85	0.12	0.1	0.15	0.7	0.07	0.6	1.2	0.7	8
Kudymkar, 1	O	D_3tm	0.89	0.76	0.85	0.06	0.5	0.3	0.8	1.1	0.23	0.7	0.5	1.8
Krasnokamsk, 207	O	D_3tm	1.13	0.73	0.65	0.11	0.5	0.4	0.7	0.64	0.65	0.6	0.5	2.5
Kuyeda, 2	O	D_2ps	0.63	0.81	1.19	0.04	0.4	0.4	0.9	0.71	0.13	1.3	0.8	2.4
Kasib, 3	O	D_2ps	1.29	0.67	0.53	0.17	0.6	0.3	0.7	0.65	0.6	0.6	0.5	3.2
Mishkino, 185	O	D_3dm	0.55	1.02	1.76	0.02	0.7	0.4	0.9	1.3	0.09	1.6	0.9	1.4
Kuligino, 61	O	D	0.68	0.79	1.13	0.05	0.5	0.3	0.9	–	0.19	–	–	–
Savino, 140	O	C_1t	0.62	1.09	1.78	0.02	0.7	0.3	0.9	0.68	0.14	1.2	0.8	1.8
Gozhan, 3	O	C_1bb	0.63	0.93	1.38	0.02	0.6	0.3	0.9	1.1	0.2	1.0	0.9	1.7
Krasnovishersk, 2.4 (1 extr)	E	V_2kc	1.0	0.78	0.8	0.26	1.2	1.12	0.7	0.09	0.5	1.0	0.7	3.9
Krasnovishersk, 2.4 (hot)	E	V_2kc	0.24	0.95	1.0	0.1	1.2	1.1	0.6	0.06	0.5	1.1	0.9	2.2
Krasnovishersk, 2.4 (cold)	E	V_2kc	0.07	0.77	0.76	0.05	1.1	1.1	0.6	0.12	0.5	1.0	1.0	1.4
Krasnovishersk, 301-2	E	V_2kc	0.23	0.56	0.54	0.07	0.9	0.85	0.7	0.03	0.5	2.6	0.9	5.0
Krasnovishersk, 301-2 (extr)	E	V_2kc	1.04	0.79	0.79	0.3	1.1	1.12	0.7	0.1	0.5	1.1	0.7	3.4
Krasnovishersk, 301-2 (hot)	E	V_2kc	0.13	0.72	0.85	0.11	1.1	1.2	0.6	0.07	0.5	1.3	1.0	1.6
Krasnovishersk, 301-2 (cold)	E	V_2kc	0.04	0.72	0.67	0.04	1.0	1.0	0.6	0.07	0.5	0.8	0.9	1.3
Krasnovishersk, 301-26	E	V_2kc	0.18	0.53	0.48	0.07	0.9	0.8	0.7	0.04	0.5	2.0	0.9	4.6

Note: O – oil; E – extracts; DBT – dibenzothiophenes; P – phenanthrene; Pr – pristine; Ph – phytane; n-C_{17-18} – normal alkanes; C27:C28:C29 – steranes; t19/t23 – cheilanthanes; Ts/Tm – trisnorhopanes.

Genetic peculiarities. Let us characterize genetic peculiarities of organic matter and oils (Fig.3, *a*). The ratios DBT/P and Pr/Ph (Fig.3, *b*) demonstrate that the Vendian OM belongs to lithofacies zone 2 (sulfur-poor lacustrine deposits). Values obtained by results of studying V-Pz oils are also located over there. Part of samples gravitate to zone 3 (marine clays and other lacustrine deposits). Samples of Domanik deposits of the Volga-Urals petroleum basin [28] are practically completely located in the zone 1B (marine carbonates and marine marls).

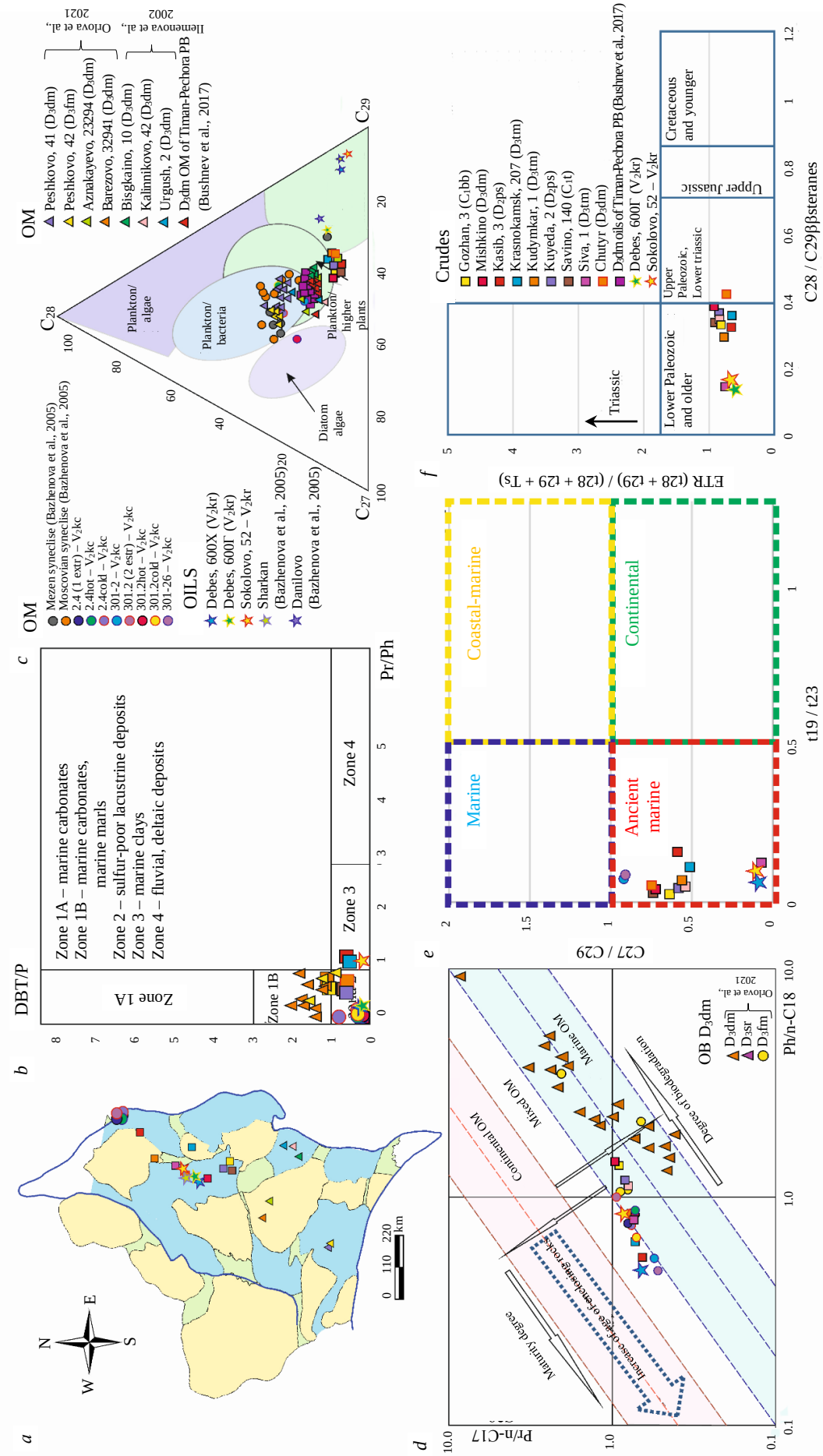

Fig.3. Results of the performed chemical analysis of OM and oil: *a* – position of oil sampling points; *b* – diagram of ratios of indices DBT/P and Pr/Ph; *c* – trigonogram of distribution of content of steranes C27:C28:C29; *d* – Connan – Cassou diagram; *e* – diagram of C27/C29 versus t19/t23 [29, 30]; *f* – diagram of ETR versus C28/C29

For genetic tie of the oils under study and for OM-oil correlation, trigonogram of ratio of steranes C27:C28:C29 was used (Fig.3, *c*). All the studied OM and oil samples are divided into four geochemical groups. The first group includes oils sampled from Precambrian pay intervals, as well as oil from the Siva field (D_3tm). These samples are characterized by a sharp dominance of sterane C29. The second group is presented by organic matter of pay rock intervals of Upper Vendian and Upper Devonian age. It is characteristic of dominance of sterane C27, that being associated with sapropelic type of initial OM [28]. The third group includes OM and oil samples from Domanik deposits of the Volga-Urals and Timan-Pechora petroleum basins in which content of sterane C29 increases. This peculiarity is explained by a mixed (II/III) type of initial organic matter.

The oils under study form the fourth group situated between the OM of Domanic deposits and the Proterozoic oils. It is established that all oils under study are characterized by significant contents of ethylcholestane C29. Its share in the total volume of steranes varies from 51 to 88 % (Fig.3, *c*). This peculiarity is indicative of mainly ancient bacteriogenic origin of OM. For complex genetic characterization of oils and OM under study, we also constructed a Connan – Cassou diagram (Fig.3, *d*). It was found out that these samples are located in zones of mixed and marine OM, while Domanik ones have solely marine genesis. It is interesting that maturity of oils and OM (determined using this diagram) regularly increases with age of host rocks.

Catagenetic characteristic. In addition to genetic peculiarities, we also made an attempt to determine degree of maturity of oils based on biomarker characteristics. For this purposes the authors conducted molecular analysis by the technique described by Matthias Radke [31]. The following coefficients were calculated (Table 3):

$$MPR = [2 - MP]/[1 - MP]; \quad (1)$$

$$MPI\ 1 = 1.5\ ([2 - MP] + [3 - MP])/([P] + [1MP] + [9 - MP]); \quad (2)$$

$$MDR = [4 - MDBT]/[1 - MDBT], \quad (3)$$

where MP – methylphenanthrenes; P – phenanthrene; MDBT – methhyldibenzothiophenes.

Subsequent computation of the parameter *Rm* (Mean Vitrinite Reflectance) was made using the diagrams presented in [32]. Grades of catagenesis were determined by data of V.T.Frolov (1992). All oils under study were generated by source rocks at MC_1-MC_2 ctagenesis grades. The Ts/Tm ratio demonstrates rather high maturity – values of this parameter vary from 0.13 to 0.65 (Table 3). The revealed values generally coincide with position of catagenetic zones determined previously for RF-V [2, 4]. Nonetheless, one cannot exclude influence of Upper Devonian-Tournaisian source rock intervals, because in adjacent structures (the Solikamsk depression, the eastern part of the Upper Kama depression, the Belaya depression and others) mature rocks of this age are present. In connection with this, it is necessary to conduct combined age characterization of HC sources in the part of the basin under study.

The following diagram implying age of source rocks is constructed based of ratios of steranes C27/C29 and cheilanthanes t19/t23 (Fig.3, *e*). The said parameters were determined by the authors for a good reason because in this case they make it possible to divide OM into purely marine and purely continental. A kind of ‘contradiction zone’ is also identified where ratio of tricyclic hydrocarbons would be indicative of aquagenic origin of OM, while steranes would indicate ancientness. As a result, plotting the obtained valued showed that the oils and bitumoids under study again got into the area of ancient marine organic matter.

For higher reliability of the obtained results, the authors constructed one more diagram that is also based upon ratio of steranes C28 and C29 and cheilanthane index (Fig.3, *f*),

$$ETR = (t28 + t29)/(t28 + t29 + Ts). \quad (4)$$

By data of T.B.Abay [32], analysis of distribution of the said coefficients makes it possible to determine age tying of source rocks, which have generated the fluid under consideration. It is interesting that on this diagram practically all samples under study (except oil from the Chutyr field)

also appeared in the zone corresponding to the age interval of the Lower Paleozoic and older (Fig.3, *f*). Since Lower Paleozoic rocks are not revealed in the section of the part under study of the Volga-Urals basin, there is no doubt that these oils were generated from the Precambrian organic matter. Ancient OM and HC compounds generated by it are characterized by presence of isotopically light carbon. In the eastern part of the Volga-Urals petroleum basin, such oils are encountered on the Sokolovo, Siva, Debes fields ($\delta^{13}C$ from –31 to –30 ‰). Carbon of the Paleozoic OM is isotopically heavier ($\delta^{13}C$ from –27 to –28 ‰) [33]. This peculiarity allows making correlation of oil to OM of a source rock interval. Based on retrospective data [33], such analysis was also made. It was found out that in Middle-Upper Devonian and Lower Carboniferous oils, the $\delta^{13}C$ indicator varies within the range of –27.3 to –30.5 ‰, not exceeding value of –29 ‰ on the average. Isotopically light carbon in oils of the Paleozoic part of the section is indicative of presence of hydrocarbons generated by ancient (Precambrian) source rock intervals. These peculiarities (OM type, TOC_0, HI_0) were used in modeling for revealing sources of HC accumulations in the part of the section under study. Analysis of modeling results was conducted with consideration of the revealed connection between oils of the Proterozoic and Paleozoic.

Results of basin modeling. The models along four regional profiles located in the Belaya and Kama parts of the Kama-Belaya aulacogen (see Fig.1, 2) are constructed with consideration of history of tectonic evolution, paleogeographic peculiarities of formation and further alteration (erosion events) of sequences in the sedimentary cover of the basin. The model was calibrated against values of present-time formation temperatures and vitrinite reflectance (see Table 2, Fig.4). Thus, these models are well posed and can be considered in studying processes of generation, migration and accumulation of hydrocarbons in the part of the basin under study.

By results of the conducted modeling, temperature gradient values were obtained for various parts of the basin. Crestal parts are characterized by highest temperature gradient values, especially in their uppermost parts where gradual decrease down the section of this parameter takes place (the Bashkir – 2.4-3.3 and South Tatar arches – 2.0-3.1 °C/100 m). High values are characteristic of major depressions: Blagoveshchensk and Upper Kama – 2.7 to 2.93 and 2.6 to 3.4 °C/100 m, respectively. In the Bym-Kungur and Yuryzan-Sylva depressions this parameter values are a bit lower. The lowest values are predicted for the Salmysh depression and the Birsk saddle – within the range of 1.0 to 2.5 °C/100 m. Assessment of catagenetic alteration degree for deposits over sections was made. The main oil windows and gas windows are situated in the depth interval of 1.36 to 4.1 km in the northern part and 1.6 to 5.8 km in the southern one. Maximum catagenesis grades are achieved at >5 km depths near the Kama depression and >6.6 km near the Belaya depression of the Kama-Belaya aulacogen. The difference in thermal regime is associated first with sedimentary cover thickness; considerable intervals of main gas window and main oil window within the Belaya depression are caused by proximity of the Pre-Urals foredeep. OM maturity degree in source rock intervals over the area was assessed by results of basin modeling with consideration of pyrolysis data from depository and retrospective sources [8, 34, 35]. Adjustment of the revealed catagenetic zones was made using structure maps. As a result there were constructed schematic maps of catagenesis for top of Lower Riphean deposits (RF_1kl) (Fig.5, *a*) and of Upper Vendian deposits (V_2vr, V_2sp) (Fig.5, *b*).

Catagenetic alteration degree of organic matter of Riphean deposits depends on depth of maximum submergence thereof. OM metamorphism degree increases in the southeastward direction and reaches its maximum within the Belaya depression (main gas window). At the same time, most studied deposits are situated within the main oil window.

Vendian deposits are characterized by a lesser alteration degree – OM metamorphism increases in the eastward and southeastward directions. The least altered deposits are located in the northwestern part of the study area – catagenesis grades over there do not exceed PC_3 values. Further eastward, a zone of MC_1 is developed, which gradually changes into MC_2. In the east, within the Yuryuzan-Sylva depression and the Solikamsk depression, OM alteration degree values reach MC_3 grade and higher. A significant part of development of the Vendian complex of deposits, the same as with the Riphean, is situated within the main oil window.

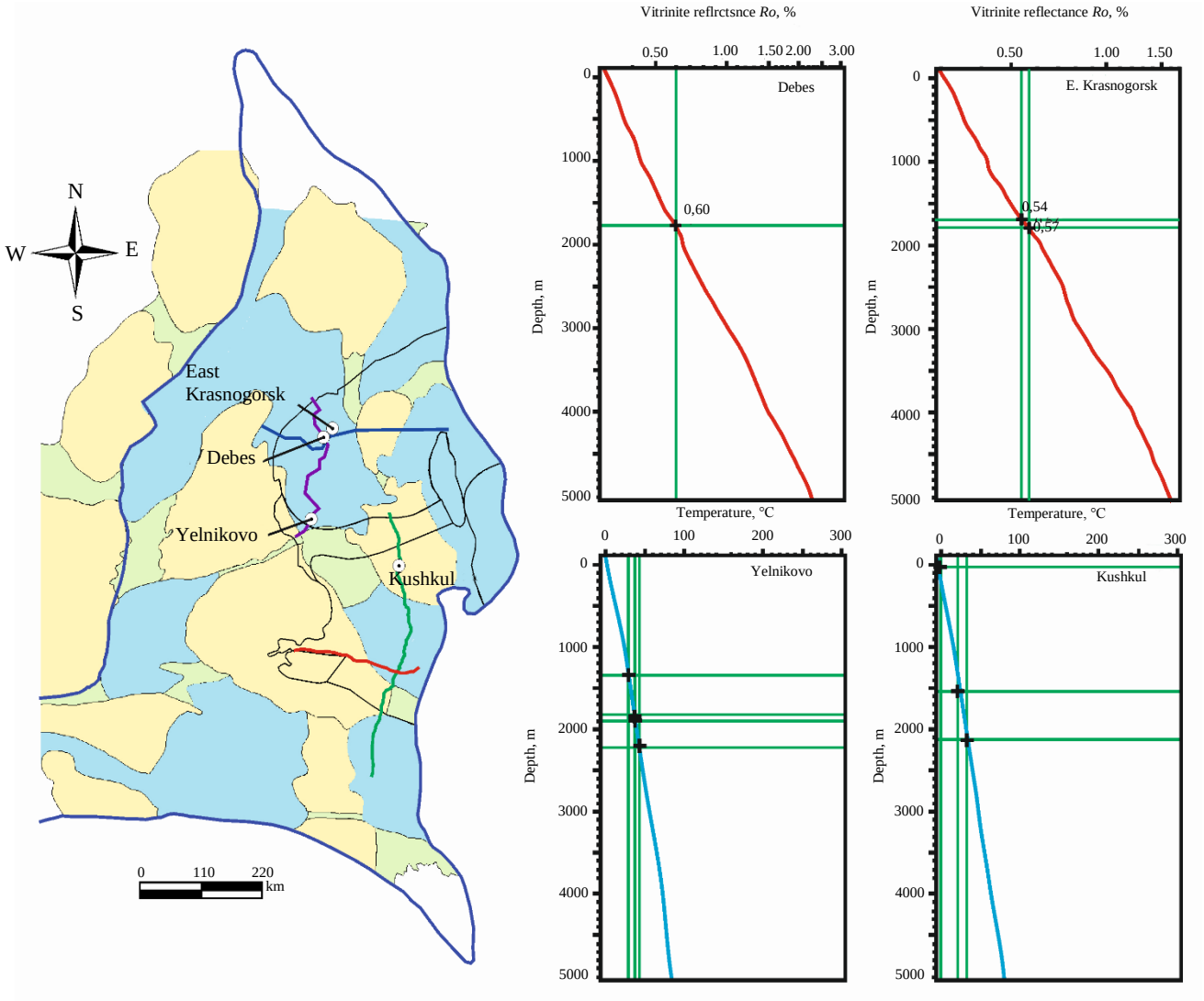

Fig.4. Examples of calibration diagrams using vitrinite reflectance and formation temperature values

The overlying Middle Devonian – Permian deposits within the study area are much less altered. Most part of the Upper Devonian-Tournaisian complex that is considered as a source rock interval is situated within MC_1 zone, maturity increases in structural lows (the Upper Kama and Blagoveshchensk depressions) and in eastward and southeastward directions where formations under consideration are altered up to MC_2-MC_3. By results of the performed modeling, oil-gas source rocks of Middle Carboniferous have not entered the main oil and gas windows in most part of the area, however within the Blagoveshchensk and Upper Kama depressions alteration degree of these deposits reaches MC_1 stage (Fig.5). Thus, most intensive generation processes progressed in the Riphean-Vendian source rock intervals.

While examining the processes taking place in petroleum systems, special attention should be paid to time of generation, migration and accumulation, as well as time of formation of traps. Manifestation of such or another process depends on history of geologic evolution of the region, specifically on deposition rate, time and intensity of erosion processes, local and regional temperature field variations.

By results of basin modeling, source rocks of the Kaltasy formation started generating liquid and gaseous hydrocarbons as early as at the end of the Early Riphean. That said, in the Belaya part of the aulacogen, generation continued up until the Late Riphean. The pre Vendian unconformity resulted in temporary suspension of generation by the Riphean source rock intervals. The subsequent oil and gas generation took place as late as in the Late Carboniferous-Permian in the Kama depression and in the Early Carboniferous in the Belaya depression [36]. The source rocks of the Upper Vendian and partly of the Devonian also reached the level needed to start HC generation, at that formation of oil and gas continued (Fig.6, 7).

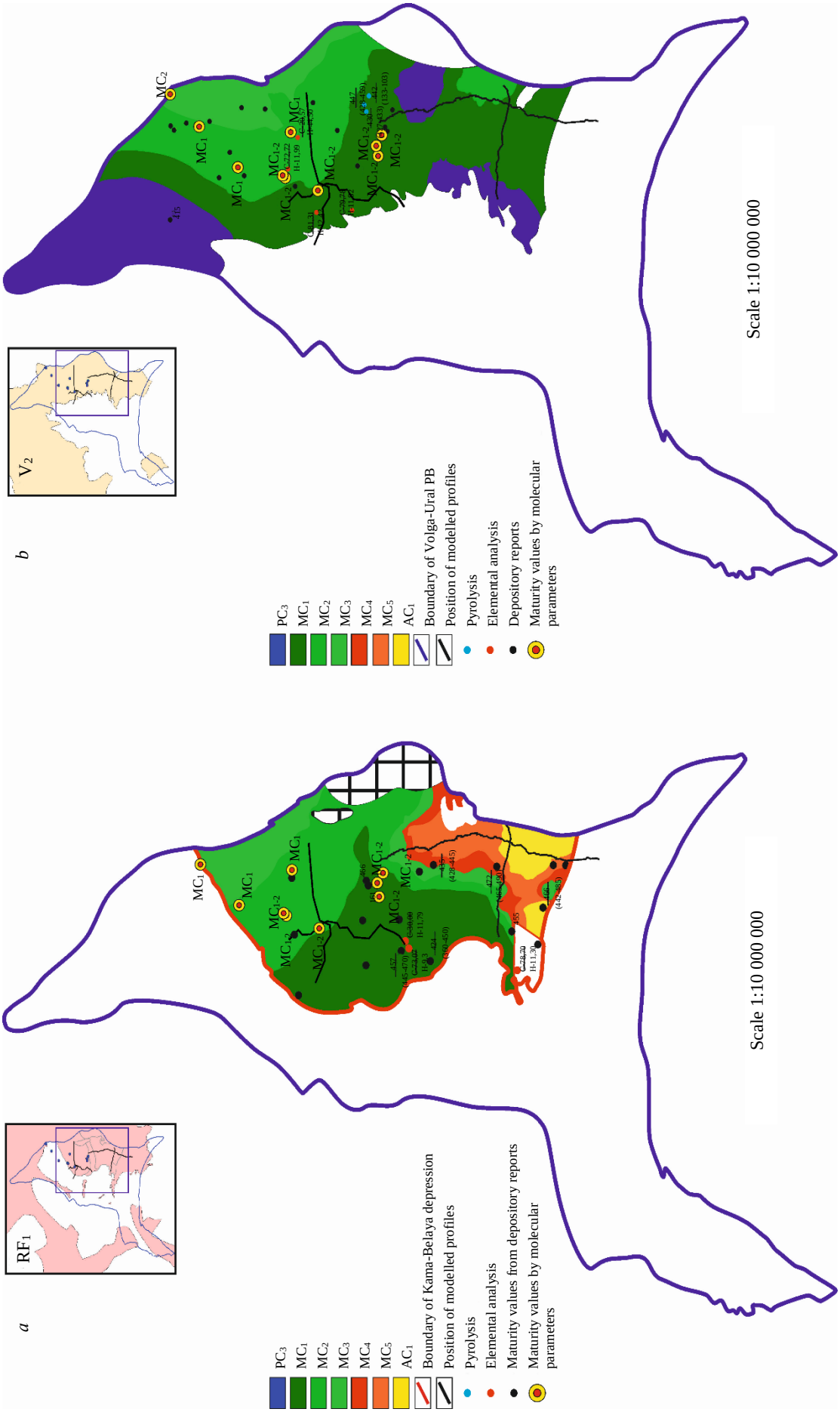

Fig.5. Schematic maps of catagenesis along top of RF_1 (*a*); top of V_2 (*b*)
Fraction denotes variation of parameter T_{max}: in numerator – mean value, in denominator – minimum and maximum

Journal of Mining Institute. 2024. Vol. 266. P. 199-217

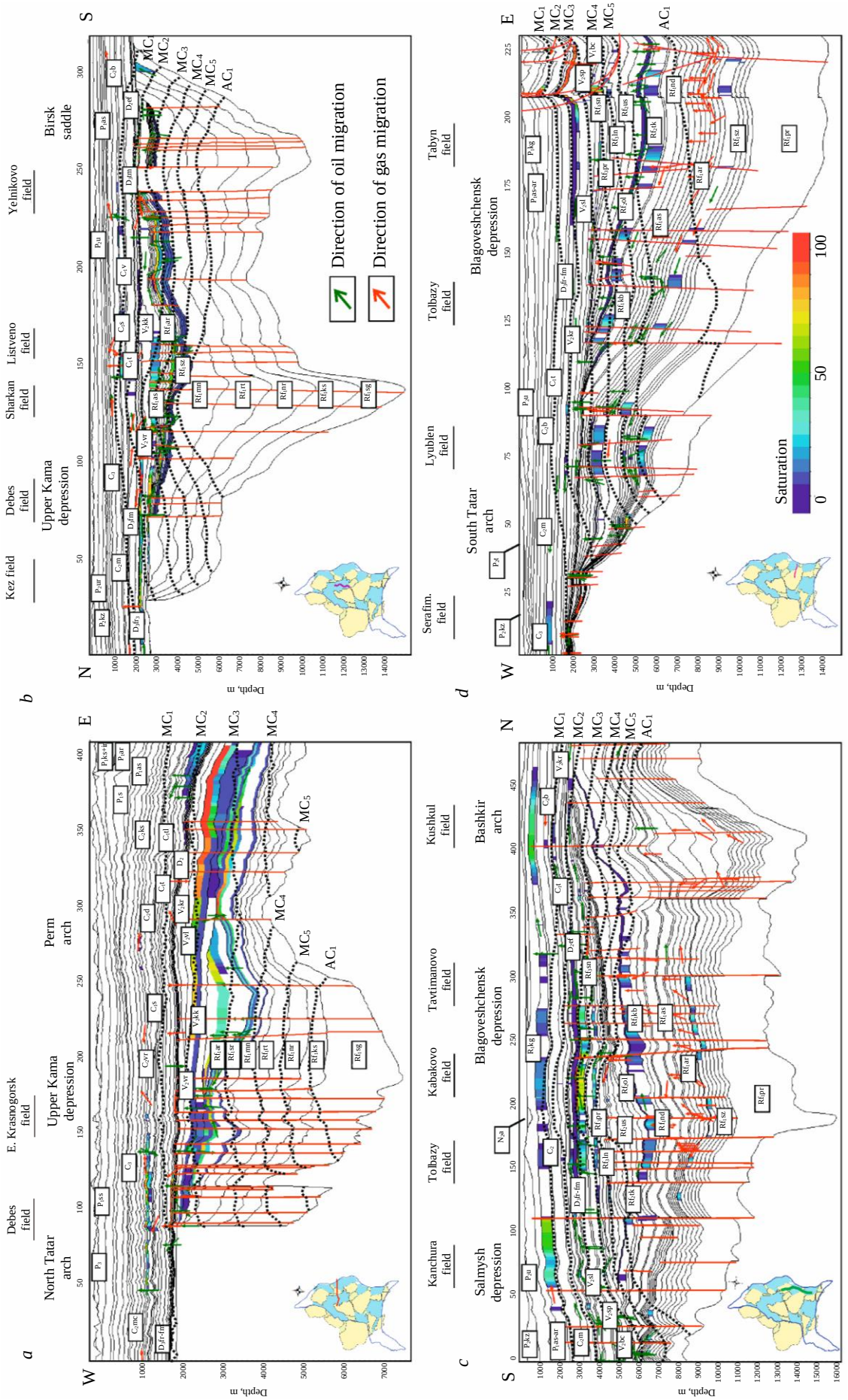

Fig.6. Position of zones of oil and gas accumulation on profiles with position of section line on a structure map of Volga-Ural petroleum basin
Dotted lines denote top boundaries of catagenetic zones

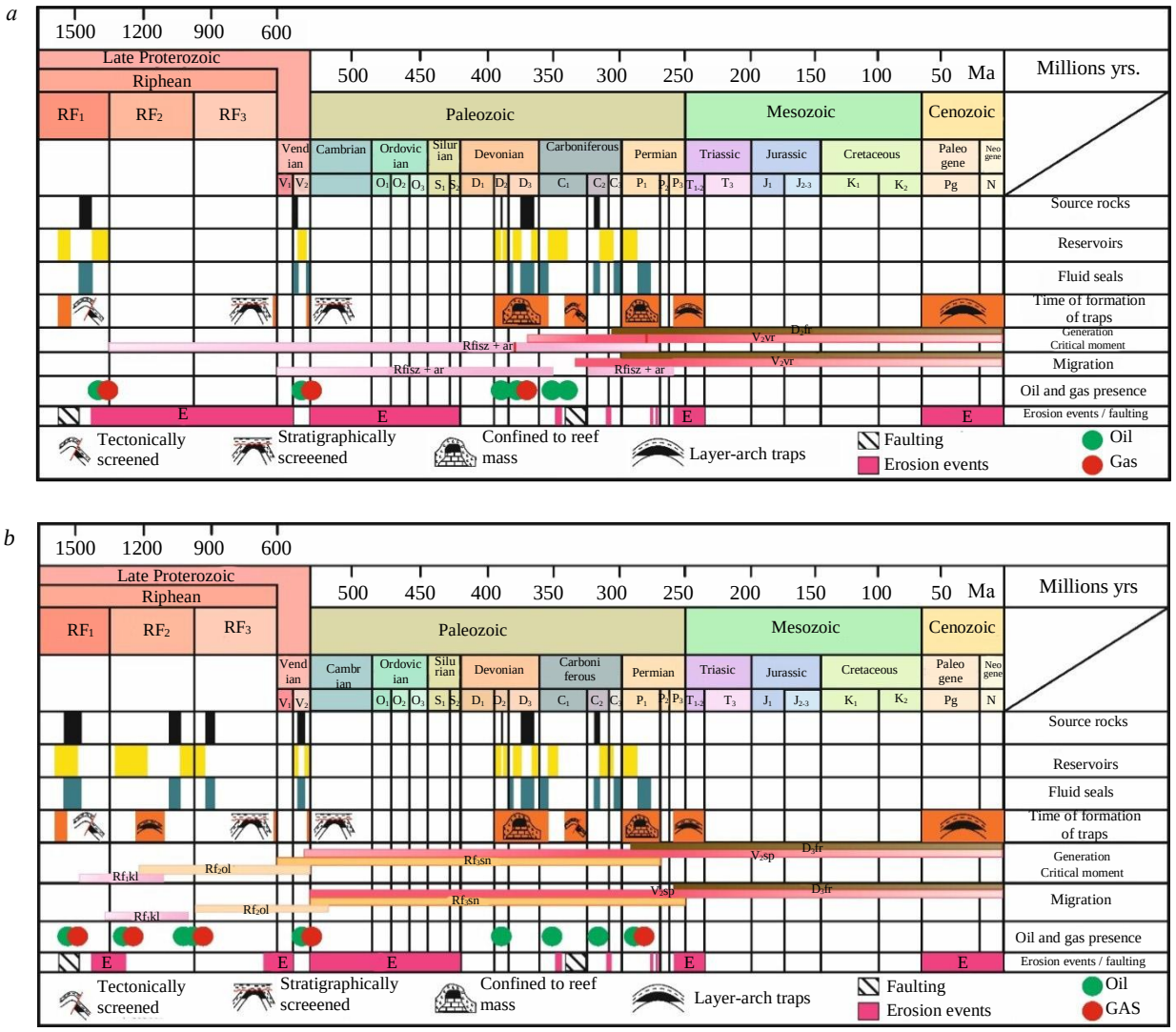

Fig.7. Scale of events constructed by results of 2D basin modeling
for the Kama (*a*) and Belaya (*b*) parts of the Kama-Belaya aulacogen

The duration of oil and gas generation processes resulted in significant alteration degree of RF-V source rocks. In particular, the transformation degree of Riphean source rock intervals reaches 85-90 % in the Kama depression, while in the Belaya depression the Riphean has completely depleted its potential. Transformation index of Vendian source rock intervals in the northern (Kama) part of the Kama-Belaya aulacogen equals approximately 50-60 %, in the southern part its values vary within the range of 31 to 97 %. Upper Devonian-Tournaisian formations are least transformed, maximum transformation degree is 52 %, though in most part it does not exceed 30 %. Thus, the Riphean-Vendian source rock intervals have run out their oil generation potential practically completely. The Domanik formations, to the contrary, have a high potential to generation of liquid and gaseous hydrocarbons, though degree of their depletion is rather low within most part of the area [37], that raising doubt in the issue of prevalence of this source in forming HC deposits in the said part of the Volga-Urals basin.

The formation of anticipated accumulations of liquid and gaseous hydrocarbons in the northern and southern parts of the study area proceeded in a number of stages. In the southern (Belaya) part, migration of fluid generated by source rocks of the Kaltasy formation started as early as at the end of the Early Riphean. At that time formation of mainly oil deposits was taking place in deposits of the Sauzovo and Ashit subformations. In the Middle Riphean, gas content in them considerably increased, new accumulations were forming in the Tukayevo formation. By the end of Late Riphean,

total volume of accumulated fluid increased, new accumulations appeared in deposits of the Usa and Leonidovo formations. In the second half of the Late Vendian, hydrocarbons filled traps in deposits of the Baykibashevo, Salikhovo and Karlino formations. Closer to the end of Devonian, oil deposits did form in the clastic Devonian. In the Middle-Late carboniferous, filling of firstly Bobriki and thereafter of Bashkirian age reservoirs took place. HC accumulations in Lower Permian deposits were formed at the very end of the Paleozoic stage of evolution and their formation continues in the present time.

In the northern (Kama) part of the basin, processes of formation of HC accumulations proceeded somewhat differently. Because of the fact that sedimentary cover thickness over there is quite thinner than in the southern part, the processes of HC generation, migration and accumulation were more 'stretched' in time. Filling of traps in deposits of the Kaltasy formation was also detected at the end of the Early Riphean. In the Vendian, during the time of activation of the general subsidence of the basin, these processes continued, though they were running on primarily under their own inertia. Filling V_2 reservoirs took place at the end of the Vendian and thereafter in the Late Paleozoic.

In the Devonian-Permian, HC deposits were formed also in Middle-Upper Devonian and Lower-Middle Carboniferous deposits. As distinct from the southern part of the Volga-Urals petroleum basin, over there the dominant type of fluid for all HC deposits is oil. The important issue in analyzing the modeling results is determining types of traps and time of formation thereof. Tectonically screened traps were formed at the end of early Carboniferous and in the Late Permian. Formation of stratigraphically screened traps is associated with major erosion events that took place in the Middle Riphean-Early Vendian time, as well as in the Early Paleozoic. Detected are traps confined to reef buildups formed in the Late Devonian-Early Carboniferous (within the Kama-Kinel system of troughs) and in the Early Permian. Modeling was performed according to several scenarios – with and without availability of source rock intervals in the RF-V play. It was established that according to the second version, anticipated HC accumulations are practically not formed (even with so rich Domanik source rocks as having TOC = 10 %, HI = 710 mgHC/gTOC and thickness > 30 m). The critical factor in the process of HC generation is the factor of source rock transformation degree.

In the eastern part of the study area, there are detected zones of accumulation of hydrocarbons generated not only by the RF-V source rock intervals but also by D_3fr_2-C_1t carbonaceous formations. Accumulation of liquid and gaseous hydrocarbons took place in deposits of the Moscovian stage of the Middle Carboniferous and in Asselian-Artinskian deposits of the Lower Permian. The anticipated oil and gas accumulations in the studied part of the section coincided with the position of real HC deposits and fields in Fig.6. In both depressions of the Kama-Belaya aulacogen, a single oil play is detected starting from Riphean deposits and ending with Lower Carboniferous deposits; within this play, RF-V formations are considered as main source rocks, reservoirs are confined to the terrigenous complex of the Middle Devonian, and Upper Devonian-Tournaisian deposits serve as the impervious top seal. Such oil play is characteristic mainly of the western and central areas of the Kama-Belaya aulacogen and for overlying complexes. In the eastern part of the basin, in immediate proximity to the Pre-Urals foredeep, the Upper Devonian-Tournaisian deposits act already not as top seals by as source rocks, that being associated with their wide areal extension and presence of zones falling within main oil and gas windows. At the same time they remain a reliable fluid seal for hydrocarbons generated by the RF-V source rock intervals.

The existence of a single oil play is also controlled by another factor – availability of a fluid seal between the Proterozoic and Paleozoic complexes. As the said element of the oil play, often considered are clayey Upper Vendian rocks – deposits of the Vereshchagino and Staropetrovo formations. However, the said deposits underwent various erosion events during geologic evolution history of the region, that having resulted in scarcity of their areal extent over the region, as well as practically complete absence thereof in the western parts of the basin. Absence of reliable fluid seals in the Vendian could contribute to cross-flow of hydrocarbons into overlying pay formations and also to formation of the single oil play from the Riphean-Vendian to the Upper Devonian-Tournaisian. That said, an interesting addendum to the suggested hypothesis is the fact of unity of the hydrodynamic system between the Riphean-Vendian clayey-carbonate complex and the Middle Devonian terrigenous complex [4, 38, 39].

By results of the performed modeling, two HC sources are revealed in the eastern part of the Volga-Urals petroleum basin – the Riphean-Vendian and Middle Frasnian-Tournaisian source rock intervals. These inferences corroborated by data of geochemical analysis conducted earlier allow us to note a considerable influence of the Precambrian source rock intervals upon formation of oil and gas presence in the eastern part of the Volga-Urals petroleum basin.

Conclusion. The following inferences have been made:

• In the section of Riphean deposits of the Kama depression and in the overlying Vendian-Paleozoic hydrocarbon plays, there are the following source rock intervals: RF_1kl, V_2vr, D_3fr_2-C_1t; in the Belaya depression – RF_1kb, RF_2ol, RF_3sn, V_2sp. Pay intervals are associated with V_2kr, D_2ps, C_1bb, C_2m deposits (in the north) and RF_2tk, RF_2ol, RF_2us, V_2bc, V_2sl, V_2kr, D_2ps, C_1bb, C_2m, P_1as,sm,ar deposits (in the south).

• By ratios of steranes, cheilanthanes and normal alkanes, a genetic link is established between the Vendian and Paleozoic oils and the Precambrian organic matter.

• Basin modeling made it possible to infer that the RF-V source rock intervals exerted a considerable impact upon formation of oil and gas presence in the study region.

• The zones of accumulation of hydrocarbons generated by the RF-V source rock intervals are near-flank and uplifted zones of the Kama-Belaya aulacogen.

• Based on geological and geochemical data, a single oil play is detected in the eastern part of the Volga-Urals petroleum basin – from RF_1 to D_3-C_1.

It has been demonstrated that Riphean-Carboniferous deposits of the sedimentary cover within the eastern part of the Volga-Urals petroleum basin should be considered as parts of a single oil play. Oil and gas accumulated in the Devonian – Carboniferous deposits were generated by both Riphean-Vendian and Paleozoic formations. Moreover, the contribution of the Precambrian source rock intervals is so substantial that exclusion thereof from modeling resulted in absence of the observed oil and gas presence in the Paleozoic.

Geochemically (by ratios of steranes, cheilanthanes and normal alkanes), a genetic link is demonstrated between oils of the Paleozoic and Proterozoic reservoirs with organic matter of the Precambrian source rock intervals. A self-consistent model of formation of oil and gas presence in the part under study of the Volga-Urals Petroleum basin has been suggested.

REFERENCES

1. Sergeeva N.D., Puchkov V.N. The stratigraphic scheme of the Riphean and Vendian of the Volga-Ural province (changes and additions). Geological collected volume N 12. Newsletter. 2015, p. 3-22 (in Russian).

2. Giniyatova L.F., Bashkova S.E., Karaseva T.V. The Analysis of Oil and Gas Potential of the Riphean-Vendian Deposits of the Northeast Part of the Volga-Ural Oil and Gas Province. *Bulletin of Perm University. Geology*. 2017. Vol. 16. N 3, p. 275-282 (in Russian). DOI: 10.17072/psu.geol.16.3.275

3. Kozhanov D.D., Bolshakova M.A., Khopta I.S. et al. Geology and geochemistry of Riphean-Vendian petroleum system (the Northern part of the Volga-Ural Basin). *Georesources*. 2021. Vol. 23. N 2, p. 73-86 (in Russian). DOI: 10.18599/grs.2021.2.7

4. Provorov V.M., Neganov V.M., Peredreeva G.L. et al. Prospects on oil and gaz of Ripherian-Vendian deposits of Bedriazhskaia and adjoining areas of Kaltasinsky aulacogen. *Bulletin of Perm University. Geology*. 2007. Iss. 4 (9), p. 32-45 (in Russian).

5. Lozin Ye.V. Abyssal structure and oil and gas content of the Volga-Ural area and adjoining territories. *Lithosphere.* 2002. N 3, p. 45-68 (in Russian).

6. Postnikov D.V., Udovichenko E.M. Anatectites and metasomatitic rocks in the composition of Precambrian deposits in the northern parts of the Russian Platform. *Reports of the USSR Academy of Sciences.* 1969. Vol. 184. N 3, p. 672-675 (in Russian).

7. Allen P.A., Allen J.R. Basin Analysis: Principles and Application to Petroleum Play Assessment. Wiley-Blackwell, 2013. 632 p.

8. Kanev A.S., Fortunatova N.K., Shvets-Teneta-Gury A.G. Oil potential of the domanic type sediments of Volgo-Ural oil-and-gas province. New Directions of Oil and Gas Geology and Geochemistry. Development of Geological Exploration Works. Collection of refereed article, 24-26 November 2017, Perm, Russia. Perm: Perm State National Research University, 2017, p. 139-148 (in Russian).

9. Masagutov R.Kh., Minkaev V.N., Ilemenova O.D. Integrated study of geology and geochemistry of the Domanik formation. in the Volga-Urals petroleum province (a case study from the Republic of Bashkortostan). Actual Problems of Oil Industry. The Collection of Reports of Scientific and Practical Conferences held by Oil Industry Journal in 2017. Moscow: Neftyanoye Khozyaistvo publishers, 2018, p. 65-78 (in Russian).

10. Kontorovich A.E., Trofimuk A.A., Basharin A.K. et al. Global regularities of the Earth's Precambrian petroleum potential. *Russian Geology and Geophysics*. 1996. Vol. 37. N 8, p. 6-42 (in Russian).

11. Sitar K.A., Georgievskiy B.V., Bolshakova M.A., Sautkin R.S. Comprehensive evaluation of Neoproterozoic source rocks formation. *Georesources*. 2022. Vol. 24. N 2, p. 47-59 (in Russian). DOI: 10.18599/grs.2022.2.8

12. Young G.M. Aspects of the Archean-Proterozoic transition: How the great Huronian Glacial Event was initiated by rift-related uplift and terminated at the rift-drift transition during break-up of Lauroscandia. *Earth-Science Reviews*. 2019. Vol. 190, p. 171-189. DOI: 10.1016/j.earscirev.2018.12.013

13. Peters K.E., Walters C.C., Moldowan J.M. The Biomarker Guide. Cambridge: Cambridge University Press, 2004. Vol. 2. Biomarkers and Isotopes in Petroleum Systems and Earth History. 1155 p. DOI: 10.1017/CBO9781107326040

14. McKirdy D.M., Hahn J.H. Composition of Kerogen and Hydrocarbons in Precambrian Rocks. *Mineral Deposits and the Evolution of the Biosphere*. Dahlem Workshop Report. Berlin: Springer, 1982. Vol. 3, p. 123-154. DOI: 10.1007/978-3-642-68463-0_8

15. Agrawal V., Sharma S. Testing Utility of Organogeochemical Proxies to Assess Sources of Organic Matter, Paleoredox Conditions, and Thermal Maturity in Mature Marcellus Shale. *Frontiers in Energy Research*. 2018. Vol. 6. N 42. DOI: 10.3389/fenrg.2018.00042

16. Woltz C.R., Porter S.M., Agić H. Total organic carbon and the preservation of organic-walled microfossils in Precambrian shale. *Geology*. 2021. Vol. 49. N 5, p. 556-560. DOI: 10.1130/G48116.1

17. Melnik D.S., Parfenova T.M. Aromatic Hydrocarbons and Dibenzothiophenes from the Late Neoproterozoic Khatyspyt Formation (Siberian Platrofm). 30th International Meeting on Organic Geochemistry, 12-17 September 2021, Montpellier, France. European Association of Geoscientists & Engineers, 2021. Vol. 2021, p. 2. DOI: 10.3997/2214-4609.202134203

18. Parfenova T.M., Melnik D.S. First insights into organic geochemistry of the Late Neoproterozoic Kharayutekh formation, Northeastern Siberia. 30th International Meeting on Organic Geochemistry, 12-17 September 2021, Montpellier, France. European Association of Geoscientists & Engineers, 2021, p. 2. DOI: 10.3997/2214-4609.202134024

19. Spaak G., Weijers J., Akbas F. et al. Significance of long chain alkylated aromatic compounds for Neoproterozoic-Cambrian petroleum systems. Third EAGE Geochemistry Workshop. European Association of Geoscientists & Engineers, 2021, p. 6. DOI: 10.3997/2214-4609.2021623003

20. Dakhnova M.V., Zheglova T.P., Mozhegova S.V. Generation characteristics of organic matter and distribution of biomarkers in bitumens of the Riphean, Vendian, and Cambrian source rocks of the Siberian Platform. *Russian Geology and Geophysics*. 2014. Vol. 55. N 5-6, p. 755-762. DOI: 10.1016/j.rgg.2014.05.018

21. Kashirtsev V.A., Sovetov Y.K., Kostyreva E.A. et al. New homologous series of biomarker molecules from Vendian deposits of the Sayan-adjacent Biryusa area. *Russian Geology and Geophysics*. 2009. Vol. 50. N 6, p. 541-545. DOI: 10.1016/j.rgg.2008.12.001

22. Craig J., Biffi U., Galimberti R.F. et al. The palaeobiology and geochemistry of Precambrian hydrocarbon source rocks. *Marine and Petroleum Geology*. 2013. Vol. 40, p. 1-47. DOI: 10.1016/j.marpetgeo.2012.09.011

23. Swanner E.D., Maisch M., Wu W., Kappler A. Oxic Fe(III) reduction could have generated Fe(II) in the photic zone of Precambrian seawater. *Scientific Reports*. 2018. Vol. 8. N 4238. DOI: 10.1038/s41598-018-22694-y

24. Tosca N.J., Jiang C.Z., Rasmussen B., Muhling J. Products of the iron cycle on the early Earth. *Free Radical Biology and Medicine*. 2019. Vol. 140, p. 138-153. DOI: 10.1016/j.freeradbiomed.2019.05.005

25. Dongya Zhu, Quanyou Liu, Jingbin Wang et al. Transition of seawater conditions favorable for development of microbial hydrocarbon source – Reservoir assemblage system in the Precambrian. *Precambrian Research*. 2022. Vol. 374. N 106649. DOI: 10.1016/j.precamres.2022.106649

26. Kuznetsov V.G. Geochemical Environments of Precambrian Sedimentation. *Lithology and Mineral Resources*. 2020. Vol. 55. Iss. 2, p. 99-110. DOI: 10.1134/S0024490220010034

27. Peng Liu, Yonggang Liu, Yiran Peng et al. Large influence of dust on the Precambrian climate. *Nature Communications*. 2020. Vol. 11. N 4427. DOI: 10.1038/s41467-020-18258-2

28. Orlova A.Yu., Khisamov R.S., Bazarevskaya V.G. et al. Geochemistry of organic matter in carbonate Devonian sediments of the South Tatar arch. *Georesources*. 2021. Vol. 23. N 2, p. 87-98. DOI: 10.18599/grs.2021.2.8

29. Bazhenova O.K., Bazhenova T.K., Fadeeva N.P. Upper Proterozoic Formations of Russian Plate-Independent Petroleum Systems. 67th EAGE Conference & Exhibition, 13-16 June 2005, Madrid, Spain. European Association of Geoscientists & Engineers, 2005. DOI: 10.3997/2214-4609-pdb.1.P143

30. Bushnev D.A., Smirnov M.B., Burdel'naya N.S., Valyaeva O.V. Molecular and structural-group characteristics of hydrocarbons in Late Devonian oils of the Timan–Pechora Province. *Geochemistry International*. 2017. Vol. 55. Iss. 9, p. 802-813. DOI: 10.1134/S001670291708002X

31. Radke M. Application of aromatic compounds as maturity indicators in source rocks and crude oils. *Marine and Petroleum Geology*. 1988. Vol. 5. Iss. 3, p. 224-236. DOI: 10.1016/0264-8172(88)90003-7

32. Abay T.B., Fossum K., Karlsen D.A. et al. Petroleum geochemical aspects of the Mandawa Basin, coastal Tanzania: the origin of migrated oil occurring today as partly biodegraded bitumen. *Petroleum Geoscience*. 2021. Vol. 27. Iss. 1. N petgeo2019-050. DOI: 10.1144/petgeo2019-050

33. Galimov E.M., Vinnikovskii S.A., Pyankov N.A., Kuznetsova N.G. Genetic types of oils of the Permian Near Kama region by isotopic composition of carbon. *Oil and Gas Geology*. 1972. N 1, p. 33-39 (in Russian).

34. Kozlova I.A., Shadrina M.A. Geological and geochemical assessment of oil and gas in the upper proterozoic possibility sediments in the Perm region. *Bulletin of Perm National Research Polytechnic University. Geology. Oil & Gas Engineering & Mining*. 2013. Vol. 12. N 8, p. 18-27 (in Russian).

35. Bazhenova T.K. Petroleum source formations of the Russian ancient platforms and their petroleum potential. *Neftegazovaya Geologiya. Teoriya i Praktika*. 2016. Vol. 11. N 4, p. 29 (in Russian). DOI: 10.17353/2070-5379/45_2016

36. Kuznetsov N.B., Kerimov V.Y., Osipov A.V. et al. Geodynamics of the Ural Foredeep and Geomechanical Modeling of the Origin of Hydrocarbon Accumulations. *Geotectonics*. 2018. Vol. 52. N 3, p. 297-311. DOI: 10.1134/S0016852118030044

37. Prischepa O., Nefedov Y., Nikiforova V., Ruiming X. Raw material base of Russia's unconventional oil and gas reserves (hydrocarbons shale strata). *Frontiers in Earth Science*. 2022. Vol. 10, p 22. DOI: 10.3389/feart.2022.958315

38. Koryakin S.Yu., L'vovskaya Ya.L. Underexplored territory of eastern part of Rakshinsky Saddle, Visimsky Monocline, and southern end of Kamsky Arch: prediction of oil and gas occurrence using depositional and basin modelling. *Russian Oil and Gas Geology*. 2022. № 5, p. 31-38 (in Russian). DOI: 10.31087/0016-7894-2022-5-31-38

39. Koryakin S.Yu., Lvovskaya Ya.L., Vinokurova E.E. et al. Forecast of Oil and Gas Potential of the Devonian Terrigenous Complex in Central Part of the Perm Region Based on the Results of Sedimentation and Basin Modeling. Geomodel, 6-10 September 2021, Gelendzhik, Russia. European Association of Geoscientists & Engineers, 2021. Vol. 2021, p. 6. DOI: 10.3997/2214-4609.202157028

Authors: **Dmitrii D. Kozhanov,** *Postgraduate Student, dmitriikozhanov@yandex.ru, https://orcid.org/0000-0002-2641-918X (Lomonosov State University, Moscow, Russia),* **Mariya A. Bolshakova,** *Candidate of Geological and Mineralogical Sciences, Leading Researcher, https://orcid.org/0000-0001-9240-291X (Lomonosov State University, Moscow, Russia).*

The authors declare no conflict of interests.

ISSN 2411-3336; e-ISSN 2541-9404

JOURNAL OF MINING INSTITUTE

Zapiski Gornogo instituta

Journal homepage: pmi.spmi.ru

Research article

Microstructural features of chromitites and ultramafic rocks of the Almaz-Zhemchuzhina deposit (Kempirsai massif, Kazakhstan) according to electron backscatter diffraction (EBSD) studies

Dmitrii E. Saveliev[1]✉, **Semen N. Sergeev**[2], **Darkhan K. Makatov**[3]

[1] *Institute of Geology, Ufa Federal Research Centre of the RAS, Ufa, Russia*

[2] *Institute for Metals Superplasticity Problems of the RAS, Ufa, Russia*

[3] *Abylkas Saginov Karaganda Technical University, Karaganda, Republic of Kazakhstan*

How to cite this article: Saveliev D.E., Sergeev S.N., Makatov D.K. Microstructural features of chromitites and ultramafic rocks of the Almaz-Zhemchuzhina deposit (Kempirsai massif, Kazakhstan) according to electron backscatter diffraction (EBSD) studies. Journal of Mining Institute. 2024. Vol. 266, p. 218-230.

Abstract. Microstructural features of the main rock-forming minerals of host ultramafic rocks (olivine, orthopyroxene) and chrome spinel from ores of the Almaz-Zhemchuzhina deposit were studied using the electron backscatter diffraction method. For ultramafic rocks, statistical diagrams of the crystallographic orientation of olivine and orthopyroxene were obtained, indicating the formation of a mineral association in conditions of high-temperature subsolidus plastic flow in the upper mantle. The main mechanisms were translation gliding and syntectonic recrystallization. Olivine deformation occurred predominantly along the (010)[100] and (001)[100] systems. The textural and structural features of chromitites reflect plastic flow processes, most pronounced in lenticular-banded ores. Microstructure maps in inverse pole figure encoding show differences in the grain size composition of the ores: areas consisting of disseminated chromitites are characterized by a finer-grained structure compared to lens-shaped segregations of a massive structure. Analysis of microstructure maps shows that during the transition from disseminated to massive ores, there is a widespread development of recrystallization, adaptation of neighbouring grains to each other, resulting in homogenization of crystallographic orientation in aggregates. The data obtained develop ideas about the rheomorphic nature of chromitite segregations in ophiolite dunites. It is assumed that the coarsening of the structure of massive chromitites is critically associated with an increase in the concentration of ore grains during solid-phase segregation within a plastic flow, when individual chrome spinel grains, initially separated by silicate material, begin to come into direct contact with each other.

***Keywords*:** ophiolites; chromitites; olivine; plastic deformation; EBSD; Kempirsai

Acknowledgments. The work was supported by the Russian Science Foundation grant N 22-17-00019. The research was carried out at the Collaborative Access Centre "Structural, Physical, and Mechanical Research of Materials" (IPSM RAS).

Received: 27.02.2023 ***Accepted: 25.10.2023*** ***Online: 08.02.2024*** ***Published: 25.04.2024***

Introduction. Ultramafic rocks of the Kempirsai massif in the Aktobe region of the Republic of Kazakhstan are associated with the largest reserves of ophiolite-type chromitites, "podiform deposits" [1-3], which differ from stratiform deposits by a sharp variability of morphological features and a constant association with extremely depleted mantle dunites. The specific morphology of deposits, sharp morphostructural variability, constant association with dunites and the absence of obvious signs of magmatic formation contributed to the emergence of various models of the origin of deposits of this type. To interpret the genesis of podiform deposits over the long history of their study, various models have been proposed with a predominant role of both magmatic and metasomatic processes. In recent decades, the reaction-magmatic [4-6] and fluid-metasomatic hypotheses [7, 8] have become the most widespread. Some works suggest the leading role of solid phase differentiation [9].

It is difficult to imagine the construction of full-fledged dynamic formation models of podiform chromitites without the use of quantitative data on their structure at various scale levels. Until the beginning of the 21st century and the advent of electron backscatter diffraction (EBSD) methods, this was practically impossible. Microstructural studies were limited to the study of transparent anisotropic host rock minerals, olivine and pyroxenes, using the Fedorov method [10-12].

Widespread use of electron microscopy with EBSD detectors since the beginning of the 21st century made it possible to obtain quantitative information about the internal structure of optically isotropic and non-transparent materials, including minerals of the cubic system [13-15] and various ore minerals [16-18]. In recent years, this research method has become widely used to assess the role of plastic deformations in mantle associations [19-21] and determine seismic anisotropy in the upper mantle of various regions based on the microstructure features of ultramafic xenoliths in kimberlites and alkali basalts [22-24].

To clarify the formation conditions for chromitites at the Almaz-Zhemchuzhina deposit in the southeastern part of the Kempirsai massif, the authors studied the material, macro- and micro-structural features of chromitites and their host ultramafic rocks using electron backscatter diffraction (EBSD). The main objectives of the research were: obtaining statistical data on the crystallographic orientation of rock-forming silicates (olivine, orthopyroxene) of ultramafic rocks, comparing them with experimental data; determination of the mechanisms of plastic deformation and recrystallization of olivine and orthopyroxene; microstructural study of aggregates of chrome spinel grains, obtaining data on the real structure of ore grains; assessment of the role of deformation and recrystallization in the formation of chromitites. Preliminary results of studying the samples are partially presented in [25].

Methods. In the 2022 field season, the authors studied chromitite samples of various structural types from dumps and boreholes of the Almaz-Zhemchuzhina deposit (Fig.1), as well as the most recent samples of host dunites and lherzolites selected from the core of the deep horizons at this site (depth from 420 to 1100 m).

At the preliminary stage, optical and electron microscopy methods were used. A total of 50 samples of peridotites, dunites, and chromitites, selected both from borehole cores and from deposit dumps, were studied. The composition of minerals was determined using a Tescan Vega Compact scanning electron microscope with an Xplorer-15 Oxford Instruments energy-dispersive detector at the Institute of Geology, Ufa Federal Research Centre of the Russian Academy of Sciences. The spectra were processed automatically by the AzTec One software package using the TrueQ technique. The following settings were used during the scanning: accelerating voltage 20 kV, probe current 3 nA, spectrum accumulation time at a point 60 s in Point&ID mode, beam diameter about 3 μm.

Three samples of the most recent ultramafic rocks from the GT-HY-1 borehole and two samples of chromitites from the dump of the Almaz-Zhemchuzhina deposit were selected for microstructural studies. From them, preparations were made that were oriented relative to the macroscopic elements of texture, banding, foliation, and lineation. The microstructure study of the preparations was carried out using the electron backscatter diffraction (EBSD) method on a Tescan Mira microscope at the Institute for Metals Superplasticity Problems of the Russian Academy of Sciences. The surface of the preparations for EBSD analysis was prepared by two-stage polishing, first mechanically using diamond pastes, and then by finishing mechanical and chemical polishing using a suspension based on colloidal silicon oxide (to remove hardening).

The main method of microstructural studies in this work, EBSD, is based on local anisotropic electron scattering on a crystal lattice [26, 27], which makes it possible to obtain Kikuchi lines, which are compared with reference ones for the phases present in the sample, then converted into data on the crystallographic orientation at any point of the sample under study. The phases are automatically identified at each point, and the *X* and *Y* coordinates of these points are stored in memory. Modern devices are capable of high-speed scanning with steps from tenths to several tens of μm [28], as a result of which software (for example, Channel 5) makes it possible to construct various maps in Hough space with a resolution of 100 pixels.

Journal of Mining Institute. 2024. Vol. 266. P. 218-230

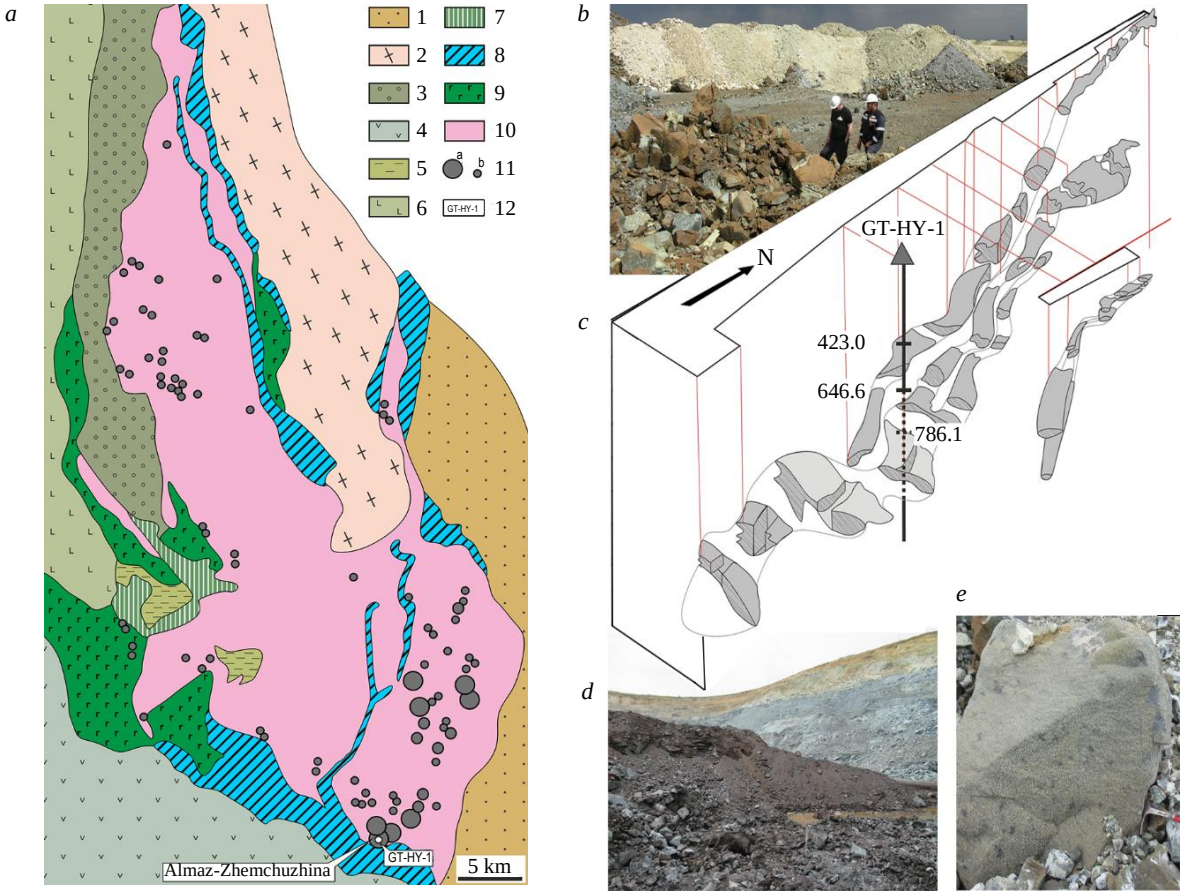

Fig.1. Geological position of the Almaz-Zhemchuzhina deposit and location of the studied samples:
a – small-scale map of the massif according to [34]; 1-6 – stratified rocks; 1 – South Mugodzhar zone (basalts (S-D_1, D_2), flyschoids and olistostromes (D_3-C_1); 2 – Ebety zone (basalt-andesite-rhyodacite, carbonate-silicite and greywacke formations (V?PZ_{1-2}); 3-6 – Sakmara zone (3 – basalt-andesite-dacite, greywacke, phtanite and carbonate formations (PZ_{1-2}), 4 – pillow lavas and pyroclastics of the basalt-andesite-rhyodacite formation with the participation of phtanites and clay-siliceous shales (PZ_{1-2}), 5 – phtanites and carbonate shales (O_2), 6 – pillow lavas of tholeiitic basalts with phtanite lenses (O_2); 7-10 – Kempirsai massif: 7 – sets of parallel diabase dikes and isotropic hornblende gabbros, 8 – Kyzylkain formation of pyroxenite-gabbro composition, 9 – Kokpekty formation of olivine gabbros and troctolites, 10 – rocks of the upper mantle section: harzburgites, lherzolites, dunites; 11 – chromitites (a – unique and large deposits; b – ordinary deposits and ore shows), 12 – location of studied boreholes and deposits; *b* – dumps of the Almaz-Zhemchuzhina deposit; *c* – block diagram of the ore cluster, including the Almaz-Zhemchuzhina, Millionnoe, and Pervomaiskoe deposits, location of the studied core samples; *d* – massive chromitites in the face of one of the open pits; *e* – sample of densely disseminated chromitite

In this work, EBSD scanning of preparations was carried out in steps of 10 to 20 μm with detail in some cases to 2 μm. In samples of serpentinized ultramafic rocks, predominantly texture diagrams were obtained, and in chromitites, it was possible to obtain fairly high-quality maps in inverse pole figure (IPF) encoding. A total of 25 areas were studied on seven preparations from five samples.

Research results. The Kempirsai massif is one of the largest ophiolite-type ultramafic massifs in the Urals, containing the world's largest deposits of chromium ores of this formation type. At the modern erosional truncation level, the massif is a pear-shaped body. It is elongated from north to south, according to the main direction of the Ural structures, and expands to the southeast (Fig.1). The massif is almost entirely composed of rocks of the so-called mantle section, harzburgites, lherzolites, and dunites, which near the surface are completely transformed into serpentinites. Due to the fact that serpentinization was limited to low-temperature facies with the formation of loop-shaped serpentine, the primary nature of serpentinites can be easily diagnosed by the presence of bastite pseudomorphs after pyroxenes. The most widespread in the massif are harzburgite serpentinites containing 70-80 vol.% olivine, 20-25 vol.% orthopyroxene, and a minor admixture of chrome spinel, which usually retains its composition.

In the southeastern part of the massif, along with homogeneous harzburgites, the dunite-harzburgite complex is widespread. Its structure is determined by the frequent alternation of harzburgite serpentinites and serpentinites without pseudomorphs after orthopyroxene (dunite). The most productive chromitite deposits of the massif are associated namely with the dunite-harzburgite complex.

In addition to ultramafic rocks, quite a lot of mafic dikes are found within the massif, among which gabbrodiabases of the Tygasha-Sai formation are the most widespread [29]. Rather large bodies of differentiated composition (Kokpekty complex) [29, 30], as well as tholeiitic basalts of the Sugraly complex and amphibolites [31] are developed in the near-contact parts of the massif. It should be noted that amphibolites cover the southern contact of the massif, under which the chromitite body of the largest deposit of the massif, Almaz-Zhemchuzhina, subducts.

When studying thin sections and polished sections using optical and electron microscopy, we found that the main minerals of the ores are high-chromium spinels (Cr/Cr + Al = 0.8-0.83) (Table 1), which is completely consistent with [1, 2], as well as serpentine and chlorite, replacing primary olivine. Chrome spinels contain mineral inclusions that are distributed very unevenly. The most common inclusion minerals are olivine (often serpentinized) and amphibole; less common are phlogopite, pyroxenes, and sulphides of basic metals (Fe, Ni, Cu, Co), as well as platinum group minerals [32, 33].

Table 1

Composition of ore-forming chrome spinels from the Almaz-Zhemchuzhina deposit

Oxide	Composition, wt.%*								
TiO_2	0.22	0.46	0.20	0.18	0.17	–	–	0.28	0.23
Al_2O_3	9.66	10.32	8.88	8.79	9.04	8.64	8.85	10.56	9.56
Cr_2O_3	62.16	61.97	63.18	62.64	62.56	63.13	63.64	61.03	62.47
Fe_2O_3**	2.1	0.24	3.48	2.37	2.94	3.23	3.12	2.11	1.34
FeO	13.13	13.1	11.1	12.3	11.85	11.33	12.5	12.2	12.4
MgO	13.39	13.28	14.92	13.72	14.33	14.42	14.09	14.00	13.77
NiO	–	–	–	–	0.18	0.24	–	0.20	–
Total	100.7	99.5	101.8	100.0	101.1	101.0	102.2	100.4	99.8
Element	Composition, apfu								
Al	0.367	0.395	0.332	0.336	0.341	0.326	0.331	0.398	0.364
Cr	1.582	1.590	1.582	1.606	1.580	1.599	1.597	1.545	1.597
Mg	0.642	0.642	0.704	0.663	0.682	0.688	0.666	0.668	0.663
Fe^{3+}	0.052	0.010	0.081	0.065	0.064	0.083	0.080	0.054	0.019
Fe^{2+}	0.352	0.351	0.297	0.325	0.324	0.298	0.325	0.322	0.351
Ti	0.005	0.011	0.005	0.004	0.004			0.007	0.006
Ni					0.005	0.006		0.005	
#Cr	0.81	0.80	0.83	0.83	0.82	0.83	0.83	0.79	0.81
#Mg	0.65	0.65	0.70	0.67	0.68	0.70	0.67	0.67	0.65

* SEM EDS data [33]; dash – contents below the detection limit.
** Contents are calculated based on the mineral stoichiometry.

Almost all ultramafic samples from borehole cores are characterized by clearly defined macroscopic structural elements – foliation (*S*) and lineation (*L*) (Fig.2, *a*, *b*). Foliation is due to the preferred orientation of tabular pyroxene grains in shape and to the aggregate banding often parallel to the same plane. Lineation is determined by the elongation of grains (pyroxene, olivine) or aggregates of chrome spinels in the plane of foliation. In chromitites, these macroscopic structural elements are most clearly manifested in samples of banded disseminated ores and in lenticular-banded ores, which we found in fairly copious quantities in the dumps of the Almaz-Zhemchuzhina deposit (Fig.2, *c*-*e*). Ores of this type most clearly show the participation in their formation of solid-phase plastic flow of mantle material. Samples of chromitites of this variety were used for microstructural studies.

Journal of Mining Institute. 2024. Vol. 266. P. 218-230

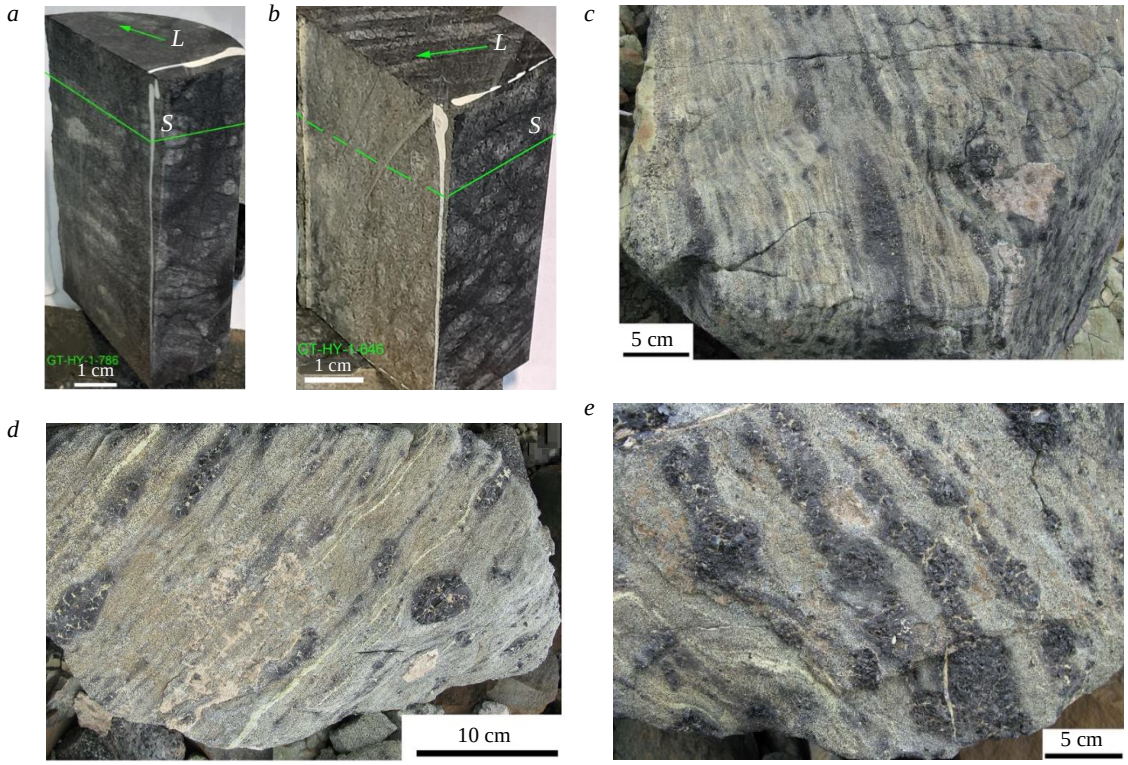

Fig.2. General view of the studied samples of host ultramafic rocks from deep borehole cores (*a*, *b*) and lenticular-banded chromitites from dumps (*c*-*e*)

Petrographic study of the host ultramafic rocks showed that dunites are significantly affected by serpentinization (at least 70 vol.%), while lherzolites contain areas with fairly good preservation (serpentine makes up less than 40 vol.% of the rock). The main rock-forming minerals of lherzolites show signs of high-temperature deformation: kink-band structures, undulose extinction (Fig.3, *a*), porphyroclastic structures caused by the association of deformed large orthopyroxene grains and zones of syntectonic recrystallization (RZ), composed of aggregates of small grains – neoblasts (Fig.3, *b*). Inside large deformed enstatite grains, the formation of diopside, amphibole lamellae and tiny chrome spinel grains is often observed (Fig.3, *c*). An idea of the typical mineralogical composition of lherzolites, the size and morphology of grains of rock-forming minerals is given by the EDS map in Fig.3, *d*.

The composition of the rock-forming minerals of ultramafic rocks is typical for rocks of the ophiolite mantle section: high-magnesium olivine; besides, from lherzolites to dunites the concentration of the forsterite minal increases from 90-92 to 95-96 %. Orthorhombic pyroxene is also represented by a high-magnesium variety, enstatite, and clinopyroxene by a calcium-magnesium variety, diopside. The composition of chrome spinels varies over a fairly significant range but is limited by isomorphism in the picotite-chromite series from 0.4 Cr# ($(Mg_{0.645}Fe_{0.355})_{1.00}(Al_{1.187}Cr_{0.759}Fe_{0.054})_{2.00}O_4$) in lherzolites to 0.8-0.85 ($(Mg_{0.704}Fe_{0.296})_{1.00}(Cr_{1.582}Al_{0.332}Fe_{0.081}Ti_{0.005})_{2.00}O_4$) in dunites and chromitites. In lherzolites, the permanent minor mineral is amphibole, the composition of which corresponds to calcium-magnesium varieties (pargasite-magnesian hornblende). In chromitites, olivine from inclusions in chrome spinel grains has the maximum magnesium composition (Fo_{97-98}) and abnormally high concentrations of nickel (to 1.8 wt.% NiO) (Table 2). According to the geothermometers [35-37], the closure of exchange reactions between olivine and chrome spinel occurred in the temperature range of 700-850 °C and oxygen fugacity from –1.04 to +2.8 ΔFMQ.

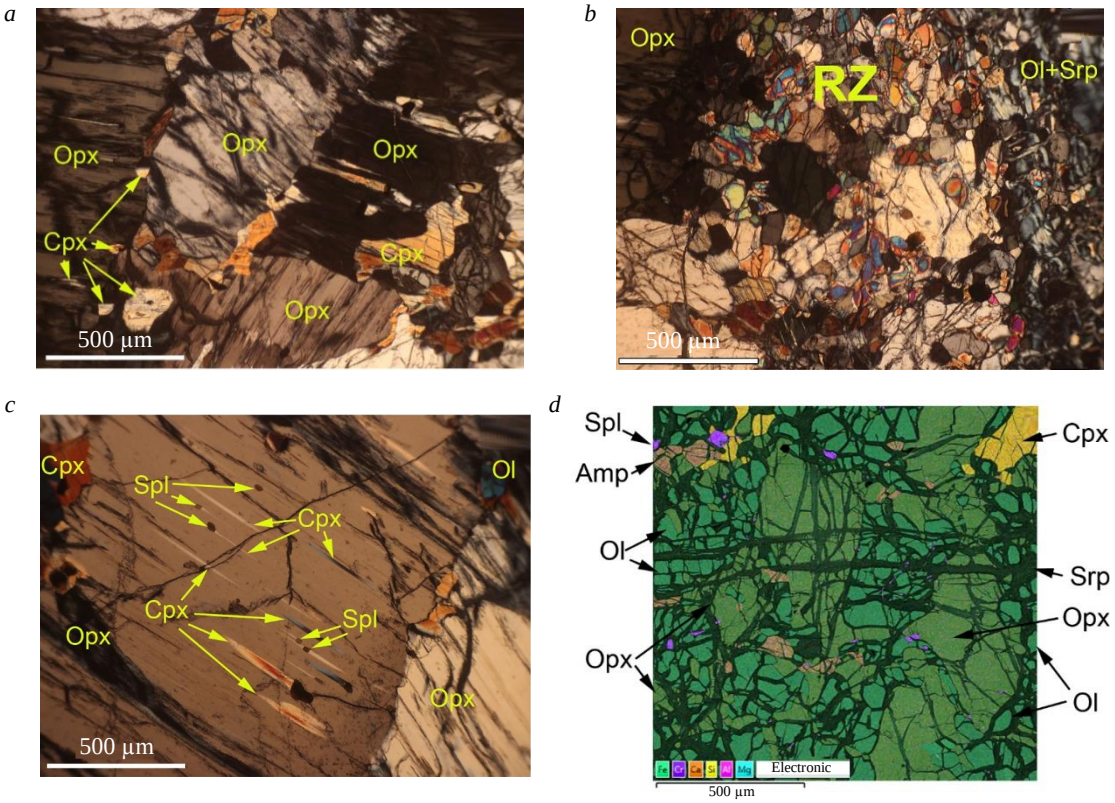

Fig.3. Petrographic features of ultramafic rocks from borehole GT-HY-1:
a – large deformed orthopyroxene grains with clinopyroxene inclusions;
b – recrystallization zone (RZ) composed of small newly formed grains (neoblasts) near a large deformed orthopyroxene grain;
c – isolation of new phases inside an orthopyroxene grain subject to plastic deformation;
d – typical EDS map of lherzolite from the ore-hosting strata of the Almaz-Zhemchuzhina deposit; Amp – amphibole;
Cpx – clinopyroxene; Ol – olivine; Opx – orthopyroxene; Spl – chrome spinel; Srp – serpentine

Table 2

Composition of olivine from inclusions in chrome spinels from the Almaz-Zhemchuzhina deposit

Oxide	Composition, wt.%								
SiO_2	41.30	41.31	41.38	41.11	40.61	41.50	41.10	42.56	42.75
FeO	2.77	2.94	1.87	2.12	2.45	2.58	2.62	2.97	2.51
MgO	54.71	55.38	55.06	54.47	53.84	56.05	54.78	54.94	55.26
NiO	0.65	0.69	1.66	1.83	1.51	0.95	0.94	1.41	0.67
Total	99.4	100.3	100.0	99.5	98.4	101.1	99.4	101.9	101.2
Element	Composition, apfu								
Si	0.982	0.973	0.978	0.978	0.978	0.969	0.977	0.993	1.000
Fe	0.055	0.058	0.037	0.042	0.049	0.050	0.052	0.058	0.049
Mg	1.951	1.956	1.953	1.944	1.944	1.963	1.953	1.923	1.939
Ni	0.012	0.013	0.032	0.035	0.029	0.018	0.018	0.027	0.013
Fo	0.973	0.971	0.981	0.979	0.975	0.975	0.974	0.971	0.975

Studying ultramafic samples using the EBSD method allowed us to obtain a series of texture diagrams (straight pole figures) for the main rock-forming minerals, olivine and orthopyroxene. Unfortunately, we did not manage to obtain complete microstructural maps due to significant serpentinization of the rocks, and in some cases due to the distorted crystal lattice of orthopyroxenes.

Textures obtained for olivine and orthopyroxene from host ultramafic rocks show a fairly strong preferred crystallographic orientation of both minerals. The following types of olivine textures are identified: 1) the maximum of the [100] axis near the foliation plane and near the lineation exposure, while the [001] axis forms a maximum on the flattening plane perpendicular to lineation, and the

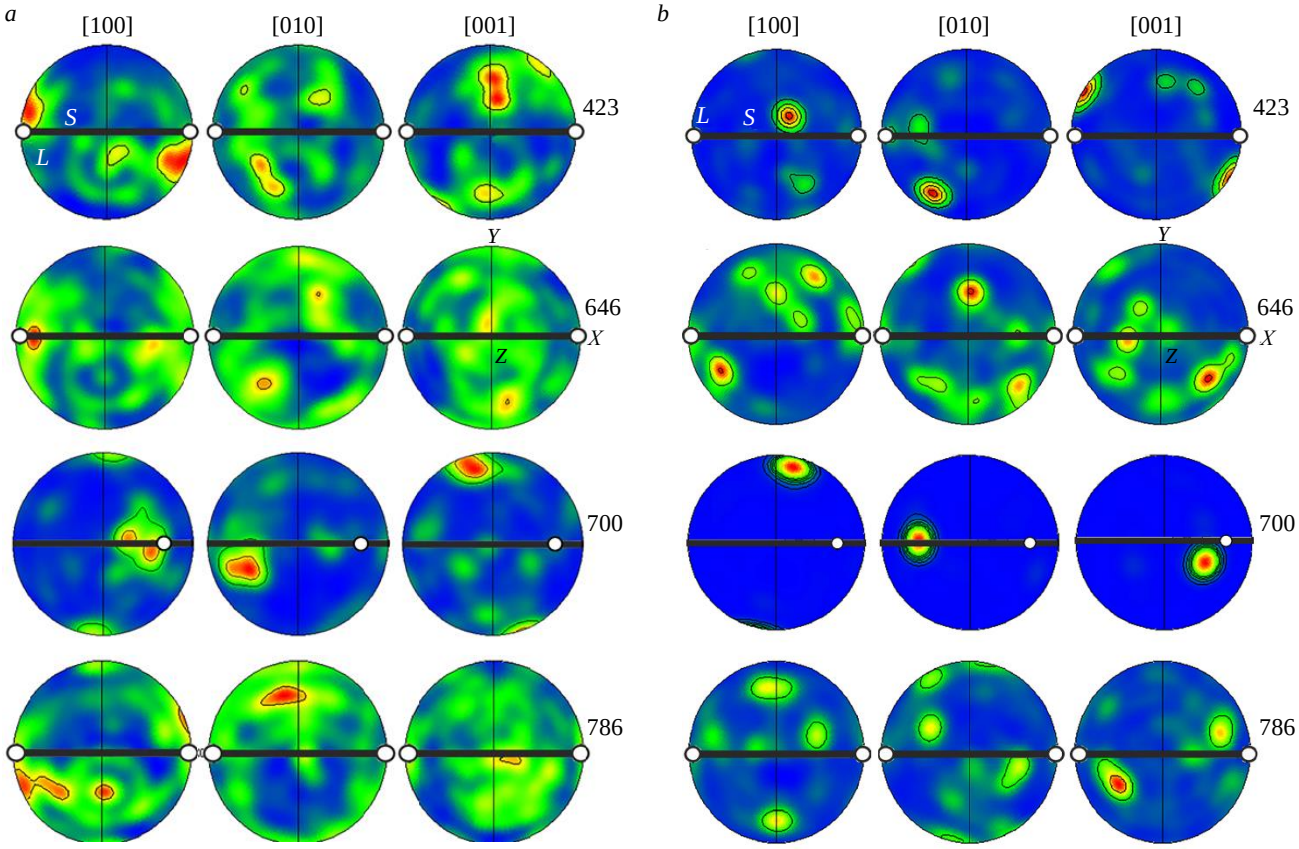

Fig.4. Straight pole figures for rock-forming olivine (*a*) and orthopyroxene (*b*)
from ultramafic rock samples from borehole GT-HY-1. Upper hemisphere of equal area projection;
S – projection of the plane of mineral flattening and banding; *L* – linearity exposures

maximum of the [010] axis is perpendicular to the flattening plane (samples 646, 786, Fig.4, *a*); 2) the maximum of the [100] axis is also near the flattening plane and the lineation exposure, but the other two axes change places: the [010] maximum is on the flattening plane, and the [001] maximum is perpendicular to it (sample 700, Fig.4, *a*).

In orthopyroxene, in almost all cases, coincidence or slight deviation of the [001] axis from the lineation exposure is registered (Fig.4, *b*), which indicates the direction of gliding. Glide planes in different samples are determined differently: (100) – in sample 700, (010) – in sample 423, and multiple planes in two other samples (Fig.4, *b*). Along with translation gliding, syntectonic recrystallization played a significant role in the studied ultramafic rock samples, which to some extent complicated the petrostructural patterns.

For microstructural studies, we selected a sample of densely disseminated chromitite with a lenticular-banded texture (Fig.5, *a*) with clearly defined macroscopic structural elements – banding and lineation, from which made preparations measuring 20×30 mm (Fig.5, *b*).

Macroscopic and mineragraphic study showed that the sample is a combination of sections with banded texture and medium-dense disseminated structure with the size of chrome spinel individuals 0.1-1 mm and chrome spinel aggregates of a massive lens-shaped structure with inclusions of silicate material. The size of individuals in massive aggregates is visually determined within 1-5 mm, however, it is not possible to determine the grain size more accurately due to the isotropic nature of the optical properties of chrome spinel (cubic system, opacity) and grain jointing (Fig.5, *c-e*). Microstructure studies using EBSD methods were carried out on preparation *c* (Fig.5, *b*), the scanning step was 20 μm in most areas, and one of them was studied in more detail with a step of 10 μm (Fig.5, *c-e*).

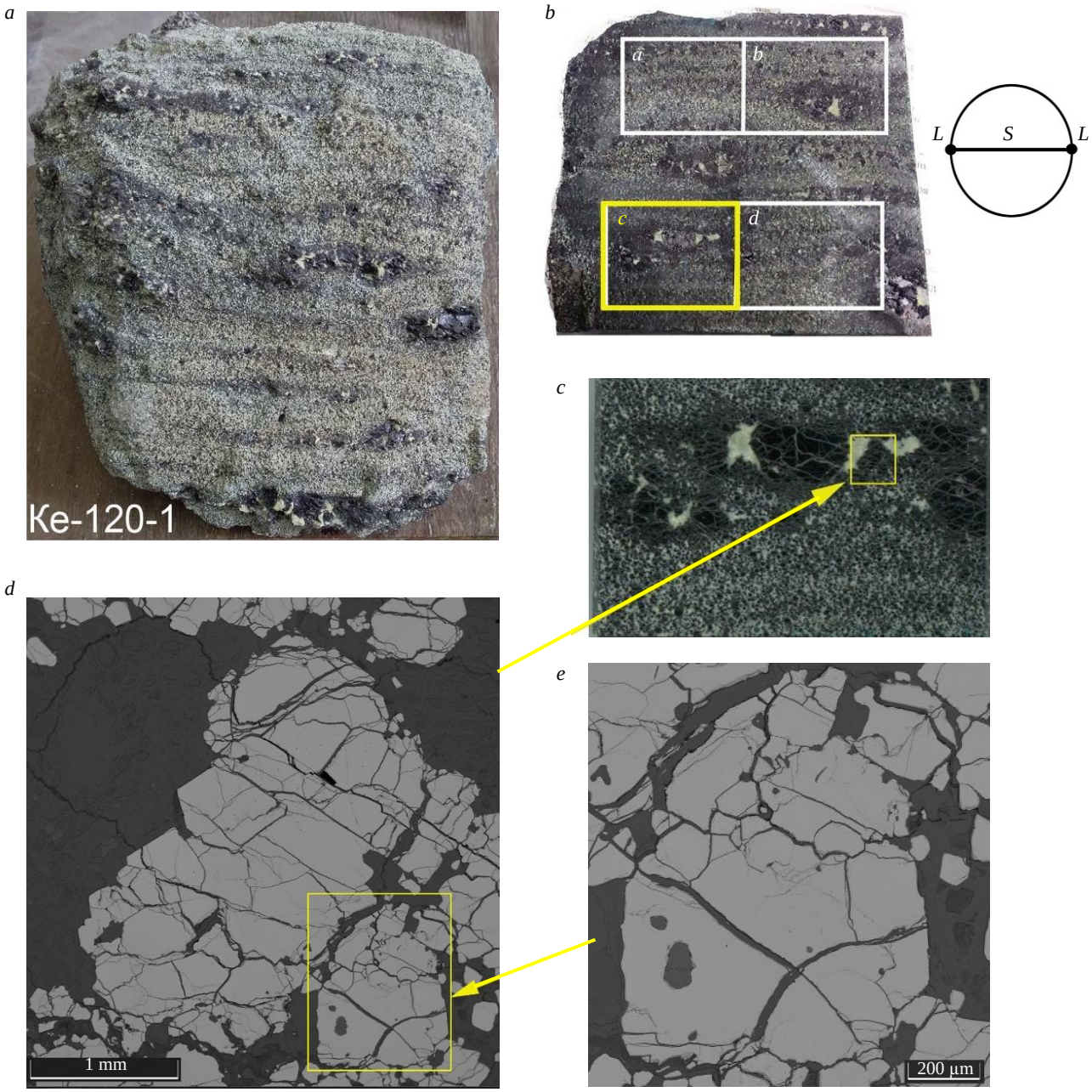

Fig.5. General view and structural details of the studied chromitite sample of lenticular-banded texture Ke-120-01: *a* – general view of the sample before preparation; *b* – view of part of the section perpendicular to the banding and macroscopic structural elements; *c* – general view of the preparation studied by the EBSD method; *d* – detail of the preparation with aggregates of a massive structure; *e* – one of the studied areas

The conducted instrumental microstructural studies generally confirmed the assumptions about the different grain size composition of sections with different textures (structures), which is most clearly manifested in maps compiled in colour-coded inverse pole figures (IPF) (Fig.6). The left part of Fig.6 shows the contrast maps of Kikuchi bands (KB), which characterize the quality of the measurements performed. In all the examples given, it is good, as evidenced by the uniform images and the predominance of light tones (sharp contrast of the KB). Darker areas indicate a greater degree of distortion in the crystal lattice of minerals. To understand the IPF maps, the inset (Fig.6, *h*) shows a typical colour key for the cubic system crystals.

In sections with disseminated structure, where chromite grains are separated from each other by a silicate matrix, most grains have a uniform orientation, the grain size is 70-250 μm (Fig.6, *a*, *b*).

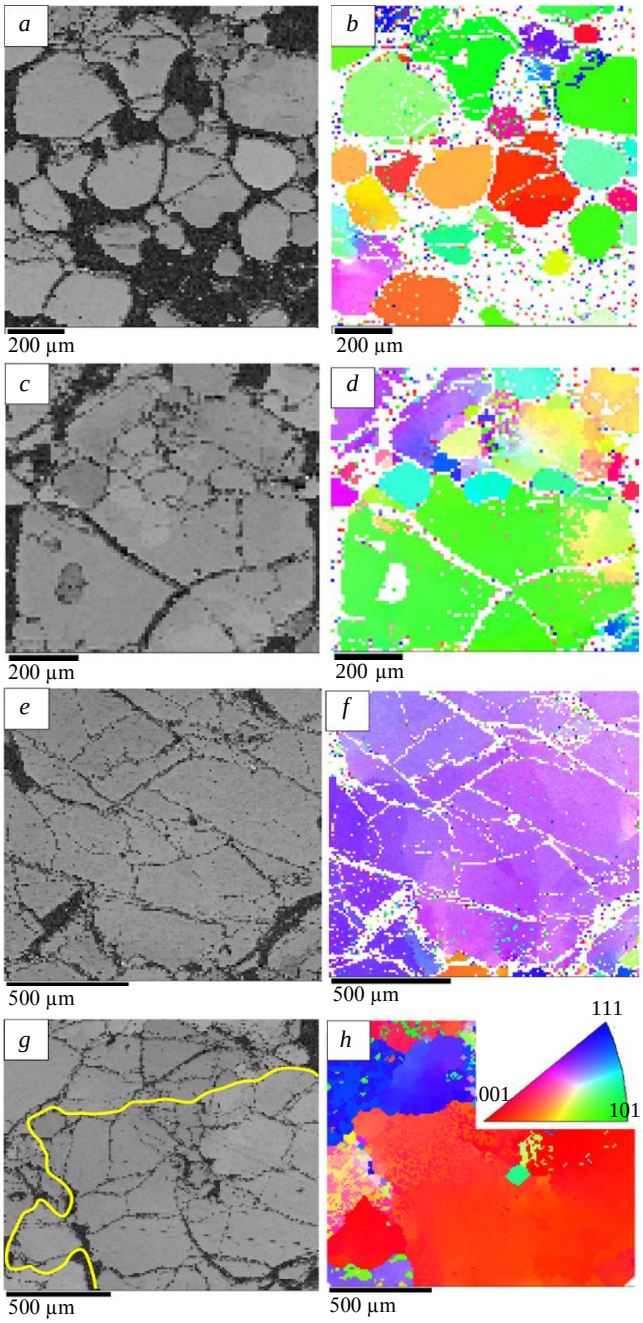

Fig.6. Microstructural maps of chromitite sample sections with lenticular-banded texture Ke-120-01:
a, *b* – section with disseminated structure (*a* – contrast of Kikuchi bands (KB), *b* – IPF map);
c, *d* – section with the transitional structure from disseminated to massive, shown in Fig.5, *e* (*c* – KB contrast, *d* – IPF map);
e-*h* – sections with massive structure (*e*, *g* – KB contrast, *f*, *h* – IPF maps); *g* – yellow colour shows the grain boundary with the {001} orientation on fragment *h*, in the inset – the colour key to the IPF maps

However, some grains exhibit a domain (subgrain) structure, the misorientation between subgrains is to 15°.

In transition-type chrome spinel aggregates (at the contact of the disseminated and massive zones) the presence of a heterogeneous structure with two maximum sizes of sections with uniform orientation is noted: 70-200 μm and over 500 μm (Fig.6, *c*, *d*). Within sections of the second type, one can often observe both local heterogeneities with low-angle boundaries of 1-10°, and small-sized inclusions separated from the matrix by high-angle boundaries (over 15°).

The internal parts of the sections with massive structure are areas with an almost uniform structure, the misorientation angle does not exceed 5° (Fig.6, *e*, *f*). The boundaries between blocks with homogeneous structure can be sharp and at the same time completely independent of the visually observed physical sections expressed by thin fractures (Fig.6, *g*, *h*).

In addition to studying the main rock-forming and ore-forming minerals of ultramafic rocks (olivine and orthopyroxene) and chromitites (chrome spinels) in the southern part of the Kempirsai massif, we investigated the internal structure of minerals rarer for ultramafic rocks, clinopyroxenes, which are represented by the calcium-magnesium variety, diopside ($CaMg(Si_2O_6)$). A noticeable presence of diopside is observed in three studied samples of partially serpentinized peridotites, 646, 700, and 786. The EBSD study revealed the presence of rather strong preferred crystallographic orientations of this mineral at index values M = 0.1-0.4 (Fig.7). It should be noted that only in sample 700 there is a coincidence between the maximum intensity of the exposures of one of the [001] axes with the lineation direction and the maximum of the [100] axis, perpendicular to the foliation plane, which is characteristic of the (100) [001] slip system. This slip system is also the most typical for orthopyroxenes. In the other two samples, more diffuse texture patterns were obtained, which may be due to two main reasons: a considerable proportion of recrystallized diopside grains in the studied samples, as well as the presence of crystals that have undergone melting (fragments of a crystallized partial melt).

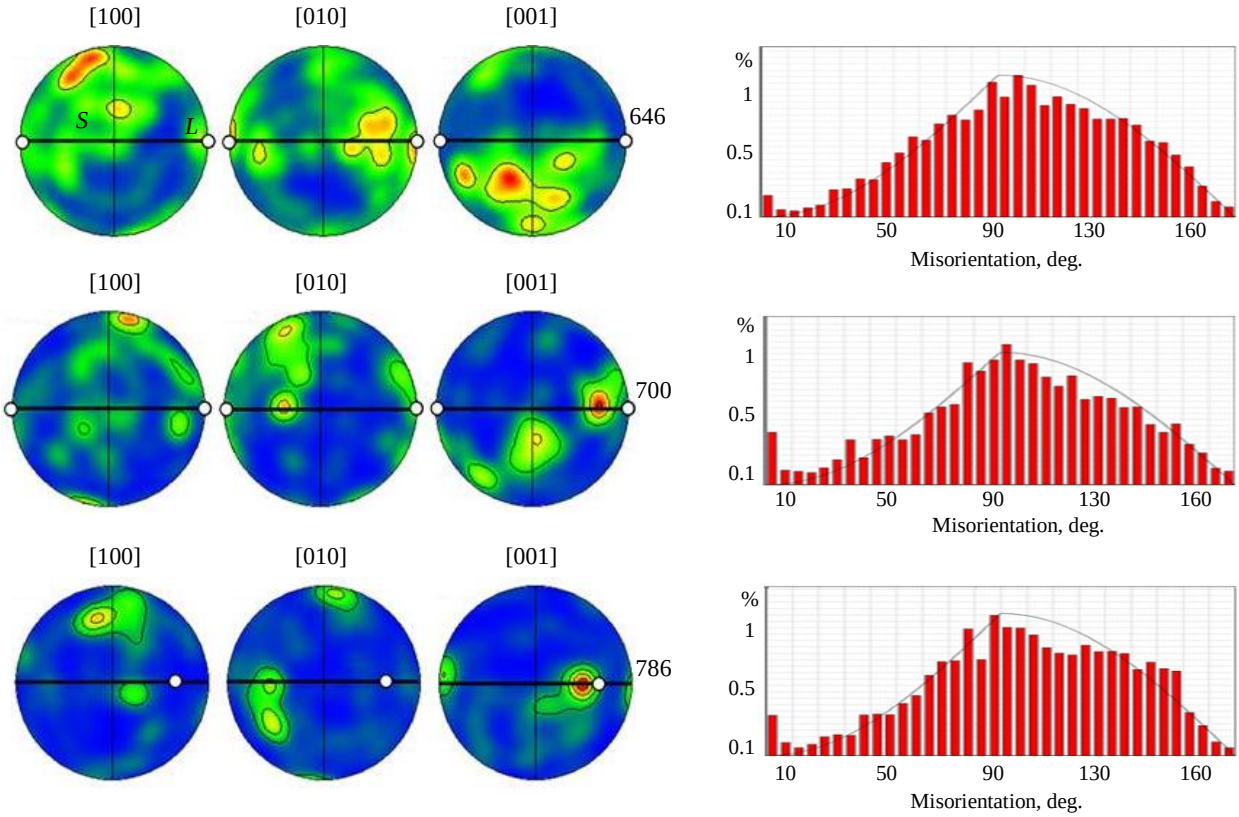

Fig.7. Straight pole figures for clinopyroxenes from ultramafic rock samples from borehole GT-HY-1

Discussion of the results. The obtained petrographic, mineralogical, and microstructural data are generally consistent with the overall structural patterns of ultramafic rock complexes and chromitite deposits [4], although in part they diverge from some well-known provisions. In the studied chromite-bearing section, lherzolites with aluminous spinel are quite widespread. Dunites contain high-chromium accessory chrome spinel, and olivine from inclusions is very enriched in nickel [32, 33]. All this indicates a high degree of depletion of wallrock ultramafic rocks, although in general the section is represented by relatively weakly depleted rocks of the upper mantle.

The obtained microstructural data indicate the formation of ultramafic rocks in the conditions of high-temperature plastic flow, accompanied by syntectonic recrystallization [25]. Judging by the texture diagrams, two slip systems (010)[100] and (001)[100] appeared in olivine, which correspond to texture types A and E according to the classification [38]. Both types of textures were diagnosed in experiments under stress to 300 MPa, type A being observed in “dry” (<200 ppm H/Si), and type E in “wet” conditions (200-1000 ppm H/Si) [38] .

More complex petrostructural patterns were obtained in orthopyroxene, which is associated with the lower plasticity of this mineral compared to olivine [39, 40] and, as a consequence, the presence of several groups of grains, deformed porphyroclasts with a domain structure and neoblasts formed during syntectonic recrystallization.

Macrotextural and microstructural features of chromitites were also formed in the conditions of plastic flow of host dunites with dispersed ore material. This is especially pronounced in lenticular-banded varieties of ores. Differences in the grain size composition of sections with disseminated and massive structure are well explained precisely from the position of the solid-phase genesis of ores. According to the rheomorphic model [9, 32, 41], the most mobile members of the mantle sections of ophiolites are dunites, formed as a result of the deformation-induced decomposition of orthopyroxenes [41]. The same process leads to a primary increase in the concentration of chrome spinels, which

crystallize from impurity amounts of chromium and aluminium included in pyroxenes. Since olivine is the mineral with the weakest rheological properties in the upper mantle [39], plastic flow and associated solid-phase differentiation of matter are localized in dunite zones. Due to a significantly higher rheological rigidity, chrome spinel grains in an olivine aggregate predominantly behave as rigid inclusions, which are energetically advantageous to form clusters – segregations – in such a solid-phase flow, as was shown by physical and mathematical modelling in [9].

Thus, inside the dunites, segregation of chromite grains could occur with the formation of lenticular-banded accumulations. In the central parts of the lenses, conditions were created for the contact of initially scattered ore grains. At their contacts, the initial misorientation was levelled, i.e. a new grain with a uniform crystallographic orientation was formed. A similar mechanism was proposed to explain the microstructure features in Indian chromitites [42] and is close to "high-P sintering", which is proposed to explain the genesis of coarse-grained massive chromitites in both ophiolitic and layered complexes [43, 44].

Microstructural studies confirmed the previously stated assumption that the sizes of chrome spinel individuals critically depend on structural features, and those, in turn, on the segregation stage. At the early stage, each chrome spinel grain is surrounded by olivine grains, therefore, the size of ore grains has one maximum, corresponding to deformation conditions and is always equal to or less than the size of olivine grains. However, when segregation reaches a certain critical level, which can be conventionally designated as "the beginning of grain contact," the growth of chromite aggregates (accretion) and the erasure of orientation differences begin. This direction of the process is facilitated by the significantly lower deformability of chromite compared to olivine and the slowdown of plastic flow near areas with increased concentration of ore grains. A similar mechanism for the growth of large grains (porphyroblasts) of minerals with stronger rheological properties (in particular, garnets) in metamorphic rocks was described in [45].

Conclusion. Microstructural studies of chromitites and host ultramafic rocks of the Almaz-Zhemchuzhina deposit allowed us to obtain quantitative data on the internal structure of the rocks. We found out that the formation of ultramafic rocks occurred in the conditions of subsolidus high-temperature (650-950 °C) plastic flow. Statistical data on the crystallographic orientation of olivine indicate that the main mechanism of deformation was translation gliding along the (010)[100] and (001)[100] systems; syntectonic recrystallization was of subordinate importance. In orthopyroxene, plastic flow was also realized by the mechanism of translation glide: systems (100)[001] and (010)[001], while syntectonic recrystallization was much stronger compared to olivine. Chromitites also exhibit textures and structures formed in plastic flow conditions. Disseminated ores have a finer-grained structure compared to massive ones: in the structure formation of the latter, the accretion of ore grains played a significant role, which was accompanied by the unification of their crystallographic orientation.

REFERENCES

1. Kravchenko G.G. The role of tectonics in the crystallization of chromite ores in the Kempirsai pluton. Moscow: Nauka, 1969, p. 217 (in Russian).

2. Pavlov N.V., Kravchenko G.G., Chuprynina I.I. Chromites of the Kempirsai pluton. Moscow: Nauka, 1968, p. 179 (in Russian).

3. Melcher F., Grum W., Simon G. et al. Petrogenesis of the Ophiolitic Giant Chromite Deposits of Kempirsai, Kazakhstan: a Study of Solid and Fluid Inclusions in Chromite. *Journal of Petrology*. 1997. Vol. 38. Iss. 10, p. 1419-1458. DOI: 10.1093/petroj/38.10.1419

4. González-Jiménez J.M., Griffin W.L., Proenza J.A. et al. Chromitites in ophiolites: How, where, when, why? Part II. The crystallization of chromitites. *Lithos*. 2014. Vol. 189, p. 140-158. DOI: 10.1016/j.lithos.2013.09.008

5. Yao Wu, Mengjing Xu, Zhenmin Jin et al. Experimental constraints on the formation of the Tibetan podiform chromitites. *Lithos*. 2016. Vol. 245, p. 109-117. DOI: 10.1016/j.lithos.2015.08.005

6. Fahui Xiong, Basem Zoheir, Richard Wirth et al. Mineralogical and isotopic peculiarities of high-Cr chromitites: Implications for a mantle convection genesis of the Bulqiza ophiolite. *Lithos*. 2021. Vol. 398-399. N 106305. DOI: 10.1016/j.lithos.2021.106305

7. Johan Z., Martin R.F., Ettler V. Fluids are bound to be involved in the formation of ophiolitic chromite deposits. *European Journal of Mineralogy*. 2017. Vol. 29. Iss. 4, p. 543-555. DOI: 10.1127/ejm/2017/0029-2648

8. Pushkarev E.V., Kamenetsky V.S., Morozova A.V. et al. Ontogeny of ore Cr-spinel and composition of inclusions as indicators of the pneumatolytic-hydrothermal origin of PGM-bearing chromitites from Kondyor massif, the Aldan Shield. *Geology of Ore Deposits.* 2015. Vol. 57. Iss. 5, p. 352-380. DOI: 10.1134/S1075701515050049

9. Saveliev D.E., Fedoseev V.B. Solid-state redistribution of mineral particles in the upwelling mantle flow as a mechanism of chromite concentration in the ophiolite ultramafic rocks (by the example of Kraka ophiolite, the Southern Urals). *Georesursy.* 2019. Vol. 21. N 1, p. 31-46 (in Russian). DOI: 10.18599/grs.2019.1.31-46

10. Kazakov A.N. Dynamic analysis of microstructural orientations of minerals. Leningrad: Nauka, 1987, p. 272 (in Russian).

11. Saranchina G.M., Kozhevnikov V.N. Fedorov method (determination of minerals, microstructural analysis). Leningrad: Nedra, 1985, p. 208 (in Russian).

12. Chernyshov A.I., Yurichev A.N. The Structural Evolution of Dunite and Chromite Ore from the Kharcheruz Massif, the Polar Urals. *Geotectonics.* 2016. Vol. 50. N 2, p. 62-77. DOI: 10.1134/S0016852116020035

13. Klepikov I.V., Vasilev E.A., Antonov A.V., Kudryavtsev A.A. Growth of pyramids {110} in natural diamonds. *Geology of Ore Deposits.* 2022. Vol. 64. Iss. 8, p. 670-675. DOI: 10.31857/S0869605521010068

14. Klepikov I.V., Vasilev E.A., Antonov A.V. Regeneration Growth as One of the Principal Stages of Diamond Crystallogenesis. *Minerals*. 2022. Vol. 12. Iss. 327. DOI: 10.3390/min12030327

15. Vasilev E.A., Kriulina G.Y., Garanin V.K. Thermal history of diamond from Arkhangelskaya and Karpinsky-I kimberlite pipes. *Journal of Mining Institute.* 2022. Vol. 255, p. 327-336. DOI: 10.31897/PMI.2022.57

16. Till J.L., Moskowitz B.M. Deformation microstructures and magnetite texture development in synthetic shear zones. *Tectonophysics*. 2014. Vol. 629, p. 211-223. DOI: 10.1016/j.tecto.2014.04.026

17. Vukmanovic Z., Barnes S.J., Reddy S.M. et al. Morphology and microstructure of chromite crystals in chromitites from the Merensky Reef (Bushveld Complex, South Africa). *Contributions to Mineralogy and Petrology*. 2013. Vol. 165. Iss. 6, p. 1031-1050. DOI: 10.1007/s00410-012-0846-1

18. Yudovskaya M.A., Costin G., Shilovskikh V.V. et al. Bushveld symplectic and sieve-textured chromite is a result of coupled dissolution-reprecipitation: a comparison with xenocrystic chromite reactions in arc basalt. *Contributions to Mineralogy and Petrology*. 2019. Vol. 174. Iss. 9. N 74. DOI: 10.1007/s00410-019-1613-3

19. Bernard R.E., Behr W.M., Becker T.W., Young D.J. Relationships Between Olivine CPO and Deformation Parameters in Naturally Deformed Rocks and Implications for Mantle Seismic Anisotropy. *Geochemistry, Geophysics, Geosystems*. 2019. Vol. 20. Iss. 7, p. 3469-3494. DOI: 10.1029/2019GC008289

20. Kumamoto K.M., Warren J.M., Hansen L.N. Evolution of the Josephine Peridotite Shear Zones: 2. Influences on Olivine CPO Evolution. *Journal of Geophysical Research: Solid Earth*. 2019. Vol. 124. Iss. 12, p. 12763-12781. DOI: 10.1029/2019JB017968

21. Soustelle V., Manthilake G. Deformation of olivine-orthopyroxene aggregates at high pressure and temperature: Implications for the seismic properties of the asthenosphere. *Tectonophysics*. 2017. Vol. 694, p. 385-399. DOI: 10.1016/j.tecto.2016.11.020

22. Michibayashi K., Mainprice D., Fujii A. et al. Natural olivine crystal-fabrics in the western Pacific convergence region: A new method to identify fabric type. *Earth and Planetary Science Letters*. 2016. Vol. 443, p. 70-80. DOI: 10.1016/j.epsl.2016.03.019

23. Munjae Park, Youngwoo Kil, Haemyeong Jung. Evolution of Deformation Fabrics Related to Petrogenesis of Upper Mantle Xenoliths Beneath the Baekdusan Volcano. *Minerals*. 2020. Vol. 10. Iss. 9. N 831. DOI: 10.3390/min10090831

24. Skemer P., Hansen L.N. Inferring upper-mantle flow from seismic anisotropy: An experimental perspective. *Tectonophysics*. 2016. Vol. 668-669, p. 1-14. DOI: 10.1016/j.tecto.2015.12.003

25. Saveliev D.E., Makatov D.K., Sergeev S.N. Microstructural features of chromitite and ultramafic rocks of Almaz-Zhemchuzhina deposit (Kempirsay massif, Kazakhstan). *Problemy mineralogii, petrografii i metallogenii. Nauchnye chteniya pamyati P.N.Chirvinskogo*. 2023. N 26, p. 230-235 (in Russian). DOI: 10.17072/chirvinsky.2023.230

26. Varyukhin V.N., Pashinskaya E.G., Zavdoveev A.V., Burkhovetskii V.V. Capabilities of the electron backscatter diffraction method for analysing the structure of deformed materials. Kiev: Naukova dumka, 2014, p. 104.

27. Adams B.L. Electron Backscatter Diffraction in Materials Science. Moscow: Tekhnosfera, 2014, p. 544.

28. Danilenko V.N., Mironov S.Y., Belyakov A.N., Zhilyaev A.P. Application of EBSD analysis of material physics (review). *Industrial Laboratory. Diagnostics of Materials.* 2012. Vol. 78. N 2, p. 28-46 (in Russian).

29. Savelyev A.A., Savelyeva G.N. The Kempersay massif ophiolites: main characteristics of the structure and substance evolution. *Geotectonics.* 1991. N 6, p. 57-75 (in Russian).

30. Balykin P.A., Konnikov E.G., Krivenko A.P. et al. Petrology of post-harzburgite intrusions of the Kempirsai-Khabarninskii ophiolite association (Southern Urals). Sverdlovsk: Institut geologii i geokhimii, 1991, p. 159 (in Russian).

31. Abdullin A.A., Avdeev A.V., Seitov N.S. Silurian ophiolites of the Sakmara and Or-Iletsk zones of the Mugodzhar. *Trudy Instituta geologicheskikh nauk KazSSR*. 1975, p. 39-74 (in Russian).

32. Saveliev D.E., Makatov D.K., Rakhimov I.R. et al. Silicates from Lherzolites in the South-Eastern Part of the Kempirsay Massif as the Source for Giant Chromitite Deposits (the Southern Urals, Kazakhstan). *Minerals*. 2022. Vol. 12. Iss. 8. N 1061. DOI: 10.3390/min12081061

33. Saveliev D.E., Makatov D.K., Vishnevskiy A.V., Gataullin R.A. Accessory Minerals in the Chromitite Ores of Dzharlybutak Ore Group of Kempirsai Massif (Southern Urals, Kazakhstan): Clues for Ore Genesis. *Minerals*. 2023. Vol. 13. Iss. 2. N 263. DOI: 10.3390/min13020263

34. Saveleva G.N., Pertsev A.N. Mantle ultramafic rocks in ophiolites of the Southern Urals, Kempirsai massif. *Petrologiya*. 1995. Vol. 3. N 2, p. 115-132 (in Russian).

35. Ballhaus C., Berry R.F., Green D.H. High pressure experimental calibration of the olivine-orthopyroxene-spinel oxygen geobarometer: implications for the oxidation state of the upper mantle. *Contributions to Mineralogy and Petrology*. 1991. Vol. 107. Iss. 1, p. 27-40. DOI: 10.1007/BF00311183

36. Ono A. Fe-Mg partitioning between spinel and olivine. *The Journal of the Japanese Association of Mineralogists, Petrologists and Economic Geologists*. 1983. Vol. 78. Iss. 4, p. 115-122. DOI: 10.2465/ganko1941.78.115

37. Roeder P.L., Campbell I.H., Jamieson H.E. A re-evaluation of the olivine-spinel geothermometer. *Contributions to Mineralogy and Petrology*. 1979. Vol. 68. Iss. 3, p. 325-334. DOI: 10.1007/BF00371554

38. Haemyeong Jung. Crystal preferred orientations of olivine, orthopyroxene, serpentine, chlorite, and amphibole, and implications for seismic anisotropy in subduction zones: a review. *Geosciences Journal*. 2017. Vol. 21. Iss. 6, p. 985-1011. DOI: 10.1007/s12303-017-0045-1

39. Yamamoto J., Ando J., Kagi H. et al. In situ strength measurements on natural upper-mantle minerals. *Physics and Chemistry of Minerals*. 2008. Vol. 35. Iss. 5, p. 249-257. DOI: 10.1007/s00269-008-0218-6

40. Saveliev D.E. Chromitites of the Kraka ophiolite (South Urals, Russia): geological, mineralogical and structural features. *Mineralium Deposita*. 2021. Vol. 56. Iss. 6, p. 1111-1132. DOI: 10.1007/s00126-021-01044-5

41. Saveliev D.E., Puchkov V.N., Sergeev S.N., Musabirov I.I. Deformation-induced decomposition of enstatite in mantle peridotite and its role in partial melting and chromite ore formation. *Doklady Earth Sciences.* 2017. Vol. 476. N 1, p. 1058-1061. DOI: 10.1134/S1028334X17090161

42. Ghosh B., Misra S., Morishita T. Plastic deformation and post-deformation annealing in chromite: Mechanisms and implications. *American Mineralogist*. 2017. Vol. 102. Iss. 1, p. 216-226. DOI: 10.2138/am-2017-5709

43. Johnson C. Podiform chromite at Voskhod, Kazakhstan: Submitted in partial fulfilment of the requirements for the degree of Ph.D. Cardiff University, 2012, p. 468.

44. White J.C., White S.H. On the structure of grain boundaries in tectonites. *Tectonophysics*. 1981. Vol. 78. Iss. 1-4, p. 613-628. DOI: 10.1016/0040-1951(81)90032-9

45. Spiess R., Peruzzo L., Prior D.J., Wheeler J. Development of garnet porphyroblasts by multiple nucleation, coalescence and boundary misorientation-driven rotations. *Journal of Metamorphic Geology*. 2001. Vol. 19. Iss. 3, p. 269-290. DOI: 10.1046/j.1525-1314.2001.00

***Authors*: Dmitrii E. Saveliev,** *Doctor of Geological and Mineralogical Sciences, Chief Researcher, savl71@mail.ru, https://orcid.org/0000-0001-8910-6992* (*Institute of Geology, Ufa Federal Research Centre of the RAS, Ufa, Russia*), **Semen N. Sergeev**, *Junior Researcher, https://orcid.org/0000-0001-5494-390X* (*Institute for Metals Superplasticity Problems of the RAS, Ufa, Russia*), **Darkhan K. Makatov**, *PhD Student, https://orcid.org/0009-0006-5059-2851* (*Abylkas Saginov Karaganda Technical University, Karaganda, Republic of Kazakhstan*).

The authors declare no conflict of interests.

ISSN 2411-3336; e-ISSN 2541-9404

JOURNAL OF MINING INSTITUTE

Zapiski Gornogo instituta

Journal homepage: pmi.spmi.ru

Research article

Optimization of specific energy consumption for rock crushing by explosion at deposits with complex geological structure

Yurii I. Vinogradov[1]✉, **Sergei V. Khokhlov**[1], **Ramil R. Zigangirov**[1], **Aleksei A. Miftakhov**[2], **Yurii I. Suvorov**[2]

[1] *Empress Catherine II Saint Petersburg Mining University, Saint Petersburg, Russia*

[2] *AO "Polyus Aldan", set. Nizhnii Kuranakh, Republic of Sakha (Yakutiya), Russia*

***How to cite this article*:** Vinogradov Y.I., Khokhlov S.V., Zigangirov R.R., Miftakhov A.A., Suvorov Y.I. Optimization of specific energy consumption for rock crushing by explosion at deposits with complex geological structure. Journal of Mining Institute. 2024. Vol. 266, p. 231-245.

Abstract. The selection of efficient drilling and blasting technology to achieve the required particle size distribution of blasted rock mass and reduce ore dilution is directly related to the accurate definition of rock mass properties. The zoning of the rock massif by its hardness, drillability and blastability does not consider the variability of the geological structure of the block for blasting, resulting in an overestimated specific consumption of explosives. The decision of this task is particularly urgent for enterprises developing deposits with a high degree of variability of geological structure, for example, at alluvial deposits. Explosives overconsumption causes non-optimal granulometric composition of the blasted rock mass for the given conditions and mining technology. It is required to define physical and mechanical properties of rocks at deposits with complex geological structure at each block prepared for blasting. The correlation between the physical and mechanical properties of these rocks and drilling parameters should be used for calculation. The relation determined by the developed method was verified in industrial conditions, and the granulometric composition of the blasted rock mass was measured by an indirect method based on excavator productivity. The results demonstrated an increase in excavation productivity, thus indicating the accuracy of given approach to the task of identifying the rocks of the blasted block.

***Keywords*:** drilling and blasting; drilling energy intensity; measurement of drilling parameters; specific consumption of explosives

Received: 10.04.2023 ***Accepted: 27.12.2023*** ***Online: 22.02.2024*** ***Published: 25.04.2024***

Introduction. Open mining accounts for 70 % of all mineral deposits exploitation [1, 2]. As open-cast mines get deeper, the rock strength coefficient increases, which results in the intensification of blasting operations and an increase in the costs of blasting [3]. It is worth mentioning that blast crushing is the first link in the chain of technological processes of mining production and represents about 30 % of the total costs of mineral extraction [4-6]. Therefore, it is essential to rationally distribute the blast energy to reduce the cost of drilling and blasting while providing the optimum granulometric composition of the blasted rock mass according to the extraction cost, that would maximize profits [7-10]. The above factors are set in the drilling and blasting parameters, their calculation takes into account the properties of the explosive materials and explosion object characteristics – the rock massif. The rock mass is characterized by physical and mechanical properties of its forming rocks and the degree of fracturing, that cause the strength properties of the destroyed object, which also affects the rational justification of the field development system [11].

Problem statement. One of the world key problems in the field of blasting is the uncertain structure of the blasted block, and consequently the inability to determine the physical and mechanical properties of the rocks forming the block. These properties directly influence the quality of crushing, and, as a result, the mining cost of the mineral. The study by S.N.Zharikov shows that a large explosive

reserve is put into the drilling and blasting parameters, which leads to overuse of explosives [12]. Therefore, identifying the block structure for blasting is an important task in terms of economics and rational use of resources. The resulting solution will be a rational distribution of the charge energy according to the physical and mechanical properties of the block's rocks.

In case of open-pit mining, the calculation of blasting and drilling parameters is based on the volumetric hypothesis of S.Vauban, setting the correlation between the volume of the blasted block V and the amount of explosive required for this purpose Q [13]:

$$Q = qV,$$

where q – specific consumption of the explosives, kg/m^3.

The explosive energy supplied to the rock, as is known, depends on the properties of the explosives, the conditions and the properties of the rock. Consequently, the value of the charge can be expressed as a function of all variables influencing the quality of the explosion [14]:

$$Q = f\left(W, H, a, l_c, d_c, E, \rho, D, c_i\right),$$

where W, H, a, l_c, d_c – geometrical parameters – line of least resistance (LLR), ledge height, charge spacing, charge length, charge diameter, respectively; E, ρ, D – the explosives parameters – weight power, density, detonation velocity, respectively; c_i – coefficient of rock properties, charge location, etc.

U.Langefors offered to change the volumetric concentration of energy in different parts of the borehole – for better development of the ledge bottom, the charge density in the lower part of the borehole should be increased by 60 % compared to the main part of the charge. He also suggests using the simplest explosives based on ammonium nitrate and oil additives as the main charge, and charging dynamites in the lower part, as these explosives have high water resistance, density and energy content.

Langefors' method can be used in the explosion of a heterogeneous rock massif. Generating in different parts of the borehole explosive charges with different energy corresponding to physical and mechanical properties of rocks, it allows to rationally distribute the explosion energy in the blasted block and thus to ensure the optimal quality of crushing [15]. At that time, there were no technologies that would provide a quick way to determine rock formations of a block. It should be noted that the issue of rational distribution of explosion energy based on the physical and mechanical properties is not a novel one. In the 50-ies of the last century in the USA the explosive substances for the solution of this problem were developed. Their specific heat of explosion could be varied right at the time of charging through changing the density of explosives and the percentage ratio of components. These explosives are called “Slurry”. They are an aqueous liquid solution of an oxidizing agent (usually ammonium nitrate) acting as a solid or dispersing phase containing both excess solid oxidizer and sensitizing combustible additives dispersed in it [16, 17]. B.L.Baron and V.H.Kantor discuss the American company “Mc Kissick” charging machine, that prepares a mixture of ammonium nitrate and fuel oil (ANFO) with aluminum additive. The amount of the additive can be adjusted, and the supply can be started and stopped at any moment of charging the borehole [18]. This enables to create a charge with variable energy along the height of the ledge and widens the application of ANFO mixture. “Ireko Chemicals” charging machine, for charging water-containing explosives, is shown there. The machine allows to manage the volumetric concentration of the charge energy depending on the physical and mechanical properties of rocks.

The Vauban hypothesis is the key to estimate the required amount of explosives in the borehole and for the entire block. The only major task is to identify the optimum specific consumption of explosives, which is the main energy indicator of blasting.

B.N.Kutuzov also suggested to calculate the specific design consumption on the basis of the reference for a given rock type at the charge diameter of 200-250 mm [19]:

$$q_{\text{des}} = \frac{q_{\text{ref}} e k_d \rho}{2{,}6}, \quad (1)$$

where q_{ref} – reference specific consumption for a given rock massif, defined according to experimental explosions and considering physical-mechanical properties of rocks and fracturing of the given massif; e – performance factor of the explosives; k_d – correction factor for the standard block size; ρ – rock density.

The following physical and mechanical properties of rocks are taken into account in formula (1): uniaxial compressive strength of the rock sample through the reference specific consumption and rock density. Structural weakness of the massif due to fracturing is also accounted. The value of the reference specific consumption is not a constant, since the physical and mechanical properties of rocks and fracturing of massifs with different genesis and the same petrographic composition can differ.

V.V.Rzhevskii offered to compute the reference specific consumption for crushing a rock massif as follows [20]:

$$q_{\text{ref}} = 0.1 k_{\text{m}} \left(\sigma_{\text{compr}} + \sigma_{\text{tens}} + \sigma_{\text{sh}} \right) + 40\rho, \quad (2)$$

where k_{m} – coefficient related to fracturing of the massif; σ_{compr} – compressive strength; σ_{tens} – tension strength; σ_{sh} – shear strength; ρ – rock density.

The calculation formula for the design specific consumption by V.V. Rzhevskii method is related to the calculation of consumption through the reference flow [21]:

$$q_{\text{des}} = q_{\text{ref}} K_{\text{expl}} K_{\text{d}} K_{\text{m}} K_{\text{c}} K_{\text{v}} K_{\text{o.a}},$$

where K_{expl} – coefficient, considering the type of explosives; K_{d} – coefficient considering borehole diameter; K_{m} – coefficient considering massif fracturing; K_{c} – coefficient considering the actual shape and concentration of the charge; K_{v} – coefficient considering volume of blasted rock; $K_{\text{o.a}}$ – coefficient considering the number of open air.

The formula developed by "Giproruda" (Russian mining enterprise) is quite similar to the formula of V.V.Rzhevskii, as the reference for this type of rocks is used to calculate the design specific consumption rate [19]:

$$q_{\text{des}} = q_{\text{ref}} K_{\text{expl}} K_{\text{d}} K_{\text{cr}} K_b,$$

where K_{cr} – coefficient considering the degree of crushing; K_b – coefficient considering the borehole deviation.

The "Soyuzvzryvprom" (a leading organization for drilling and blasting operations) formula considers rock strength directly, and fracturing – through the average size of a piece in the massif [13]:

$$q_{\text{des}} = 0.13\rho f^{0.25} \left(0.6 + 3.3 \cdot 10^{-3} d_{\text{c}} d_0 \right) \left(\frac{0.5}{d_{\text{s}}} \right)^{0.4} K_{\text{expl}} \cdot 10^{-3},$$

where d_{c} – charge diameter, mm; d_0 – average size of a piece in the massif, m; d_{s} – size of the standard piece in the rock mass breakdown, m.

The physical sense of the specific consumption of explosives is that it represents the specific energy consumption of explosives for crushing of a given rock massif [21]:

$$e_{\text{expl}} = qE,$$

where E – explosive energy of 1 kg explosives, kJ/kg.

Analyzing the presented formulas of specific consumption, it can be observed that three of these formulas include the type of explosives through the relative workability coefficient [22]:

$$K_{\text{expl}} = \frac{E_{\text{ref}}}{E_{\text{expl}}},$$

where E_{expl}, E_{ref} – explosion energy of 1 kg of used and reference explosives, respectively.

Then, if you know the reference energy consumption for crushing of 1 m^3 of rocks, you can identify its specific consumption according to the energy characteristics of the explosives. That, in turn, will make it possible to change the volumetric concentration of energy at different depths of the borehole in accordance with the physical and mechanical properties of the rocks at a given depth.

M.F.Drukovanyi et al. proposed to apply the weighted average value of specific consumption, defined in accordance with the thickness of each layer, for calculations of charges in a layered massif *:

$$q = \frac{q_1 H_1 + q_2 H_2 + q_3 H_3}{H_1 + H_2 + H_3},$$

where q_1, q_2, q_3 – specific consumption of explosives for rocks of the first, second and third layers, respectively; H_1, H_2, H_3 – capacity of each layer.

This relation may be applicable for deposits where the layering is rather precisely defined by rock outcrops on the free surfaces of the block. For those massifs where the structure is not constant and changes within a small area of the blasted block, it is not reasonable to apply the formula of M.F.Drukovanyi et al. Consequently, we face the following challenge: how to determine the geological structure of the blasted block and the physical and mechanical properties of the rocks composing this block.

The existing dependencies do not allow us to establish reference specific energy inputs for each type of rock of a particular deposit. Actually, formula (2) is based on the assumption that compression, tension and shear loads play the equal role during rock explosion. However, modern concepts of physics of rock fracture during explosion indicate the prevailing tension load. Also, this fact is applicable only for monolithic pure objects, as rock massifs are not. This means that the reference specific energy consumption for rock crushing by explosion can be determined only experimentally, and these values will be valid just for the studied deposit rocks. Nevertheless, regardless of the reference specific energy consumption values for rock crushing by explosion, the task of structure determination of the block for explosion is still unsolved (specific explosive consumption).

Now we will take a look at the technological parameters showing the complex of physical-mechanical properties of rocks.

As it is well-known, the rock strength coefficient of M.M.Protodyakonov is used for relative assessment of the rock fracture resistance [23]:

$$f = \frac{\sigma_{compr}}{10}, \quad (3)$$

where σ_{compr} – compression strength, MPa.

This coefficient is a criterion for relative assessment of rock properties, and its value is correct only for rocks of a particular deposit where the assessment was performed.

Drillability classifications are used for classification of rocks by difficulty of destruction. A series of classifications is developed on the basis of drilling time of a linear meter of borehole, drilling complexity (dimensionless coefficient), specific energy consumption [24]. The existence of different classifications for the same process indicates both the complexity of the problem and the incompleteness of its solution. It is impractical to compare the scales based on drilling time, as different machines are applied. In the classification according to Building Code and Regulations-82 – drilling hammer PR-30 is for all rocks, and in the Unified Classification of Drillability for rocks up to 11 categories the machine tool SBR-160 (rock drilling machine) is used, from 12 and above – SBSh-250 (rotary drilling rig).

* Drukovanyi M.F., Dubnov L.V., Ivanov K.I. et al. Drilling and Blasting Manual. Moscow: Nedra, 1976, p. 631.

There is a general classification of blastability for rock evaluation according to the required amount of explosives for crushing, developed by B.N.Kutuzov and V.F.Pluzhnikov for standard conditions (ledge height 12-15 m, borehole diameter about 250 mm, explosives – grammonite 79/21, initiation scheme – diagonal with short-delayed explosion), at explosion the yield of coarse fraction (more than 1000 mm) is close to zero*. Consequently, the values of specific consumption for each explosivity category were determined, and the classification also includes fracturing and the content in the massif of separates greater than 500 mm and greater than 1500 mm. This classification has two disadvantages – a large range of specific consumption values for the same category and the correspondence of several categories of drillability for one category of blastability. Table 1 demonstrates the correspondence of the three categories.**

Table 1

Summary table of rock classifications by strength, drillability and blastability

Tensile strength uniaxial compression, Pa·10^5	Strength coefficient according to the scale M.M.Protodyakonov	Drillability index (Unified production standards, USSR)	Blastability index according to B.N.Kutuzov and V.F.Pluzhnikov
100-300	1-3	V-VII	I
200-450	2-5	VII-X	II
300-650	3-7	IX-XII	III
500-800	5-8	XI-XIII	IV
700-1200	7-12	XIII-XV	V
1100-1600	11-16	XIV-XVI	VI
1450-2050	15-20	XV-XVIII	VII
1950-2500	20	XVII-XX	VIII
2350-3000	20	XIX-XX	IX
2850 and more	20	XX	X

The massif zoning by blastability, drillability, rock strength categories, i.e. in fact by physical and mechanical properties of rocks and fracturing of the massif, is required for making optimal decisions on mining planning. However, all the ways of zoning are based on direct contact with the array of explosives or photography of ledges, open pit sides. Meanwhile, none of the methods may provide an idea of physical and mechanical properties of rocks directly. Due to the fact that the scales of drillability, blastability and strength are incomplete, the properties of rocks should be determined on the blasted block with certain tools.

Laboratory tests based on the samples collected from the coring of rock massifs help to identify the physical and mechanical properties of rocks with sufficient accuracy [25]. Currently, rock samples make it possible to obtain a large amount of data that help to design drilling and blasting operations. The main disadvantage of this method is the great time spent from the moment of sampling to obtaining information. Besides, it is necessary to carefully polish the end surfaces, their parallelism and monolithicity of the samples are required [26]. On top of that, it is required to ensure the safety of core samples during removal and transportation. According to the standards, a high volume of material by weight and length is demanded, that is not always feasible [26].

The proposed solution to this task is the testing of irregular-shaped rock samples by compressing them with spherical indenters, developed at the St. Petersburg Mining University [27]. The main idea is to fix the destructive force and measure the surface area of the break and the fractured rock zones in

* Kutuzov B.N. Methods of blasting. Part 1. Destruction of rocks by explosion. Moscow: Mining Book, 2007, p. 471.
** Trubetskoy K.N., Potapov M.G., Vinitsky K.E. et al. Open-pit mining operations. Moscow: Bureau of Mines, 1994, p. 590.

contact with the indentors. Such tests do not require properly shaped samples, reducing the time and cost. Studies have shown the validity of this method – the variation between cylindrical and irregularly shaped samples is not great. However, it still demands appropriate equipment, manpower, and the processing of a large amount of data.

One promising approach to define physical and mechanical properties of rocks and rock fracturing is the MWD (measurement while drilling) technology [28-31]. The main idea of the technology is to measure drilling parameters, such as feed pressure, pressure on the rotator, energy characteristics of the corresponding units, drilling speed, etc. To get data on rock properties, no special equipment (except for the one installed on the drilling machine) and properly trained people are required. Data interpretation is accomplished with computer programs that calculate drilling and blasting parameters based on the defined patterns.

The first time this technology was used in 1911 in the oil industry, and only in the 1970s it was introduced in the mining industry. Classification of rocks according to their specific mechanical drilling energy was suggested by R.Teale, who worked out formulas for calculating this energy for different drilling methods [32]. The equations consider the load on the drill bit, bit rotation speed, its torque and drilling speed.

H.Schunnesson showed that drilling parameters may be applied to assess the physical and mechanical properties of rocks if these properties differ significantly, i.e. the geological structure changes [33, 34].

I.E.Dolgiy and N.I.Nikolaev claim that in drilling the energy spent on destruction is determined by the total set of physical and mechanical properties of rocks, and propose to evaluate rocks by specific volumetric work of destruction [35].

I.A.Tangaev developed a classification of rocks by drillability, suggesting to estimate rocks by their specific energy consumption of drilling with a roller cone method [36]:

$$e = \frac{N}{v},$$

where N – rotator power, kW; v – drilling speed.

Since physical and mechanical properties of rocks, both on samples and by geophysical methods, are extremely labor-intensive and require special conditions, MWD technology is the best way to solve the issue of rock identification [32].

Rock identification algorithm:

• identify the rock types composing the massif of the given deposit;

• determine physical and mechanical properties of these rocks in a laboratory using samples;

• get correlation dependence between drilling parameters and physical and mechanical properties of rocks;

• determine the specific energy consumption for blast crushing of each rock type.

Methods. In order to define the relation between drilling parameters and physical and mechanical properties of the Kuranakh ore field rocks, the following technique was developed:

• The geological service picks one or more technological blocks that, in the opinion of the geologist, correspond to characteristic rock types composing the Kuranakh ore field deposit array.

• While technological drilling, some parameters are analyzed starting from the depth of 4-5 m from the borehole mouth (drilling energy consumption, axial loads, technical drilling speed, etc.) according to the data of the onboard controller “Kobus”.

• There are three or four boreholes with the same parameters (specific drilling energy consumption is taken as a basis) for each characteristic rock type.

• Close to the selected boreholes the exploration drilling is performed with sampling of core from a depth of 4-5 m from the mouth. The exploration borehole distance should not exceed 1 m. From

each exploration well 1-1.5 m of core of one rock type is taken. For each rock type, at least 3 m of core is sampled.

A Boart Longyear LV 75 crawler-mounted core drilling machine was applied in geological exploration. It can drill boreholes with a diameter of 108 mm (outer pipe diameter) and obtain a core with a diameter of 67 mm. The core was collected in accordance with the State Standard 12071 "Soils. Selection, packing, transportation and storage of samples". Each selected sample was put in a stretch wrap to protect it from moisture and labeled (name of the rock, depth and location of sampling). Simultaneously, there was a field log with more extensive description of each core meter.

The Atlas Copco DML machine was applied for drilling technological boreholes, their diameter is 230 mm. The machine is equipped with a "Kobus" on-board controller, which is part of the BlastMaker software system that transmits information on drilling parameters in real time. New bits were used to exclude the influence of roller cone bits wear on drilling parameters.

The following physical and mechanical properties were determined in a laboratory: uniaxial compression, tension strength, compression shear and density, in accordance with the relevant State Standard Specifications. While drilling technological boreholes, the color of cuttings, their moisture, various drilling sounds (knocking, scraping) were recorded.

The results were approved by blasting the technological block. Specific energy consumption of drilling and drilling products (cuttings) were analyzed and identified based on the observation method.

Based on the analysis of geological documentation, the following types of rocks characteristic of the studied deposit were identified: fine-grained dolomitized limestones; medium-grained dense dolomitized limestones; fine-grained sandstones; loams of different plasticity. The results of geological drilling are given in Table 2. The results of the obtained rock samples laboratory tests for uniaxial compression, tension and compression shear are presented in Table 3.

Table 2

Geological structure of the sites

Engineering geological borehole	Depth, m	Capacity, m	Short description of soils
1	0.0-1.7	1.7	Plastic sandy loam
	1.7-5.4	3.7	Brown-gray dolomitized limestone
	5.4-9.1	3.7	Crushed stone soil (limestone, up to 10 cm)
	9.1-9.5	0.4	Brown-gray dolomitized silicified limestone
	9.5-10.9	1.4	Crushed stone soil (gray-brown rusty cavernous limestone, pieces up to 20 cm)
	10.9-14.0	3.1	Gray-brown rusty cavernous limestone (silicon dioxide)
2	0.0-4.9	4.9	Heavy red-brown, soft-plastic loam (from 0.7 m up to 0.7 m tight-plastic), rusty
	4.9-8.0	3.1	Brown dense water-saturated sand, heterogeneous, inclusions of fine gravel up to 10 %
	8.0-11.3	3.30	Heavy red-brown tight plastic loam
	11.3-14.0	2.7	Light brown tight plastic loam (to soft-plastic)
	14.0-15.0	1.0	Red-brown rusty cavernous limestone
3	0.0-1.0	1.0	Brown plastic sandy loam with crushed stone up to 25 % (sedimentary rocks)
	1.0-1.5	0.5	Crushed stone soil (up to 10 cm), sedimentary rocks – sandstone
	1.5-4.0	2.5	Gray-brown fine-grained, weathered, weakly cemented rusty sandstone, RQD = 40 %
	4.0-5.0	1.0	Crushed stone soil (up to 20 cm) (sedimentary rocks – sandstone)

Journal of Mining Institute. *2024. Vol. 266. P. 231-245*

End of Table 2

Engineering geological borehole	Depth, m	Capacity, m	Short description of soils
3	5.0-13.5	8.5	Gray-brown fine-grained sandstone, RQD = 40 %, from 10 m brown spots of iron formation up to 2 cm appeared, from 11 m caverns up to 0.5 cm occurred
	13.5-15.0	1.5	Crushed stone soil (sedimentary rock – sandstone) silicified up to 20 cm
4	0.0-1.2	1.2	Heavy red-brown tight-plastic loam, rusty (inclusions of sedimentary rocks – 30 %) with frequent interlayers of brown sand up to 0.5-1 cm thick
	1.2-4.3	3.1	Crushed stone soil (gray limestone up to 10 cm)
	4.3-7.9	3.6	Soft red-brown loam with frequent interlayers of red-brown sand up to 3 cm thick, inclusions of fine crushed sedimentary rocks up to 15 %, frozen ground
	7.9-9.9	2.0	Crushed stone soil (light gray limestone up to 20 cm), light gray loam aggregate up to 20 %
	9.9-15.0	5.1	Brown-gray limestone, rusty dolomitized, RQD = 80 %, thin interlayers of quartzite

Table 3

Test results of rock samples in uniaxial compression, tension and compression shearing

Engineering geological borehole	Soil type	Sampling depth, m	Density ρ, g/cm^3	σ_{compr}, MPa	σ_{tens}, Mpa	τ_{shear}, MPa
1	Limestone	2.5-2.65	–	–	–	51.40
	–"–	3.5-3.7	2.49	105.5	11.65	–
	–"–	4.3-4.8	2.66	107.5	11.88	–
	–"–	5.0-5.15	2.28	66.3	6.5	–
	–"–	9.3-9.4	–	–	–	67.65
	–"–	11.3-11.65	2.15	19.1	1	–
	–"–	12.5-12.7	2.38	59.9	3	–
	–"–	12.7-13.0	2.6	73.8	3.55	46.66
	–"–	13.0-13.25	2.36	46.6	2.3	–
2	Limestone	14.6-14.75	2.12	30.4	1.5	–
3	Sandstone	1.65-1.8	2.58	14.3	0.57	–
	–"–	1.8-2.0	2.58	19.3	0.77	–
	–"–	3.0-3.3	2.62	28.7	2.5	–
	–"–	3.5-3.8	2.25	28.7	–	6.22
	–"–	5.1-5.3	2.57	40.4	1.62	–
	–"–	5.5-5.7	2.54	36.6	1.46	–
	–"–	5.7-6.0	2.61	32.5	1.33	–
	–"–	7.0-7.3	2.32	47.9	4.57	35.67
	–"–	9.0-9.3	2.58	14.3	0.57	–
	–"–	9.6-9.7	2.61	14.6	0.6	–
	–"–	10.0-10.2	2.55	37.4	3.4	–
	–"–	10.2-10.4	2.35	37.4	–	21.93
	–"–	10.4-10.7	2.53	12.8	0.53	–
	–"–	11.5-11.7	2.58	32.5	2.1	–
	–"–	12.0-12.5	2.56	30.7	1.25	–
	–"–	13.1-13.25	–	–	4.41	57.12

End of Table 3

Engineering geological borehole	Soil type	Sampling depth, m	Density ρ, g/cm^3	σ_{compr}, MPa	σ_{tens}, Mpa	τ_{shear}, MPa
4	Limestone	12.0-12.15	–	–	25.02	206.2
	–"–	12.5-12.7	2.59	94	3.9	–
	–"–	12.7-13.0	–	–	–	61.55
	–"–	13.0-13.2	2.62	95	4.2	–
	–"–	13.3-13.7	2.55	111.7	7.67	91.53
	–"–	14.65-15.0	2.63	69	2.8	–

Before starting, the engineer-designer of drilling and blasting operation in the BlastMaker program complex set the location of work sites (blocks) on the field plan and specified the number of boreholes for each block (Table 4).

Table 4

Correspondence of blocks and production wells to engineering geological boreholes

Engineering geological borehole	The block number	Borehole number
1	5-550-1	BLOCK-5-550-1-1
		BLOCK -5-550-1-2
		BLOCK -5-550-1-3
2	5-550-2	BLOCK -5-550-2-1
		BLOCK -5-550-2-2
		BLOCK -5-550-2-3
		BLOCK -5-550-2-4
3	5-550-3	BLOCK -5-550-3-1
		BLOCK -5-550-3-2
		BLOCK -5-550-3-3
4	5-550-4	BLOCK -5-550-4-1
		BLOCK -5-550-4-2
		BLOCK -5-550-4-3

Figures 1, 2 present the drilling parameters recorded by the onboard controller and the distribution graph of specific energy consumption by the roller cone method. Figure 3, *a* shows the distribution of drilling energy consumption values, produced by the BlastMaker program, depending on the rock strength coefficient, received from the results of testing rock samples. The rock hardness coefficient was estimated by the formula (3) via the uniaxial compression strength of the sample. This distribution shows that a part of values is incorrect. The reason is the fact that drilling with a roller cone machine was performed on disturbed rocks. This phenomenon is caused by the extreme variability of the Kuranakh ore field massif structure. Thus, the sampling was based on the results of observations, in particular, on drilling sludge. The acquired data set was processed by cluster analysis method with the ANN classifier. Cluster analysis provides a smaller amount of data for modeling [37], and the use of neural networks helps to "evolve" the mathematical model as new data become available [38, 39]. Figure 3, *b* demonstrates the distribution of the filtered values and shows the correlation between the specific energy consumption of drilling and the hardness coefficient of the selected rocks.

The graph (Fig.3, *b*) shows that the values of specific energy consumption of drilling by the roller cone method and rock hardness coefficient are approximated by a logarithmic function with a validity coefficient of 0.84:

$$E = 14.566 \ln f + 9.3502,$$

where E – specific drilling energy consumption in BlastMaker, MJ/m^3; f – rock hardness coefficient.

Then, the hardness coefficient can be calculated as:

$$f = e^{\frac{E-9.3502}{14.566}}.$$

Journal of Mining Institute. 2024. Vol. 266. P. 231-245

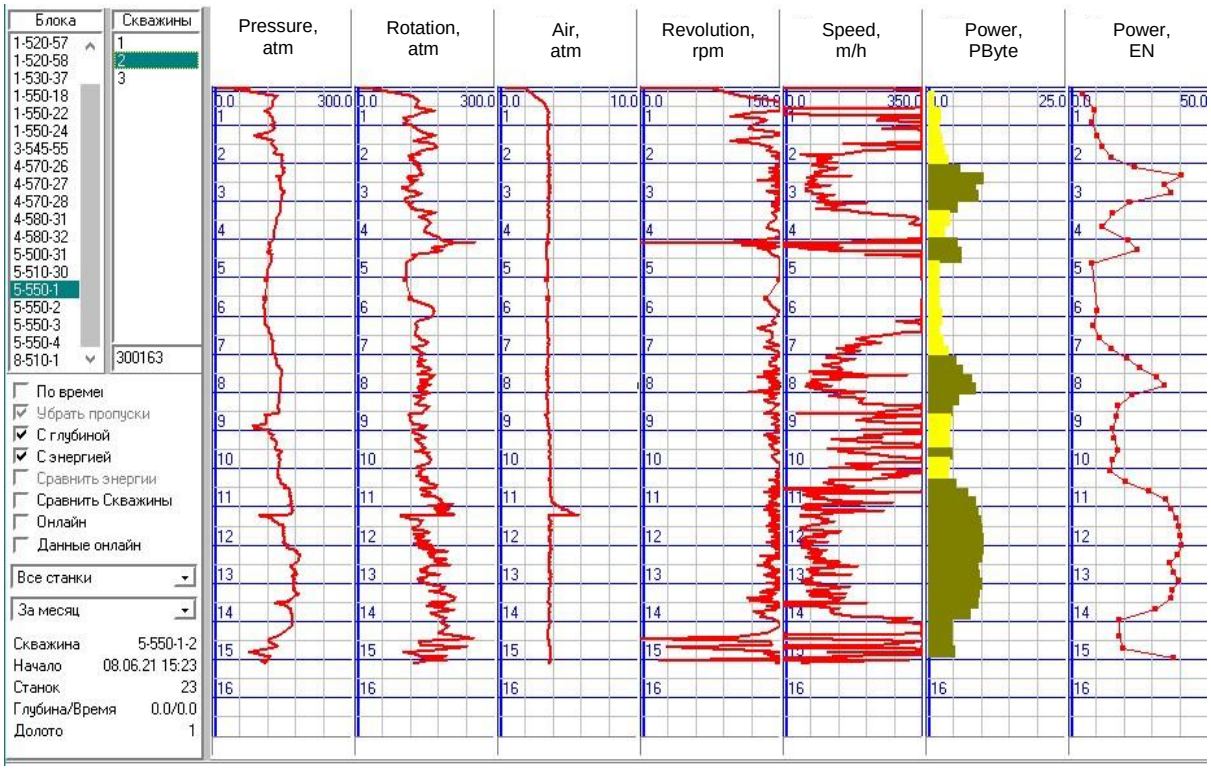

Fig.1. Blast drilling parameters provided by BlastMaker software

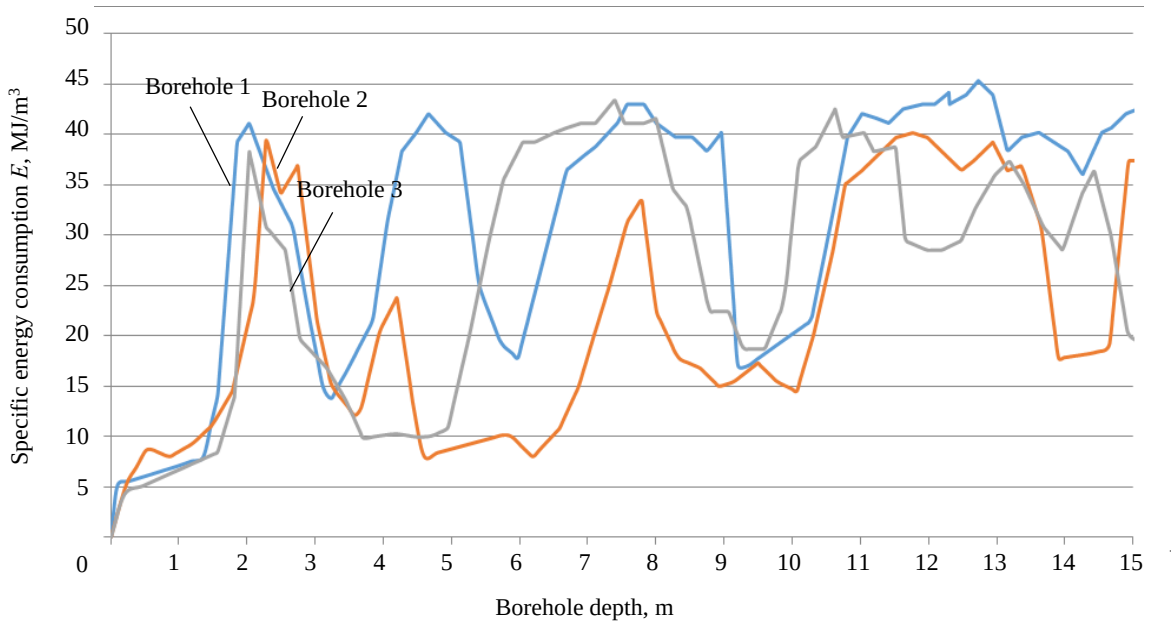

Fig.2. Dependence of specific energy consumption of roller cone drilling on block 5-550-1 on well depth

Data analysis revealed the following:

• rock density does not affect the parameters of roller cone drilling;

• the tension strength of the sample has an influence on the axial pressure values;

• the number of rock sample compressive shear strength values is insufficient to reveal statistically significant correlation dependencies.

Therefore, the specific energy consumption of drilling was taken as the main parameter of drilling boreholes using the roller cone method.

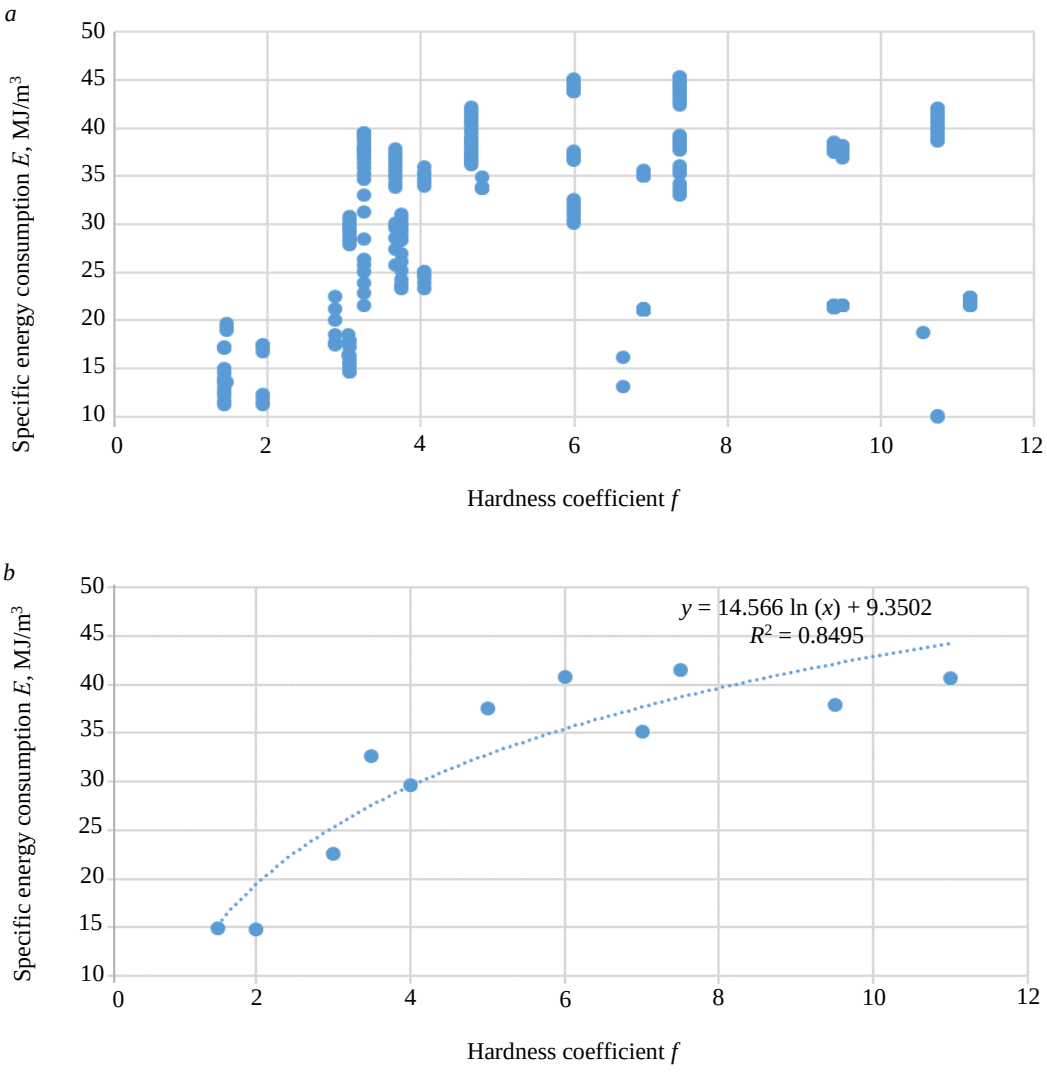

Fig.3. Distribution of drilling energy consumption values in correlation with the values of rock hardness coefficient recorded by BlastMaker (*a*) and after data filtration (*b*)

We tested the results on technological blocks consisting of clay rocks and limestone, according to geological exploration data. Initially, the explosive block was drilled by the roller cone drilling machines with the "Kobus" on-board controller. Then, the obtained data on drilling energy consumption were used to select the required charge design and calculate the mass of explosives in each hole. During block preparation for explosion one-half was charged using the technology approved at the enterprise.

Drilling and blasting parameters at the experimental blocks: borehole grid $a \times b$ – 6×7, 6×6, 6×6 m; specific consumption q – 0.58, 0.57, 0.69 kg/m^3; stemming type – sand-clay mixture; initiation system – non-electric ("Iskra").

The second part was charged in accordance with the drilling data. That is, in the boreholes where the coefficient of rock hardness was more than two, solid charges of granulite RP were made; in case of a lower hardness coefficient there were deck charges. The same construction was also implemented in the boreholes, where hardness coefficient of rocks was less than two. A sand-clay mixture was used as stemming, that kept the gaseous explosion products inside the borehole sufficiently for a long time to fully transfer the explosion energy to the walls of the blast hole [40]. At the same time, the borehole grid remained unchanged.

Journal of Mining Institute. 2024. Vol. 266. P. 231-245

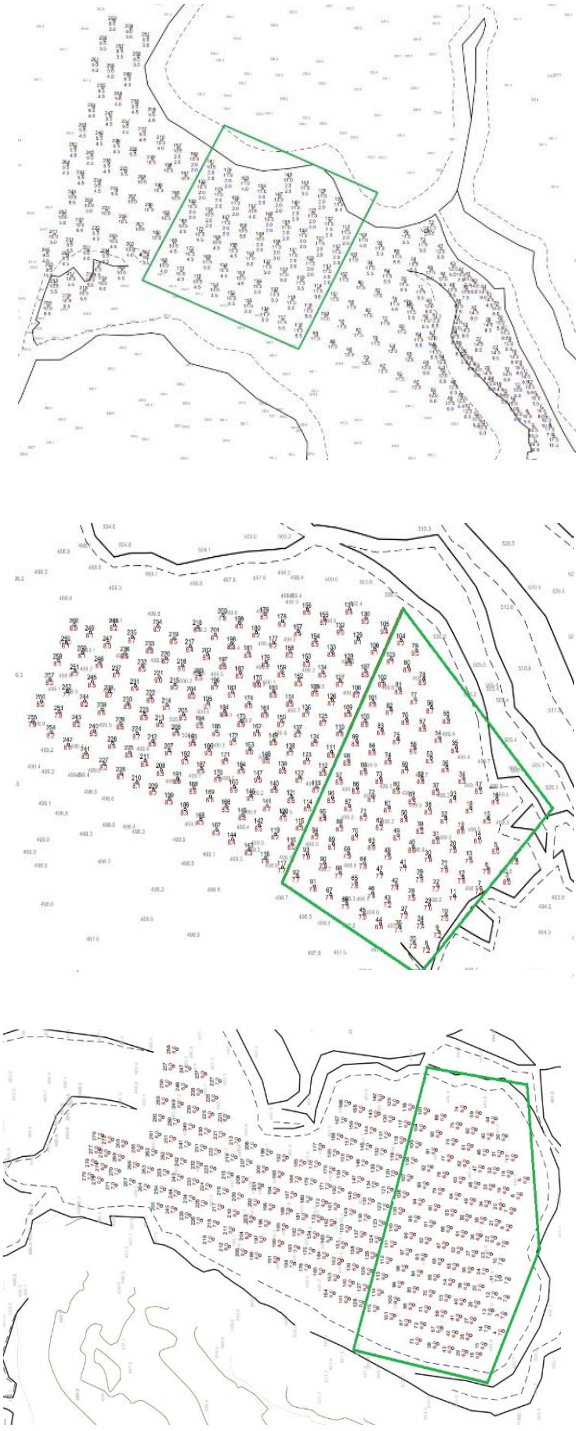

Fig.4. Location plans of drilling and blasting wells on the experimental blocks (green contour are areas where explosive charging was done according to the specific energy consumption of drilling)

Figure 4 shows the plans of the experimental blocks with the areas where charging was done with the proposed method. The initiation means at the sections with standard parameters of blasting and drilling and at the experimental sections were linked into a single explosive system.

It was determined from the site examination that in the standard block sections with concentrated charges the explosion caused ejection funnels, thus indicating an excessive mass of explosives, and on the experimental sites the number and size of the funnels were smaller (Fig.5). Excavation performance at the experimental sections of blocks, according to the excavation data, was 15 to 20 % higher than at the standard ones. That indicates the relevance of the proposed approach to determine blasting and drilling parameters based on the results of specific drilling energy consumption measurement.

Results and discussion. It is essential to emphasize that the correlation between the physical and mechanical properties of rocks and drilling parameters is the only reliable way to identify rocks, since each parameter is determined directly on the samples and on the rock mass. It is worth to know that the obtained correlation dependence is valid only for the Kuranakh ore field rocks. However, the proposed method is applicable to all deposits. The application of this technique is reasonable at those deposits where physical and mechanical properties of rocks are sharply different.

The next step is to estimate the reference specific energy consumption for rock crushing by the explosion of different strength of rocks that compose the massif of the Kuranakh ore field. It will allow to achieve the optimization of energy costs and calculation of the charge mass necessary for crushing of the rock massif in this area.

Conclusion. Based on the study of national and international experience, it was found that the quality of the explosion depends on the specific energy consumption for rock crushing by explosion, which, in turn, depends on the physical and mechanical properties of rocks. Despite the charge energy distribution, achieving the necessary volumetric concentration of energy in different parts of the borehole, these methods are useful only in the mining enterprises where the massif structure is known with accurate. These include, for example, deposits with unchanging layering, and that can be identified by layer exposures on the scarp slope. At the deposits with complex

Fig.5. Results of drilling and blasting on the experimental block (yellow color indicates funnels with standard parameters, green – with experimental ones)

geological structure, where the massif structure varies within small areas, it is not reliable to determine the structure on exposed surfaces. As a result, the calculation of drilling and blasting parameters, as a rule, is based on the hardest rocks, resulting in overconsumption of explosives and suboptimal crushing quality.

These properties are obtained at each blasted block by testing rock samples, which is a very labor-intensive and time-consuming job. However, it is known that drilling parameters – drilling speed, drilling energy, axial pressure exerted on the bottom hole, rotator power – respond to changes in these properties during rock fracture. We propose the algorithm for the task of rational energy distribution over the borehole depth depending on rock physical-mechanical properties. The correlation between the drilling parameters and these properties will make it possible to identify the block rocks. This will provide data on rock physical and mechanical properties, but it will not make it possible to determine the required amount of explosives both at the borehole depth and over the area. To achieve the task, it is essential to estimate the reference specific energy consumption for each rock type that forms the rock massif. As a result, the rock classification based on the values of drilling parameters and the specific energy consumption for crushing of these rocks makes it possible to rationally distribute the explosion energy both at the depth of the borehole and over the block area. Further, it will provide an excellent opportunity to obtain the required quality of crushing.

REFERENCES

1. Yastrebova K.N., Moldovan D.V., Chernobay V.I. Solving the Issue of Ventilating Atmosphere of Opencast Mining by Resloping Bench Face. *International Journal of Advanced Science and Technology*. 2020. Vol. 29. N 1, p. 1-6.

2. Fomin S.I., Govorov A.S. Validation of the chosen cutoff grade value in open pit mine design. *Mining Informational and Analytical Bulletin.* 2023. N 12, p. 169-182 (in Russian). DOI: 10.25018/0236_1493_2023_12_0_169

3. Kanchibotla S.S., Vizcarra T.G., Musunuri S.A.R. et al. Mine to mill optimisation at Paddington gold operations. The 6th International conference on Semi-Autogenous and High Pressure Grinding Technology, 20-24 September 2015, Vancouver, Canada. Canadian Institute of Mining and Metallurgy, 2015, p. 13.

4. Saadoun A., Fredj M., Boukarm R., Hadji R. Fragmentation analysis using digital image processing and empirical model (KuzRam): a comparative study. *Journal of Mining Institute.* 2022. Vol. 257, p. 822-832. DOI: 10.31897/PMI.2022.84

5. Bhatawdekar R.M., Edy M.T., Danial J.A. Building Information Model for Drilling and Blasting for Tropically Weathered Rock. *Journal of Mines, Metals and Fuels*. 2019. Vol. 67. Iss. 11, p. 494-500.

6. Dolzhikov V.V., Ryadinsky D.E., Yakovlev A.A. Influence of deceleration intervals on the amplitudes of stress waves during the explosion of a system of borehole charges. *Mining Informational and Analytical Bulletin.* 2022. N 6-2, p. 18-32 (in Russian). DOI: 10.25018/0236_1493_2022_62_0_18

7. Vinogradov Y.I., Khokhlov S.V. The drilling-and-blasting parameters determination method for specified grain-size composition of the blasted rock mass. *Mining Informational and Analytical Bulletin.* 2015. N S1-4, p. 20-29 (in Russian).

8. Marinin M.A., Rakhmanov R.A., Dolzhikov V.V., Sushkova V.I. Study of the effect of blasted rock mass parameters on the performance of excavator-automobile complex. *Mining Informational and Analytical Bulletin.* 2023. N 9-1, p. 35-48 (in Russian). DOI: 10.25018/0236_1493_2023_91_0_35

9. Abbaspour H., Drebenstedt C., Badroddin M., Maghaminik A. Optimized design of drilling and blasting operations in open pit mines under technical and economic uncertainties by system dynamic modelling. *International Journal of Mining Science and Technology*. 2018. Vol. 28. Iss. 6, p. 839-848. DOI: 10.1016/j.ijmst.2018.06.009

10. Zhukovskiy Y.L., Korolev N.A., Malkova Y.M. Monitoring of grinding condition in drum mills based on resulting shaft-torque. *Journal of Mining Institute.* 2022. Vol. 256, p. 686-700. DOI: 10.31897/PMI.2022.91

11. Rasskazov M.I., Potapchuk M.I., Tsoi D.I. et al. Study of mining and geological features and definition of physical and mechanical properties of rocks of Delken gold deposits. *Problems of Subsoil Use.* 2020. N 2 (25), p. 116-126 (in Russian). DOI: 10.25635/2313-1586.2020.02.116

12. Zharikov S.N. Correlation of specific energy characteristics of roller drilling and rock mass explosive destruction processes: Candidate's thesis, Ekaterinburg: The Institute of Mining UrO RAN, 2011, p. 25 (in Russian).

13. Kryukov G.M. Model of explosive rock loosening at pits. Boulder frequency. Average size of rock fragments in the break-down. Moscow: Izd-vo Moskovskogo gosudarstvennogo gornogo universiteta, 2005, p. 28 (preprint) (in Russian).

14. Langefors U., Kihlström B. The modern technique of rock blasting. Moscow: Nedra, 1968, p. 298.

15. Salmi E.F., Sellers E.J. A review of the methods to incorporate the geological and geotechnical characteristics of rock masses in blastability assessments for selective blast design. *Engineering Geology*. 2021. Vol. 281. N 105970. DOI: 10.1016/j.enggeo.2020.105970

16. Simioni S., Sidler R., Dual J., Schweizer J. Field measurements of snowpack response to explosive loading. *Cold Regions Science and Technology*. 2015. Vol. 120, p. 179-190. DOI: 10.1016/j.coldregions.2015.06.011

17. Zou D. Explosives. Theory and Technology of Rock Excavation for Civil Engineering. Singapore: Springer, 2017, p. 105-170. DOI: 10.1007/978-981-10-1989-0_3

18. Baron V.L., Kantor V.Kh. Blasting techniques and technology in the USA. Moscow: Nedra, 1989, p. 376 (in Russian).

19. Rzhevskii V.V. Physical and technical parameters of rocks. Moscow: Nauka, 1975, p. 212 (in Russian).

20. Ugolnikov V.K., Simonov P.S. Identifying conversion factors in the calculation of equivalent crushing charges. *Vestnik Magnitogorskogo gosudarstvennogo tekhnicheskogo universiteta im. G.I.Nosova*. 2007. N 4 (20), p. 14-17 (in Russian).

21. Zharikov S.N. The energy intensity of excavation of rock mass and the relationship of the extract with similar processes of mining operations. *Journal of Fundamental and Applied Mining Sciences.* 2017. Vol. 4. N 1, p. 179-186 (in Russian).

22. Khomenko O.E., Kononenko M.N., Lyashenko V.I. Rationale for Technologies and Facilities for Carrying out Horizontal Mine Workings Using Emulsion Explosives. *Vestnik Magnitogorskogo gosudarstvennogo tekhnicheskogo universiteta im. G.I.Nosova.* 2021. Vol. 19. N 3, p. 5-15 (in Russian). DOI: 10.18503/1995-2732-2021-19-3-5-15

23. Avdeev A.N., Sosnovskaia E.L., Bolotnev A.Y. Strength coefficient estimation by indirect methods. *Izvestiya vysshikh uchebnykh zavedenii. Gornyi zhurnal.* 2021. N 3, p. 28-35 (in Russian). DOI: 10.21440/0536-1028-2021-3-28-35

24. Neobutov G.P. Drillability estimation of the Nezhdaninskoe gold deposit in Yakutia. *Mezhdunarodnyi nauchno-issledovatelskii zhurnal*. 2019. N 7 (85), p. 38-43. DOI: 10.23670/IRJ.2019.85.7.007

25. Gospodarikov A.P., Trofimov A.V., Kirkin A.P. Evaluation of deformation characteristics of brittle rocks beyond the limit of strength in the mode of uniaxial servohydraulic loading. *Journal of Mining Institute.* 2022. Vol. 256, p. 539-548. DOI: 10.31897/PMI.2022.87

26. Kuznetsov N.N., Pak A.K. Influence of the hard rock specimens' size ratio on the results of their strength determination under uniaxial compression. *Vestnik of MSTU.* 2014. Vol. 17. N 2, p. 246-253 (in Russian).

27. Korshunov V.A., Pavlovich A.A., Bazhukov A.A. Evaluation of the shear strength of rocks by cracks based on the results of testing samples with spherical indentors. *Journal of Mining Institute.* 2023. Vol. 262, p. 606-618. DOI: 10.31897/PMI.2023.16

28. Navarro J., Seidl T., Sanchidrián J.A. et al. Blastability and Ore Grade Assessment from Drill Monitoring for Open Pit Applications. *Rock Mechanics and Rock Engineering*. 2021. Vol. 54. Iss. 6, p. 3209-3228. DOI: 10.1007/s00603-020-02354-2

29. Navarro J., Schunnesson H., Ghosh R. et al. Application of drill-monitoring for chargeability assessment in sublevel caving. *International Journal of Rock Mechanics and Mining Sciences.* 2019. Vol. 119, p. 180-192. DOI: 10.1016/j.ijrmms.2019.03.026

30. Rai P., Schunnesson H., Lindqvist P.-A., Kumar U. Measurement-while-drilling technique and its scope in design and prediction of rock blasting. *International Journal of Mining Science and Technology*. 2016. Vol. 26. Iss. 4, p. 711-719. DOI: 10.1016/j.ijmst.2016.05.025

31. Khorzoughi M.B., Hall R., Apel D. Rock fracture density characterization using measurement while drilling (MWD) techniques. *International Journal of Mining Science and Technology*. 2018. Vol. 28. Iss. 6, p. 859-864. DOI: 10.1016/j.ijmst.2018.01.001

32. Teale R. The concept of specific energy in rock drilling. *International Journal of Rock Mechanics and Mining Sciences & Geomechanics Abstracts*. 1965. Vol. 2. Iss. 1, p. 57-73. DOI: 10.1016/0148-9062(65)90022-7

33. Schunnesson H. RQD predictions based on drill performance parameters. *Tunnelling and Underground Space Technology*. 1996. Vol. 11. Iss. 3, p. 345-351. DOI: 10.1016/0886-7798(96)00024-7

34. van Eldert J., Schunnesson H., Johansson D. et al. Application of Measurement While Drilling Technology to Predict Rock Mass Quality and Rock Support for Tunnelling. *Rock Mechanics and Rock Engineering*. 2020. Vol. 53. Iss. 3, p. 1349-1358. DOI: 10.1007/s00603-019-01979-2

35. Dolgiy I.E., Nikolaev N.I. Resistance of rocks to crushing during well drilling. *Journal of Mining Institute.* 2016. Vol. 221, p. 655-660. DOI: 10.18454/PMI.2016.5.655

36. Tangaev I.A. Energy consumption of extraction and refining processes. Moscow: Nedra, 1986, p. 231 (in Russian).

37. Ignatiev S.A., Sudarikov A.E., Imashev A.Z. Modern Mathematical Forecast Methods of Maintenance and Support Conditions for Mining Tunnels. *Journal of Mining Institute.* 2019. Vol. 238, p. 371-375. DOI: 10.31897/PMI.2019.4.371

38. Koteleva N.I., Valnev V.V., Korolev N.. Augmented reality as a means of metallurgical equipment servicing. *Tsvetnye metally*. 2023. N 4, p. 14-23 (in Russian). DOI: 10.17580/tsm.2023.04.02

39. Klyuchnikov N., Zaytsev A., Gruzdev A. et al. Data-driven model for the identification of the rock type at a drilling bit. *Journal of Petroleum Science and Engineering*. 2019. Vol. 178, p. 506-516. DOI: 10.1016/j.petrol.2019.03.041

40. Moldovan D.V., Chernobay V.I., Sokolov S.T., Bazhenova A.V. Design concepts for explosion products locking in chamber. *Mining Informational and Analytical Bulletin.* 2022. N 6-2, p. 5-17 (in Russian). DOI: 10.25018/0236_1493_2022_62_0_5

Authors: **Yurii I. Vinogradov,** *Candidate of Engineering Sciences, Associate Professor, Vinogradov_YuI@pers.spmi.ru, https://orcid.org/0000-0001-9468-2214* (*Empress Catherine II Saint Petersburg Mining University, Saint Petersburg, Russia*), **Sergei V. Khokhlov,** *Candidate of Engineering Sciences, Associate Professor, https://orcid.org/0000-0003-1040-8328* (*Empress Catherine II Saint Petersburg Mining University, Saint Petersburg, Russia*), **Ramil R. Zigangirov,** *Postgraduate Student, https://orcid.org/0000-0003-4876-3456* (*Empress Catherine II Saint Petersburg Mining University, Saint Petersburg, Russia*), **Aleksei A. Miftakhov,** *Chief Operating Officer, https://orcid.org/0009-0004-4287-2496* (*AO "Polyus Aldan", set. Nizhnii Kuranakh, Republic of Sakha* (*Yakutiya*), *Russia*), **Yurii I. Suvorov,** *Head of Kuranakh mine, https://orcid.org/0009-0008-1256-4387* (*AO "Polyus Aldan", set. Nizhnii Kuranakh, Republic of Sakha* (*Yakutiya*), *Russia*).

The authors declare no conflict of interests.

ISSN 2411-3336; e-ISSN 2541-9404

JOURNAL OF MINING INSTITUTE

Zapiski Gornogo instituta

Journal homepage: pmi.spmi.ru

Review article

Directions in the technological development of aluminium pots

Evgenii S. Gorlanov[1]✉, **Leopold I. Leontev**[2]

[1] *Empress Catherine II Saint Petersburg Mining University, Saint Petersburg, Russia*

[2] *Russian Academy of Sciences, Moscow, Russia*

How to cite this article: Gorlanov E.S., Leontev L.I. Directions in the technological development of aluminium pots. Journal of Mining Institute. 2024. Vol. 266, p. 246-259.

Abstract. Directions for the technical and technological development of aluminium industry, existing and promising projects to reduce the energy consumption and the environmental impact are analyzed. The active participation of the state in the organization of financial instruments for the ecological reconstruction of obsolete production facilities is discussed. In spite of the fact that the technology of aluminium pots is developed towards the increase of a single capacity, but with limited potential of reducing energy consumption and greenhouse gases emission, the possibilities for the increase of specific output are practically non-existent. Therefore, such projects like pots, equipped with inert anodes and drained cathodes arise and are under development, the successful completion of which is unlikely after multi-year researches and pilot tests. To continue the works related to inert anodes the decisive answer about the industrial safety of local sources of the massive oxygen emissions to atmosphere is required from competent entities. The drained cathode project, after discussing the existing problems, seems unfeasible. As opposed to the existing technology the development of the pots with vertical electrodes offers great opportunities to the designs of inert anodes and drained cathodes. Positive results of using shaped electrodes, homogenizing their surface and developing the methods for the synthesis of composite cathodes directly during the electrolytic process were obtained in laboratory conditions. It is expected that the combination of these trends and the successive dimensional scaling shall allow using the vertical electrodes at the next level for the fold increase of specific pot capacity and for the decrease of energy consumption and greenhouse gas emissions.

***Keywords*:** aluminium pot; best available technologies; energy consumption; inert anode; drained cathode; wettability; vertical electrode; specific capacity

Received: 20.07.2023 ***Accepted: 25.10.2023*** ***Online: 11.12.2023*** ***Published: 25.04.2024***

Introduction. To develop the mineral-raw material and fuel-and-energy complexes it is necessary to develop new technical solutions and technologies for the production of science-intensive commercial output [1-3]. It is obvious that the selection of industrial technologies and directions for the modernization shall be guided by best parameters and conceivable mechanisms for their implementation [4-7]. In addition, for the purpose of global energy transition and in pursuit of using carbonless energy sources the need to adapt the production to progressively more stringent environmental restrictions increases [8-10]. In that event the state and industrial companies propose to use the conception of best available technologies that is world-recognized and known from 1960-s [11].

In Russia the elaboration of approaches to the estimation of production efficiency related to resources started up by enacting the special Federal Law N 219-FZ dated 21.07.2014.[1] Its provisions introduced the concept of "best available technology" (BAT) to the regulatory environment for the first time and they established criteria for its achievement. Powers of federal agencies of executive authority, order and rules for BAT definition were evidenced in the Government decree N 1458 of

[1] Federal law "On Amendments to the Federal Law on Environmental Protection and Certain Legislative Acts of the Russian Federation" dated 21.07.2014 N 219-FZ. URL: https://www.consultant.ru/document/cons_doc_LAW_165823/ (accessed 31.10.2023).

December 23, 2014.[2] According to this decree the exercise of powers within federal budget allocations and its supervision were assigned to the RF Ministry for Industry and Trade and to the Federal Technical Regulation and Metrology Agency. This same decree defines participants of BAT development, working conditions for the Bureau for best available technologies (BAT Bureau – Federal State Independent Institution "Research Institute Center of Environmental Industrial Policy"[3]) and working groups to collect, analyze and generate data for information and technical reference books on best available technologies. The rules underlay conditions for the actualization of these reference books in order to renew obsolete data and to introduce new ones. In accordance with milestone schedule, approved by RF Government edict N 2178-p dated 31.10.2014,[4] the process of BAT reference-book development started up.

Under this work, the first information and technical reference book for aluminium industry ITS NDT 11-2016 "Aluminium Production" was issued in 2016. Its actualization took place every three years – in 2019 and in 2022. The conception for the definition of normative and technical documentation and rules for the compilation of reference books, adopted by the government, uses the evolutionary development of technical facilities, technologies and materials, i.e. the reconstruction of basic production and environmental protection technologies. From the other side, to provide the development of up-to-date technologies of electrolytic aluminium production the scientific centers of companies work hard on new projects. At the stage of new tendencies planning the accent is made on the reduction of energy consumption and environmental impact, on the increase of aluminium pots capacity and service life. The implementation of the projects, in particular, strategic ones, requires and spends considerable financial resources. Therefore, at the stage of projects planning and during their realization it is very important to be aware of the risks of possible unsatisfactory results and to correct them on time.

In 2014 the mechanism of ecological and technological modernization of obsolete production facilities was started up in Russia. The internal projects of industrial companies gather speed. The time period is rather long in order to discuss and analyze the ecological reconstruction, organized by state entities, and promising trends of modernization, which is initiated and implemented by aluminium producers. Even at this stage it is possible to define perspectives of aluminium industry development and perspectives of existing and promising projects for the decrease of energy consumption and environmental impact by aluminium pots.

The purpose of analytical overview presented is to define most promising technology for the production of aluminium by electrolytic method.

Ecological reconstruction. BAT Information and technical reference books that contain the description of available technologies, production efficiency indices and maximum admissible levels of harmful emissions, are prepared in BAT Bureaus with participation of industry experts, and these reference books are the platform for the decision making on the modernization of obsolete technologies. Reference books of 2019[5] and 2022[6] are focused on ecological and environmental protection parameters. As to technical and technological parameters, sections 4 and 5 related to best available technologies, fix parameters of raw material consumption and current efficiency only. Such important parameter like specific consumption of electric energy for the aluminium production is not provided

[2] RF Government edict dated 23.12.2014 N 1458 "On the procedure for determining technology as the best available technology, as well as the development, updating and publication of information and technical reference books on the best available technologies". URL: https://www.consultant.ru/document/cons_doc_LAW_172796/ (accessed 31.10.2023).

[3] Federal State Autonomous Institution "Scientific Research Institute "Center for Environmental Industrial Policy". From January 1, 2017 the Government of the Russian Federation has assigned the functions of the Bureau of the Best Available Technologies to the "Scientific Research Institute "Center of Ecological Industrial Policy".

[4] RF Government edict dated 31.10.2014 N 2178-p "On approval of a phased schedule for the creation of industry reference books of the best available technologies in 2015-2017". URL: https://www.consultant.ru/document/cons_doc_LAW_170718/ (accessed 31.10.2023).

[5] Aluminium production: information and technical reference book on best available technologies. ITS NDT 11-2019. Moscow: NDT Bureau, 2019, p. 238.

[6] Aluminium production: information and technical reference book on best available technologies. ITS NDT 11-2022. Moscow: NDT Bureau, 2022, p. 263.

in BAT normative and technical documentation. Upon the results of the consideration of economic aspects of the best available technologies implementation and levels of capital expenses on the modernization, the reference books state "…The conversion of Soderberg technology into the technology of aluminium production using pre-bake anodes shall require at least $ 2-4 thousand of capital investments per 1 ton of aluminium. Taking into account the current price level, production profitability and cost of borrowing, such project shall not be cost-effective". However, in spring of 2021 UC RUSAL announces the modernization of four Siberian Soderberg smelters. It is said that the project is of environmental protection nature – half of the pots, operating according to the old technology in Krasnoyarsk, Bratsk, Irkutsk, and Novokuznetsk, shall be substituted by most modern ones – PA-550[7]. Under this project RUSAL modernizes pots that produce more than 1.4 Mt of aluminium (35 % from all capacities). As the result, the production volume shall not change but the emission of fluorides from modernized pots shall drop by 73 % and the emission of benzopyrene shall decrease by 100 %. At the same time in April 2021, the company En+ Group (RUSAL) announced the production of aluminium using the inert anode technology and declared the target to achieve the zero level of greenhouse gas emissions by the year of 2050, and by 2030 to reduce reducing them by 35 %[8].

In 2021 in support of information and technical reference books the decree of RF government approved *criteria for RF sustainable development projects*, including those for aluminium industry[9]. First of all, it highlights the need to correlate parameters of resource and energy efficiency with parameters, fixed in the reference book of second generation ITS 11-2019 "Aluminium production". Criteria stipulate current technical and technological parameters of primary aluminium production. It is proposed to use ecological parameters, already achieved:

• direct emissions of greenhouse gases – not more than 1.514 t CO_2-equ/t aluminium (Scope 1);

• total emissions from electrolytic reduction process and from electric energy production – 3 t CO_2-equ/t Al (current emissions – 2.2 t CO_2-equ/t Al for ALLOW brand[10], Scope 2).

Then, in March 2023 the RF Government decree made *alterations to the criteria for RF sustainable development projects*[11]. In the new edition the criterion of the necessary correlation of resource and energy efficiency parameters with parameters, fixed in reference books related to best available technologies, is not already mentioned. So, the need in achievement of best indices for energy saving and for increase of the efficiency of resources use, which provide ecological parameters of the production, is excluded from top targets of the projects. In addition, the criterion of compliance "… with lower level of indicative parameter (IP2) of specific greenhouse gas emissions" is established for the processes of electrolytic primary aluminium production in accordance with information and technical reference book on best available technologies "Aluminium Production (ITS 11-2022)". However, in accordance with this reference book, greenhouse gases are not available in the list of pollutant matters, subjected to the state regulation (RF Government edict N 1316-p dated 08.07.2015). Therefore, we have to acknowledge that to modernize existing electrolytic reduction technologies it is proposed to use current parameters of direct greenhouse gas emissions within 1.5-3.2 t CO_2-equ/t Al (Scope 1). As to the parameter of total emissions from reduction facilities and from energy production facilities (Scope 2), it is missing in criteria for sustainable development projects. Consequently, the approval of alterations resulted in that the criteria for sustainable development projects are not such; it means the step back has been made relative to the first 2021 edition of criteria.

[7] RUSAL modernizes its smelter in Siberia. URL: https://www.interfax.ru/russia/761125 (accessed 31.10.2023).

[8] En+ Group reports and results: 2020 annual report. URL: https://enplusgroup.com/ru/investors/results-and-disclosure/annual-reports/ (accessed 31.10.2023).

[9] RF Government edict dated 21.09.2021 N 1587 "On approval of criteria for sustainable (including green) development projects in the Russian Federation and requirements for the verification system for sustainable (including green) development projects in the Russian Federation". URL: http://publication.pravo.gov.ru/Document/View/0001202109240043 (accessed 31.10.2023).

[10] Sustainable development report: RUSAL, 2021. URL: https://rusal.ru/sustainability/report/ (accessed 31.10.2023).

[11] RF Government edict dated 11.03.2023 N 373 "On Amendments to the Decree of the Government of the Russian Federation dated September 21, 2021. N 1587". URL: http://publication.pravo.gov.ru/Document/View/0001202303140005 (accessed 31.10.2023).

Additional criteria for production facilities under modernization and for newly built ones that are listed in the documents of RF government belong entirely to the ecological criteria. Enterprises have to meet one additional criterion at least; for example, promising technologies:

• aluminium production using inert anodes;

• use of the heat of exhaust gases from pyro-metallurgical processes for the production of thermal and electric energy in waste-heat boilers;

• technology for (CO_2) – CCS Carbon Capture & Storage.

In other words, the technology of inert oxygen-emissive anode, developed by UC RUSAL in 2004, is under consideration; but in this respect, the promising development of the technology for carbon dioxide capture and storage is prudently offered.

Thus, the best available technologies for the aluminium production are fixed in industrial information and technical reference books as achieved ones. Based on this, the edicts of RF government define criteria for ecological projects in aluminium branch including electrolytic aluminium production. Documents provide the basis for the involvement of "green financing" for the realization of specific projects – green and adaptation projects (jointly, projects of sustainable development); they provide the basis for national infrastructure of responsible investments[12]. In fact, the mutually profitable deal is concluded between the government and metallurgists. An aluminium company raises the finances for the modernization of obsolete production facilities and gets a chance for the technical and technological development. The state regains confidence in providing ecological standards and working places in modern production sectors.

Promising directions. Over the last 120-125 years on the aluminium production the level of greenhouse gas emissions has been almost halved – in average to 1.4 t CO_2-equ/t Al, the significant progress in energy consumption reduction was achieved – from 40 to 13.0-135 kWh/kg Al [12, 13]. However, the volume of greenhouse gas emissions remains high, and the energy cost item in the metal cost value – significant (30-40 %) depending on energy source. In addition, the attempts of aluminium companies to increase the specific capacity of the pots are restricted by admissible limits of current density increase and by horizontal configuration of electrodes. These circumstances encourage continuous investigations, developments and tests of new technologies purposing the reduction in specific electric energy consumption and in harmful matters emissions, and the increase of aluminium pots capacity.

***Energy consumption*.** In conditions of up-to-date pot operation under control of automated process control system with maximum available current efficiency and optimal busbar design the reduction in energy consumption is possible by minimization of pot voltage only

$$U = E_{\text{EMF}} + I\sum_{i}^{n} R_i ,$$

where I – pot amperage (in potline); R_i – resistance of electrolytic bath within the space between anode and cathode, resistances of bubble layer, electrodes, contacts and connecting systems in cathode and anode assemblies.

With standard technology management and use of high-quality pre-bake anodes it is difficult or impossible to have in influence on the back electromotive force E_{EMF}. In practice a certain reduction in ohmic voltage loss $I\sum_{i}^{n} R_i$ is achieved by so called millivolts pursuit strategy that comprises the up-to-dating of the design of anode yokes and stubs, contact units in the busbar system, anode risers and cathode flexibles [14, 15]. Taking into consideration the long-term application of this strategy in practice, the potential saving amounts to approx. 120 kWh/t Al. The energy consumption is reduced by about the same amount if use slot anode blocks (by reducing the thickness of gas film on the anode table) ~ 240 kWh/t Al in total. This is a substantial saving considering the annual aluminium output.

[12] The Government of Russia approved the criteria of green projects. URL: https://www.economy.gov.ru/material/news/ pravitelstvo_rossii_utverdilo_kriterii_zelenyh_proektov.html (accessed 31.10.2023).

However, it could be fully balanced by increase of micro-impurities content in raw material, mostly in petroleum coke. The process of sulphure, sodium, titanium, vanadium and other metals recovery taking place on the cathode can considerably decrease the current efficiency and, accordingly, increase the electric energy consumption for the electrolytic process [16-18].

A lot of attention is paid to voltage losses in cathode blocks: summarized voltage drop in the pot bottom averages about 380 mV; which corresponds to the electric energy consumption of approx. 1200 kWh/t Al. The voltage losses in this unit can be reduced to 250 mV by applying best available coupling technology in the contact between collector bar and block and by selecting cathode blocks with higher content of graphite; i.e. there is a possibility to save about 420 kWh/t Al. However, this achievement could be saved during the whole service life of the pot only in case of successful selection of the cathode assembly design and adequate technological policy for erection and electrolytic process conduction. The word "successful" is quite appropriate here because it is impossible to predict accurately the results of the movements of cathode blocks and block joints during the pot operation, during the infiltration of the melt through the carbon bottom, its accumulation within liquid and solid phases. It is also impossible to predict the state of the collector bar/block contact and other factors.

The main reserve for the energy consumption decrease within the aluminium pot is localized in the narrow space between anode and cathode. Voltage losses take place in the electrolytic bath layer having the specific resistance of about 0.5 Ohm·cm. At the current density of 0.80 A/cm^2 and current efficiency of 0.93 % the change of 1 cm in anode-cathode distance corresponds to the voltage of about 400 mV, i.e. to the energy component of about 1300 kWh/t Al. This means that for the potline consisted of 300-600 kA pots, the reduction in the distance between anode and cathode from 4 to 3 cm allows theoretically to decrease the electric energy consumption from 13200 to 11900 kWh per 1t of produced aluminium. It is obvious that even considering the potentials of Automated Process Control System, busbar and lining materials these values shall be limit values for the standard available reduction technology using horizontal electrodes.

The further insignificant reduction of anode-cathode distance and electric energy consumption is only possible by involving cathode materials wettable with molten aluminium. In this case the conditions shall be established to bring the metal level on the wettable bottom from 10-15 to 5-7 cm and thereby to lower the threshold of MHD-instability (Magneto-Hydro-Dynamic). With moderate melt circulation, equal distribution of alumina concentration within electrolytic bath and evacuation of anode gases from the table of electrodes there is a probability for the reduction of anode-cathode distance for another 0.5 cm (to 2.5 cm), i.e. there is a provision for the decrease of energy consumption to 11250 kWh/t Al. Maybe, this is a limit for standard Hall – Heroult technology with elements of innovative cathode materials. Nevertheless, it is necessary to correlate this apparently attainable level of electric energy consumption with costs on the creation of special composite materials.

Inert anode. The conception of inert anodes for the electrolysis of the melts was firstly proposed by C.M.Hall in famous patent of 1886 [19] and extended by A.I.Belyaev and Ya.V.Studentsov in 1930-s [20-22]. C.Hall tried to use copper anodes and Russian researchers – metallic, oxide, and ferrite anodes. Further, a huge amount of papers was related to inert anodes [23-25], which was evidenced in reviews [26, 27], articles [28-30] and reports[13].

Therefore, for the discussion we propose the direction that was not considered in above mentioned publications. Let us notice right away that it is not the results of our research that are being discussed, but the existing ideas of specialists in industrial safety. The question is about oxygen that is released on the inert anode in amount of 0,9 t while producing 1 t of aluminium; which according to En+

[13] Bradford D.R. Inert Anode Metal Life in Low Temperature Reduction Process. Final Technical Report for September 17, 1998 through March 31, 2005. Award Number: DE-FC36-98ID13662. 2005, p. 106. URL: https://ntrl.ntis.gov/NTRL/dashboard/searchResults/titleDetail/DE2006841153.xhtml (accessed 31.10.2023).

Group company is equivalent to 70 ha of forest[14]. Continuing this arithmetic, the supposed operation of an aluminium smelter with annual capacity of 500,000 t Al is equivalent to the release of about 1230 t of oxygen per day and to the plantation of 35 million ha of forest area over year. Apparent prospects satisfy both potential oxygen producers and local authorities and population around the smelter.

From the other side V.Marshall, a known English scientist in the field of industrial safety insists that the massive release and prolong outflow of gases could result in the formation of gas-vapor clouds [31]. The mixing of the clouds, containing the excess of oxygen, with air retains the excess of oxygen in atmosphere. For example, while mixing 50 % of oxygen with 50 % of air the mixture is formed that contains more than 50 % of oxygen in its composition. Main problem, related to oxygen excess consists in the enhanced combustibility[15] – the threshold of initial flash energy, which initiates combustion, lowers; the burning speed increases; the flame extinguishment becomes difficult [32].

The change in air composition and the concentration of atmospheric pollutants depend on the emission amount and height, on meteorological conditions, atmospheric pressure, wind direction and speed. It is found that in general case the maximum height of the emission source determines its greater dispersion and lesser concentration of impurities. This is facilitated by the stability of atmosphere, by dense high clouds, negative temperature gradient, formation of inversion over the stack or below the emission point.

However, in conditions of strong convective turbulence the undulating plume flame is observed, propagating the emission to the land level where its concentration could be significant (Fig.1)[16]. The high concentration of emission is also fixed with smoking plume when the stable air layer is at the small distance over the emission point and the unstable layer is below the emission point. When the unstable air layer reaches the height of the stack, big volumes of emission from the stack are transferred downwind to the land surface. This lasts not more than half an hour, but during this time the ground-level concentration of emissions can achieve high values and keep for a long time (Fig.2)[17].

When with increase of the height the temperature goes up, the temperature gradient is negative and atmospheric conditions are defined as an inversion. The presence of inversion reduces the vertical mixing of emission (oxygen masses); which results in the increase of its concentration in the surface atmospheric air. The repeatability of surface inversions and gentle breeze at continental areas determines the possibility of air blanketing at these areas, the concentration of emissions and their accumulation in the surface layer of the atmosphere.

Fig.1. Drifting emission in Novotroitsk

Fig.2. Smoke spread in the main square in Bratsk

[14] En+ Group ESG-Report: Pathway to net zero 2021. URL: https://enplusgroup.com/upload/iblock/fe0/EN_Pathway-to-net-zero.pdf (accessed 31.10.2023).

[15] Baratov A.N. Combustion – fire – explosion – safety. Moscow: Publishing House of FBGU VNIIPO Emercom of Russia, Russia, 2003, p. 363.

[16] Is there a limit to the number of factories in Novotroitsk? URL: https://orenburzhie.ru/news/est-li-predel-kolichestvu-zavodov-v-novotroicke/ (accessed 31.10.2023).

[17] 15 most polluted cities in Russia according to ecologists. URL: https://bigpicture.ru/15-samyx-gryaznyx-gorodov-rossii-po-ocenkam-ekologov/?ysclid=ljr5ivnrf0966035699 (accessed 31.10.2023).

Maximum capacities and intensity of inversions are observed in winter. A kind of barrier is formed that prevents the rise of polluted air to upper atmosphere. The degree of atmospheric air contamination is influenced by nebulosity, fogs, radiation regime, and precipitations. Therefore, low nebulosity prevents the turbulent interaction in atmosphere and promotes the emergence of long inversion, under which the concentration of emissions and the quantity of impurities in air increases from 10 to 60 %.

Thus, we attract the attention to the serious problem – presence of local source of massive oxygen emissions to atmosphere. Before to begin the design work on such sources this problem has to be thoroughly examined and analyzed by competent entities, specializing in industrial safety.

Pot with drained cathode. It is supposed that big economic dividends could be received at the startup of the potline consisting of the pots equipped with drained cathodes, i.e. pots having the thin layer of aluminium distributed on the bottom and the anode-cathode distance reduced to 1.5-2 cm. For this purpose, it is necessary to solve a problem of creating the cathode surface wettable with aluminium by involving special materials based on carbides and borides of refractory metals – titanium, zirconium, vanadium, tantalum, columbium, and hafnium.

The conception of applying refractory compounds was developed by British Aluminum Company Ltd (BACO) and Kaiser Aluminum in 1960s [33, 34]. At the same time Kaiser Aluminum developed the technology of drained cathode having an inclined bottom and a thin layer of aluminium formed on the cathode surface [35]. The following products were developed and tested in laboratory and semi-industrial conditions by scientific centers of aluminium and refractory companies:

• compact products from carbides and borides of refractory metals in form of plates, cylinders and T-shaped elements [36, 37];

• composite coatings on the surface of carbon bottom [38];

• titanium diboride-based emulsion coatings [39].

In subsequent years the conception of the pots with drained cathodes allowing to reduce the electric energy consumption and to cut the costs on busbar, was under development in many scientific centers [40-42], but until now the commercial materials for wettable cathodes do not exist. Until now, the task put in the middle of 20th century did not find any solution on the industrial level. However, this idea is so attractive that even now scientific centers of aluminium companies continue to deal with designs of the pots equipped with drained cathode. That is why, it is necessary to consider problems faced by researchers when they tested wettable cathode materials.

Compact products from borides and carbides of refractory metals having a satisfactory corrosion resistance in molten salts and aluminium, are liable to thermal cracking and scaling from current conducting base[18]. Attempts to create products by combining individual compounds, like TiB_2-TiC, did not eliminate these defects of pressed materials. The serious obstacle for the development of the technology of wettable cathodes was their value. For example, in 70-80s of last century the price of titanium diboride powder made approx. 55 dol./kg in comparison with traditional carbon compounds, about 1.32 $/kg. At present, the cost of TiB_2 makes 500-3000 $/kg depending on the purity and production method [43], while the cost of carbon materials practically did not change. Therefore, for the most part of tests titanium diborid TiB_2 combined with carbon [44, 45] or with colloidal solution of aluminium oxide (Tinor and Thicknor [46, 47]) was used as wetting agent. The mixture of TiB_2, carbon material and other components was applied as paste with a thick centimeter layer onto the carbon bottom, as it was done in Martin Marietta Aluminum and Comalco, or with a thin millimeter layer of colloidal material – in Moltech. However, in both cases the coatings cracked and degraded. The thick paste layer dissolved forming Al/TiB_2 suspension layer on the bottom surface [48]; the thin colloidal layer cracked and scaled further rising to the surface of the melts.

[18] Bruggeman J.N., Alcorn T.R., Jeltsch R. et al. Wettable Ceramic-Based Drained Cathode Technology for Aluminum Electrolysis Cell. Final Technical Progress Report for the Period 1997 October to 2002 December. DOE/ID/13567. 2002, p. 46. URL: https://digital.library.unt.edu/ark:/67531/metadc740532/ (accessed 31.10.2023).

Without denying the prospects of drained cathode development, J.Keniry expresses his critical considerations concerning their feasibility [24]: "Drained cathode exposes the carbon component of the coating to the aggressive impact of the electrolytic bath; which results in its destruction. The degree of wear has to be rather uniform throughout the pot, and any local coating damage caused by particularities of the design, startup or operation methods can have a negative effect on the life circle of the whole pot. Though the pots with drained cathodes proved their feasibility, their industrial application would raise doubt, until the economic profit would be increased to compensate the operational risk". J.Keniry, employee of private Australian company Alumination Consulting Pty Ltd, was well informed about results of drained cathode testing in Comalco. The key argument in his critical attitude to wettable coating is non-uniform wear degree of the composite coating surface. This disadvantage is difficult to eliminate as it is practically impossible to create a composite layer having the uniform adhesion to the matrix, the density, porosity, electric conductivity, strength, and other operational properties within the whole cathode surface. This is impossible to do both at the stage of erection and layer compaction and during its baking and pot startup. Moreover, the design of the pot with drained cathode is not ecological; it is oriented to the possibility of reducing the energy consumption and increasing the capacity. To provide the energy balance and insufficient heat generation within reduced anode-cathode space the pot design has to be based on the higher current density. This will further exacerbate the negative consequences.

It is recognized that no one of scientific research centers of aluminium producers solved completely and finally these problems. This explains the absence of commercial pots with drained cathode in spite of more than 70-year attempts to develop them. Therefore, most likely the engineering of the pot with drained cathode is unpromising (of little promise) direction due to following reasons:

• There are no any technologies for the creation of coatings wettable with aluminium and having uniform operational properties within their whole areas and volumes. Moreover, there is no any technical and technological possibility to synchronize the movement of cathode block with processes of surface layer shrinkage and expansion.

• There are no any cost-efficient technologies for the creation of massive compact products wettable with aluminium (cathode blocks) with uniform operational properties within their whole areas and volumes.

• The thin layer of aluminium on the cathode surface does not allow to uniformly distributing the current density within the large bottom area, which creates conditions for the uneven distribution of current and potential, for the cathode passivation and for the instability of the process.

• The existing technology of electrolytic reduction with prebake anodes came close to supposed energy consumption of the pots with drained cathode.

• Objectively, there are no prospects for the changes (increase) of specific capacity compared with existing technology.

Pots with vertical electrodes. The history of electrolytic aluminum production began with this direction. In 1854 R.Bunsen and A.Deville first, then such famous scientists of 19th century as F.Lontin, C.Bradley and finally P.Heroult and C.Hall started laboratory experiments in the cells with vertical electrodes [49, 50]. Moreover, first pilot pots of Pittsburgh Reduction Co followed this operation procedure in the beginning, but then they spontaneously switched over to the electrolytic reduction process using horizontal anode and cathode.

Since then attempts to develop the electrolysis of alumina-cryolite melts using solid electrodes continued [51, 52] and are currently ongoing [53, 54][19]. This persistence, on the one hand, is explained

[19] Hryn J.N., Tkacheva O.Y., Spangenberger J.S. Ultrahigh-Efficiency Aluminum Production Cell // Report of Energy Systems Division, Argonne National Laboratory. Award Number: DE-AC02-06CH11357. URL: https://www.energy.gov/eere/amo/downloads/ultrahigh-efficiency-aluminum-production-cells (accessed 31.10.2023).

by the desire to minimize the electric energy consumption and by the approach to theoretically possible 6.3 and 9.2 kWh/kg Al when using carbon and inert electrodes accordingly. Such possibility appears if use vertical electrodes with anode-cathode distance of ~ 1.5-2 cm. On the other hand, this layout of the electrodes allows the multi-fold growing of specific capacity in the limited area of the pot.

Specific capacity. The standard capacity depends on the power of aluminium pots, i.e. amperage and on the amount of metal losses caused by low-productive processes and current leakage. In order to increase the capacity, the pot is designed for high amperage, the design provides for the application of structural components and technology allowing the maximum increase of current efficiency. Thus, the single capacity of any pot or enterprise in the whole, expressed in Al kilograms per day or in Al tons per year, can be increased by aluminium companies that accumulated high scientific and engineering potential and gained big experience in operating several generations of the pots.

It is not the case of specific capacity *P*, which is expressed by mass production of aluminium in 24 h per square meter of occupied area or area of anode/cathode block in the horizontal plane, – kg Al/m^2·day. The specific capacity does not practically vary with increase of the pot power as with the increase of amperage the dimensions of the pot increase proportionally in terms of to accommodate electrodes and busbar that provide the design current density and current efficiency. Therefore, the specific capacity is a suitable parameter for the characterization of applied technology and for its comparison with new technologies of aluminium production by electrolytic method or with such technologies being under design.

If associate the standard capacity of any pots with area of anode block in horizontal plane, i.e. with area occupied by production premises (potroom), the specific capacity would have following parameters:

- for pots with horizontal electrodes ~ 60 kg Al/m^2·day;
- for pots with vertical electrodes ~ 450 kg Al/m^2·day.

The calculation of the capacity is done for vertical electrodes embedded into the electrolytic bath on 1 m.

This difference in specific capacity (almost 8-fold) is exactly what determines sustained efforts to develop pots with solid vertical electrodes. The unique feature of vertical position of anodes and cathodes consists in multiple reduction of capital expenses on the construction of new smelters. This implies the reduction in expenses not only on building structures, but on the aluminium busbar as well, as there are no any strict requirements to the provision of MHD-stability of the melts in the pot.

However, there are serious constraining factors, limiting the development of solid vertical electrodes; these are absence of commercial wettable cathodes and uneven current distribution on the polycrystalline surface of electrodes.

Cathodes wettable with aluminium. The direction of creating wettable cathode surface as pastes and adhesion coatings is not developing now as experiments proved the rather quick destruction of continuous layer of any thickness on the surface of the block. The point is not just the absence of practical technologies for the creation of coatings (being created on the cathode surface before it is put into operation) with uniform operational properties within the whole area and volume of the block. Uncontrolled movement of cathode block could not be completely synchronized with processes of surface layer shrinkage and expansion. Besides, the cost of mechanically mixed carbon-based compositions with TiB_2 powder for coatings and, particularly for cathode blocks is unacceptably high per one pot. Therefore, the direction to synthesize composite cathode products of any configurations and dimensions just during the process of electrolytic aluminium production looks attractive [55, 56]. It is clear that in quoted patents there is no any information about know-how technology.

The Scientific Center "Mineral and anthropogenic resource processing problems" of Empress Catherine II Saint Petersburg Mining University examined the possibility to synthesize composite cathode material carbon – titanium diboride/carbide (C-TiC/TiB_2) during the electrolytic process in laboratory conditions. Petroleum coke, titanium and boron oxides and carbon-bearing binding agent were used as initial components for the preparation of electrodes. After pressing and baking at the temperature of 1050 °C the electrodes were installed into the graphite electrolytic cell, containing molten bath of $NaF/AlF_3 \approx 2.5$ at the temperature of 960 ± 5 °C. Composite electrodes with titanium and boron oxides were subject to the cathode polarization during 24 h.

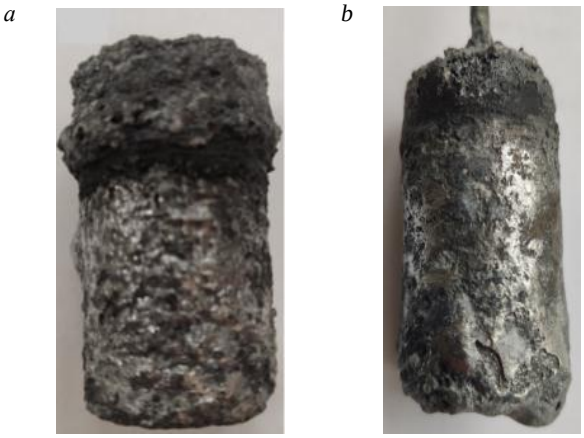

Fig.3. Specimens of composite after electrolysis: *a* – C-TiC; *b* – C-TiB_2

After taking electrodes out of the cell and cleaning them against bath the layer of aluminium was discovered on the surface; which evidenced the wettability of cathodes with metal (Fig.3). *X*-ray phase analysis shown that the composition of electrodes contains titanium carbide TiC (Fig.4, *a*), only titanium oxide was dosed at the preparation. During the creation of initial C-TiO_2/B_2O_3 composite the *X*-ray phase analysis of final product after electrolysis shown the presence of TiC and titanium borate $TiBO_3$ (Fig.4, *b*), product of titanium diboride oxidation at the moment of electrode removal from the electrolytic cell. Hereby, the possibility of creating cathode composite material with wetting properties just during the electrolytic process was confirmed. Considering roughly the same range of prices on carbon materials, titanium and boron oxides, the production of composites of any dimensions shall change slightly.

Uneven current distribution. This problem is not obvious at the visual observation over the electrolytic process when using solid electrodes, but it is expressed by voltage instability in the system, higher consumption of anodes and passivation of cathode by bath components. It is precisely these consequences, but not the causes of the instability of the process, that researchers have tried and are

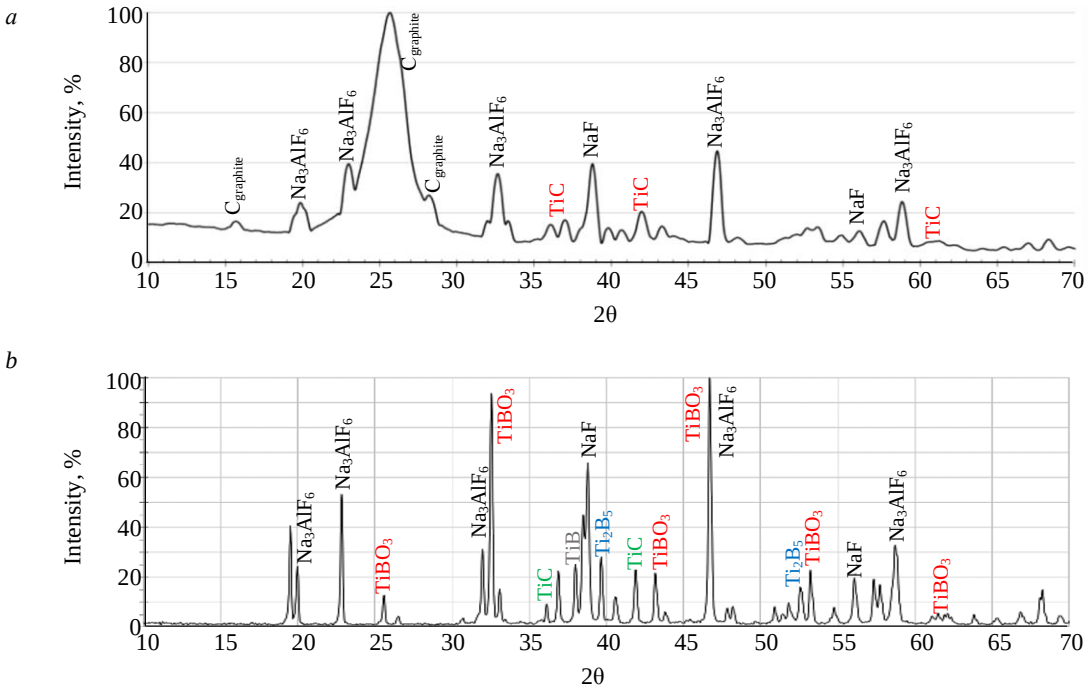

Fig.4. Results of *X*-ray phase analysis of C-TiC (*a*) and C-TiB_2 (*b*) electrodes

trying to cope with [54, 57]. The destabilization of electrolysis in laboratory conditions occurs when the current density becomes higher than 0.5 A/cm^2 [58-60]. Recommendations, proposed for the decrease of electrolytic reduction temperature, corrections in electrolytic bath and electrode compositions do not solve the problem and do not allow starting the development on the commercial basis.

Based on experimental data [61, 62] and numerical investigations [63, 64] it is proposed to consider the physical and chemical heterogeneity of surface structure of polycrystalline electrodes as the cause of these problems and restrictions. During the operation the chemical heterogeneity transforms gradually into physical one. That is right both for coatings and for compact electrode products of any composition – based on carbon, borides/carbides of refractory metals or their compounds.

Current lines at the micro-level would be concentrated on asperities of the rough surface, pores, cracks, scratches. The same effects take place at the macro-level for peripheral areas of electrodes – ribs or sharp edges. At the areas where the current density and potential are higher, the speed of electrode processes increases with the development of concentration polarization and uncontrollable formation of critical electrode potentials for simple and complex ions present. This would result to greater or lesser extent in the release of gas fluorocarbons on the carbon anode and the release of fluorine on the inert anode with corresponding negative consequences, i.e. increase in electrode consumption.

On the wettable cathode the charge of electrically negative impurities and the decomposition of electrolytic bath components take place with subsequent passivation of the surface and progressing destabilization of electrolytic process (these negative consequences are typical for the drained cathode as well). By this means we can distinguish the micro-heterogeneity, related to the rough surface in the entire area, and the macro-heterogeneity of current distribution on the peripheral areas of electrodes (edge effect). This approach determines the development of different technologies for flattering current distribution throughout electrodes.

Elliptical shape of electrodes with adequate increase of anode-cathode distance and electrolytic bath resistance from the center to the periphery allows compensating the edge effect and reducing significantly the macro-heterogeneous current distribution. As opposed to the application of rectangular electrodes, during the whole experiment the proceeding of electrolytic process was stable in the electrolytic cell with metallic anode and cathode of elliptical shape; the passivation of cathode was not observed, the rate of anode corrosion was approx. three times reduced [62].

However, the special shape is not sufficient for the stability of the process using solid electrodes, polycrystalline and cast, one-phase and multi-phase, which a priori have physical and chemical heterogeneities in their volume and surface structures. Therefore, one of feasible methods of surface homogenization directly within the electrolytic process was proposed and realized – *electrochemical micro-boriding of cathodes* which composition included refractory metals and their oxides [61]. The method is based on the significant, almost twice, difference between standard potentials of the charges of aluminium (E^0_p = –1.18 V) and boron (E^0_p = –0.63 V). When they are jointly present in the melt, the conditions for the charges in the cavities are favorable for more electrically positive ions. If after the reduction in the cavity boron meets, for example, titanium or its oxide on the surface, the synthesis of titanium diboride shall smooth any heterogeneous surface. This method could be applied to any reactive or inert cathodes, which heterogeneous surface is smoothed by chemical interaction of boron with impurities present, and thereby, the physical state of the surface homogenates.

Thereby it is possible to deduce a simple formula of the electrolytic process procedure in the pot with vertical solid electrodes: complex application of elliptical electrodes and electro-chemical micro-boriding of composite cathodes. This formula in general terms can be used for the prospective development of aluminium industry according to the following roadmap of scaling up technologies:

- technology of electrolytic reduction as per flowchart of vertical elliptical electrodes;
- technology of synthesis of composite cathodes wettable with aluminium directly during the electrolytic process;
- technology of electrochemical micro-boriding of cathode surface.

Combining these technologies into one shall allow taking unique advantages of electrolytic reduction technology using vertical solid electrodes (see Table).

Comparative characteristics of electrolytic reduction technologies

Parameters	Position of electrodes	
	Horizontal	Vertical
Electric energy consumption, kWh/kg Al	~13.5	~11.0
CO_2 emissions* kg CO_2-equ/kg Al	~ 1.4	→ 1.0** → 0***
Specific capacity, kg Al/m^2·day	~ 60	~ 450

* Direct emissions (Scope 1).
** Composite electrodes.
*** Inert electrodes.

Conclusion. Following conclusions were made based on above-mentioned overview:

• In Russia the process of ecological reconstruction of obsolete production facilities was organized on the governmental level. It supposes the self-financing of the tightening state environmental regulation. At the same time, private companies satisfy their challenging technological and environmental ambitions.

• For existing technology of electrolytic reduction using horizontal electrodes and up-to-date automated process control system, busbar and lining materials, there is a real possibility of energy consumption in amount of`~12000 kWh per 1 t of aluminium produced. The further decrease of specific consumption of electric energy to 11250-11500 kWh/t Al is possible with the use of cathode materials wetted with molten aluminium. These values of energy efficiency are limiting values for existing technology.

• The development of the technology of inert (oxygen evolving) anode requires the thorough examination by competent entities of industrial safety. Under certain climate and meteorological conditions at the area of intensive oxygen emission source the situation with increased fire hazard can emerge.

• The design of the pot with drained cathode is of little promise.

• The most promising technology of alumina-cryolite melt electrolysis is the technology of the pots with vertical electrodes. The use of composite anodes and cathodes with reduced carbon activity can decrease considerably emissions of greenhouse gases. The specific capacity of such pots can be 7-8-fold higher; which means the multiple reduction of capital expenses on the construction of new smelters in comparison with the existing technology using horizontal electrodes.

REFERENCES

1. Litvinenko V.S., Petrov E.I., Vasilevskaya D.V. et al. Assessment of the role of the state in the management of mineral resources. *Journal of Mining Institute*. 2023. Vol. 259, p. 95-111. DOI: 10.31897/PMI.2022.100

2. Zhukovskiy Yu.L., Batueva D.E., Buldysko A.D. et al. Fossil Energy in the Framework of Sustainable Development: Analysis of Prospects and Development of Forecast Scenarios. *Energies*. 2021. Vol. 14. Iss. 17. N 5268. DOI: 10.3390/en14175268

3. Pyagay I.N., Lebedev A.B. Effects of alumina on the stability of ferrite-calcium sinter with dicalcium silicate. *CIS Iron and Steel Review*. 2023. Vol. 25, p. 10-16. DOI: 10.17580/cisisr.2023.01.02

4. Kosolapova S.M., Smal M.S., Rudko V.A., Pyagay I.N. A New Approach for Synthesizing Fatty Acid Esters from Linoleic-Type Vegetable Oil. *Processes*. 2023. Vol. 11. Iss. 5. N 1534. DOI: 10.3390/pr11051534

5. Zubkova O.S., Alexeev A.I., Sizyakov V.M., Polyanskiy A.S. Research of suxfuric acid salts influence on sedimentation process of a clay suspension. *ChemChemTech.* 2022. Vol. 65. N 1, p. 44-49. DOI: 10.6060/ivkkt.20226501.6447

6. Kudinova A.A., Poltoratckaya M.E., Gabdulkhakov R.R. et al. Parameters influence establishment of the petroleum coke genesis on the structure and properties of a highly porous carbon material obtained by activation of KOH. *Journal of Porous Materials*. 2022. Vol. 29. Iss. 5, p. 1599-1616. DOI: 10.1007/s10934-022-01287-1

7. Litvinenko V.S., Dvoynikov M.V., Trushko V.L. Elaboration of a conceptual solution for the development of the Arctic shelf from seasonally flooded coastal areas. *International Journal of Mining Science and Technology*. 2022. Vol. 32. Iss. 1, p. 113-119. DOI: 10.1016/j.ijmst.2021.09.010

8. Khalifa A.A.E.I.A., Bazhin V.Y., Kuskova Y.V. et al. Study the Recycling of Red Mud in Iron Ore Sintering Process. *Journal of Ecological Engineering*. 2021. Vol. 22. Iss. 6, p. 191-201. DOI: 10.12911/22998993/137966

9. Sharikov F.Y., Rudko V.A., Smyshlyaeva K.I. Oxidation thermolysis kinetics of asphaltenes with various chemical prehistory. *Thermochimica Acta*. 2023. Vol. 726. N 179550. DOI: 10.1016/j.tca.2023.179550

10. Zubkova O.S., Pyagay I.N., Pankratieva K.A., Toropchina M.A. Development of composition and study of sorbent properties based on saponite. *Journal of Mining Institute.* 2023. Vol. 259, p. 21-29. DOI: 10.31897/PMI.2023.1

11. Volosatova A.A., Pyatnitsa A.A., Guseva T.V., Almgren R. Best Available Techniques as a Universal Instrument for Improving State Policies. *Economics of sustainable development.* 2021. N 4 (48), p. 17-23 (in Russian). DOI: 10.37124/20799136_2021_4_48_17

12. Haupin W., Frank W. Current and Energy Efficiency of Hall-Heroult Cells. *Light Metal Age*. 2002. N 5/6, p. 6-13.

13. Choate W.T., Green J.A.S. U.S. Aluminum Production Energy Requirements: Historical Perspective, Theoretical Limits and New Opportunities. ACEEE Summer Study on Energy Efficiency in Industry, 29 July – 1 August 2003, New York, USA. Proceedings from the ACEEE Summer Studies on Energy Efficiency in Industry, 2003, p. 12-24.

14. Bardel A., Droste C., Ovstetun F. et al. HAL4e – Hydro's New Generation Cell Technology. TMS Annual Meeting and Exhibition, 15-19 November 2009, San Francisco, CA, USA. TMS Light Metals 2009: Proceedings of the technical sessions presented by the TMS Aluminum Committee at the TMS, 2009, p. 371-376.

15. Lange H.P., Holt N.J., Linga H., Solli L.N. Innovative Solutions to Sustainability in Hydro. TMS Annual Meeting and Exhibition, 9-13 March 2008, New Orleans, LA, USA. TMS Light Metals 2008: Proceedings of the technical sessions presented by the TMS Aluminum Committee at the TMS, 2008, p. 211-216.

16. Thonstad J., Rolseth S., Rodseth J. et al. The content of sodium in aluminium in laboratory and industrial cells the Content of Sodium in Aluminum in Laboratory and in Industrial Cells. Light Metals: Proceedings of Sessions, TMS Annual Meeting, Warrendale, Pennsylvania, 2000, p. 441-447.

17. Makushin D.V. Increase of aluminium reduction efficiency based on the optimization of micro-impurities distribution within the "bath-cathode aluminium" system: Avtoreferat dis. ... kand. tekhn. nauk. St. Petersburg: Sankt-Peterburgskii gornyi institut, 2007, p. 22 (in Russian).

18. Meirbekova R., Haarberg G.M., Thonstad J. et al. Effect of Operational Parameters on the Behavior of Phosphorus and Sulfur in Aluminum Reduction. *TMS Light Metals*. 2015, p. 559-564. DOI: 10.1007/978-3-319-48248-4_93

19. Hall C.M. Patent N 400766 US. Process of Reducing Aluminum by Electrolysis. Publ. 02.04.1889.

20. Belyaev A.I., Studentsov Ya.E. Electrolysis of alumina using fire-proof (metal) anodes). *Legkie metally*. 1936. N 3, p. 15-24 (in Russian).

21. Belyaev A.I., Studentsov Ya.E. Electrolysis of alumina using fire-proof oxide containing anodes. *Legkie metally*. 1937. N 3, p. 17-21 (in Russian).

22. Belyaev A.I. Electrolysis of alumina using fire-proof ferrite containing anodes. *Legkie metally*. 1938. N 1, p. 7-20 (in Russian).

23. Brown G.D. TiB2 Coated Aluminium Reduction Cells: Status and Future Direction of Coated Cells in Comalco. Proceedings of the 6th Australasian Aluminium Smelter Technology Conference and Workshop, 1998, Queenstown, New Zealand. Kensington, NSW: University of New South Wales, 1998, p. 499-508.

24. Keniry J. The economics of inert anodes and wettable cathodes for aluminum reduction cells. *JOM*. 2001. N 53, p. 43-47. DOI: 10.1007/s11837-001-0209-2

25. Kvande H., Haupin W. Inert anodes for Al smelters: Energy balances and environmental impact. *The Journal of the Minerals, Metals & Materials Society*. 2001. Vol. 53. Iss. 5, p. 29-33. DOI: 10.1007/s11837-001-0205-6

26. de Nora V. VERONICA and TINOR 2000: New Technologies for Aluminum Production. *The Electrochemical Society Interface*. 2002. Vol. 11. Iss. 4, p. 20-24. DOI: 10.1149/2.F02024IF

27. Welch B. Inert anodes – The Status of the Materials Science, the Opportunities They Present and the Challenges That Need Resolving before Commercial Implementation. Light Metals 2009: Proceedings of the Technical Sessions Presented by the TMS Aluminum Committee at the TMS 2009 Annual Meeting and Exhibition, 15-19 February 2009, San Francisco, California, USA. 2009. p. 971-978.

28. Pawlek R. Inert Anodes: An Update. *TMS Light Metals*. 2014, p. 1309-1313. DOI: 10.1007/978-3-319-48144-9_219

29. Padamata S.K., Yasinskiy A.S., Polyakov P.V. Progress of Inert Anodes in Aluminium Industry: Review. *Journal of Siberian Federal University. Chemistry*. 2018. Vol. 11. N 1, p. 18-30. DOI: 10.17516/1998-2836-0055

30. Gupta A.K., Basu B. Sustainable Primary Aluminium Production: Technology Status and Future Opportunities. *Transactions of the Indian Institute of Metals*. 2019. Vol. 72. Iss. 8, p. 2135-2150. DOI: 10.1007/s12666-019-01699-9

31. Marshall V. Major chemical hazards. Moscow: Mir Publishers, 1989, p. 671.

32. Maltsev V.M., Maltsev V.I., Kashporov L.Ya. Main combustion characteristics. Moscow: Khimiya, 1977, p. 320 (in Russian).

33. Ransley C.E. Patent N 802905 GB. Improvements in or relating to electrolytic cells for the production of aluminium. Publ. 15.10.1958.

34. Lewis R.A. Patent N 2915442 US. Production of aluminum. Publ. 01.12.1959.

35. Lewis R.A., Hildebrandt R.D. Patent N 3400061 US. Electrolytic cell for production of aluminum and method of making the same. Publ. 03.09.1968.

36. McIntyre J., Mitchell D.N., Simpson S. Performance Testing of Cathodic Materials and Designs in a 16 KA Cell and a Test Bed. Light Metals; The Minerals, Metals & Materials Society: Proceedings of the Technical Sessions Sponsored by the TMS Light Metal Committee at the 116th Annual Meeting, 24-26 February 1987, Denver, Colorado, 1987, p. 335-344.

37. Tucker K.W. et al. Stable TiB2 – Graphite Cathode for Aluminium Production. Light Metals; The Minerals, Metals & Materials Society: Proceedings of the Technical Sessions Sponsored by the TMS Light Metal Committee at the 116th Annual Meeting, 24-26 February 1987, Denver, Colorado, 1987, p. 345-349.

38. Joo L.A., Tucker K.W., McCown F.E. Patent N 4376029 US. Titanium diboride-graphite composits. Publ. 08.03.1983.

39. Øye H.A., de Nora V., Duruz J.-J., Johnston G. Properties of a Colloidal Alumina-Bonded TiB_2 Coating on Cathode Carbon Materials. Essential Readings in Light Metals, Electrode Technology for Aluminum Production. 2016. Vol. 4, p. 1171-1178. DOI: 10.1007/978-3-319-48200-2_155

40. Hudson T.J. Cathode Technology for Aluminum Electrolysis Cells. Light Metals; The Minerals, Metals & Materials Society: Proceedings of the Technical Sessions Sponsored by the TMS Light Metal Committee at the 116th Annual Meeting, 24-26 February 1987, Denver, Colorado, 1987, p. 321-325.

41. Gessing A.J., Wheeler D.J. Screening and Avaluation Methods of Cathode Materials for Use in Aluminum Reduction Cells in Presence of Molten Aluminum and Cryolite up to 1000 °C. Light Metals; The Minerals, Metals & Materials Society: Proceedings of the Technical Sessions Sponsored by the TMS Light Metal Committee at the 16th Annual Meeting, 24-26 February 1987, Denver, Colorado, 1987, p. 327-334.

42. Alcorn T.R. Pilot Reduction Cell Operation Using TiB2-G Cathodes. Light Metals; The Minerals, Metals & Materials Society: Proceedings of the Technical Sessions Presented by the TMS Light Metals Committee at the 119th TMS Annual Meeting, 18-22 February 1990, Anaheim, California, 1990, p. 413-418.

43. Efimova K.A., Galevsky G.V., Rudneva V.V. The current status of titanium diboride production: Assessment and determination of the dominant trends and prospects. *St. Petersburg Polytechnical University Journal: Physics and Mathematics.* 2017. Vol. 23. Iss. 2, p. 144-158. DOI: 10.18721/JEST.230213

44. Boxall L.G., Cooke A.V., Hayden H.W. Use of TiB_2 Cathode Material Application and Benefits in Conventional VSS Cells. Essential Readings in Light Metals, Electrode Technology for Aluminum Production. 2016, p. 1145-1152. DOI: 10.1007/978-3-319-48200-2_152

45. Cooke A.V., Buchta W.M. Use of TiB_2 Cathode Material: Demonstrated Energy Conservation in VSS Cells. Essential Readings in Light Metals, Electrode Technology for Aluminum Production. 2016, p. 1153-1163. DOI: 10.1007/978-3-319-48200-2_153

46. Sekhar J.A., Vittorio de Nora. Patent N 5364513 US. Electrochemical cell component or other material having oxidation preventive coating. Publ. 15.11.1994.

47. Sekhar J.A., Duruz J.-J., Liu J.J. Patent N 6783655 US. Slurry and method for producing refractory boride bodies and coatings for use in aluminium electrowinning cells. Publ. 31.08.2004.

48. Watson K.D., Juric D.D., Shaw R.W., Houston G.J. Patent N 5658447 US. Electrolysis cell and method for metal production. Publ. 19.08.1997.

49. Richards J.W. Aluminium: Its History, Occurrence, Properties, Metallurgy and Applications, Including Its Alloys. London: Sampston Low, Marston, Searle & Rivington, 1887, p. 346.

50. Minet A. The Production of Aluminium and Its Industrial Uses. London: Chapman & Hall, Limited, 1905, p. 266.

51. Griswold Jr. T. Patent N 1070454 US. Electrolytic cell. Publ. 19.08.1913.

52. Johnson A.F. Patent N 2480474 US. Method of producing aluminum. Publ. 30.08.1949.

53. Zaikov Y., Khramov A., Kovrov V. et al. Electrolysis of aluminum in the low melting electrolytes based on potassium cryolite. *TMS Light Metals*. 2008. N 1, p. 505-508.

54. Shengzhong Bao, Dengpeng Chai, Zhirong Shi et al. Effects of Current Density on Current Efficiency in Low Temperature Electrolysis with Vertical Electrode Structure. 147th Minerals, Metals & Materials Society Annual Meeting and Exhibition, 11-15 March 2018, Phoniex, AZ, USA. TMS Light Metals, 2018, p. 611-619. DOI: 10.1007/978-3-319-72284-9_79

55. Mirtchi A.A., Bergeron D. Patent N 2232211 RU. Carbon composite materials capable of wetting, erosion\oxidation resistant. Publ. 10.07.2004 (in Russian).

56. Polyakov A.A., Gorlanov E.S., Pyagay I.N. et al. Patent N 2793027 RU. Method for producing composite carbon-containing material. Publ. 28.03.2023. Bul. N 10 (in Russian).

57. Tkacheva O.Yu. Low-temperature electrolysis of alumina in the melts of fluorides: Avtoref. dis. ... d-ra khim. nauk. Ekaterinburg: Uchebno-metodicheskii tsentr Uralskogo gosudarstvennogo tekhnicheskogo universiteta, 2013, p. 36 (in Russian).

58. Suzdaltsev A.V., Nikolaev A.Y., Zaikov Y.P. Towards the Stability of Low-Temperature Aluminum Electrolysis. *Journal of the Electrochemical Society*. 2021. Vol. 168. N 4. N 046521. DOI: 10.1149/1945-7111/abf87f

59. Nikolaev A.Y., Yasinskiy A.S., Suzdaltsev A.V. et al. Aluminum electrolysis in the $KF\text{-}AlF_3\text{-}Al_2O_3$ melts and suspensions. *Melts.* 2017. N 3, p. 205-213 (in Russian).

60. Nikolaev A.Y., Suzdaltsev A.V., Zaikov Y.P. Cathode Process in the $KF\text{-}AlF_3\text{-}Al_2O_3$ Melts. *Journal of the Electrochemical Society*. 2019. Vol. 166. N 15, p. D784-D791. DOI: 10.1149/2.0521915jes

61. Gorlanov E.S. Alloying of aluminium pot cathodes by method of low-temperature titanium diboride synthesis: Avtoref. dis. ... d-ra tekhn. nauk. St. Petersburg: Sankt-Peterburgskii gornyi universitet, 2020, p. 40 (in Russian).

62. Polyakov A.A. Distribution of the current and potential within the surface of vertical electrodes during the electrolytic production of aluminium: Avtoref. dis. … kand. tekhn. nauk. St. Petersburg: Sankt-Peterburgskii gornyi universitet, 2022, p. 20 (in Russian).

63. Gorlanov E.S., Polyakov A.A. On the question of using solid electrodes in the electrolysis of cryolite-alumina melts. Part 3. Electric field distribution on the electrodes. *iPolytech Journal*. 2021. Vol. 25. N 2, p. 235-251. DOI: 10.21285/1814-3520-2021-2-235-251

64. Polyakov A.A., Gorlanov E.S., Mushihin E.A. Analytical Modeling of Current and Potential Distribution over Carbon and Low-Consumable Anodes during Aluminum Reduction Process. *Journal of the Electrochemical Society*. 2022. Vol. 169. N 5. N 053502. DOI: 10.1149/1945-7111/ac6a16

***Authors*: Evgenii S. Gorlanov,** *Doctor of Engineering Sciences, Deputy Director of Scientific Center, gorlanov_es@pers.spmi.ru, https://orcid.org/0000-0003-2990-3601* (*Empress Catherine II Saint Petersburg Mining University, Saint Petersburg, Russia*), **Leopold I. Leontev,** *Doctor of Engineering Sciences, Academician of the RAS, https://orcid.org/0000-0002-4343-914X* (*Russian Academy of Sciences, Moscow, Russia*).

The authors declare no conflict of interests.

ISSN 2411-3336; e-ISSN 2541-9404

JOURNAL OF MINING INSTITUTE

Zapiski Gornogo instituta

Journal homepage: pmi.spmi.ru

Research article

Localization of sites for the development of geomechanical processes in underground workings based on the results of the transformation and classification analysis of seismic data

Sergei M. Danilev, Darya D. Sekerina, Natalya A. Danileva✉
Empress Catherine II Saint Petersburg Mining University, Saint Petersburg, Russia

***How to cite this article*:** Danilev S.M., Sekerina D.D., Danileva N.A. Localization of sites for the development of geomechanical processes in underground workings based on the results of the transformation and classification analysis of seismic data. Journal of Mining Institute. 2024. Vol. 266, p. 260-271.

Abstract. The paper considers an approach to localizing the intervals of development of geomechanical processes in underground structures based on the classification and transformation of seismic data. The proposed approach will make it possible to identify the intervals of fracturing, rock decompression, water inflow and other geomechanical processes when interpreting the results of seismic surveys. The technique provides for the formation of matrices of longitudinal (V_p), transverse (V_s) velocities and velocity ratios (V_s/V_p) along the research profile to perform sequential filtration. The filtration results serve as the basis for the formation of a bank of informative materials for further classification. Based on the domestic KOSKAD 3D software, four approaches have been implemented for a combined digital model of the V_p, V_s and V_s/V_p parameters. One of the key elements in the classification process is to combine grids to increase the probability of detecting intervals with heterogeneous identification features. The result of the application of this methodical approach is the construction of a comprehensive interpretative model, on which potential zones of geomechanical risks development are clearly manifested.

***Keywords*:** classification; transformation; longitudinal wave velocities; transverse wave velocities; complex interpretation; interpretative model

***Received:* 06.04.2023** ***Accepted:* 27.12.2023** ***Online:* 13.03.2024** ***Published:* 25.04.2024**

Introduction. The current state of urbanized territories cannot be imagined without the intensive development of the mineral resource sector aimed at the development and processing of minerals. This trend implies an increase in production capacities, exploration and development of new deposits, construction of new mining and technical facilities, as well as an increase in operational loads on existing facilities. More intensive mining operations, the tunneling of new workings, the formation of rock dumps and additional loading of existing ones can contribute to the development of geomechanical risks due to deformation, stress redistribution and destruction of rock masses. Often, the geomechanical processes occurring in the rock mass are hidden and are not visually manifested. The influence of tectonic and operational factors on stress changes in the rock mass is a very relevant topic of research in recent decades [1]. Therefore, in order to ensure the safety of mining operations, it is necessary to timely identify the intervals of formation of the zones of geomechanical processes intensification that potentially affect the operational reliability of mining facilities due to stress redistribution in the rock mass. Hidden zones of development of geomechanical phenomena associated with the activation of tectonic processes manifest themselves in the form of the development of zones of decompression, fracturing and leaching. The development of these processes leads to the formation of water supply channels in the rock mass, which increase water flow into underground workings and act as a catalyst for the further development of denudation processes at a more intense rate, and, as a result, the appearance of visible deformations and increased risks during mining operations.

For forecasting, a standard set of geotechnical monitoring works is performed at the mines, including surveying observations on reference points, monitoring of seismic phenomena within the seismic ranges of the seismic pavilion of mine, and hydrogeological monitoring. However, before the appearance of visual and noticeable deformations in the rock mass, which are well localized according to the results of surveying and hydrogeological work, hidden deformation intervals may form in the body of the rock mass, bearing potential geomechanical risks, timely identification of which is possible based on the involvement of modern geophysical technologies and algorithms [2, 3].

To solve the problem of forecasting geomechanical risk zones, the paper proposes conducting underground high-resolution seismic exploration on longitudinal and transverse waves. Processing and interpretation of research results implies the use of algorithms for transformation and classification of velocity sections.

At the processing stage, as a promising set of tools, it is possible to identify transformations of the source data through filtering by various methods and classification of the combined block of source matrices with the filling of missing or unsuitable data for subsequent analysis [3]. This approach has been well studied within the framework of the tasks of interpreting potential fields, but it is specific for the seismic data transformation. It is proposed to use alternative filtering methods that have successfully proven themselves in processing geopotential field data [4]. This direction can add new useful sources of information, will allow to localize the decompressed and weakened zones that form the area of geomechanical risks development in the rock mass, based on data from specialized seismic surveys.

Methods. Timely detection of disturbed intervals in the field of interaction of underground workings with the host rock mass and into the depth of the rock mass, control of the stress-strain state (SSS) of the rock mass are possible on the basis of the development of underground geophysics technologies. Underground geophysical surveys at mines have been successfully used for more than half a century. The experience of their approbation, taking into account modern hardware and technological progress, allows to determine the most optimal methods of geophysics for assessing and predicting the SSS of rock mass, which allow conducting studies of the state of mining and technical structures on the principles of minimizing invasive impact in order to reduce the risks of developing new geomechanical processes [5-7].

As part of the research work at the mines of the Talkhanskoe and Oktyabrskoe fields (Norilsk), complex geophysical studies of underground mining were carried out. The complex consisted of methods of georadiolocation, seismic studies and registration of natural electromagnetic emissions (NEME). The data of the NEME method for the tasks of transformational-classification constructions cannot be represented in the form of a two-dimensional model, therefore transformations and classifications in the framework of this study are not applied to these data. The georadiolocation method is also not subject to transformation and classification due to the limited depth of research (up to 8 m).

In the context of the considered geotechnical tasks, it is possible to formulate general requirements for the geophysical methods proposed for research:

• the main vector of research is mainly focused on the investigation of the structure and the forecast of stability (disturbance) of the rock-bearing mass of the workings roof [6];

• examination of the workings roof of located in complex SSS by geophysical methods should be carried out with minimal invasive impact, without additional deformation risk;

• in most cases, the monitoring of the workings roof is complicated by the presence of a dense network of communications (water pipes, concrete pipelines, cables, etc.), therefore, geophysics methods should be able to obtain useful information in these conditions [8];

• the applied methods of geophysics should have the potential for long-term prediction of SSS and physical and mechanical properties of the rock mass [9, 10].

Taking into account the requirements for geophysical technologies and the possibilities of presenting data in the form of data matrices in a two-dimensional domain, the seismic refraction wave method (SRM) with subsequent tomographic data processing (PKMPV-CT) is the most optimal, despite the labor costs associated with the specifics of the work [11-13].

When working out seismic profiles in mine conditions on the workings roof, the following registration parameters were used: the pitch of the receiving points (RP) is 2 m; the pitch of the vibration points (VP) is 2 m; the number of RP on the profile is 76; elastic vibrations were aroused by a hammer weighing 6 kg. This type of installation was selected on the basis of experimental and methodical work and the size of the studied areas, corresponding to the size of the bin. The seismic research method involves working with the removal of vibration points beyond the main alignment by 10 m, which contributes to obtaining seismic records to a depth of up to 50 m. Field seismic work was carried out using a modern telemetric seismic survey station "TELSS-3" manufactured by OOO "Geosignal" (Moscow). The station has an advantage, according to its technical characteristics, over analogues for the implementation of underground observations, consisting in the possibility of forming an individual noise-proof line of alignment due to a segmented seismic spit connected by telemetry modules [14].

The processing of seismic data is divided into several stages: the first is the evaluation of field data, the performance of primary filtering and amplification of the initial signal, the second is the assignment of the geometry of the alignment in the local coordinate system (X, Y, Z), the third is the picking of the hodographs of deflected and refracted longitudinal and transverse waves, followed by the calculation of tomographic sections (V_p, V_s). The tomographic inversion of hodographs consists in solving the inverse problem of tomography using the Fourier transform and the least squares method, which involves minimizing the discrepancy when ray tracing obeys the basic laws of geometric seismics with a minimum time of passage of an elastic wave through a system of elementary cells [15].

Further processing of seismic data consists in calculating the ratio of the velocities of transverse and longitudinal waves and preparing the initial matrices (V_p, V_s, V_s/V_p) of the data (Fig.1) for the procedure of transformation and classification analysis of seismic data.

The first stage of the transformation of the processed data is the assessment of the input materials for the quality, unity and soundness of the values for the research object under consideration. Then the transformants are calculated, including such filters as averaging in a sliding window (Moving Average) with selected sizes of the semi-axes of the averaging ellipse of 5×7 and 15×25 m, in which the most informative results are obtained by the minimum size of the axes, taken as optimal; low-frequency convolution filtering (Low-Pass Gaussian) with a standard window size 3×3, Mean Absolute Deviation (MAD); Standard Deviation, which allows to estimate the spread of values relative to the standard for the measured parameter V_s or V_p (the standard deviation is the square root of the variance); calculation of the horizontal gradient, which allows to identify destruction zones by changing the nature of the field from a positive to a negative value, etc. [16]. The main task of filtering is to suppress interference and extract useful information for the correct interpretation of the results obtained [17]. A more detailed description of the filters used is given in the Table.

After the formation of a working bank, including maps of calculated transformants, the quality of the obtained materials is assessed [18, 19]. The most informative transformants are selected for involvement in the processes of complex interpretation and classification of transformed materials [20-22].

At the second stage, classification is performed using the KOSKAD 3D software [23-26]. To begin with, the initial matrices for the values of the velocities of longitudinal and transverse waves and their ratios are loaded. The next procedure is to fill in missing or incorrect values that could have been mistakenly recorded and not eliminated at the stage of primary data processing. After filling in the missing values, the three "grids" are combined to apply the classification operation.

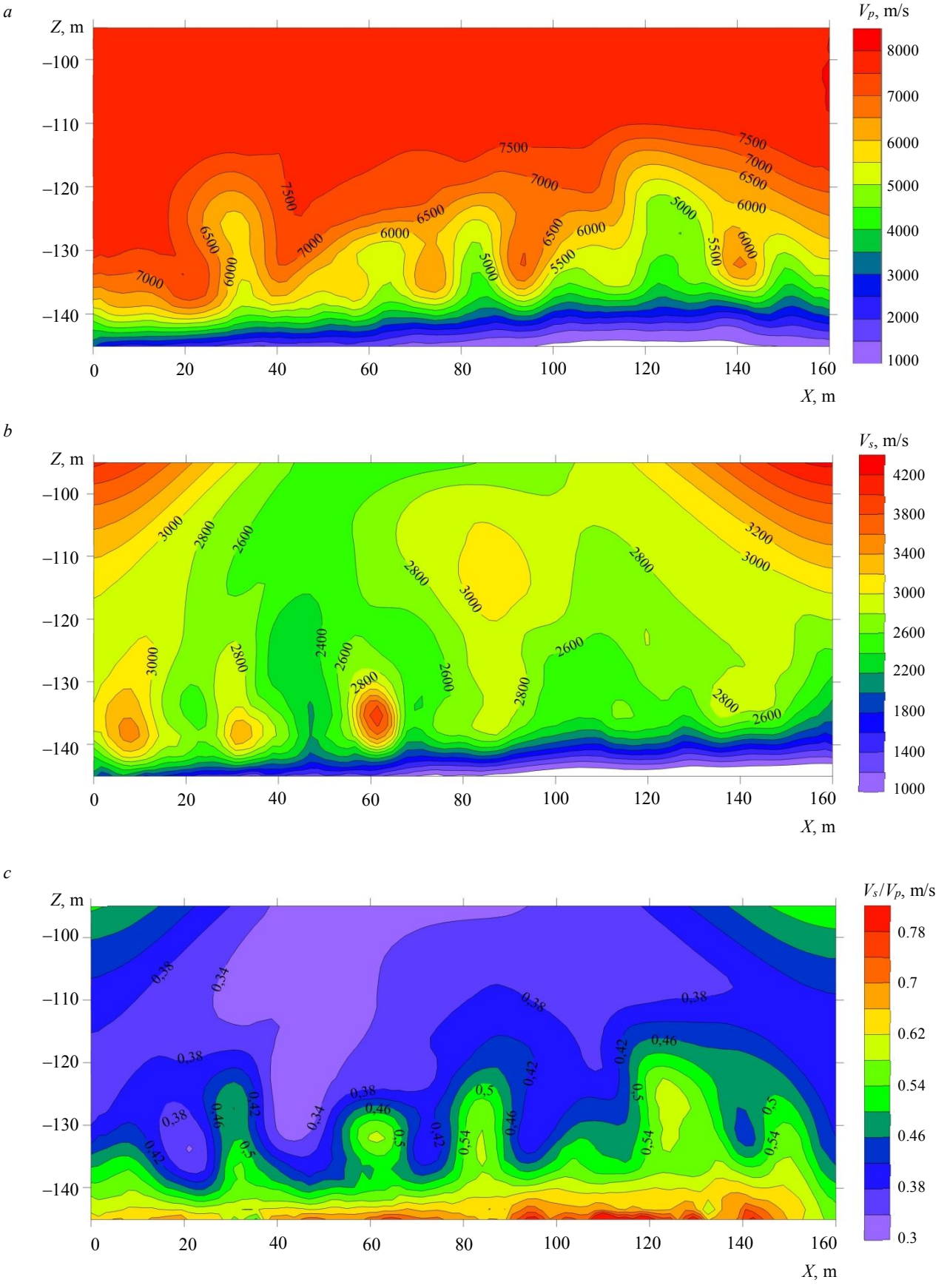

Fig.1. Initial tomographic sections of longitudinal (*a*), transverse (*b*) velocities and velocity ratios (*c*)

Characteristics of the applied filtrations

Title	Description	Formula
Averaging in a sliding window	The method of constructing a moving average grid allows to assign values to grid nodes by averaging data within the ellipse of the grid node search. Due to the specifics of this method, its use for small and medium-scale maps is not recommended, however, this tool is useful when working with a large bank of spatial data, since it allows you to identify regional anomalies, the amplitude of which depends on the size of the specified averaging window [13]. The minimum amount of data sets the value of the points when interpolating a grid node. For each grid node, neighboring data is identified by centering the search ellipse on the node. The value of the output node of the grid is set equal to the arithmetic mean of the identified neighboring data [16].	Arithmetic mean averaging is performed using a radial-annular or square pallet, or within a certain interval according to the formula $\bar{Z} = \frac{1}{N\sum Z_i}$, where $\bar{Z}$ is the average value of the field within the averaging area; Z_i is the value of the field in the i-th node of the pallet; N is the total number of nodes.
Low-frequency convolution operation	The low-pass filter removes high-frequency noise, resulting in a smoother grid at the output. When working with one of the four low-frequency filters, it must be taken into account that the width and height of the filter neighborhood must be positive odd numbers [15]. With a Gaussian low pass filter, the weight decreases with increasing distance. This weight function has the shape of half of the total bell curve. The parameter α determines how fast the weight decreases with distance. The lower the value of α, the more weight the neighborhood points have in the grid value and the slower the weight decreases. The higher the value of α, the greater the weight of the central point in the grid value and the faster the weight of other points decreases [17].	With the height of the neighborhood S and the width T the distance weighting function is $W(i,j) = \exp\left(-\alpha\left(\left(\frac{i}{S}\right)^2 + \left(\frac{j}{T}\right)^2\right)\right)$; $A_i = -\frac{S}{2},\cdots,\frac{S}{2}$; $A_j = -\frac{T}{2},\cdots,\frac{T}{2}$, where α is a positive value.
The average absolute deviation	Determining the nature of the distribution of the difference between the absolute and average values of the points [18, 19] allows to estimate the amount of variation that occurs around the average value in the dataset. The effect of this filter is to highlight outliers in the grid [18]. The disadvantage of this method is the limited mathematical manipulation compared to variance.	The average absolute deviation $\mathrm{MAD} = \frac{\sum_{i=1}^{n}\left\|X_i - \bar{X}\right\|}{n}$, where $\bar{X}$ – the average value of the sample; n is the number of observations in the sample.
Standard deviation	Moment statistics filters – standard deviation (mxn). The value of the output node of the grid is equal to the standard deviation of neighboring values [22].	The standard deviation is the square root of the variance $\sigma = \sqrt{\frac{\sum_{i=1}^{n}(x_i - \mu)^2}{n}}$, where x_i is the value of a single sample value; μ is the arithmetic mean of the sample; n is the sample size.

The classification procedure is a component of the functional block "Complex" [25], designed for processing multi-sign geological and geophysical information [27, 28]. With the help of classification, the area under consideration is divided into regions that are homogeneous in several ways [29, 30]. The algorithms used are based on self-learning, taking into account the correlations of the entire feature space, with the possible absence of a priori knowledge about the position of the initial centers and a finite number of classes with homogeneous features.

An interesting characteristic of this method is the processed field of features [31, 32], in which the transformed matrices [33] obtained at the previous stage can be set as source materials. As a result of applying the algorithm, a network is formed containing information about the class identification of each point. The involvement of transformed materials as secondary input data allows additional selection of the most significant results.

Taking into account the fact that at the stage of calculating transformants, interference is suppressed and eliminated and data quality is improved, and the use of improved digital matrices allows to get a more reliable picture at the output. This approach makes it possible to include additional components for the formation of a class distribution in a multi-sign space [34, 35].

Classification is implemented by four main methods:

• The total distance method, in which a finite number of classes are selected automatically.

• The method of dynamic thickening (*K*-means), in which information about a finite number of classes is set by the user, and the transformation is performed through an iterative empirical procedure.

• A method for separating multidimensional normal mixtures, implying the variability of specifying a finite number of homogeneous regions using multidimensional analysis of variance.

• A symbolic classification that divides the study area into positive and negative signs.

The final stage is the interpretation of the results obtained. For this purpose, a working data bank is formed, containing maps based on source data, transformations and classifications in a single binding [36, 37]. After that, a comprehensive analysis of a priori and transformed information is performed, according to the results of which zones of localization of abnormal values at the boundaries of the change in the nature of physical properties are identified [38-40], which are compared with the physical and mechanical parameters of the medium under study. At this stage, anomalies caused by edge effects are eliminated and a generalized interpretative model is created.

Results. As a result of the performance of seismic surveys of the PKMPV at the mines of the Talnakhskoe and Oktyabrskoe fields (Norilsk), seismograms of a common vibration point were obtained in several profiles. The uniqueness of the seismic research methodology lies in the vibration and registration of elastic waves in the roof of mine workings. The resulting seismograms are subjected to the procedures of primary filtration and assignment of the arrangement geometry. The following hodographs of elastic waves are read on seismograms: diffracted, refracted longitudinal, refracted transverse and reflected. Further tomographic processing of the data consists in the conversion of the read hodographs of elastic refracted and refracted waves in velocity using the Fourier transform. Qualitative interpretation provides for the identification and tracing in the context of anomalous areas or zones related to various geomechanical processes.

The main criteria for the occurrence of the process of rocks decompression is a decrease in the propagation velocities of longitudinal and transverse elastic waves. On seismotomographic sections of longitudinal and transverse waves of the region of increased velocities, areas where a stress state occurs due to tectonophysical effects that resonate in rocks are identified.

Another unfavorable geomechanical process in mining is the increased water inflow into the mine, which occurs due to water seepage from overlying water-bearing stratum in the field of geomechanical destruction processes. The characteristic of the areas of potential water occurrences into the mine at seismic sections is revealed as follows: a gradual decrease in the propagation velocities of longitudinal waves, a decrease in the propagation velocities of transverse waves, an increase in the velocity ratio. The obtained sections show anomalous regions characterized by reduced velocities of longitudinal and transverse waves, as well as reduced velocity ratios in the area of pickets 30-40, 60-70, 80-92, 120-135 m (Fig.1), which indicates the presence of rock decompression areas in localized areas. Further quantitative interpretation implies the calculation of transformants and the classification of the obtained high-speed tomographic sections [37].

The transformed sections obtained as a result of applying the procedures indicated in the table are subjected to a qualitative assessment for information content, namely, the preservation of abnormal areas on the sections, minimal distortion of the original data array. These requirements are met by seismic tomographic sections transformed by averaging in a sliding window (Fig.2). On the sections, it is possible to clearly trace areas with average and increased velocity values, which corresponds to zones of tension on the source materials, areas of reduced velocity values, and decompressed rocks. The most reliable picture of the geophysical properties occurred in the case of considering the section of the ratio of the velocities of transverse waves to longitudinal ones [41]. The need to select the most informative filtering results arises from the transition to the next stage of classification [39].

Discussion of results. Examples of visualization of classification results by combined V_s, V_p and V_s/V_p matrices are shown in Fig.3: *a* – the method of total distance, *b* – the method of dynamic thickening (*K*-means), *c* – by the separation method of multidimensional normal networks (according to A.V.Petrov), *d* – by the method of sign classification. Obviously, the most informative results are the classifications performed by the method of separation of multidimensional normal networks (Fig.3, *c*) and dynamic thickenings (*K*-means) (Fig.3, *b*) due to the better localization of anomalous regions and their connection with the initial data [41]. However, when filling in the missing values, edge effects have a strong influence on the final representation of the sections, which can be mistaken for abnormal indicators during interpretation. That is why it is important to analyze a priori and transformed materials to exclude incorrect conclusions [42, 43].

The method of dynamic thickening (*K*-means) is an effective way to classify multidimensional values in conditions of a minimum of a priori information about class centers through the use of *K*-means (where *K* is the number of classes) [35]. For all processed features, the value of the standard deviation is estimated, which is also given when filtering by the standard deviation method using normalization and the creation of new vector class centers. The main advantage of this method is fast convergence; the disadvantage is incomplete consideration of correlations of the feature space [23, 44]. It is the classification by the method of dynamic thickening that is chosen as the basis of the interpretative model as the most informative, since when compared with a priori sections (see Fig.1), abnormal areas are very reliably revealed in Fig.3, *b*.

In total, eight classes are allocated on the interpretative model: the 1st class corresponds to the appearance of boundary effects and localization of maximum velocity values; the 2nd class characterizes the appearance of zones of mechanical disturbances or increased stresses; the 3rd-6th classes emphasize the contours of the distribution of the main blocks characterized by the same type of signs, divided into subgroups for more convenient identification during subsequent interpretation; the 7th class accumulates signs with reduced velocity values; the 8th class accumulates signs with the most cartelized indicators. For direct interpretation, classes 2 and 8 are of the greatest interest, since it is based on them that it is possible to most reliably determine the zones of localization of stress states.

The resulting interpretative model (Fig.4) demonstrates the position of anomalous sections along the studied profile, which correspond to zones of potential excess of the normal deformation state of the studied rock mass. It is these zones that pose the greatest danger when planning underground work and require additional measures to ensure a safe working process while minimizing economic and technological risks. The comparison of the obtained localized zones with the materials of primary study, namely, with the visualized matrices of longitudinal and transverse waves along the studied profile, confirms the correctness of the application of the methodology for classifying seismic data by analogy with geopotential fields [38, 45]. The involvement of the petrophysical characteristics of the studied rock mass makes it possible to identify patterns of mapping elastic properties represented by longitudinal and transverse waves in two-dimensional space [46, 47].

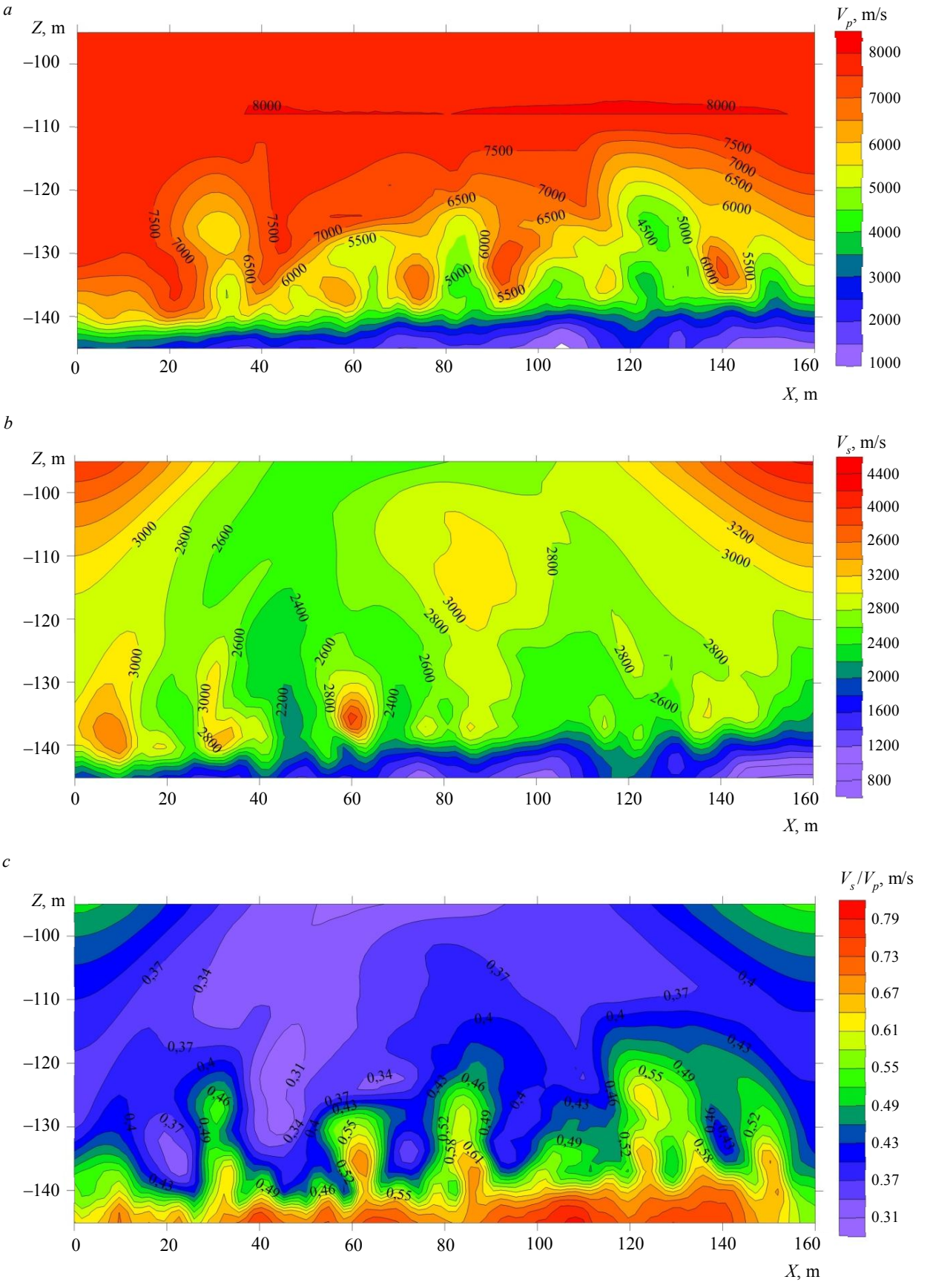

Fig.2. An example of visualization of calculated transformants by averaging in a sliding window obtained for matrices of longitudinal (*a*), transverse (*b*) velocities and velocity ratios (*c*)

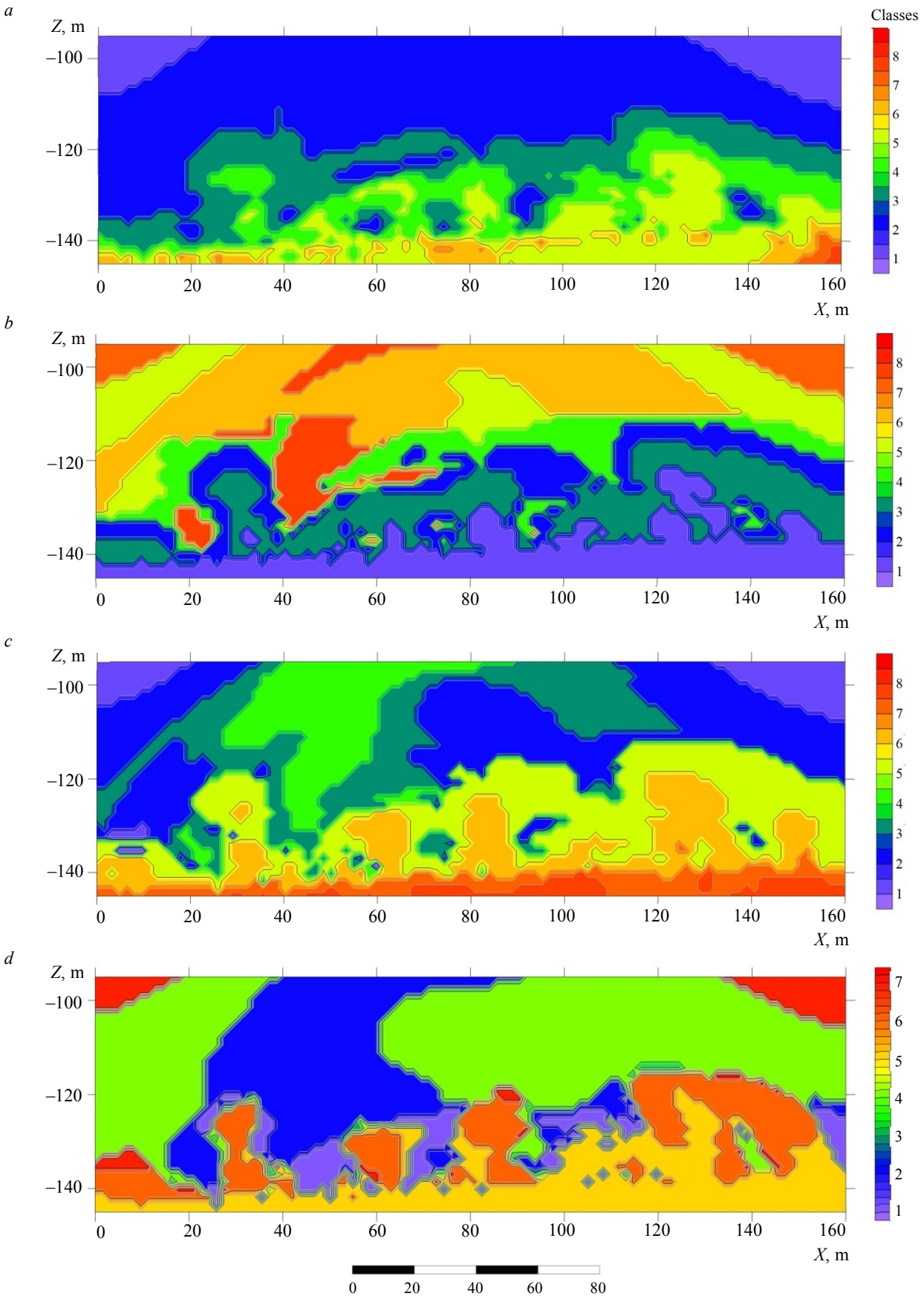

Fig.3. Classification results: *a* – the method of total distance; *b* – the method of dynamic thickening (*K*-means); *c* – the method of separation of multidimensional normal networks; *d* – the method of sign classification

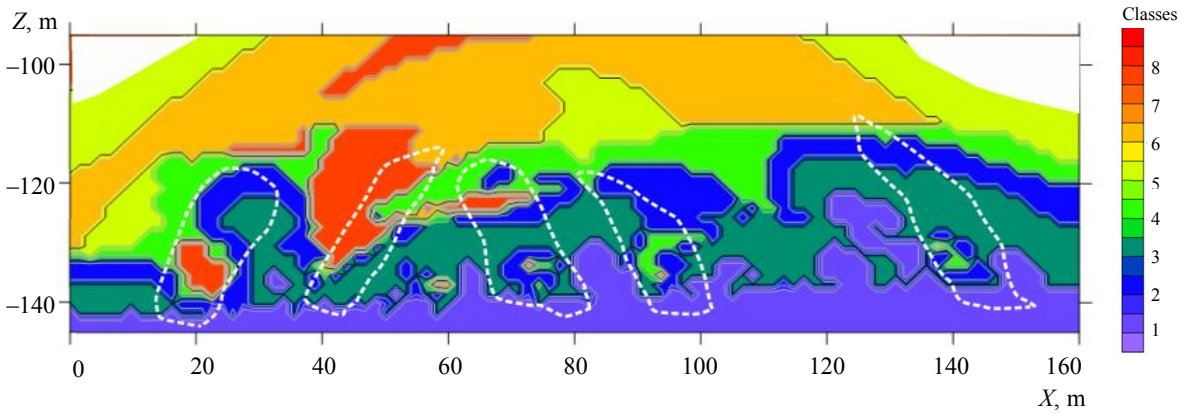

Fig.4. An interpretative model based on a priori information, transformation and classification of seismic data

Conclusion. When predicting the stress-strain state of a rock mass within the framework of mining planning, it becomes necessary to develop a methodological approach to data research and analysis with the involvement of additional tools. The geological conditions of the Talnakhskoe and Oktyabrskoe fields were considered as the object of research. The object under study is an underground mine under development in complicated operating conditions due to its sufficient proximity to the surface and the high probability of water inflow into the mine due to the development of hidden geomechanical processes.

As a result of seismic surveys, the technology for determining the nature of the propagation of elastic waves in the roof of the mine working was tested. Further work consisted in a sequential selection of qualitative data and testing of the methodology for complex processing and interpretation of seismic data using the method of transformation and classification analysis applied for geopotential fields. The novelty of the work lies in the use of effective tools that have proven themselves well when working with potential geophysical fields for data reflecting the elastic characteristics of the medium under study. This method is modernized and requires further testing on data obtained in more complex geological and technical conditions. In addition, the results demonstrate the potential for expanding the use of seismic survey technologies at the processing and interpretation stage compared with conventional approaches to analyzing profile data in the form of seismograms or images.

The proposed method of processing and interpreting seismic data with subsequent transformations and classification allows to proceed to the compilation of an interpretative model reflecting the position of the contours of the most dangerous zones (Fig.4). The interpretative model can serve as a basis for planning the safe conduct of underground mining operations, taking into account the identified intervals of increased geomechanical risk (decompressed areas, areas of stress, flooded areas).

Thus, the use of seismic data transformation in combination with the classification method in solving the problem of anomalous areas localization prone to the development of geomechanical risks makes it possible to quickly and most reliably identify areas that are dangerous from the point of view of intensification of geomechanical processes. The application of the seismic data transformation technique indicates the prospects of using modern geophysical technologies in modeling the behavior of a rock mass, taking into account the impact of operational and mechanical loads.

REFERENCES

1. Demenkov P.A., Romanova E.L. Analysis of approaches to calculation of vertical shaft support in tectonic disturbance zones. *News of the Tula state university. Sciences of Earth.* 2022. Iss. 4, p. 223-236 (in Russian).

2. Abramkin N.I., Efimov V.I., Mansurov P.A. Empirical techniques for assessing rock massif condition. *News of the Ural State Mining University.* 2021. Iss. 4 (64), p. 109-115 (in Russian). DOI: 10.21440/2307-2091-2021-4-109-115

3. Lomov M.A., Konstantinov A.V. Results analysis of seismic monitoring of the Kukisvumchorrskoye field. *Problems of Subsoil Use.* 2022. N 1 (32), p. 38-44 (in Russian). DOI: 10.25635/2313-1586.2022.01.038

4. Chepelenkova V.D., Lisitsa V.V. Application of discrete element method to estimation of strength properties of elastic media. XVIII Mezhdunarodnyi nauchnyi kongress i vystavka "Interekspo GEO-Sibir", 18-20 May 2022, Novosibirsk, Russia. Interekspo GEO-Sibir, 2022. Vol. 2. N 2, p. 209-214 (in Russian). DOI: 10.33764/2618-981X-2022-2-2-209-214

5. Dashko R.E., Romanov I.S. Safety of mining in the Kupol deposit based on the analysis and evaluation of geological processes in underground mine (CHAO, Anadyr District). *Eurasian Mining*. 2022. N 1, p. 85-89. DOI: 10.17580/em.2022.01.18

6. Kozyrev A.A., Savchenko S.N., Panin V.I. et al. Geomechanical processes in the geological environment of mining systems and geodynamic risk management. Apatity: Kolskii nauchnyi tsentr Rossiiskoi akademii nauk, 2019, p. 431 (in Russian). DOI: 10.37614/978.5.91137.391.7

7. Alexandrov P.N., Krizsky V.N. Direct and Inverse Problem of Geoelectrics in Bianisotropic Media Based on Volume Integral Equations. *Physics of the Solid Earth.* 2022. Vol. 58. N 3, p. 379-393 (in Russian). DOI: 10.1134/S1069351322030016

8. Rasskazov I.Ju., Saksin B.G., Potapchuk M.I., Anikin P.A. The Researches of Burst-Hazard on Mines in Russian Far East. ISRM European Rock Mechanics Symposium – EUROCK 2018, 22-26 May 2018, Saint Petersburg, Russia. OnePetro, 2018. N ISRM-EUROCK-2018-014.

9. Lomov M.A., Sidlyar A.V. Estimation of rockburst hazard factors of the Nikolaev deposit with the use of 3D modelling results of seismoacoustic monitoring. *Problems of Subsoil Use.* 2021. N 1 (28), p. 64-72 (in Russian). DOI: 10.25635/2313-1586.2021.01.064

10. Protosenya A.G., Iovlev G.A. Prediction of spatial stress-strain behavior of physically nonlinear soil mass in tunnel face area. *Mining Informational and Analytical Bulletin.* 2020. N 5, p. 128-139 (in Russian). DOI: 10.25018/0236-1493-2020-5-0-128-139

11. Kutepova N.A., Moseykin V.V., Kondakova V.N. et al. Specificity of properties of coal processing waste regarding their storage. *Mining Informational and Analytical Bulletin*. 2022. N 12, p. 77-93. DOI: 10.25018/0236_1493_2022_12_0_77

12. Lomov M. 3D modeling system of seismoacoustic monitoring results at the Nikolaevskoye field. VIII International Scientific Conference "Problems of Complex Development of Georesources", 8-10 September 2020, Khabarovsk, Russia. E3S Web of Conferences, 2020. Vol. 192. N 04008. DOI: 10.1051/e3sconf/202019204008

13. Izotova V., Petrov D., Pankratova K., Pospehov G. Research of Acoustic Characteristics and Physical and Mechanical Properties of Quaternary Soils. *Engineering and Mining Geophysics*. 2020. Vol. 2020, p. 7. DOI: 10.3997/2214-4609.202051130

14. Fedotov S.A., Fedotov A.S. Optimization of seismic exploration technology in engineering and geophysical research. Inzhenernaya, ugolnaya i rudnaya geofizika-2015. Sovremennoe sostoyanie i perspektivy razvitiya, 28 sentyabrya – 2 oktyabrya 2015, Sochi, Rossiya. Sochi: Mezhregionalnaya obshchestvennaya organizatsiya Evro-Aziatskoe geofizicheskoe obshchestvo, 2015, p. 22-25 (in Russian).

15. Fengqiao Zhang, Lotfollah Pahlavan, Yuguang Yang. Evaluation of acoustic emission source localization accuracy in concrete structures. *Structural Health Monitoring*. 2020. Vol. 19. Iss. 6, p. 2063-2074. DOI: 10.1177/1475921720915625

16. Dolgal A.S., Kostitsyn V.I., Novikova P.N., Pugin A.V. Approximation algorithms of geopotential fields sourcewise functions. *Journal of Geophysics.* 2016. N 5, p. 4-10 (in Russian).

17. Fuentes J. Unraveling Soft Squeezing Transformations in Time-Variant Elastic Fields. *Dynamics*. 2023. Vol. 3, Iss. 2, p. 299-314. DOI: 10.3390/dynamics3020018

18. Bharti A.K., Prakash A., Verma A. et al. Mapping of decades-old underground coal mine workings using electrical resistivity tomography. *Journal of Earth System Science*. 2022. Vol. 131. Iss. 4. N 258. DOI: 10.1007/s12040-022-02008-7

19. Alekseev S.G., Bochkov P.A., Senchina N.P., Shtokalenko M.B. The Indication in the Potential Fields of Structures Controlling Diamondiferous Magmatism. Practical and Theoretical Aspects of Geological Interpretation of Gravitational, Magnetic and Electric Fields: Springer Proceedings in Earth and Environmental Sciences Proceedings of the 45th Uspensky International Geophysical Seminar, Kazan, Russia. Springer: Cham, 2019, p. 331-338. DOI: 10.1007/978-3-319-97670-9_38

20. Shabarov A.N., Kuranov A.D., Kiselev V.A. Assessing the zones of tectonic fault influence on dynamic rock pressure manifestation at Khibiny deposits of apatite-nepheline ores. *Eurasian Mining*. 2021. Vol. 36. Iss. 2, p. 3-7. DOI: 10.17580/em.2021.02.01

21. Egorov A.S., Prischepa O.M., Nefedov Y.V. et al. Deep Structure, Tectonics and Petroleum Potential of the Western Sector of the Russian Arctic. *Journal of Marine Science and Engineering*. 2021. Vol. 9. Iss. 3. N 258. DOI: 10.3390/jmse9030258

22. Sekerina D.D., Dergileva E.A., Egorov A.S. Location patterns of caledonianand hercynian orogeny structures, rudny Altai. *Regional Geology and Metallogeny.* 2023. N 93, p. 52-62 (in Russian). DOI: 10.52349/0869-7892_2023_93_52-62

23. Schiffer C., Tegner C., Schaeffer A.J. et al. High Arctic geopotential stress field and implications for geodynamic evolution. *Circum-Arctic Lithosphere Evolution*. London: Geological Society of London, 2018. Vol. 460, p. 441-465. DOI: 10.1144/SP460.6

24. Yakovleva A.A., Movchan I.B., Shaygallyamova Z.I. Dynamic response of multi-scale geophysical systems: waves and practical applications. *Philosophical Transactions of the Royal Society A: Mathematical, Physical and Engineering Sciences.* 2022. Vol. 380. Iss. 2237. N 20210403. DOI: 10.1098/rsta.2021.0403

25. Krizsky V.N., Aleksandrov P.N., Kovalskii A.A., Viktorov S.V. Magnetometry-based mathematical modeling of transient resistance of cathode polarized pipeline. *Science and Technologies: Oil and Oil Products Pipeline Transportation.* 2022. Vol. 12. N 1, p. 68-79 (in Russian). DOI: 10.28999/2541-9595-2022-12-1-68-79

26. Raguzin I.I., Bykova E.N., Lepikhina O.Yu. Polygonal Metric Grid Method for Estimating the Cadastral Value of Land Plots. *Lomonosov Geography Journal.* 2023. Vol. 78. N 3, p. 92-103 (in Russian). DOI: 10.55959/MSU0579-9414.5.78.3.8

27. Kerimov I.A, Petrov A.V., Abubakarova E.A. The Use of Software Complex "Koskad 3D" to Analyze Potential Fields of Terek-Caspian Arch. *Dagestan State Pedagogical University. Natural and Exact Sciences.* 2018. Vol. 12. N 3, p. 88-96 (in Russian). DOI: 10.31161/1995-0675-2018-12-3-88-96

28. Bogoslovsky V.A., Samokhin A.V., Zhigalin A.D. Ecological monitoring of underground gas storehouses with geophysical methods. *Geoekologiya. Inzheneraya geologiya, gidrogeologiya, geokriologiya.* 2011. N 5, p. 465-473 (in Russian).

29. Kholmskii I., Eltsov T., Gulin V. et al. Real Time Monitoring of Seismic Survey Works Using Unmanned Aerial Systems. *83rd EAGE Annual Conference & Exhibition*. 2022. Vol. 2022, p. 5. DOI: 10.3997/2214-4609.202210988

30. Arkhipova E.V., Zhigalin A.D., Bryantseva G.V. et al. Features of long-term seismicity variations of active megastructures of the modern Earth. *Bulletin of Dubna International University for Nature, Society, and Man. Series: Natural and Engineering Sciences.* 2019. N 1 (42), p. 3-12 (in Russian).

31. Popov M.G., Popova O.G. The possibility of complex studying for the geological environment during seismic-ecological monitoring in areas of increased environmental danger. *Geology and Geophysics of Russian South.* 2021. Vol. 11. N 2, p. 152-166 (in Russian). DOI: 10.46698/VNC.2021.29.52.011

32. Bykowa E., Skachkova M., Raguzin I. et al. Automation of Negative Infrastructural Externalities Assessment Methods to Determine the Cost of Land Resources Based on the Development of a "Thin Client" Model. *Sustainability*. 2022. Vol. 14. Iss. 15. N 9383. DOI: 10.3390/su14159383

33. Phan T.H., Petrov A.V., Do M.P. et al. Geological structure of central Vietnam by interpretation processing of gravitational survey data using the "COSCAD 3D" computer technology. *Proceedings of higher educational establishments. Geology and Exploration.* 2020. Vol. 63. N 5, p. 77-90 (in Russian). DOI: 10.32454/0016-7762-2020-63-5-77-90

34. Dolgal A.S. Additive Technologies of Localization of the Geopotential Field Sources. *Bulletin of Perm University. Geology.* 2019. Vol. 18. N 4, p. 380-385 (in Russian). DOI: 10.17072/psu.geol.18.4.380

35. Popov M.G., Popova O.G. Study of Changes in Time and in Space of Stressed State of Geological Environment. *Geology and Geophysics of Russian South.* 2020. Vol. 10. N 3, p. 79-93 (in Russian). DOI: 10.46698/VNC.2020.43.14.005

36. Popova O.G., Popov M.G. Assessment of the geoenvironment stress state at the Caucasian mineral waters test plot using long-term seismic-ecological monitoring. *Geoekologiya. Inzheneraya geologiya, gidrogeologiya, geokriologiya.* 2019. N 5, p. 15-22 (in Russian). DOI: 10.31857/S0869-78092019515-22

37. Shabarov A.N., Zubkov V.V., Krotov N.V. et al. Choice of design decisions on development of fields taking into account results of geodynamic division into districts and geometrizations of dangerous zones. *Journal of Mining Institute.* 2013. Vol. 205, p. 66-69 (in Russian).

38. Balk P.I., Dolgal A.S., Pugin A.V. et al. Effective algorithms for sourcewise approximation of geopotential fields. *Izvestiya, Physics of the Solid Earth*. 2016. Vol. 52. Iss. 6, p. 896-911. DOI: 10.1134/S1069351316050025

39. Liu Q., Gu Y.J. Seismic imaging: From classical to adjoint tomography. *Tectonophysics*. 2012. Vol. 566-567, p. 31-66.

40. Putikov O., Kholmyanski M., Ivanov G., Senchina N. Application of geoelectrochemical method for exploration of petroleum fields on the Arctic shelf. *Geochemistry*. 2020. Vol. 80. Iss. 3. N 125498. DOI: 10.1016/j.geoch.2019.02.001

41. Mingaleva T., Gorelik G., Egorov A., Gulin V. Correction of Depth-Velocity Models by Gravity Prospecting for Hard-to-Reach Areas of the Shelf Zone. *Mining Informational and Analytical Bulletin.* 2022. N 10-1, p. 77-86 (in Russian). DOI: 10.25018/0236_1493_2022_101_0_77

42. Cheremisina E.N., Finkelshtein M.Ya., Deev K.V., Bolshakov E.M. GIS INTEGRO. Status and prospects for development in the context of import substitution. *Russian Oil and Gas Geology.* 2021. N 3, p. 31-40 (in Russian). DOI: 10.31087/0016-7894-2021-3-31-40

43. Cheremisina E.N., Senner A.E. The use of GIS INTEGRO in searching tasks for oil and gas deposits. *Computer Research and Modeling*. 2015. Vol. 7. N 3, p. 439-444. DOI: 10.20537/2076-7633-2015-7-3-439-444

44. Grigorev G., Islamuratov M., Bondarev E. et al. D-seis: digital field exploration twin. *Second EAGE Digitalization Conference and Exhibition*. 2022. Vol. 2022, p. 5. DOI: 10.3997/2214-4609.202239010

45. Zaycev S.V., Ahmetsafin R.D., Budennyj S.A. et al. Usage of Machine Learning Algorithms for Structural Boundaries Reconstruction Using the Non-Seismic Methods Data with Feature Selection. *Data Science in Oil and Gas*. 2021. Vol. 2021, p. 6. DOI: 10.3997/2214-4609.202156005

46. Buddo I.V., Shelokhov I.A., Misyurkeeva N.V., Agafonov Y.A. Transient electromagnetic sounding in 2D, 3D, and 4D modes: sequence of geological exploration activities. *Geodynamics & Tectonophysics.* 2021. Vol. 12. N 3S, p. 715-730 (in Russian). DOI: 10.5800/GT-2021-12-3s-0549

47. Ponomarenko M.R., Kutepov Y.I., Volkov M.A., Grinuk A.P. Satellite methods within integrated land surface deformation monitoring in a mine field. *Mining Informational and Analytical Bulletin.* 2020. N 12, p. 103-113 (in Russian). DOI: 10.25018/0236-1493-2020-12-0-103-113

***Authors*: Sergei M. Danilev,** *Candidate of Geological and Mineralogical Sciences, Associate Professor, https://orcid.org/0000-0003-3057-8527* (*Empress Catherine II Saint Petersburg Mining University, Saint Petersburg, Russia*), **Darya D. Sekerina**, *Postgraduate Student, https://orcid.org/0000-0003-3892-7947* (*Empress Catherine II Saint Petersburg Mining University, Saint Petersburg, Russia*), **Natalya A. Danileva,** *Candidate of Geological and Mineralogical Sciences, Associate Professor, Danileva_na@pers.spmi.ru, https://orcid.org/0000-0001-7707-6204* (*Empress Catherine II Saint Petersburg Mining University, Saint Petersburg, Russia*).

The authors declare no conflict of interests.

ISSN 2411-3336; e-ISSN 2541-9404

JOURNAL OF MINING INSTITUTE
Zapiski Gornogo instituta
Journal homepage: pmi.spmi.ru

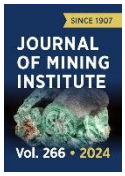

Research article

Modeling the efficiency of seasonal cooling devices when changing the statistical distribution of weather conditions

Oleg M. Ermilov[1], **Anton A. Dzhalyabov**[2], **Gennadii G. Vasilev**[3], **Igor A. Leonovich**[3]✉
[1] *OOO Gazprom Dobycha Nadym, Nadym, Russia*
[2] *OOO Gazprom Dobycha Noyabrsk, Noyabrsk, Russia*
[3] *Gubkin Russian State University of Oil and Gas, Moscow, Russia*

***How to cite this article*:** Ermilov O.M., Dzhalyabov A.A., Vasilev G.G., Leonovich I.A. Modeling the efficiency of seasonal cooling devices when changing the statistical distribution of weather conditions. Journal of Mining Institute 2024. Vol. 266, p. 272-282.

Abstract. The climatic factor of warming, which is evidenced by a significant number of scientists and research teams in Russia and the world, has a significant impact on the cryogenic state of permafrost soil, the preservation of which is one of the most common principles of construction in the North. The influence of projected climatic changes in planning up to 2050 on the efficiency of seasonal cooling devices, the principle of operation of which is based on seasonal soil freezing, is considered. The conducted modeling has shown that in a situation of stable climate, the preservation of the cryogenic state of permafrost soil is realized without the use of additional measures. With warming with a trend of 0.1 °C per year, seasonal cooling devices do not ensure the preservation of the current level of the cryogenic state of the soil and additional measures are required to increase their efficiency in the summer. In the case of more extreme warming with a rate of 0.25 °C per year, the modeling results show that seasonal cooling devices do not significantly affect the rate of soil thawing and the solution to the problem should be its complete replacement with systems with year-round action.

Keywords: permafrost; thermosiphon; seasonal cooling device; warming; climate; efficiency improvement

Received: 05.09.2022 ***Accepted: 20.09.2023*** ***Online: 06.12.2023*** ***Published: 25.04.2024***

Introduction. Promising areas for the development of the oil and gas industry in the Russian Federation tend to shift to the north and east. The development of the Yamal Gas production Center, the fields of the Gydan Peninsula, Yakutia and the Far East poses to oil and gas companies the most important task of high-quality and reliable operation of oil and gas sector facilities in conditions of continuous permafrost soil (PS).

The integrated development of deposits in the Arctic region of Russia involves the search for new methods of field exploration that would reduce the anthropogenic impact on PS by reducing the proportion of field stages of work [1, 2], new methods of field development with a reduction in thermal effects on frozen soil during drilling [3] or during construction and installation work [4], as well as new methods and technologies to ensure the reliability of the operation of fishing facilities in order to reduce the impact of emissions and leaks of extracted and transported products [5]. During the construction of natural gas production and transportation facilities in areas of continuous distribution of PS, their use is carried out according to the first principle – the preservation of permafrost during both construction [6, 7] and operation [8, 9]. Violation of the operating conditions of the soil in a cryogenic state can lead to catastrophic consequences of a natural and man-made nature [10, 11], which cause significant damage to the fragile ecosystem of the northern regions. The analysis of scientific works on Arctic exploration methods shows that at each stage of the life cycle of an industrial facility, the task of reducing the thermal impact on frozen soil is solved both through the use of new structures of grounds and foundations [4, 7] and optimization of technological processes [1, 3].

A typical technical solution for the implementation of this principle is the use of various designs of seasonal cooling devices (SCD). A review of such systems was carried out in [12], and in the article [13] it is shown how soil thermal stabilization systems during construction in the cryolithozone allow maintaining the required negative base temperature or restoring degraded permafrost. The efficiency of SCD operation directly depends on the climatic conditions of the environment, and stationary climate models based on statistical data of the climate of the construction site are usually used in their design [14].

According to estimates by a significant number of scientists [15, 16] and international climate organizations [17], active climate warming processes are underway in Russia, especially pronounced in the northern latitudes [18, 19] of the Russian North. It is shown [16] that over the past 20 years, the Yamal territory has undergone an abnormal decrease in average annual temperatures, as well as the number of days per year with low temperatures. Reports [17] of the well-known climate group Intergovernmental Panel on Climate Change record annual warming in the range from 0.03 to 0.1 °C, and data from Roshydromet [18] for the North of Russia demonstrate warming dynamics above 0.1 °C. Such climatic changes can cause significant damage to the cryogenic state of the soil and lead to its thawing, which will lead to a significant decrease in the bearing capacity of pile grounds and foundations [20, 21].

In the works [22, 23] devoted to the state of SCD, the issues of damage and destruction of these structures during construction and operation or issues of SCD efficiency depending on various anthropogenic and technogenic factors are considered [24]. The problems of the stability of engineering structures under climate warming have been studied [25, 26], some issues of modeling the operation of SCD [27, 28] or assessing the stability of piles under thermal influence [29], but the problem of reducing the efficiency of existing SCDs due to global climate warming is not considered.

The purpose of this study was to evaluate the behavior of SCD in various climate models based on the current understanding of climate change in Russia and the world. The object of the study was the frozen ground – climate – SCD system, and the subject of the study was the stability of this system to climate change.

Methods. The simulation of the joint work of frozen soil and SCD in various climatic conditions using the Borey 3D software package has been performed. The Borey 3D complex is registered with Rospatent, N 2018660189 dated 08/17/2018. Certified and meets the requirements SP 25.13330.2012 (SNiP 2.02.04-88), RSN 67-87, STO Gazprom 2-2.1-435-2010, STO Gazprom 2-2.1-390-2009, GOST R ISO/m EXTRAVK 12119-2000, GOST R ISO 9127-94, GOST R ISO 9126-93, GOST R ISO 28806-90. Implements a mathematical apparatus for numerical simulation of the propagation of temperature fields in a soil mass, taking into account the phase transition of unfrozen water in the spectrum of negative temperatures. The software package has found practical application and was used by specialists in the framework of calculations of the use of SCD on PS [30, 31].

The main objective of the study is to assess the stability of PS to warming processes, to assess the rate of permafrost degradation in the presence of SCD, absence of SCD, as well as the application of methods to increase the effectiveness of SCD for the period from 2011 to 2051 in relation to the PS site, the parameters of which correspond to the typical geocryological picture of the Yamal Peninsula. The study included options for a stable climate, annual warming of 0.1 and 0.25 °C. At the same time, the possibility of changing the geocryological picture of PS sites in their natural state (without the use of SCD), with the use of SCD and the option of ensuring the operation of SCD in the summer was considered. The calculation model of the PS site is adopted in the form of a cube measuring 50×50×50 m, with specified soil conditions. As soils, the model uses plastically frozen loams typical of the Yamal Peninsula with the following parameters: density 1750-1840 kg/m^3; total humidity 0.124-0.181 units; plasticity number 0.114; degree of salinity 0.065-0.081 %; freezing point

–0.48 °C; without peat inclusions. A SCD with a depth of 10.5 m is installed in the center of the soil mass. A thermal well 1 is modeled in 0.5 m along the *Y*-axis, a thermal well 2 in 1 m, and a thermal well 3 in 2 m. The model cube displays the area that will be sampled to perform the calculation. A boundary condition of the third kind is assumed on the upper face of the model cube. The values for the calculation are presented in terms of wind speed, thickness and density of snow cover. The boundary conditions of zero heat flow are assumed on the side and bottom faces of the model cube. To solve the differential equation of heat propagation in the soil with phase transitions in the negative temperature spectrum, a method with a dynamuic division of the region into subdomains with an explicit and implicit computational scheme is used. A simple iteration method is used as an implicit computational scheme. To improve the convergence of the implicit method, the regularization method and dynamic time step selection are used. The website of the Borey 3D software package shows the results of positive verification of the applied computational models for problems with analytical solutions. Modeling of SCD operation is performed by setting boundary conditions of the second kind in the form of internal heat sources/sinks.

The prediction of the processes of PS state dynamics was carried out based on extrapolation of data from the Marresal climate station [32, 33]. Climatic indicators for a stable climate were obtained by processing statistical data (the average temperature of a five-day period and the average thickness of snow cover) for 2011-2021, which were repeated until 2051. The prediction of the parameters of the dynamics of climate data changes for the case of warming by 0.1 and 0.25 °C was carried out by increasing the temperature of a stable climate annually by the corresponding value. The 0.1 °C warming interval was adopted on the basis of the authors' approximation of real climate data from 1990-2020 [16], as well as estimates of the warming rate in the northern regions of Russia according to Roshydromet data for 1976-2016 [34], the 0.25 °C interval is based on the worst-case scenario of climate change in the northern territories of Russia by 10-12 °C at the end of 21 century according to the report [18]. The modeling period was adopted based on the calculation methodology of the Intergovernmental Panel on Climate Change (IPCC) [17].

Based on the wind speed range of 5-7 m/s typical for the Yamal Peninsula, the average wind speed of 6 m/s is assumed in the calculations. Data on the operating mode and characteristics of SCD TK32/12.M5-03 (FSA) coolant R-744 (carbon dioxide) presented in PC Borey 3D were used for modeling. A separate climate data model for the SCD capacitor has been developed for the option of switching the SCD operating mode in the summer. In this model, in the period from May 15 to October 15, the SCD capacitor is in a temperature field of –5 °C, and during the rest of the year, the climatic data of the SCD capacitor correspond to the climatic parameters of the temperature regime of the climate variant that is being modeled. Additionally, based on the analysis of climate dynamics with a warming trend of 0.25 °C, due to a significant increase in the summer period (the temperature is consistently above 0 °C) it was decided to consider the following mode of operation: from 01.01.2024, the mode is set from 01.05 to 31.10, and starting from 01.01.2025 – from 01.04 to 31.10.

Results. Under the condition of a stable climate, the simulation showed the preservation of the cryogenic state of the soil regardless of the use of SCD. Figure 1 shows the obtained data on the cryogenic state of the soil for 2050 in the absence of SCD (Fig.1, *a*), the presence of SCD for well 1 (Fig.1, *b*), the presence of SCD and the option of transferring it to work in the warm season for well 1 (Fig.1, *c*). Figure 2 shows the average annual data on the cryogenic state of the soil in a stable climate. In the absence of SCD, the depth of seasonal soil thawing by 2050 will be 1.6 m, which corresponds to the average level of thawing depth of the Yamal Peninsula today. In the presence of SCD, the depth of soil thawing will also be 1.6 m. When used in the variant of transferring SCD to work in the warm season, the depth of seasonal warming will decrease to 1.4 m. In the absence of SCD, the depth of the soil, below which the temperature does not exceed –1 °C, will be 3.5 m, in the presence of SCD – 2.5 m, and when used in the translation version SCD for work in the warmer months is 2.25 m. Analysis of these temperature fields showed that the presence of SCD lowers the temperature of frozen soil by 1 °C at a distance of 0.5 m from SCD, 0.8 °C at a distance

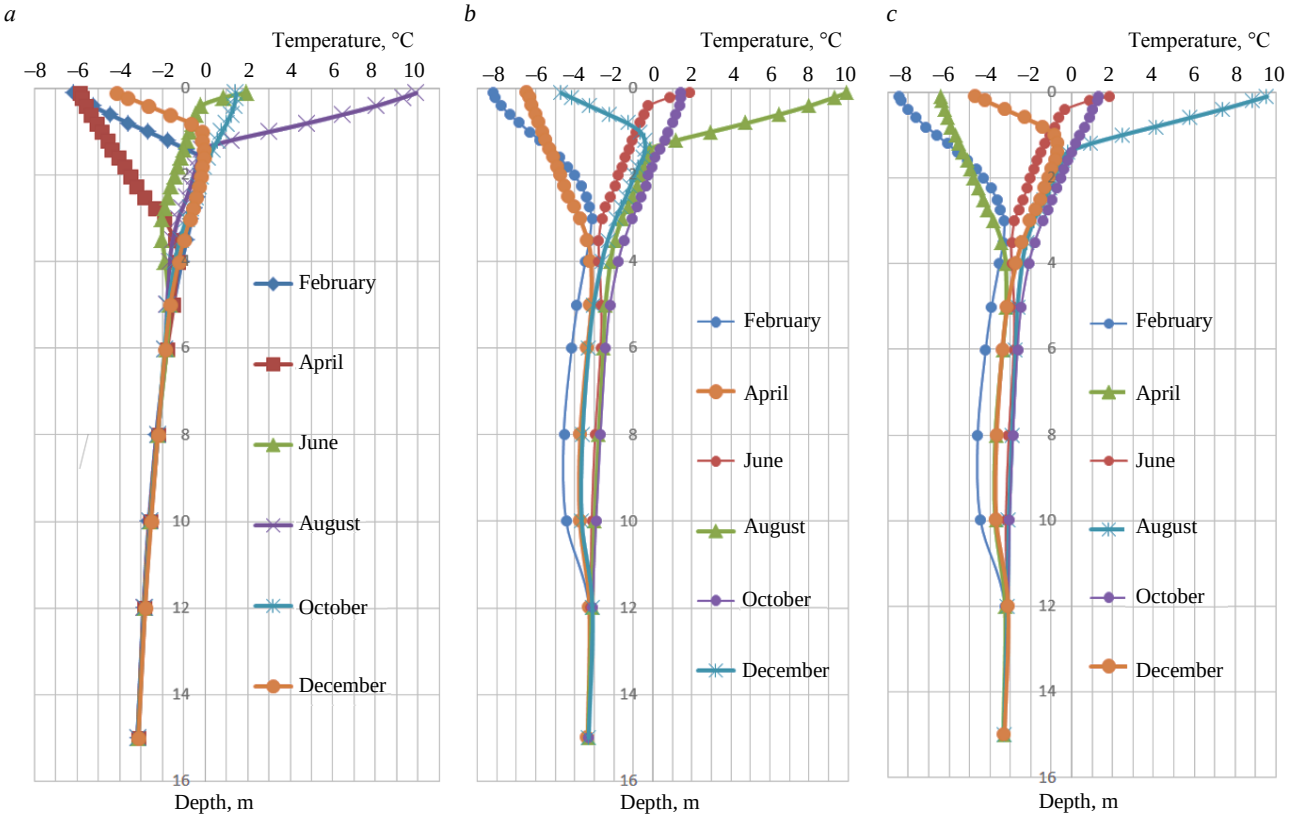

Fig.1. The state of frozen soil for a stable climate model for 2050

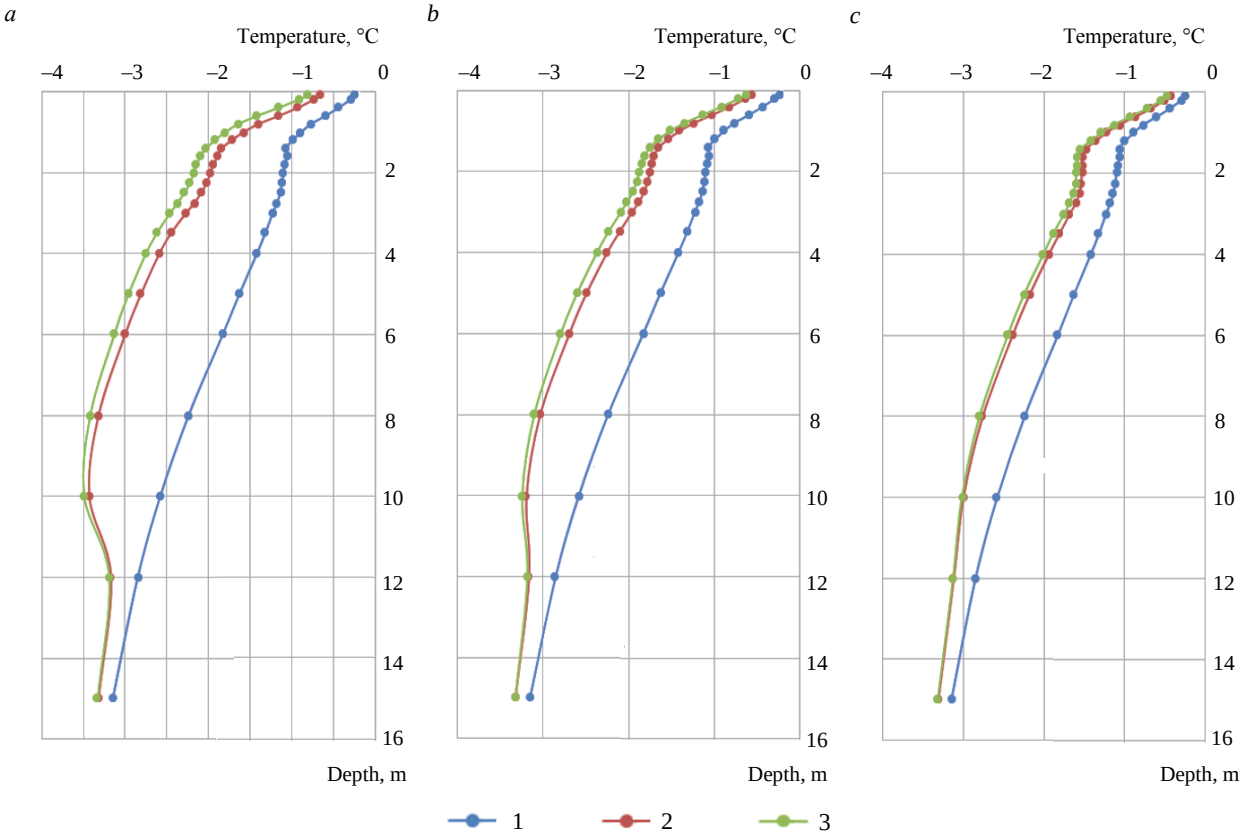

Fig.2. Forecast of the average annual soil temperature for 2050 with a stable climate:
a – thermal well 1; *b* – thermal well 2; *c* – thermal well 3
1 – without SCD; 2 – in the presence of SCD; 3 – in the presence of SCD and its transfer to work in the warm season

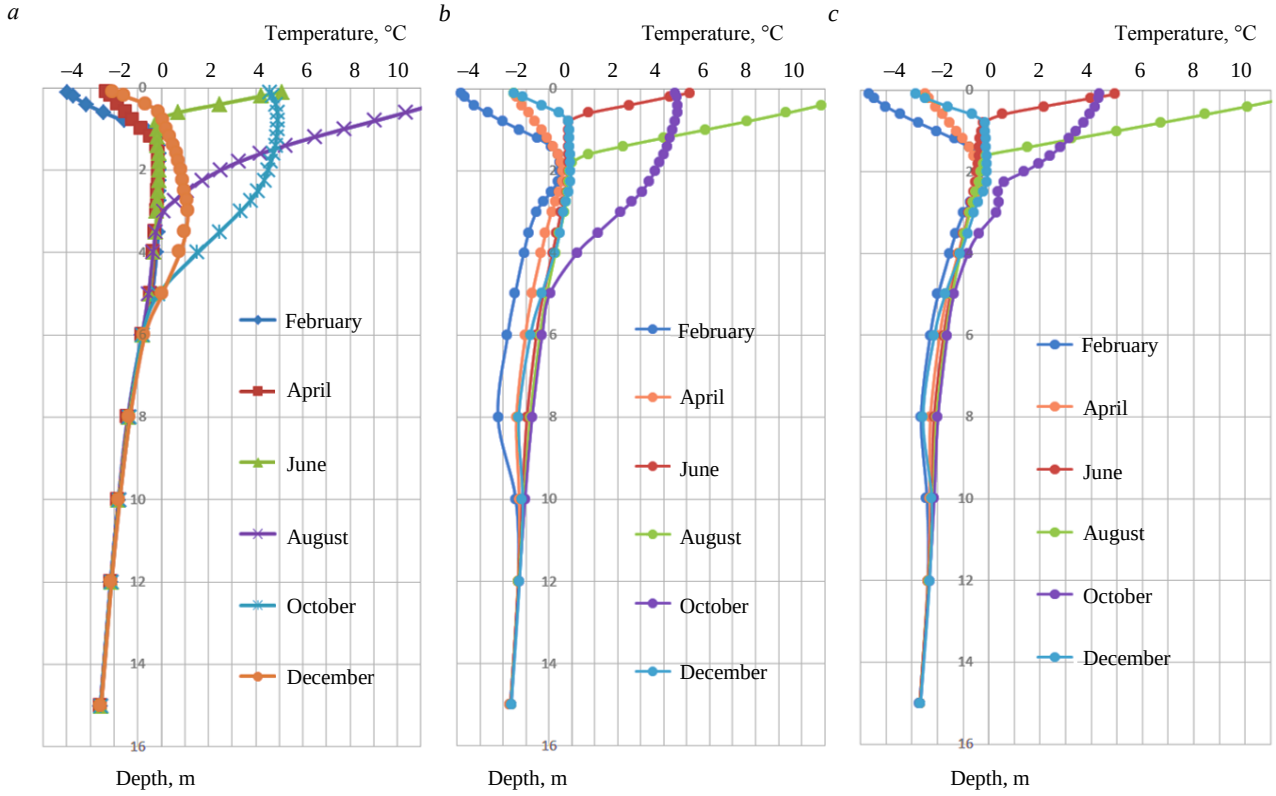

Fig.3. The state of frozen soil for the 0.1 °C warming model for 2050

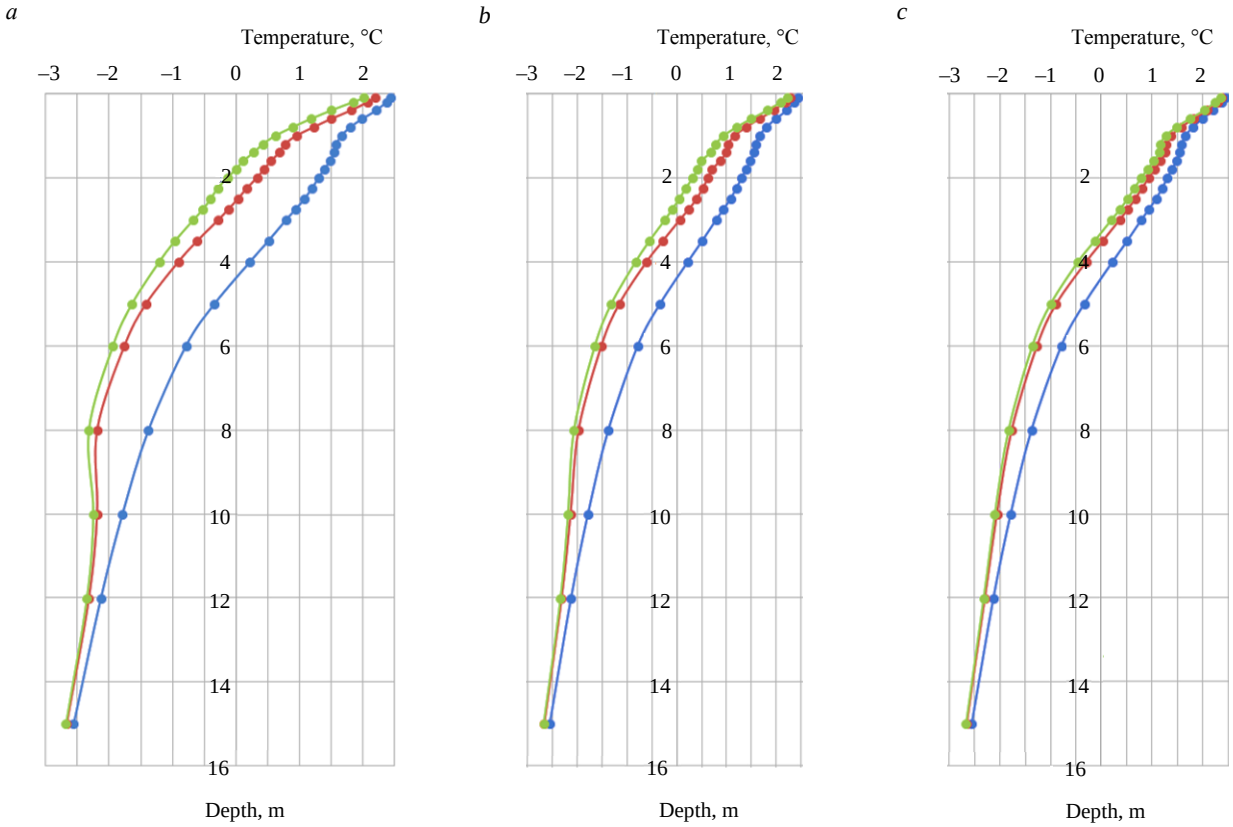

Fig.4. Forecast of the average annual ground temperature for 2050 with a warming of 0.1 °C:
a – thermal well 1; *b* – thermal well 2; *c* – thermal well 3
See the legend in Fig.2

of 1 m and 0.5 °C at a distance of 2 m. The use of SCD in the option of switching to work in the warm season will lower the average annual temperature of frozen soil in the depth range from 0.8 to 8 m by 0.5 °C at a distance of 0.5 m from SCD, 0.1 °C at a distance of 1 m from SCD and 0.07 °C at a distance of 2 m from SCD. For a stable climate, these changes are not critical, since the cryogenic state of the soil, sufficient for the effective functioning of the base, is preserved when using only SCD. However, even in this case, when used in the variant of transferring SCD to work in the warm season, the efficiency of its application increases by 15-20 %, depending on the distance from the SCD axis.

Figure 3 shows data on the cryogenic state of the soil for 2050 in the absence of SCD (Fig.3, *a*), the presence of SCD for well 1 (Fig.3, *b*), and the transfer of SCD to work in the warm season (Fig.3, *c*). Figure 4 shows the average annual data on the cryogenic state of the soil with a warming climate of 0.1 °C. In the absence of SCD, the depth of seasonal soil warming by 2050 it will be 5 m, which is significantly higher than the average depth of warming of the Yamal Peninsula at the moment (1.5-2.0 m). In the presence of SCD, the depth of soil thawing will be 4 m, when used in the variant of transferring SCD to work in the warm season, the depth of soil thawing will decrease to 3 m. In the absence of SCD, the depth of the soil, below which the temperature does not exceed –1 °C, will be 7 m by 2050, and in the presence of SCD – 5.5 m. When used in the variant of transferring SCD to work in the warm season, the permafrost layer with a temperature below –1 °C begins from a depth of 4 m, which practically corresponds to the natural state of the permafrost (3.5 m).

Analysis of these temperature fields showed that the presence of SCD lowers the temperature of frozen soil by 1.5 °C at a distance of 0.5 m from SCD, 1 °C at a distance of 1 m and 0.6 °C at a distance of 2 m. Using SCD in the option of switching to work in the warm season will lower the average annual temperature of frozen soil in the depth range from 0.8 to 8 m by 1.4 °C at a distance of 0.5 m from SCD, 1 °C at a distance of 1 m from SCD and 0.5 °C at a distance of 2 m from SCD. In such a climate model, the use of SCD in the variant of transferring to work in the warm season significantly affects the state of permafrost, increasing the efficiency of SCD application by 34-40 %. To estimate the rate of soil thawing, calculations and analysis of average annual temperatures for 2020-2050 were carried out. The average annual ground depth temperature in the model without SCD decreases by 1 °C from every 10 years and by 2050 it will be less than –1 °C, maintained from a depth of about 7 m. The presence of SCD reduced the rate of thawing by about 1 °C, and when transferring SCD to work in the warm season, it additionally lowered the temperature by 0.5 °C.

Figure 5 shows the temperature fields of the cryogenic state of the model soil with a warming of 0.1 °C. In the conditions of annual warming of 0.25 °C, modeling shows the degradation of the cryogenic state of the soil to a significant depth and large-scale thawing both in the absence of SCD and in its presence. The option of transferring SCD to work in the warm season does not have a significant positive effect for stabilizing the cryogenic state of the soil.

Data on the cryogenic state of the soil for 2050 are presented in the absence of SCD (Fig.6, *a*), the presence of SCD for well 1 (Fig.6, *b*) and the use of SCD in the option of transferring to work in the warm season (Fig.6, *c*). Figure 7 shows the average annual data on the cryogenic state of the soil with a climate warming of 0.25 °C. In the absence of SCD, the depth of seasonal soil thawing by 2050 will be 9 m, which is significantly higher than the average depth of thawing in the Yamal Peninsula now (1.5-2.0 m). In the presence of SCD, the depth of soil thawing will be 8 m. In the case of transferring SCD to work in the warm season, the depth of soil thawing will decrease to 6 m. In the absence of SCD, the depth of the soil, below which the temperature does not exceed –1 °C, by 2050 it will be 11 m, and in the presence of SCD – 10 m. The option of transferring SCD to work in the warm season did not affect this characteristic of the cryogenic state of the soil.

Data analysis of temperature fields shows that the presence of SCD will reduce the soil temperature by 0.5 °C at a distance of 0.5 m from SCD, 0.25 °C at a distance of 1 m, and 0.15 °C at

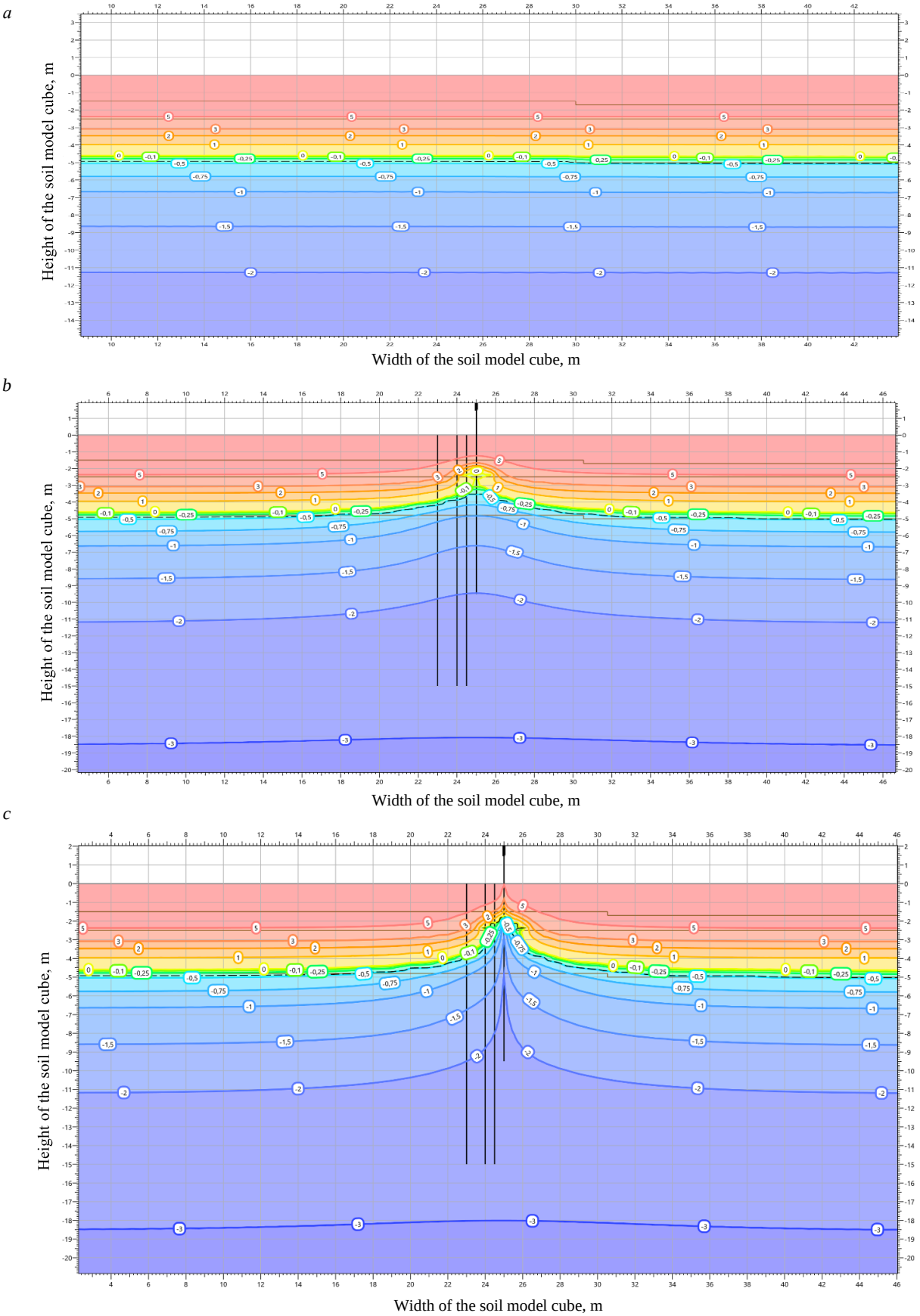

Fig.5. The temperature field of the model on 15.09.2050
The *X*-axis is indicated horizontally, the *Z*-axis is indicated vertically: *a* – in the absence of SCD; *b* – in the presence of SCD; *c* – when used in the variant of transferring SCD to work in the warm season

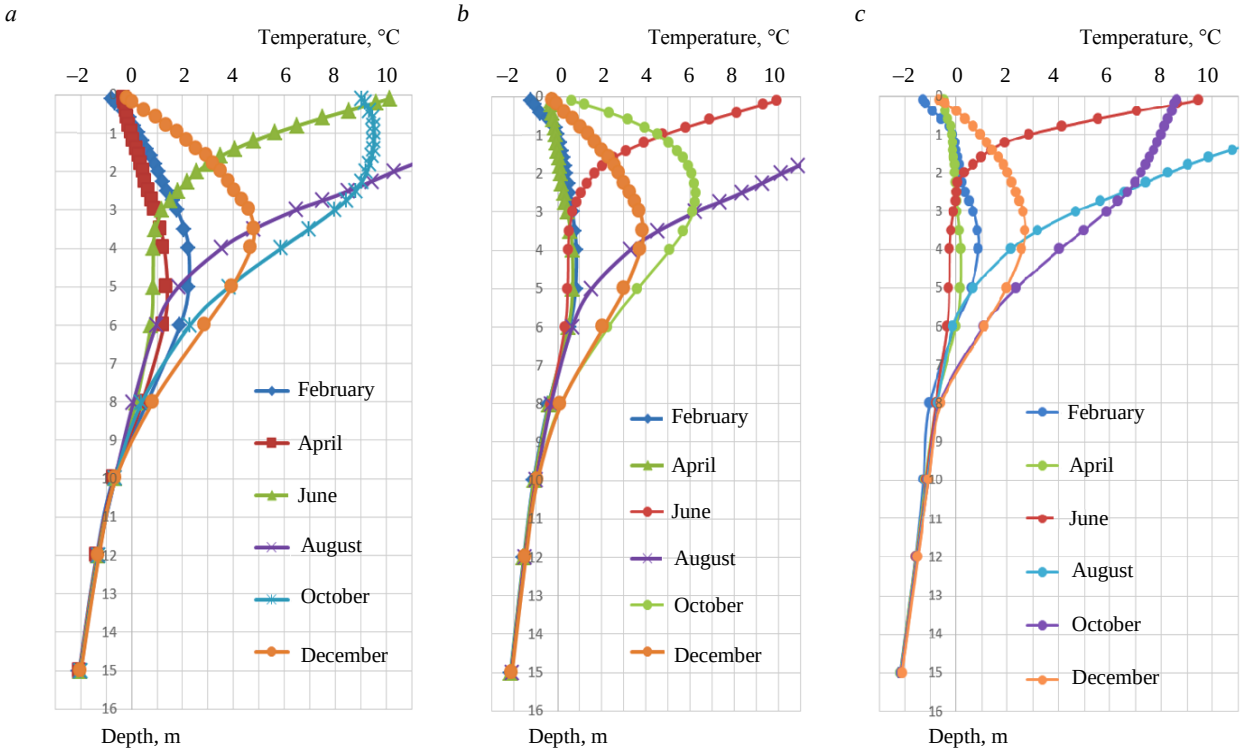

Fig.6. The state of the frozen ground for the 0.25 °C warming model for 2050

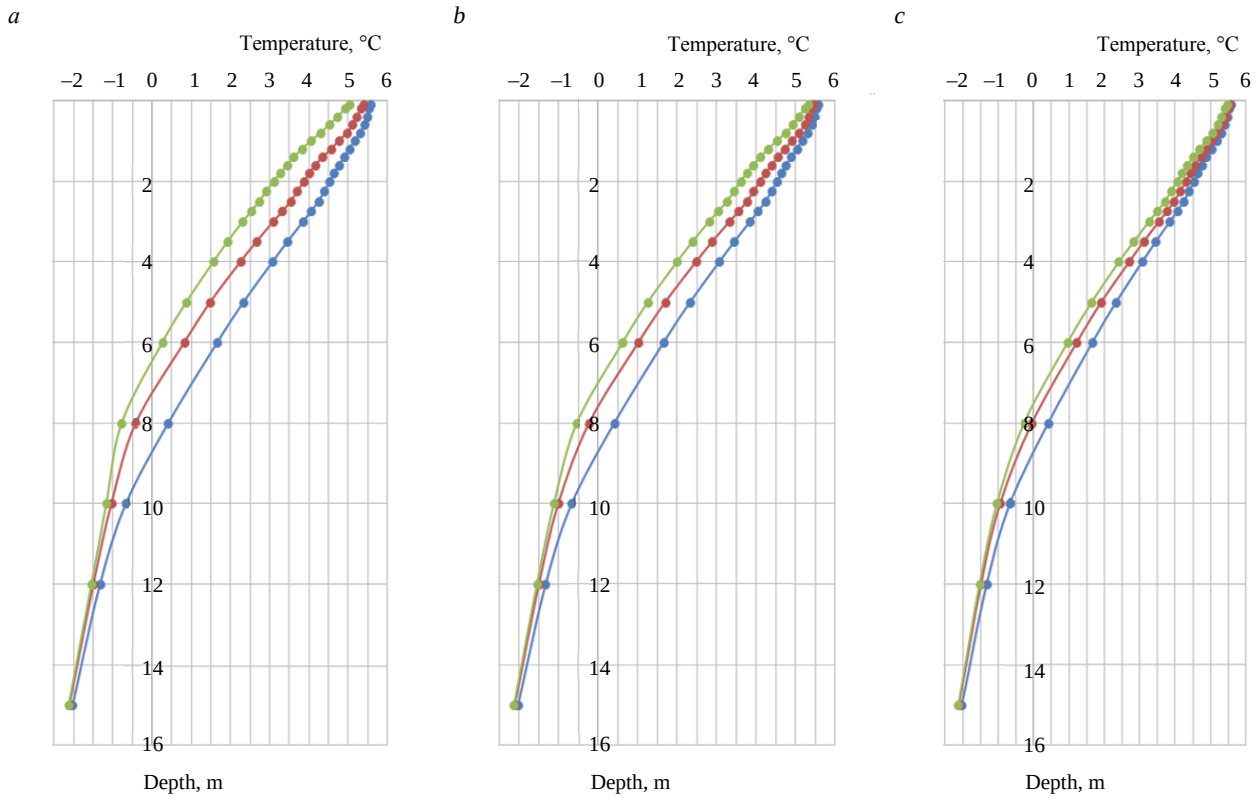

Fig.7. Forecast of the average annual ground temperature for 2050 with a warming of 0.25 °C:
a – thermal well 1; *b* – thermal well 2; *c* – thermal well 3
See the legend in Fig.2

a distance of 2 m. The option of switching SCD to work in the warm season will lower the soil temperature in the depth range from 0.8 to 8 m by 0.69 °C at a distance of 0.5 m from SCD, 0.44 °C at a distance of 1 m from SCD, and 0.23 °C at a distance of 2 m from SCD. At a warming rate of 0.25 °C, the presence of SCD did not actually have a significant effect on the cryogenic state of the soil. In this model, the option of transferring SCD to work in the warmer months has almost doubled the efficiency of using SCD. Nevertheless, this is not enough to prevent large-scale thawing of the soil and preserve the permafrost condition of the soils.

To estimate the rate of soil thawing, calculations and estimates of average annual temperatures for 2020-2050 were carried out. The presence of SCD reduced the intensity of soil thawing by an average of 0.5-1 °C, which makes it possible in practice to operate the soil mass in a frozen state for longer. The rate of warming of 0.25 °C per year for 10 years by 2030 will lead to the fact that in the presence of SCD, the depth of seasonal thawing will increase from 1.4 to 2 m, and the soil mass with a constant temperature below –1 °C will start from a depth of 3.5 m instead of 2.75.

Conclusion. The computational models proposed in the work made it possible to assess the stability of PS to warming processes and to estimate the rate of permafrost degradation for three climate variants: in the presence of SCD, in the absence of SCD, as well as the use of methods to increase the effectiveness of SCD. The modeling results showed that the efficiency of SCD decreases at any values of climate warming. The model with a warming trend of 0.1 °C per year demonstrates a large-scale thawing of PS over 30 years of operation, which will have an extremely negative impact on the bearing capacity of any pile foundations. The presence of SCD slows down the thawing trend, allows to almost halving the scale of soil warming, lower the temperature of the PS mass by 1-1.5 °C, but does not stop this process. If it is possible to transfer the device to work in the summer, it will be possible to maintain the level of permafrost without significant degradation.

A model with a warming trend of 0.25 °C per year (to assess the worst-case scenario) demonstrates catastrophic thawing of PS by 2050, SCD slightly slows down such thawing, allowing to lower the temperature of the PS mass by 0.3-0.8 °C, but does not stop this process. By 2050, in such a catastrophic model, despite the use of SCD, the depth of seasonal soil thawing will increase to 8 m at a normal depth of 1.5 m. The possibility of switching the device to work in the summer period will increase the efficiency of SCD, but not stop the process of soil thawing.

Forced year-round cooling systems built on various industrial refrigerating machines will be an effective solution to save energy in a scenario with a warming of 0.25 °C per year. However, using them to modernize the existing SCD infrastructure is practically impossible due to the significant number of individually installed SCDs and the large area of their installation.

The paper models the SCD operating mode, taking into account the option of transferring to work in the warm season. The modeling results showed that such a solution could increase the efficiency of SCD by 35-40 % and prevent soil thawing with the most likely forecast of warming by 0.1 °C per year.

REFERENCES

1. Bondar K.M., Minaev V.A., Faddeev A.O. Cost Estimate for Exploration of Oil and Gas Fields in the Arctic Zone. *IOP Conference Series: Materials Science and Engineering*. 2021. Vol. 1079. N 062069. DOI: 10.1088/1757-899X/1079/6/062069

2. Batin E.N., Dedov K.V., Kochegarova N.A. Arctic: the main directions of exploration and development, role in the oil and gas industry, transport system. *Science Time*. 2015. N 12 (24), p. 47-51.

3. Eppelbaum L.V., Kutasov I.M. Well drilling in permafrost regions: dynamics of the thawed zone. *Polar Research*. 2019. Vol. 38, p. 1-9. DOI: 10.33265/polar.v38.3351

4. Litvinenko V.S., Dvoynikov M.V., Trushko V.L. Elaboration of a conceptual solution for the development of the Artic shelf from seasonally flooded coastal areas. *International Journal of Mining Science and Technology*. 2021. Vol. 32. Iss. 1, p. 113-119. DOI: 10.1016/j.ijmst.2021.09.010

5. Grebnev Y., Moskalev A. Modelling the accidental oil spills at potentially hazardous facilities in the Arctic zone of Krasnoyarsk Krai. *IOP Conference Series: Earth and Environmental Science*. 2021. Vol. 816. N 012007. DOI: 10.1088/1755-1315/816/1/012007

6. Gilev N.G., Zenkov E.V., Poverenniy U.S. et al. Optimization of capital costs for pile foundations during construction of oil and gas production facilities on permafrost soil. *Oil Industry*. 2019. N 1, p. 46-49 (in Russian). DOI: 10.24887/0028-2448-2019-11-46-49

7. Rzaev Ch.T. Choosing the type of foundation structures on permafrost soils. Nauka segodnya: globalnye vyzovy i mekhanizmy razvitiya: Materialy mezhdunarodnoi nauchno-prakticheskoi konferentsii: v 2 chastyakh, 26 aprelya 2017, Vologda, Rossiya. Vologda: OOO "Marker", 2017. Part 1, p. 25-27 (in Russian).

8. Shepitko T.V., Lutsky S.Y., Nak G.I., Cherkasov A.M. Technological Features of Construction and Reconstruction of Geotechnical Structures in the Arctic Zone. *Designs*. 2022. Vol. 6. Iss. 2, p. 1-8. DOI: 10.3390/designs6020034

9. Gendler S., Prokhorova E. Risk-Based Methodology for Determining Priority Directions for Improving Occupational Safety in the Mining Industry of the Arctic Zone. *Resources*. 2021. Vol. 10. Iss. 3, p. 1-14. DOI: 10.3390/resources10030020

10. Bogoyavlensky V.I., Bogoyavlenskiy I.V., Kargina T.N. Catastrophic gas blowout in 2020 on the Yamal Peninsula in the Arctic. Results of comprehensive analysis of aerospace RS data. *Arctic: Ecology and Economy*. 2021. Vol. 11. N 3, p. 362-374 (in Russian). DOI: 10.25283/2223-4594-2021-3-362-374

11. Yakushev V.S., Semenov A.P., Bogoyavlensky V.I. et al. Experimental modeling of methane release from intrapermafrost relic gas hydrates when sediment temperature change. *Cold Regions Science and Technology*. 2018. Vol. 149, p. 46-50. DOI: 10.1016/j.coldregions.2018.02.007

12. Yarmak E. Permafrost Foundations Thermally Stabilized Using Thermosyphons. OTC Arctic Technology Conference, 23-25 March 2015, Copenhagen, Denmark. 2015. N OTC-25500-MS. DOI: 10.4043/25500-MS

13. Koloskov G.V., Ibragimov E.V., Gamzaev R.G. On the issue of choosing optimal systems for thermal stabilization of soils during construction in the cryolithozone. *Geotekhnika*. 2015. N 6, p. 4-11 (in Russian).

14. Abrosimov A., Zaletaev S. Soil coolers. Designs and calculation methods. London, United Kingdom: Palmarium Academic Publishing, 2012, p. 392 (in Russian).

15. Khrustalev L.N., Emelyanova L.V. Determination of the Temperature Coefficient for Calculation of the Bearing Capacity of Permafrost Beds in a Changing Climate. *Soil Mechanics and Foundation Engineering*. 2013. Vol. 50. N 1, p. 19-23. DOI: 10.1007/s11204-013-9204-1

16. Vasilev G.G., Dzhaljabov A.A., Leonovich I.A. Study of influence of climatic factor on dynamics of permafrost condition of soils beneath objects of oil and gas complex. *Proceedings of Gubkin University*. 2021. N 3 (304), p. 67-79 (in Russian). DOI: 10.33285/2073-9028-2021-3(304)-67-79

17. IPCC, 2022: Climate Change 2022: Impacts, Adaptation, and Vulnerability. Contribution of Working Group II to the Sixth Assessment Report of the Intergovernmental Panel on Climate Change. Ed. by H.-O.Pörtner, D.C.Roberts, M.Tignor. Cambridge, UK and New York, NY, USA: Cambridge University Press, 2022, p. 3056. DOI: 10.1017/9781009325844

18. Report on climate risks in the territory of the Russian Federation. Ed. bu V.M.Kattsova. St. Petersburg: Glavnaya geofizicheskaya observatoriya im. A.I.Voeikova, 2017, p. 106 (in Russian).

19. Anisimov O., Kokorev V. Cities of the Russian North in the Context of Climate Change. Sustaining Russia's Arctic Cities: Resource Politics, Migration, and Climate Change. 2016. Vol. 2, p. 141-174. DOI: 10.2307/j.ctvswx6s0.12

20. Nikiforova N.S., Konnov A.V. The bearing capacity of piles in permafrost soils under climate change. *Construction and Geotechnics*. 2021. Vol. 12. N 3, p. 14-24 (in Russian). DOI: 10.15593/2224-9826/2021.3.02

21. Nikiforova N.S., Konnov A.B. Influence of permafrost degradation on piles bearing capacity. *Journal of Physics: Conference Series*. Deep Foundations and geotechnical problems of territories, 26-28 May 2021, Perm, Russian Federation. 2021. Vol. 1928. N 012046. DOI: 10.1088/1742-6596/1928/1/012046

22. Strizhkov S.N. On the issue of the quality of operation of seasonally operating cooling devices. *Geoinfo: nezavisimyi elektronnyi zhurnal*. 2017. URL: http://www.geoinfo.ru/product/strizhkov-sergej-nikolaevich/k-voprosu-o-kachestve-raboty-sezonno-dejstvuyushchih-ohlazhdayushchih-ustrojstv-35150.shtml (accessed 15.08.2022) (in Russian).

23. Presnov O.M., Melikhov V.P., Zaytsev S.A., Slivina D.M. Construction of piles in permafrost conditions. *International Research Journal*. 2022. N 2 (116). Part 1, p. 41-43 (in Russian). DOI: 10.23670/IRJ.2022.116.2.006

24. Vasiliev G.G., Dzhalyabov A.A., Leonovich I.A. Study of the permafrost temperature mode of oil and gas objects foundation equipped by seasonally operating cooling devices. *Equipment and technologies for oil and gas complex*. 2021. N 4 (124), p. 75-80. DOI: 10.33285/1999-6934-2021-4(124)-75-80

25. Zhang A.A., Ashpiz E.S., Khrustalev L.N., Shesternev D.M. New way for thermal stabilization of permafrost under railway embankment. *Earth's cryosphere*. 2018. Vol. 22. N 3, p. 67-71 (in Russian). DOI: 10.21782/KZ1560-7496-2018-3(67-71)

26. Vasiliev G.G., Dzhaljabov A.A., Leonovich I.A. Analysis of the causes of engineering structures deformations at gas industry facilities in the permafrost zone. *Journal of Mining Institute*. 2021. Vol. 249, p. 377-385. DOI: 10.31897/PMI.2021.3.6

27. Loli M., Tsatsis A., Kourkoulis R., Anastasopoulos I. A simplified numerical method to simulate the thawing of frozen soil. *Proceedings of the Institution of Civil Engineers – Geotechnical Engineering*. 2019. Vol. 173, p. 1-49. DOI: 10.1680/jgeen.18.00239

28. Weismüller J., Wollschläger U., Boike J. et al. Modeling the thermal dynamics of the active layer at two contrasting permafrost sites on Svalbard and on the Tibetan Plateau. *The Cryosphere*. 2011. Vol. 5. Iss. 3, p. 741-757. DOI: 10.5194/tc-5-741-2011

29. Buslaev G., Tsvetkov P., Lavrik A. et al. Ensuring the Sustainability of Arctic Industrial Facilities under Conditions of Global Climate Change. *Resources*. 2021. Vol. 10. N 12, p. 1-15. DOI: 10.3390/resources10120128

30. Ryazanov A.V., Usachev A.A. Features of calculating the temperature regime of permafrost soils of the foundations of bored piles of bridge crossings. *Fundamenty*. 2021. N 4 (6), p. 49-51 (in Russian).

31. Ryazanov A.V. Features of the design of foundations of structures on permafrost soils in a warming climate. *Fundamenty*. 2021. N 1 (3), p. 10-13 (in Russian).

32. Bulygina O.N., Razuvaev V.N., Trofimenko L.T., Shvets N.V. Certificate of state registration of the database N 2014621485. Description of the data set of the average monthly air temperature at Russian stations. URL: http://meteo.ru/data/156-temperature#описание-массива-данных (accessed 06.09.2022) (in Russian).

33. Bulygina O.N., Razuvaev V.N., Aleksandrova T.M. Certificate of state registration of the database N 2014621201. Description of the data set of snow cover characteristics at meteorological stations in Russia and the former USSR. URL: http://meteo.ru/data/165-snow-cover#описание-массива-данных (accessed 06.09.2022) (in Russian).

34. Gruza G.V., Bardin M.Yu., Platova T.V. et al. The report on the peculiarities of the climate in the territory of the Russian Federation for 2016. Moscow: Rosgidromet, 2017, p. 70 (in Russian).

Authors: **Oleg M. Ermilov,** *Doctor of Engineering Sciences, Academician of the RAS, Deputy Chief Engineer for Science* (*OOO Gazprom Dobycha Nadym, Nadym, Russia*), **Anton A. Dzhalyabov,** *General Director, https://orcid.org/0000-0002-4269-5555* (*OOO Gazprom Dobycha Noyabrsk, Noyabrsk, Russia*), **Gennadii G. Vasilev,** *Doctor of Engineering Sciences, Professor, Head of the Department, https://orcid.org/0000-0002-9503-7337* (*Gubkin Russian State University of Oil and Gas, Moscow, Russia*), **Igor A. Leonovich,** *Candidate of Engineering Sciences, Associate Professor, ned.flander@mail.ru, https://orcid.org/0000-0001-9054-1537* (*Gubkin Russian State University of Oil and Gas, Moscow, Russia*).

The authors declare no conflict of interests.

ISSN 2411-3336; e-ISSN 2541-9404

JOURNAL OF MINING INSTITUTE

Zapiski Gornogo instituta

Journal homepage: pmi.spmi.ru

Research article

Predictive assessment of ore dilution in mining thin steeply dipping deposits by a system of sublevel drifts

Askar Zh. Imashev, Aigerim M. Suimbaeva✉, Aibek A. Musin
Abylkas Saginov Karaganda Technical University, Karaganda, Kazakhstan

***How to cite this article*:** Imashev A.Zh., Suimbaeva A.M., Musin A.A. Predictive assessment of ore dilution in mining thin steeply dipping deposits by a system of sublevel drifts. Journal of Mining Institute. 2024. Vol. 266, p. 283-294.

Abstract. The purpose of research is the study of stress-strain state of marginal rock mass around the stope and predictive assessment of ore dilution with regard for changes in ore body thickness in mining thin ore deposits on the example of the Zholymbet mine. Study of the specific features of the stress-strain state development was accomplished applying the methodology based on numerical research methods taking into account the geological strength index (GSI) which allows considering the structural features of rocks, fracturing, lithology, water content and other strength indicators, due to which there is a correct transition from the rock sample strength to the rock mass strength. The results of numerical analysis of the stress-strain state of the marginal part of the rock mass using the finite element method after the Hoek – Brown strength criterion made it possible to assess the geomechanical state in the marginal mass provided there are changes in ore body thickness and to predict the volume of ore dilution. It was ascertained that when mining thin ore deposits, the predicted value of ore dilution is influenced by the ore body thickness and the GSI. The dependence of changes in ore dilution values on the GSI was recorded taking into account changes in ore body thickness from 1 to 3 m. Analysis of the research results showed that the predicted dimensions of rock failure zone around the stopes are quite large, due to which the indicators of the estimated ore dilution are not attained. There is a need to reduce the seismic impact of the blasting force on the marginal rock mass and update the blasting chart.

***Keywords*:** ore dilution; thin ore bodies; numerical simulation; stress-strain state; geological strength index

Acknowledgments. The research was funded by the Science Committee of the Ministry of Science and Higher Education of the Republic of Kazakhstan (grant AP13268891).

Received: 14.03.2023 ***Accepted: 25.10.2023*** ***Online: 22.02.2024*** ***Published: 25.04.2024***

Introduction. In the world practice, mining of thin ore deposits is increasingly accomplished by a system of sublevel drifts [1-3]. The main advantage of such mining system is its high productivity, and among the main disadvantages are high losses and ore dilution. A high level of ore dilution leads to a growing cost of ore transportation and processing, and the cost of the mineral increases accordingly [4-6]. Research in the course of this work is aimed at establishing the dependence of ore dilution index on rating assessment values of the rock mass.

Various sets of measures and recommendations are used to significantly reduce ore dilution. They are associated with choice of the mining system in accordance with geological structure of the deposit and its stripping method, improvement of mining technology, changing the main parameters of mining systems, introducing additional elements to the technology used, separate mining of part of reserves, etc. There is a large number of methods for determining and accounting for ore dilution. Over the past decades, researchers such as S.Korigov [7], H.D.Jang [8], I.Masoumi [9], E.Villaescusa [10], A.Papaioanou [11], M.Marinin [12], S.N.Fomin [13], V.M.Lizunkin [14], I.N.Savich [15], S.M.Tkach [16], S.A.Batugin [17], I.V.Sokolov [18],

A.M.Pavlov [19], M.Mohseni [20], E.Topal [21], M.A.Hefni [22, 23], D.P.Cordova [24], T.R.Câmara [25], and others, made a great contribution to the development and improvement of the methodology for calculating ore dilution.

The problem of ore dilution in mining of thin deposits is urgent. A specific feature of the technology for mining thin deposits by a system of sublevel drifts is the above-plan ore dilution due to entrapment of adjacent host rock strata. For example, in the course of stoping at the Zholymbet mine, over-plan ore dilution occurs – the actual indicators reach 70-75 % whereas the approved design values dot not exceed 38 %. Based on the mining and geological occurrence conditions of ore deposits and capabilities of the mine, a system for mining sublevel drifts was adopted.

The purpose of the study is predictive assessment of primary ore dilution based on the study of structural features of the rock mass taking into account changes in ore body thickness during mining of thin ore deposits at the Zholymbet mine.

At the Zholymbet deposit, two gold-bearing areas are geographically separated from each other: Central and Southern. The Central area has the largest reserves, is most productive and offers a high potential. Two morphological types of ore bodies were identified: gold-bearing quartz veins and stockwork zones. The length of veins along the strike is 100-150 m, downdip to 100-150 m, thickness of veins ranges from 0.5 to 3.0 m, dip angle usually steep varying from 45 to 80°. Hardness factor *f* after M.M.Protodyakonov for quartz veins is 12-15, for stockwork ores – 10-15, and host rocks – 10-16. As for drillability, the rocks belong to category XVI. Volumetric weight of ores and rocks is on average 2.7 t/m^3.

Methods. Ore dilution level is determined by the morphological structure of ore deposits, the applied mining system, ore breaking parameters, structural and strength properties of the rock mass, the impact of blasting force on host rocks, the use of artificial support of mined-out area, natural stress field of rock mass, geometric characteristics of the vein, thickness and dip of the ore body [26].

The above indicators are classified [8] according to characteristics of drilling and blasting operations; design factors of the stoping face; mining and geological factors; human factors (mistakes of miners during drilling and blasting operations, incorrect prediction of the ore body outlines by mine surveyors, etc.).

In world practice, there are several methods for determining ore dilution. Two of them, according to research by R.C.Pakalnis [27], are most common:

- Ore dilution = Tons of rock mined × 100 / Tons of ore mined.
- Ore dilution = Tons of rock mined × 100 / (Tons of ore mined + Tons of rock mined).

The term “rock” refers to external dilution or unscheduled diluting rock mined, and the term “ore” refers to the material estimated for mining, i.e. drilled and blasted. L.M.Clark and R.C.Pakalnis proceeding from the volume of overbreak and dimensions of the working face, determined the Equivalent Linear Overbreak Slough (ELOS), which is an indirect quantitative indicator of ore dilution [24, 28]. ELOS and ore dilution indicators are determined as follows:

$$\text{ELOS} = \frac{V_{\text{overbr}}}{S_{\text{stope}}}, \quad (1)$$

where V_{overbr} – is the volume of caved rock mass, m^3; S_{stope} – surface area of the stope, m^2;

$$r_d = \frac{\text{ELOS}}{m} \cdot 100, \quad (2)$$

r_d – ore dilution, %; m – thickness of ore body, m.

J.G.Henning and H.S.Mitri [24] developed a method similar to ELOS for determining ore dilution based on a 3D numerical model, where the dilution boundary is represented by an isoline of the minimum principal stress equal to zero ($\sigma_3 = 0$ MPa). The term "ore dilution density" (DD) was used. It is determined by the ratio of the unscheduled volume of dilution to the stope area,

$$\mathrm{DD} = \frac{V_{\mathrm{unsch}.r}}{S_{\mathrm{stope}}}, \tag{3}$$

where $V_{\mathrm{unsch}.r}$ – is the unscheduled volume of dilution, m^3.

An important factor to consider in managing ore dilution is an adequate design of mine operation as regards rock mass stability. Host rock caving from the roof and sides of workings associated with poor stability conditions of the mass are not only a threat to the overall safety of miners, but also contribute to an increasing volume of ore dilution. To reduce dilution, a series of studies of the structural and strength properties of rocks, stress-strain state of the mass, seismic impact of drilling and blasting, etc. are required.

Among the traditional tools for assessing and managing the rock mass condition is the empirical stability diagram drawn by K.E.Mathews [29], which proved to be useful for an early assessment of the stability of an open stope area. Graphical stability method by K.E.Mathews is based on the calculation and mapping of two values:

• stability index N characterizing the ability of the rock mass to remain unaltered under the given stress state, structural pattern of disturbances in the mass and orientation of the stoping area;

• hydraulic radius which accounts for the geometric interdependence of outcrop dimensions,

$$HR = \frac{S_{\mathrm{stope}}}{P_{\mathrm{stope}}}, \tag{4}$$

where P_{stope} – is the detection perimeter, m.

Stability indicator is calculated from the formula

$$N = \frac{\mathrm{RQD}}{J_n}\frac{J_r}{J_a}ABC, \tag{5}$$

where RQD – is rock quality [30]; J_n – number of fracture systems; J_r – fracture surface roughness; J_a – alteration (adhesion) of fractures; A – ratio of strength to stress state of rocks; B – fracture orientation; C – dip (inclination) angle of the outcrop.

Over time, for making the stability diagram by K.E.Mathews more reliable, it was updated with major alterations and modified by researchers such as Y.Potvin [31], S.D.Nickson [32], C.Mawdesley, R.Trueman, W.Whiten [33], A.Papaioanou [11]. Thanks to these modifications, it became possible to determine the volume of ore dilution using stability diagrams. The papers by A.Papaioanou and F.Suorineni [11] deserve special attention, since the generalized schedule which they developed for determining ore dilution on the basis of the rock mass stability is applicable to all ore deposits regardless of the ore body thickness.

A.Delentas [34] gave predictive assessments of the marginal mass failure and ore dilution using numerical simulation. Software for numerical simulation allows predicting the stress-strain state of the rock mass outside the stope, which could potentially collapse. In the conditions where ore and rock have the same specific gravity, ore dilution factor is calculated from the equation

Journal of Mining Institute. 2024. Vol. 266. P. 283-294

$$K_{\text{overbr}} = K_r = \frac{100 S_{\text{overbr.z}}}{S_{\text{stope}}}, \quad (6)$$

where K_{overbr} – is failure factor; K_r – dilution factor; $S_{\text{overbr.z}}$ – area of collapse zone, m^2.

An underground mining method was adopted at the Zholymbet deposit with levels of 60 m and the use of inclined ramps. Quartz veins are mined by a system of sublevel drifts. With such a system, the vein is divided along the strike and downdip into blocks with the following parameters: length of block along the strike of the vein is 120 m, height of block along the strike through the entire height of the level downdip the ore body with breaking-down into sublevels is 15 m. Mining is carried out from the flank to the centre of the vein up-dip in descending order. Schematic diagram of the mining system is shown in Fig.1.

Stoping of ore in the block on sublevels begins with driving drill haulage drifts of cut raises with cutting of slots on them. Ore mass is broken onto a cut-out raise driven earlier (compensation space). Stope advancing step in the upper sublevels in relation to the lower ones is 20-30 m. The scheme and parameters of ore breaking are shown in Fig.2. Main indicators of longhole ore stoping are: type of explosive used – granulite AS-8; initiation method – by DShE (detonating cord); specific consumption of explosive – 1.75 kg/m^3; hole diameter – 130 mm; burden of hole – 1.6 m; distance between the ends of holes is 1.75 m.

When breaking thin ore bodies, numerical simulation of the stress-strain state of the rock mass was performed for a predictive assessment of ore dilution. Key source data are tensile strength of rock samples for uniaxial compression (σ_{compr}), ore body thickness (m) and the Geological Strength Index (GSI) of

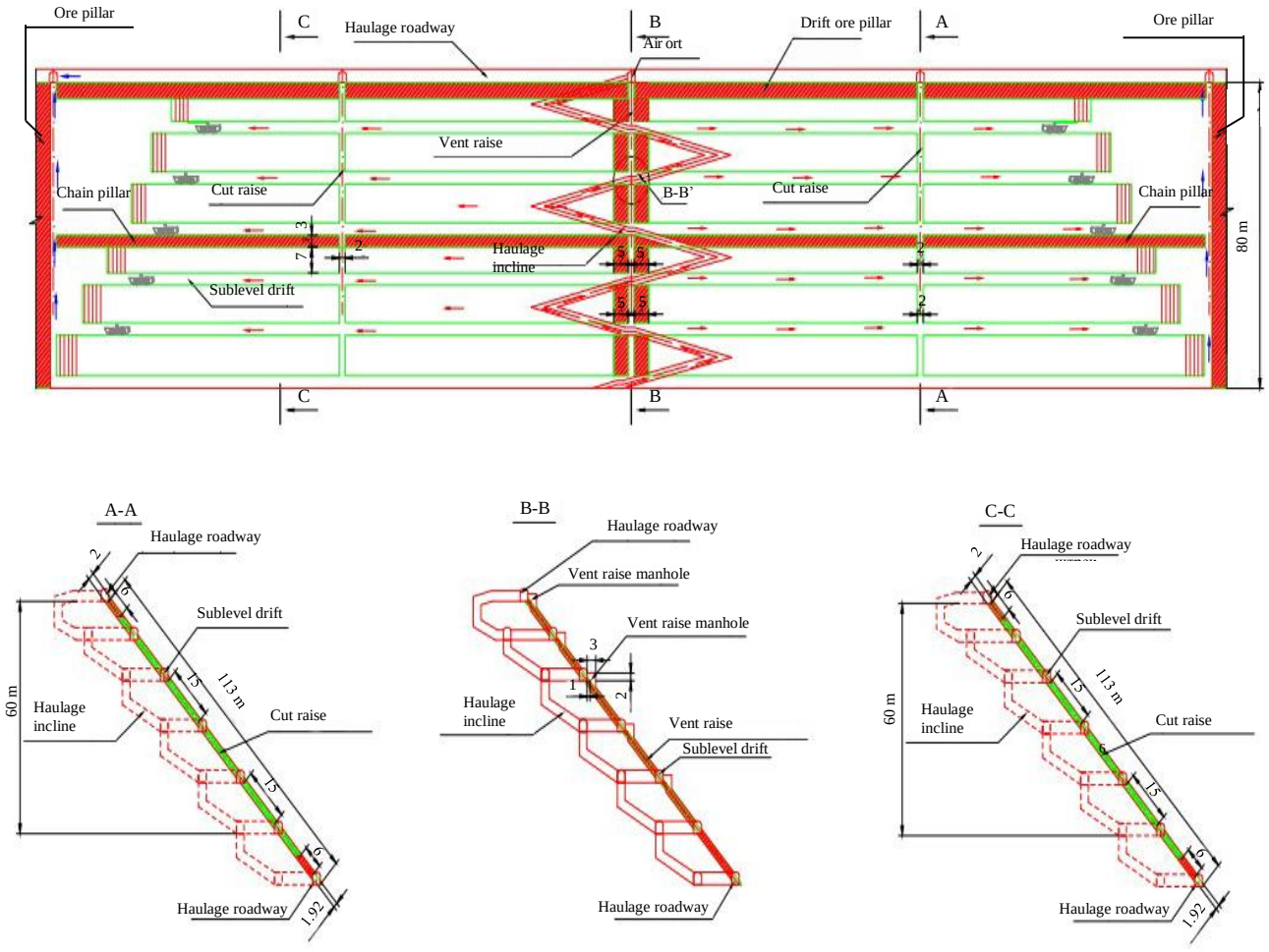

Fig.1. Schematic diagram of mining system

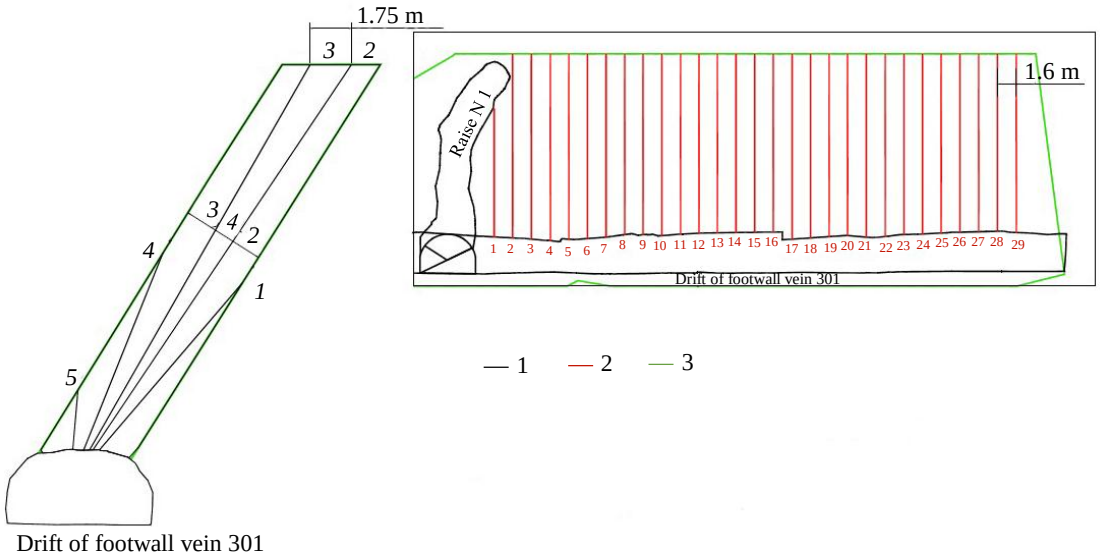

Fig.2. Scheme of borehole ore breaking
1 – actual mine workings 800 m; 2 – projected drill rings; 3 – ore contour;
1-5 – well numbers in a row

rocks [35, 36], which makes it possible to take into account rock fracturing, water content, lithology and other strength indicators, due to which the transition from rock sample strength to the strength of the rock mass occurs. The Hoek – Brown criterion [37] was chosen as the failure criterion. Numerical simulation to determine possible zones of rock failure was performed using the finite element method [38]. As a result of simulation, areas of possible failure zones around the stope are determined. Areas of marginal mass zones that are expected to cave are calculated using AutoCAD software. This software allows a quantitative measurement of areas of possible caving zones. Further, ore dilution is calculated from formula (6).

Calculation of predicted values of ore dilution using this procedure is accomplished based on ground survey which includes field studies to determine the GSI and numerical simulation of geomechanical processes occurring in marginal mass. This procedure is most applicable to the conditions of the investigated body, since at the Zholymbet mine ore and rock have on average the same specific gravity. Reliability of numerical simulation results mainly depends on the accuracy of the input data. Preparation of source data for numerical analysis was accomplished using "RSData" software which allows determining the strength parameters of the rock mass based on the Hoek – Brown [37] and Mohr – Coulomb [39] failure criteria.

GSI is a vital component of the source data. The GSI parameter is the result of research by E.Hoek and E.T.Brown on the structural features and properties of rocks. The classification is constantly updated depending on the needs of designing practice. In one of the latest studies, E.Hoek and E.T.Brown proposed to determine the GSI index as follows [40]:

$$\mathrm{GSI} = 1.5 JCond_{89} + \frac{\mathrm{RQD}}{2}, \tag{7}$$

where $JCond_{89}$ – is the parameter of rating classification of rock fracturing determined in accordance with the methodology of the International Society of Rock Mechanics (ISRM) [41];

$$JCond_{89} = J_{A4} = J_{A41} + J_{A42} + J_{A43} + J_{A44} + J_{A45},$$

J_{A4} – indicator of the quality of contact along fractures: J_{A41} – roughness, J_{A42} – length, J_{A43} – opening, J_{A44} – filling, J_{A45} – weathering of fracture walls.

When assessing the geomechanical state of the rock mass, data from the Geological Survey of the Zholymbet mine were used [42]. According to characteristics of the core from these boreholes, rocks were divided into three domains:

• weathered rocks to a depth of 30-40 m, RQD = 12-34 (rock category "weak");

• slightly weathered silty sandstones, silicified with a massive texture, RQD = 50-72 (rock category "medium");

• gabbro diorites greenish-grey, dense, massive, RQD = 72-78 (rock category "strong") [42].

At the Zholymbet mine, thin ore veins occur at a depth of 800 m. Thus, for determining the GSI indices, RQD values are taken from 50 to 80. As a result of research at the Zholymbet mine during fracture surveying, rating indicators that make up the indicator of the quality of contact along fractures according to the ISRM method [41] were determined. Point values are given in Table 1, where $JCond_{89} = J_{A4} = J_{A41} + J_{A42} + J_{A43} + J_{A44} + J_{A45} = = 5 + 2 + 1 + 2 + 5 = 15$.

Table 1

Rating assessments of geological characteristics of fracturing for conditions of the Zholymbet deposit

Parameter	Value intervals				
Roughness	Very rough	Rough	Slightly rough	Smooth surfaces	Slip marks
J_{A41}	6	5	3	1	0
Length	< 1 m	1-3 m	3-10 m	10-20 m	> 20 m
J_{A42}	6	4	2	1	0
Opening	none	< 0.1 mm	0.1-1.0 mm	1-5 mm	> 5 mm
J_{A43}	6	5	4	1	0
Filler	None	Solid filler < 5 mm	Solid filler > 5 mm	Soft filler < 5 mm	Soft filler > 5 mm
J_{A44}	6	4	2	2	0
Weathered walls	None	Slightly weathered	Moderately weathered	Strongly weathered	Crushed
J_{A45}	6	5	3	1	0

After a series of ground surveys, geological strength indices were determined from formula (7) for different RQD values, and data for simulation were prepared (Table 2).

Table 2

Source data for numerical simulation

Rock type	RQD	GSI	Rock strength σ_{ci}, MPa	Volumetric weight of rock	Rock mass disturbance by blasting D	Parameter of undisturbed rock m_i	Young's modulus
Silty sandstones	50	48	82	2.65	0.8	17	2,800
Silty sandstones	55	50	82	2.65	0.8	17	2,800
Silty sandstones	60	53	82	2.65	0.8	17	2,800
Silty sandstones	65	55	82	2.65	0.8	17	2,800
Gabbro diorites	70	58	103	2.76	0.8	25	3,000
Gabbro diorites	75	60	103	2.76	0.8	25	3,000
Gabbro diorites	80	63	103	2.76	0.8	25	3,000

For numerical analysis of the stress-strain state of marginal mass and predictive assessment of ore dilution, 21 models were implemented taking into account changes in the GSI (48, 50, 53, 55, 58, 60, 63) and ore body thickness from 1 to 3 m. Numerical analysis of the stress-strain state of the mass was accomplished in accordance with actual mining level and the following stope parameters: mining depth 800 m; stope height 45 m; sublevel height 15 m; width 1-3 m; ore body occurrence angle 75°. The main predictive indicator for assessing the stability and analysing the stress-strain state of the rock mass around the stope is the Strength Factor – ratio of possible rock strength to induced stress at the considered point.

Discussion of results. It is not possible to evaluate the results of numerical simulation of 21 versions of models, so it is advisable to analyse the stress-strain state of the mass around the stope and give a predictive assessment of ore dilution for the minimum and maximum GSI values. Further, the results of numerical simulation will be presented at the GSI = 48 and 63 for ore body thickness from 1 to 3 m.

When mining thin deposits at the Zholymbet mine, the lag of the underlying sublevel from the overlying one reaches 20-30 m. Breaking of the overlying sublevel is accomplished by blasting the blasthole rings and loading the broken rock mass using self-propelled equipment. The stoping space remains open, i.e. there is no backfilling. Consequently, in numerical simulation and predictive assessment of ore dilution of the underlying (unmined) sublevel, the influence of the stoping space of the overlying mined sublevel is taken into account (Fig.3).

Analysis of the distribution pattern of isolines based on the strength factor showed that at the GSI = 48 (siltstones) there is a uniform distribution of the safety factor along the contour of the stope, minor deformations along the roof are recorded as well as a redistribution of load on the sides of the stope, caving under its own weight is predicted due to structural weakening of the mass, weak adhesion of rocks to each other caused by blasting, and further rock mass caving is possible. Area of a possible caving zone varies depending on ore body thickness – from 85.2 m^2 at m = 1 m to 77.8 m^2 at m = 3 m, correspondingly.

At the GSI = 63 (gabbro diorites), uneven distributions of safety margin isolines are recorded, and the contours differ from the previous version; possible zones of rock mass failure are predicted in the sides of stopes. Areas of possible caving zones vary depending on ore body thickness – from 29.1 m^2 at m = 1 m to 25.1 m^2 at m = 3 m, respectively. Compared to the previous case, areas of possible caving zones are reduced three-fold. Thus, at the GSI = 63, there is an increase in the safety factor and a decrease in the volume and area of possible caving around the stope. This is due to changes in strength properties and structural features of the rock mass.

The experience of mining thin deposits at the Zholymbet and Akbakai mines shows that the dimensions of possible failure zones around the stope are not strongly affected by the thickness of ore bodies [43]. Presumably, the size of the failure zone depends on parameters of drilling and blasting operations and seismic blasting force on marginal rock mass.

As a result of simulation, areas of possible failure zones around the stope were determined for all model versions (Fig.4). Using data of numerical simulation on the area of a possible caving zone around the stope the predicted values of ore dilution were determined from formula (6) for each model under study taking into account changes in the GSI (48, 50, 53, 55, 58, 60, 63) and ore body thickness from 1 to 3 m (Table 3).

Fig.5 shows the summary and comparative diagrams of changes in the predicted values of ore dilution depending on the GSI when mining thin ore veins. According to predictive calculations, when stoping 1 m thick quartz veins, the predicted ore dilution indicators average 78-84 %, while the actual dilution indicators when mining ore bodies of the same thickness reach 65-70 %.

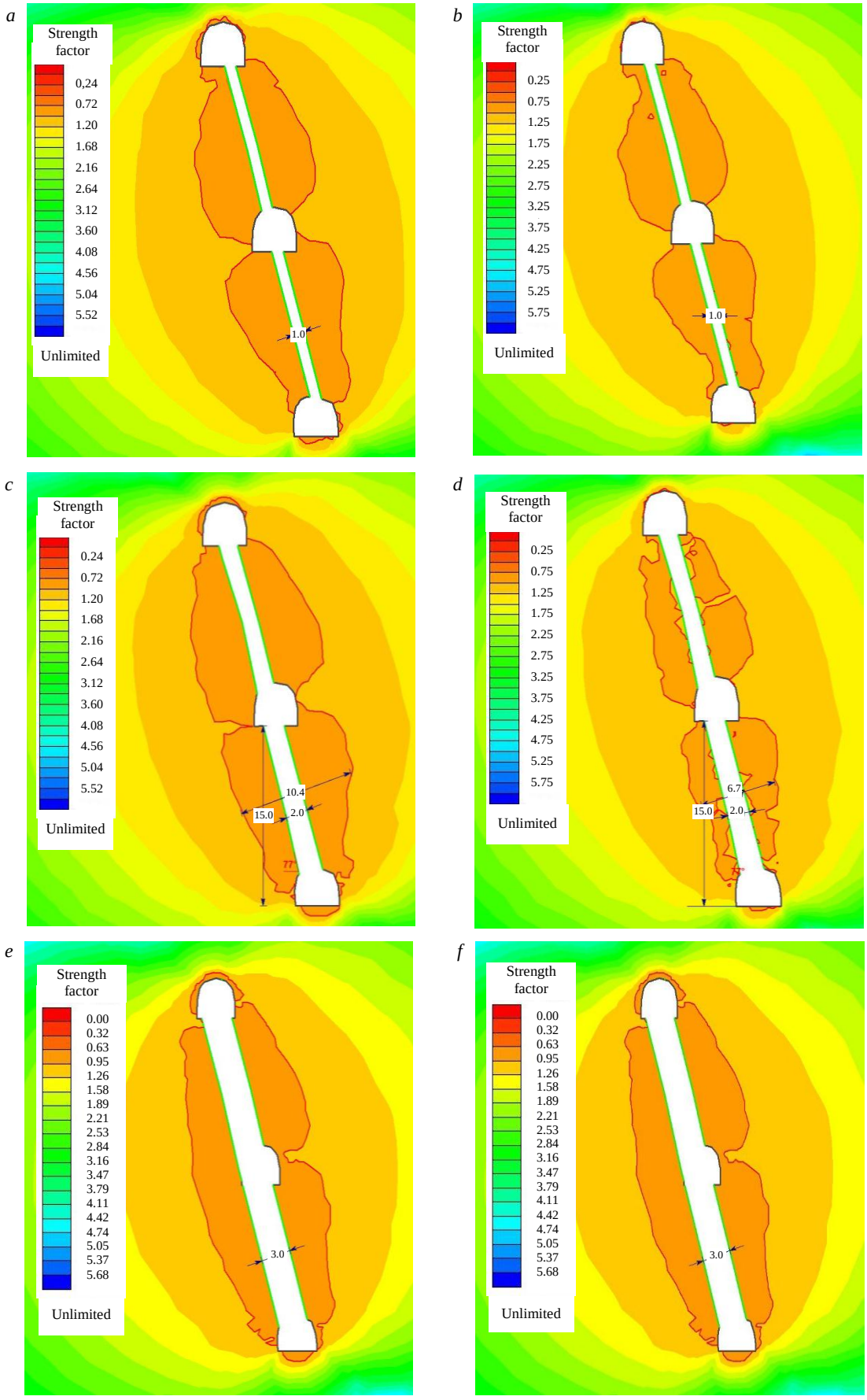

Fig.3. Areas of possible failure zones at GSI = 48 (*a*, *c*, *e*) and GSI = 63 (*b*, *d*, *f*):
a, *b* – ore body thickness 1 m; *c*, *d* – 2 m; *e*, *f* – 3 m

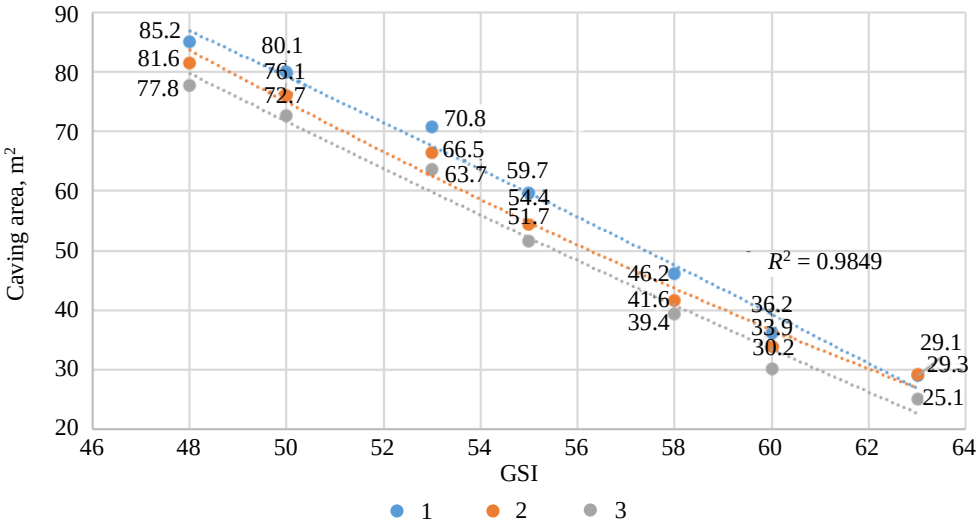

Fig.4. Diagram of changes in thickness of a possible caving zone depending on GSI
1 – thickness 1 m; 2 – 2 m; 3 – 3 m

Table 3

Predicted values of ore dilution in thin deposits at the Zholymbet mine

GSI	Ore body thickness, m					
	1		2		3	
	Area of possible caving zone, m²	Dilution, %	Area of possible caving zone, m²	Dilution, %	Area of possible caving zone, m²	Dilution, %
63	29.1	70.6	29.3	51.7	25.1	40.1
60	36.2	74.3	33.9	55.2	30.2	44.3
58	46.2	78.1	41.6	58.6	39.4	48.4
55	59.7	82.3	54.4	65.4	51.7	56.5
53	70.8	84.5	66.5	70.1	63.7	60.2
50	80.1	86.8	76.1	73.5	72.7	65.8
48	85.2	87.5	81.6	74.9	77.8	67.3

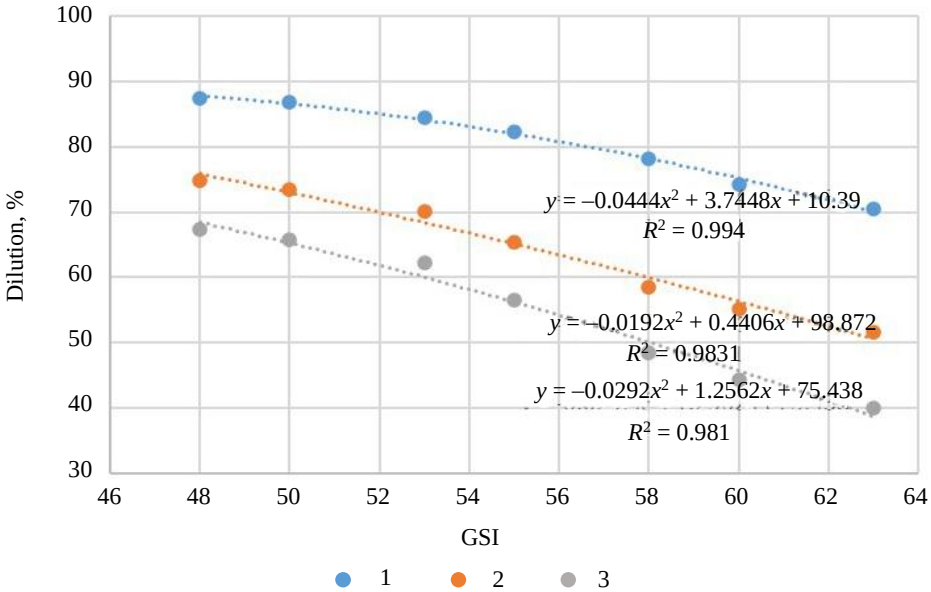

Fig.5. Diagram of changes in predicted ore dilution values depending on GSI
1 – thickness 1 m; 2 – 2 m; 3 – 3 m

Results of the study show that the predicted values of ore dilution are influenced by ore body thickness and the geological strength index, which takes into account the geological features of the rock mass, its structure and fracturing. The dependence of ore dilution index on the GSI index was recorded at different thicknesses of the ore body.

It should be noted that in numerical analysis, the seismic influence of blasting force on marginal rock mass was not taken into account in detail. However, when performing numerical simulation, the indicator of rock disturbance by blasting *D* was applied; its value corresponded to blasting of good quality. In future, it is planned to determine the pattern of changes in the indicator of rock mass disturbance by blasting depending on the category of rock stability. This will allow adjusting the geomechanical model in numerical analysis, assessing the geomechanical state more correctly and predicting ore dilution when mining thin ore bodies.

Conclusion. General review of the methods for determining and accounting for ore dilution showed that in foreign practice, the calculation of ore dilution is based on the studies of the stress-strain state of the rock mass and a predictive assessment of the marginal mass caving using rating classifications of rocks and numerical simulation methods. A comparison of the predicted values of ore dilution with actual indicators confirms a good convergence of the research results, which was about 83 %.

Based on results of the accomplished numerical analysis, it can be assumed that in mining thin deposits, the predicted ore dilution values are influenced by the ore body thickness and the GSI. Analysis of the research results showed that with a decreasing GSI index, there is a decrease in the safety margin and an increase in the area of possible caving around the stope. Accordingly, the volume of ore dilution increases due to entrapment of adjacent host rock strata. Further direction of research is to improve the methodology for determining the parameters of drilling and blasting operations taking into account the GSI rating for the conditions of mining thin ore bodies by systems with caving of ore and host rocks.

REFERENCES

1. Chilala G.C., de Assuncao J., Harris R., Stephenson R.M. Initial effects of improved drill and blast practices on stope stability at Acacia's Bulyanhulu Mine. Underground Design Methods 2015: Proceedings of the International Seminar on Design Methods in Underground Mining, 17-19 November 2015, Perth, Australia. Australian Centre for Geomechanics, 2015, p. 241-254. DOI: 10.36487/ACG_rep/1511_12_Chilala

2. Purwanto, Shimada H., Sasaoka T. et al. Influence of Stope Design on Stability of Hanging Wall Decline in Cibaliung Underground Gold Mine. *International Journal of Geosciences*. 2013. Vol. 4. N 10A, p. 1-8. DOI: 10.4236/ijg.2013.410A001

3. Cai S., Lyu W., Wu D., Yang P. Mining method optimisation of Bayi gold mine based on the value engineering principle. Underground Mining Technology 2017: Proceedings of the First International Conference on Underground Mining Technology, 11-13 October 2017, Sudbury, ON, Canada. Australian Centre for Geomechanics, 2017, p. 511-521. DOI: 10.36487/ACG_rep/1710_41_Cai

4. Wu-sheng Huang, Si-jing Cai, Di Wu et al. Stability Assessment of Underground Mined-Out Areas in a Gold Mine Based on Complex System Theory. *Geotechnical and Geological Engineering*. 2015. Vol. 33. Iss. 5, p. 1295-1305. DOI: 10.1007/s10706-015-9901-9

5. Dorval A. Narrow vein mining using sublevel method at Red Lake Gold Mine – Campbell Complex. 36e Session d'étude sur les techniques de sautage, 21-22 November 2013, Québec, QC, Canada. 23 p.

6. An Long, Wang Ri-dong, Hou Peng-yuan, Liang Rui-yu. Caving Mining of Steeply Inclined Narrow Veins and Supporting Mechanism of Caved Rock. *Journal of Northeastern University (Natural Science)*. 2019. Vol. 40. Iss. 2, p. 278-283. DOI: 10.12068/j.issn.1005-3026.2019.02.024

7. Korigov S., Adoko A.C., Sengani F. Unplanned Dilution Prediction in Open Stope Mining: Developing New Design Charts Using Artificial Neural Network Classifier. *Journal of Sustainable Mining*. 2022. Vol. 21. Iss. 2, p. 157-168. DOI: 10.46873/2300-3960.1356

8. Hyong Doo Jang. Unplanned Dilution and Ore-Loss Optimisation in Underground Mines via Cooperative Neuro-Fuzzy Network: This thesis is presented for the Degree of Doctor of Philosophy of Curtin University. Perth: Western Australia School of Mines, 2014. 170 p.

9. Masoumi I., Kamali Gh.R., Asghari O. Assessment of an ore body internal dilution based on multivariate geostatistical simulation using exploratory drill hole data. *Journal of Mining and Environment*. 2019. Vol. 10. Iss. 1, p. 271-286. DOI: 10.22044/jme.2019.7622.1618

10. Villaescusa E. Geotechnical Design for Sublevel Open Stoping. Boca Raton: CRC Press, 2014. 541 p. DOI: 10.1201/b16702

11. Papaioanou A., Suorineni F.T. Development of a generalised dilution-based stability graph for open stope design. Transations of the Institutions of Mining and Metallurgy, Section A: Mining Technology. 2016. Vol. 125. Iss. 2, p. 121-128. DOI: 10.1080/14749009.2015.1131940

12. Marinin M., Marinina O., Wolniak R. Assessing of Losses and Dilution Impact on the Cost Chain: Case Study of Gold Ore Deposits. *Sustainability*. 2021. Vol. 13. Iss. 7. N 3830. DOI: 10.3390/su13073830

13. Fomin S.I., Kava P.B., Marinin M.A. Open cast geological conditions analysis and the mining units formation in ore losses and dilution determining. *Journal of Mining Institute.* 2014. Vol. 207, p. 74-77 (in Russian).

14. Lizunkin V.M., Lizunkin M.V., Rabolt A.N., Gurov S.G. Pilot test results of technology with widening stopes in mining thin gently dipping and sheetlike ore bodies. *Gornyi Zhurnal.* 2019. N 1, p. 37-40 (in Russian). DOI: 10.17580/gzh.2019.01.08

15. Savich I.N. Widespread in foreign and domestic practice was layered-end way to release sublevel ore. *Mining informational and analytical bulletin.* 2014. N S1, p. 366-373 (in Russian).

16. Tkach S.M., Batugin S.A., Barakaeva I.D. Objective assessment of ore dilution – A promising way of enhancing mineral resource potential. *Gornyi Zhurnal.* 2016. N 1, p. 37-40. DOI: 10.17580/gzh.2016.01.08

17. Batugin S.A., Tkach S.M., Barakaeva I.D. Development of the methodological basis of the definitions and accounting dilution of ore. *Mining informational and analytical bulletin.* 2012. N 9, p. 312-319 (in Russian).

18. Sokolov I.V., Antipin Yu.G., Nikitin I.V. Methodology of choosing the underground geotechnology in combined mining of ore deposits. Ekaterinburg: Ural Federal University named after the first President of Russia B.N.Yeltsin, 2021, p. 340 (in Russian) DOI: 10.25635/b6795-6297-2078-t

19. Pavlov A.M., Vasiliev D.S. Improving underground mining technology of steeply dipping thin ore bodies of konevinskoe gold deposit. *Proceedings of the Siberian Department of the Section of Earth Sciences RANS. Geology, Exploration and Development of Mineral Deposits*. 2017. Vol. 40. N 2, p. 88-94.

20. Mohseni M., Ataei M., Khaloo Kakaie R. A new classification system for evaluation and prediction of unplanned dilution in cut-and-fill stoping method. *Journal of Mining and Environment*. 2018. Vol. 9. Iss. 4, p. 873-892. DOI: 10.22044/jme.2018.6483.1468

21. Jang H., Topal E., Kawamura Y. Unplanned dilution and ore loss prediction in longhole stoping mines via multiple regression and artificial neural network analyses. *Journal of the Southern African Institute of Mining and Metallurgy*. 2015. Vol. 115. N 5, p. 449-456. DOI: 10.17159/2411-9717/2015/v115n5a13

22. Abdellah W.R.E., Hefni M.A., Ahmed H.M. Factors Influencing Stope Hanging Wall Stability and Ore Dilution in Narrow-Vein Deposits: Part I. *Geotechnical and Geological Engineering*. 2020. Vol. 38, p. 1451-1470. DOI: 10.1007/s10706-019-01102-w

23. Abdellah W.R.E., Hefni M.A., Ahmed H.M. Factors Influencing Stope Hanging Wall Stability and Ore Dilution in Narrow-Vein Deposits: Part II. *Geotechnical and Geological Engineering*. 2020. Vol. 38, p. 3795-3813. DOI: 10.1007/s10706-020-01259-9

24. Cordova D.P., Zingano A.C., Gonçalves Í.G. Unplanned dilution back analysis in an underground mine using numerical models. *REM – International Engineering Journal*. 2022. Vol. 75. Iss. 4, p. 379-388. DOI: 10.1590/0370-44672021750093

25. Câmara T.R., Leal R.S., Peroni R.L. Accounting for operational dilution by incorporating geological uncertainties in short-term mine planning. *DYNA*. 2020. Vol. 87. N 213, p. 178-183. DOI: 10.15446/dyna.v87n213.83661

26. Mussin A., Imashev A., Matayev A. et al. Reduction of ore dilution when mining low-thickness ore bodies by means of artificial maintenance of the mined-out area. *Mining of Mineral Deposits*. 2023. Vol. 17. Iss. 1, p. 35-42. DOI: 10.33271/mining17.01.035

27. Ngoma K., Mutambo V. Factors Influencing Ore Recovery and Unplanned Dilution in Sublevel Open Stopes. Case Study of Shaft No.4 at Konkola Mine, Zambia. *Current World Environment*. 2020. Vol. 15. Spec. Iss. 1, p. 31-46. DOI: 10.12944/CWE.15.Special-Issue1.03

28. Suorineni F.T. Reflections on Empirical Methods in Geomechanics – The Unmentionables and Hidden Risks. AusRock 2014: Third Australian Ground Control in Mining Conference, 5-6 November 2014, Sydney, NSW, Australia. 2014, p. 143-156.

29. Eero T. Mining method evaluation and dilution control in Kittilä mine: Master's Thesis. Aalto University, 2014, p. 67.

30. Imashev A., Suimbayeva A., Zhunusbekova G. et al. Research into stress-strain state of the mass under open pit with a change in the open-pit bottom width. *Mining of Mineral Deposits*. 2022. Vol. 16. Iss. 3, p. 61-66. DOI: 10.33271/mining16.03.061

31. Delentas A., Benardos A., Nomikos P. Linking Stability Conditions and Ore Dilution in Open Stope Mining. International Conference on Raw Materials and Circular Economy, 5-9 September 2021, Athens, Greece. Materials Proceedings, 2021. Vol. 5. Iss. 1. N 34. DOI: 10.3390/materproc2021005034

32. Vallejos J., Miranda R., Azorin J. et al. Stability graph using major geological structure. *Fluid Mechanics Research International Journal*. 2018. Vol. 2. Iss. 5, p. 243-246. DOI: 10.15406/fmrij.2018.02.00044

33. Mortazavi A., Osserbay B. The Consolidated Mathews Stability Graph for Open Stope Design. *Geotechnical and Geological Engineering*. 2022. Vol. 40. Iss. 5, p. 2409-2424. DOI: 10.1007/s10706-021-02034-0

34. Delentas A., Benardos A., Nomikos P. Analyzing Stability Conditions and Ore Dilution in Open Stope Mining. *Minerals*. 2021. Vol. 11. Iss. 12. N 1404. DOI: 10.3390/min11121404

35. Hoek E., Carter T., Diederichs M. Quantification of the Geological Strength Index Chart. Proceedings of the 47th US Rock Mechanics/Geomechanics Symposium, 23-26 June 2013, San Francisco, CA, USA. New York: Red Hook, 2013, p. 1757-1764.

36. Marinos V., Carter T.G. Maintaining geological reality in application of GSI for design of engineering structures in rock. *Engineering Geology*. 2018. Vol. 239, p. 282-297. DOI: 10.1016/j.enggeo.2018.03.022

37. Hoek E., Brown E.T. The Hoek–Brown failure criterion and GSI – 2018 edition. *Journal of Rock Mechanics and Geotechnical Engineering*. 2019. Vol. 11. Iss. 3, p. 445-463. DOI: 10.1016/j.jrmge.2018.08.001

38. Erhunmwun I.D., Ikponmwonsa U.B. Review on finite element method. *Journal of Applied Sciences and Environmental Management*. 2017. Vol. 21. N 5, p. 999-1002. DOI: 10.4314/jasem.v21i5.30

39. Hackston A., Rutter E. The Mohr–Coulomb criterion for intact rock strength and friction – a re-evaluation and consideration of failure under polyaxial stresses. *Solid Earth*. 2016. Vol. 7. Iss. 2, p. 493-508. DOI: 10.5194/se-7-493-2016

40. Imashev A.Z., Suimbayeva A.M., Abdibaitov S.A. et al. Justification of the optimal cross-sectional shape of the mine workings in accordance with the rating classification. *Ugol*. 2020. N 6, p. 4-9 (in Russian). DOI: 10.18796/0041-5790-2020-6-4-9

41. Ulusay R. The ISRM Suggested Methods for Rock Characterization, Testing and Monitoring: 2007-2014. Springer, 2015, p. 293. DOI: 10.1007/978-3-319-07713-0

42. Sukhanova A.A., Kambetova G.T. Determination of rock mass rating according to the MRMR geomechanical classification for the conditions of the Zholymbet deposit. *Molodoi uchenyi* (*Young scientist*). 2020. N 14 (304), p. 130-133 (in Russian).

43. Imashev A.Z., Sudarikov A.E., Musin A.A. et al. Improving the quality of blasting indicators by studying the natural stress field and the impact of the blast force on the rock mass. *News of the National Academy of Sciences of the Republic of Kazakhstan. Series of geology and technical sciences*. 2021. Vol. 4. N 448, p. 30-35. DOI: 10.32014/2021.2518-170X.78

Authors: **Askar Zh. Imashev,** *PhD, Head of Department, https://orcid.org/0000-0002-9799-8115 (Abylkas Saginov Karaganda Technical University, Karaganda, Kazakhstan),* **Aigerim M. Suimbaeva,** *PhD, Associate Professor, suimbayeva.aigerim@mail.ru, https://orcid.org/0000-0001-6582-9977 (Abylkas Saginov Karaganda Technical University, Karaganda, Kazakhstan),* **Aibek A. Musin,** *PhD, Senior Lecturer, https://orcid.org/0000-0001-6318-9056 (Abylkas Saginov Karaganda Technical University, Karaganda, Kazakhstan).*

The authors declare no conflict of interests.

ISSN 2411-3336; e-ISSN 2541-9404

JOURNAL OF MINING INSTITUTE
Zapiski Gornogo instituta
Journal homepage: pmi.spmi.ru

Research article

Technology of absorption elimination with cross-linking plugging material based on cement and cross-linked polymer

Andrei A. Predein[1,2], **Olga V. Garshina**[1], **Aleksandr A. Melekhin**[2]✉
[1] *"PermNIPIneft" Branch of OOO "LUKOIL-Inzhiniring" in Perm, Perm, Russia*
[2] *Perm National Research Polytechnic University, Perm, Russia*

How to cite this article: Predein A.A., Garshina O.V., Melekhin A.A. Technology of absorption elimination with cross-linking plugging material based on cement and cross-linked polymer. Journal of Mining Institute. 2024. Vol. 266, p. 295-304.

Abstract. The peculiarity of the geological structure of carbonate reservoirs is their complex permeability and porosity characteristics, reflecting the simultaneous presence of cavities variety (fractures, caverns, pores). Loss of circulation during penetration of fractured rock intervals significantly increases well construction time due to lack of efficient plugging isolation compositions. The main disadvantages of traditional compositions are high sensitivity to dilution in the process of their injection into the absorption zone, as well as insufficient structural strength to prevent the isolation composition from spreading during the induction period. For efficient isolation of catastrophic absorption zones in conditions of high opening of absorption channels a new cross-linking plugging isolation composition has been developed, which allows to exclude disadvantages of traditional isolation compositions. Application of the composition will allow to reduce the injection volume of the isolation composition and the time of isolation works due to its resistance to dilution and movement of formation water in the absorption interval.

Keywords: drilling; lack of circulation; absorption elimination; catastrophic absorption; cross-linking plugging materials; quick-setting plugging compositions

Acknowledgment. The research was supported by the Ministry of Science and Higher Education of the Russian Federation (project N FSNM-2023-0005).

Received: 26.09.2022 ***Accepted: 20.09.2023*** ***Online: 13.12.2023*** ***Published: 25.04.2024***

Introduction. At present, it is necessary to reduce well construction costs in order to ensure profitable hydrocarbon production. The solution to this task requires high-quality well construction with a multiple reduction in construction time [1]. At the modern level of technologies, it is not possible to exclude the costs of prevention [2-4] and elimination of complications during drilling [5-7]. Thus, on average 20-25 % of the calendar time of well construction is spent on elimination of complications. Absorption intensity is divided into three categories: filtration (less than 3 m^3/h), partial (3-15 m^3/h) and catastrophic (more than 15 m^3/h) absorption [8]. The issue of catastrophic absorption zones isolation is especially relevant [9], which are characteristic for rocks with karst cavities, caverns, complicated by tectonic dislocations [1, 10]. The task of reducing the cost of eliminating complications associated with the absorption of technological liquids becomes more complicated when penetrating highly drained zones in the intervals of absorbing channels [11-13]. As a rule, when penetrating such zones, an increase in rate of penetration is observed, up to drilling tool dips, with subsequent loss of circulation. Isolation of fractured zones in carbonate formations with the use of bridging materials can be ineffective. To achieve the result, a large volume of isolation materials is used and a large number of repeated isolation works are carried out [14].

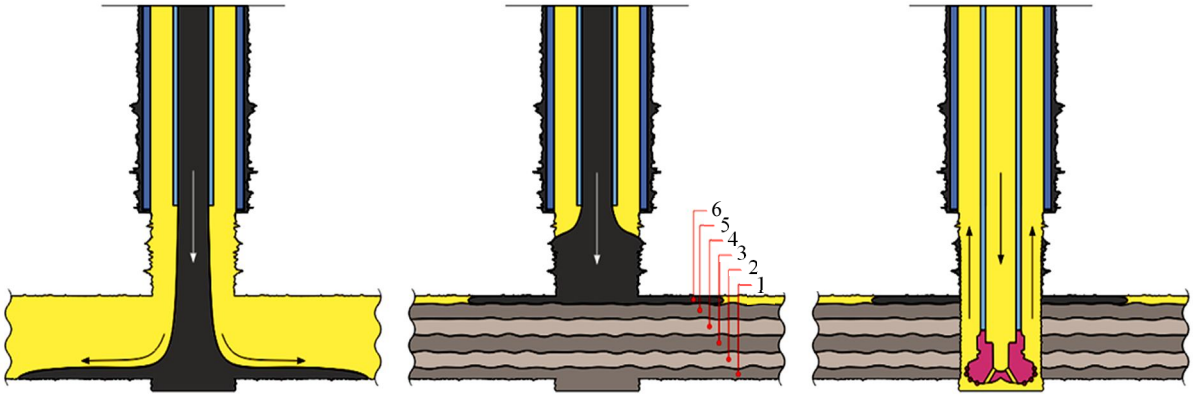

Fig.1. Mechanism of cavity space filling with conventional plugging compositions
1-6 – operation number

The practice of absorption zone isolation shows that low- and medium-intensity absorptions are successfully isolated using standard technologies accepted in drilling and service companies (bridging, sediment-forming compositions, instantaneous filtration compositions, plugging and foam-cement materials) [15]. Isolation of catastrophic absorption zones is achieved by gradual filling of the cavity space with the use of traditional plugging materials or by installing a profile blocker. In some cases, in agreement with the customer, the drilling contractor continues well construction without circulation output, taking measures to reduce flushing fluid consumption [16, 17], which allows to reduce the equivalent circulation density in the absorbing interval [18, 19]. Such a solution reduces the probability of fracture opening and drilling mud loss. This approach allows reaching the design bottomhole with a significant increase in well construction time, whereas drilling necessitates control of pressure in the annular space to prevent oil-and-gas influx or drill string sticking [18, 20]. Isolation of catastrophic absorption zones is mandatory in conditions of significant reduction of static fluid level in the well, which can provoke oil, gas and water influx (when penetrating the productive interval with high formation pressure).

Low efficiency of traditional plugging compositions is caused by the fact that in conditions of high opening of absorbing channels the cement solution moves along the most drained channels of maximum opening with subsequent spreading and bottom positioning under the effect of gravitational forces (Fig.1).

The isolation method is based on gradual filling of cavity space in the formation channel. A large number of operations is required to achieve a positive effect, the number of isolation operations can be reduced by adjusting the structural properties of the plugging composition.

Relevance of the problems in elimination of catastrophic absorptions during well construction. The problem of efficient solution for elimination of drilling mud absorption is relevant for the majority of oil and gas fields. At present, there are no unified approaches and technologies to eliminate absorption because there is no unified and generally recognized classification of absorption by intensity. At each field (area), different classifications of absorptions and technologies of absorption control based only on drilling experience are applied [21].

The efficiency of isolation works with the use of fillers depends on their proper selection (material, size and concentration) [22, 23]. High-intensity absorptions are counteracted by pumping large volumes of fillers into the well, with clay solution used as a carrier liquid. The plugging ability of the isolation material is determined by a properly selected particle size. It is believed that the plugging

material should contain a certain number of particles with a size approximately equal to the diameter of perforations in the rock, as well as a set of smaller particles [24]. At high opening of absorbing channels, conditions are created when the maximum size of rigid bridging agent does not meet the requirements of formation isolation. In such cases, increasing the concentration and volume of the isolation composition cannot guarantee channel plugging.

The most common isolation material for absorption elimination is Portland cement plugging composition. Traditionally used methods for isolation of absorbing formations by injection of plugging compounds into the formation through the open end of pipes or with the help of packer do not always lead to isolation of the absorption interval [25]. Work mechanism of plugging compositions is based on gradual filling of cavity space in the formation channel. The composition moves in the opened channel of absorbing intervals not in a continuous and uniform flow, but along the most drained channels of the highest opening. Spreading far deep from the wellbore zone, it tends to take a bottom position in the formation under the effect of gravitational force. As a result, the most opened channels, being filled with plugging material for a short time, are subsequently "thinned", as the resistance force in the channel is insufficient to fix the solution in it. The process is complicated by the fact that when moving down the wellbore below the drill pipes and in the formation, the solution inevitably mixes with the flushing fluid and loses its plugging properties [21].

To prevent spreading of isolation compositions, plugging compositions with high thixotropic properties are used, which consist of cement, suspension stabilizer and retarder [26]. Due to high thixotropic properties and flow resistance, the compositions should prevent spreading in the absorption zone with subsequent strength gain after hardening [27, 28]. The experience of isolation works has shown that structural and rheological properties of plugging compositions based on clay-cement, gel-cement are insufficient for isolation of zones with channel opening of more than 10 mm. Further increase of structure is possible only at reduction of water-cement ratio, which can lead to rapid growth of structural strength in the injection process, transitioning to the onset of setting.

In some cases, quick-setting compositions based on Portland cement [29] are used, the strength of the structure in which is achieved by introducing sulphuric acid salts into the composition. As a result of reaction between cement and these types of salts, gypsum is formed, which causes such behaviour of cement that after 10-12 min the plugging mixture thickens sharply. If such a sample of plugging solution is kept in motion for more than 20 min, the time of setting can be significantly increased from 30 min to 10 h. In this regard, the works on isolation of absorption zones using components based on gypsum binder should be carried out within 20 min from the moment of their preparation. If this condition is not fulfilled, the gypsum structure is destroyed [30].

High thixotropic properties, excluding the spreading of the isolation material, are characteristic for compositions based on cross-linked polymers [31-33]. In laboratory conditions, these compositions form an elastic gel without water loss with a "ringing" structure. The advantage of cross-linked systems is their ability to adapt to different channel volumes. At differential pressure, they penetrate into the absorbing interval and fill the channels without restrictions on opening and morphology. At the same time, the structurally high rheological characteristics prevent the composition from spreading after removal of the overpressure occurring in the injection process. This is because the presence of spatial structures prevents the internal movement of layers in the composition. The disadvantages include the occurrence of viscous flow at the appearance of external forces exceeding the value of the ultimate yield stress, at which the destruction of its structure occurs [34]. Isolation of catastrophic absorption involves injection of cross-linked polymer in the volume providing the reduction of filtration characteristics of the absorption zone with subsequent consolidation by hardening plugging composition based on Portland cement [35].

In conditions of highly fractured (channel opening of more than 10 mm) and karst rocks, the values of ultimate yield stress for compositions are significantly reduced. As a result, when fixing the

plugging composition, the pressure is applied to the gel screen, at which viscous flow of isolation compositions into the absorption zone occurs that significantly reduces the efficiency of isolation works. To exclude viscous flow of cross-linked compositions it is necessary to increase the strength of the gel structure and its adhesion to the rock [36]. Catastrophic absorptions are often accompanied by a significant drop in the liquid level in the well (500 m and more). When filling the well with drilling mud after isolation works, excessive hydrostatic pressure equivalent to the static level value acts on the isolation composition from the well side. Thus, the necessary property of isolation materials for elimination of high-intensity absorptions is the ability to withstand rather high pressure drops (5 MPa and more). Therefore, cross-linked isolation compositions are not suitable for isolation of zones with high channel opening.

High efficiency for isolation of catastrophic absorption zones is achieved using local well wall support equipment [37-39]. The disadvantages of this technology include limited application in directional and horizontal wells, high cost and significant duration of work (7 days on average). At present, there is no effective technology for elimination of catastrophic absorption, where the absorption zone is complicated by fractured and cavernous rocks with reduced formation pressure.

It can be concluded that none of the isolation compositions provides effective isolation of high-intensity absorption zones, where the complication is confined to high opening of the absorption channel (presence of fractured rocks, paleokarst). It is necessary to develop an isolation composition capable of adapting to the morphology of the fracture space, combining the properties of cross-linked gel and cement solution, which will prevent the spreading of the isolation composition during the induction period and withstand the pressures arising during the resumption of the well construction process after the isolation works [30].

Methods. ***Technique for elimination of catastrophic absorptions during well construction.*** Attention should be paid to the necessity of developing an isolation composition capable of adapting to the morphology of the fracture space with the effect of complete filling of absorbing channels, as well as withstanding sufficiently high pressure drops (5 MPa and more) after the waiting for setting.

To solve the problems of low efficiency for isolation of catastrophic absorption zones, the authors developed cross-linking plugging isolation material (CLPIM). The composition is a combination of cement and cross-linked polymer possessing transverse chemical bonds. After mixing, the composition undergoes three phase transitions from the linear gel stage to the cross-linked gel stage, with the final stage being crystallisation (solidification). The composition is pumped into the well as a linear liquid (Fig.2), the movement of the composition through the drill pipes is mainly in the liquid state. The concentration of cross-linking agent is selected so that cross-linking takes place in the lower part of the drill string. Thus, the composition enters the absorption zone in the cross-linked state, which prevents its spreading in the cavernous cavity of the absorbing formation. After completion of the injection, the well is left to wait for cement hardening to build up the strength of the isolation composition. The achieved strength allows the composition to withstand hydrodynamic pressure that occurs when the well construction process is resumed.

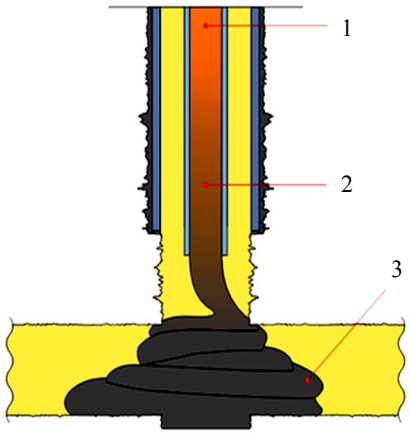

Fig.2. Mechanism of cavity space filling with CLPIM plugging compositions

1 – no cross-linking; 2 – beginning of cross-linking; 3 – end of cross-linking

The required properties are ensured by using the basic composition (cement, mixing liquid, functional additives) and polymer. The composition is a stoichiometric mixture of oxides, carbonates, magnesium and calcium sulphates. When added to the magnesium chloride solution, it forms a cement mixture, that when entering the

polymerisation reaction, forms an inorganic polyhydrate of magnesium hydroxysulphate/chloride, characterized by high compressive strength. The polymer from the group of heteropolysaccharides contained in the composition acts as a structure-forming agent and forms covalent chemical bonds of the polymer when interacting with the crosslinking agent. As a result, polymer chains are cross-linked with simultaneous increase in structural strength of the composition. The combination of reagents allows obtaining a homogeneous mixture, density and gelation time can be selected according to specific geological and technological conditions by adding conventional cement additives (retarding agents).

Laboratory tests were carried out at the laboratory base of "PermNIPIneft", a branch of OOO "LUKOIL-Inzhiniring" in Perm. Gelation time and rheological characteristics of the isolation composition were determined.

The gelation time of the plugging material was determined by measuring its viscosity (consistency) on a consistometer in conditions close to wellbore parameters. Temperature, pressure, and rate of their gain were set according to geological and technical conditions of wells. Chandler 7322 high pressure and temperature sealed consistometer was used to determine the gelation time.

The rheological properties were determined on a modular rheometer MSR-102 manufactured by Anton Paar with a plane-to-plane measuring system (d = 50 mm), and gap size of 1 mm. The effective (dynamic) viscosity was determined at shear rates of 1-5 s^{-1} to minimize disruption of the composition structure and to avoid extrusion of the sample from the measuring system. To minimize the slipping effect of the sample in the measuring system, which leads to underestimation of the results, measurements were carried out under load (normal force 5 N).

Results. Fig.3 shows the consistency gain profiles (gelation time) of traditional magnesia binder-based isolation materials of fast-setting composition (FSC) without the effect of cross-linked gel stage and the proposed CLPIM composition with and without polymer. The traditionally used composition (FSC) is designed for bridge installation and absorption elimination. The composition is inert to hydrocarbon-based drilling muds, resistant to hydrogen sulphide aggression, has high adhesion characteristics, adjustable gelation time, fast strength gain, but has a number of disadvantages when isolating catastrophic absorption zones.

Graphs in Fig. 3 show that the technical result when using FSC is a sharp increase in the gelation time at the end of the induction period, short setting time (4-8 h), high thixotropic properties. Such result for carrying out isolation works in oil and gas wells is achieved by giving the plugging composition short setting and hardening times with provision of technological properties of injectability, simultaneous increase of compressive strength due to the use of caustic magnesite, stability regulator, bischofite, water, setting and hardening regulator (additives based on organophosphates) in the composition. The gelation time and consistency gain profile were determined on a consistometer at a pressure of 2-5 MPa and a temperature of 25-32 °C, the most typical for the fields of Perm region.

In the isolation compositions CLPIM and FSC, caustic magnesite is used as a binder, which includes functional additives that ensure its cross-linking. Cross-linking, which is expressed by a sharp increase in consistency, at maximum amount of additives occurs after 6-8 min (Fig.3, *b*), the time of the gelation beginning of the plugging part starts not earlier than 2.15 h (Fig.3, *c*).

When pumped into the cavernous cavities, the plugging compositions pass through a large volume of water and are diluted, which leads to deterioration of the isolation composition properties. Thus, a substantial part of the plugging compositions is spent on dilution. The technical result of the proposed composition is that the combination of components provides a shortened yield loss time due to internal cross-linking of the polymer. After the beginning of cross-linking the composition becomes resistant to degradation during its injection into the formation, it is not subject to dilution even in conditions of formation water movement. Contamination of the composition with well or formation

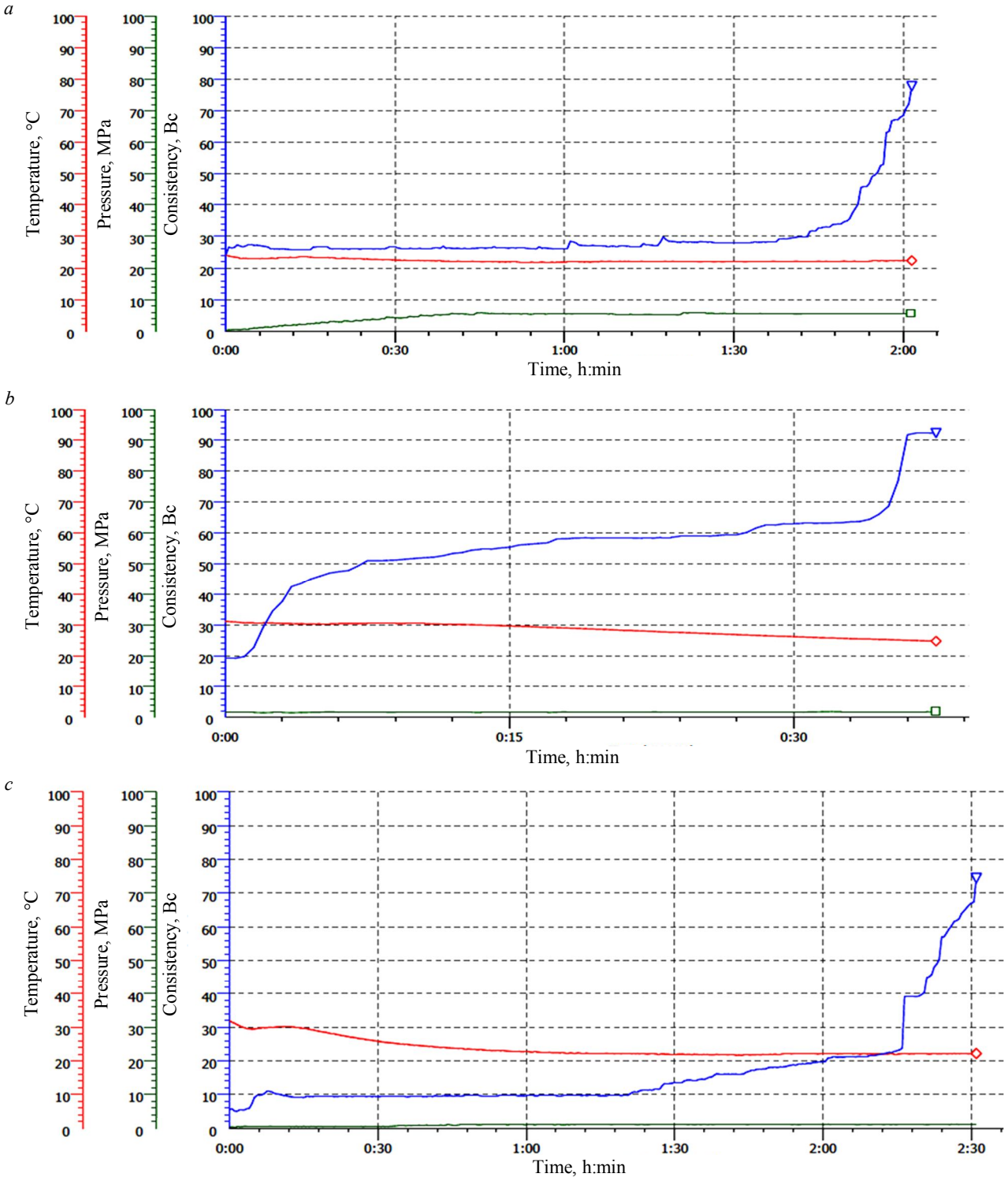

Fig.3. Consistency gain profiles: *a* – fast-setting composition; *b* – CLPIM composition with maximum amount of polymer for gelation; *c* – CLPIM composition without polymer, regulating the gelation

fluids does not affect the process of strength gain, including in conditions of hydrogen sulphide aggression. Stability is confirmed by laboratory investigations in different environments. According to the results of investigations, it was concluded that polymer cross-linking inside the plugging composition makes the composition non-degradable.

In laboratory conditions, the composition after mixing for the first 15 min does not differ from conventional cement solutions and is in a liquid, flowing state, which allows the composition to be

pumped into the well at minimum pressure. In 15 min after mixing, internal cross-linking takes place and the composition changes to an elastic gel state, but still flows. After 20 min, the composition is in a fully cross-linked state, withstands significant tensile forces and restores its shape after their removal. It should be emphasized that the proposed formulation of the composition after cross-linking provides low flowability while maintaining the conditions of injectability due to low adhesion to the well equipment. Thus, in the high pressure cell of a dynamic filter press the composition is pressed out at minimum pressure drop through a simulated model of a fracture with 10 mm opening.

In order to determine the safe time of operations with plugging compositions it is important to know the time of their gelation and setting. Two parallel processes – cement cross-linking and hydration – take place simultaneously in the proposed composition. When determining the gelation time, a consistency of 70 Bc (which characterizes the viscosity of a non-pumpable cement dough) will be reached at the time when polymer cross-linking starts (after 5 min). This is because when the polymer swells, a viscous linear gel is formed, which interacts with the cross-linking agent to form a three-dimensional elastic structure. The cross-linking process has no effect on the timing of the gelation onset – these are two independent processes. Consequently, the safe time of work can be determined by the gelation time of the base formulation without the addition of polymer.

The development is currently being prepared for pilot field testing, and the risks associated with the pressure generated during the injection process have been identified. The safety of operations when using plugging compositions is a priority. In order to predict the pressure, to exclude the risks associated with the impossibility of pumping the isolation composition during the period of its cross-linking, a mathematical calculation for predicting the injection pressure at changing the rheological parameters of the isolation composition was performed. The calculation of pressure on the injection line was carried out in OptiCem module (LandMark) under the following conditions: static level before the start of works is 500 m, setting the open end of drill pipes above the absorption zone is 500 m, the depth of the absorption zone is 1 500 m, the volume of the injected composition is 20 m^3, the flow rate (pumping rate) is 6 l/s, the composition is injected into the well with the open annular space. MSR-102 rheometer was used to measure the rheological characteristics of the cross-linked isolation composition, which allows obtaining highly accurate results of any viscous liquids, including cross-linked ones. Based on the obtained data, a graph of pressure dependence on the volume of injected CLPIM composition was plotted (Fig.4).

In conditions of high opening of the channels in the absorbing interval, the pressure during filling of the pipe space with the isolation composition and its injection into the formation will not exceed 3.5 MPa (lines 1 and 2). In case of low opening of the absorbing channels, when there are preconditions of the isolation composition movement into the annular space, it will be necessary to wash out the isolation composition by circulation. Movement of the cross-linked isolation composition through the annulus will be accompanied by higher values of wellhead pressure 4.5-5.0 MPa (line 3), in case of increasing the flow rate up to the design value the maximum pressure will increase up to 5.8 MPa. The injection technology implies setting the open end of the drill pipe above the absorption zone in such a way as to place 10-20 m^3 of isolation composition in the open wellbore, i.e. no reaming and washing out of the isolation composition will be required. The risk associated with high pressure and the subsequent inability to pump the isolation composition in the designed volume at the specified flow rate is eliminated.

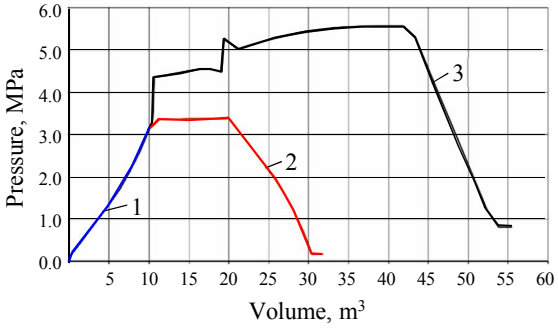

Fig.4. Injection pressure of the composition into the well
1 – injection of CLPIM into the pipe space; 2 – injection of CLPIM into the absorption zone; 3 – direct circulation

After injection of the isolation composition it is common practice to wash out the cement solution from the tool, there is an increase in hydrostatic pressure acting on the isolation composition, which may result

in its viscous flow into the absorption zone. In order to increase the efficiency of isolation works, the test program at the object will recommend excluding the stage of tool washing, which may lead to clogging of drilling tools with cement solution. To exclude these risks, reagents have been added to the formulation of the composition to reduce adhesion in the pair of isolation composition – metal, thus minimizing adhesion of the composition to the inner surface of the tool. The tests show that after condensing a sample of CLPIM in a pressure and temperature regulated cell (HTHP) for 20 min after the start of cross-linking, the composition was pressed out through an opening of 10 mm with minimum pressure, the formation of "tongues" on the inner surface of the cell was not recorded.

The results of the tests indicate that there are no risks when CLPIM isolation composition passes through the bottomhole assembly during its gelling period. In the cross-linked state, the composition does not provide high hydraulic resistance, and adhesion-reducing reagents minimize adhesion of the composition to the inner surface of the tools.

Conclusion. The developed composition meets the requirements for isolation of catastrophic absorption zones complicated by high opening of absorption channels: shortened yield loss time due to internal cross-linking of the polymer; after the beginning of cross-linking the composition becomes resistant to degradation during its injection into the formation; the achieved strength allows the composition to resist hydrodynamic pressure occurring when the well construction process is resumed.

The use of magnesia binder in the formulation of the developed composition allows its destructuring by acid compositions during the development period, and also expands the area of application in conditions of hydrogen sulphide aggression. The advantages of the composition include short setting time and resistance to degradation in conditions of formation water movement. Parameters of density, gelation time, as well as the beginning of cross-linking can be selected in accordance with specific geological and technical conditions by adjusting the water-cement ratio, as well as by introducing retarders and cross-linking agents. At the first stage the area of application is limited by formation temperature (35 °C) as well as by the depth of the absorption zone (1500 m). After pilot tests the area of application can be expanded.

Tests of the developed technology are planned in order to assess the efficiency of eliminating catastrophic absorptions confined to formations with high opening of absorption channels. If the results of pilot tests are satisfactory, the use of CLPIM will significantly reduce the volume of injected isolation compositions, as well as the time of isolation works.

REFERENCES

1. Kumar A., Savari S., Whitfill D.L., Jamison D.E. Wellbore Strengthening: The Less-Studied Properties of Lost-Circulation Materials. SPE Annual Technical Conference and Exhibition, 19-22 September 2010, Florence, Italy. OnePetro, 2010. N SPE-133484-MS. DOI: 10.2118/133484-MS

2. Rezaei A., Nooripoor V., Shahbazi K. Applicability of Fe_3O_4 nanoparticles for improving rheological and filtration properties of bentonite-water drilling fluids in the presence of sodium, calcium, and magnesium chlorides. *Journal of Petroleum Exploration and Production Technology*. 2020. Vol. 10. Iss. 6, p. 2453-2464. DOI: 10.1007/s13202-020-00920-6

3. Ketova Y.A., Bai B., Khizhnyak G.P. et al. Testing of preformed particles polymer gel technology on core filtration models to limit water inflows. *Journal of Mining Institute*. 2020. Vol. 241, p. 91-96. DOI: 10.31897/PMI.2020.1.91

4. Abdollahpour P., Tabatabaee Moradi S.S., Leusheva E., Morenov V. A Numerical Study on the Application of Stress Cage Technology. *Energies*. 2022. Vol. 15. Iss. 15. N 5439. DOI: 10.3390/en15155439

5. Nikolaev N.I., Tyanle L. The modern technology of drilling and casing of well during the exploration of gas hydrates. *Journal of Mining Institute*. 2016. Vol. 218, p. 206-214 (in Russian)

6. Blinov P.A., Dvoynikov M.V. Rheological and Filtration Parameters of the Polymer Salt Drilling Fluids Based on Xanthan Gum. *Journal of Engineering and Applied Sciences*. 2020. Vol. 15. Iss. 2, p. 694-697. DOI: 10.36478/jeasci.2020.694.697

7. Chernyshov S.E., Galkin V.I., Ulyanova Z.V., Macdonald D.I.M. Development of mathematical models to control the technological properties of cement slurries. *Journal of Mining Institute*. 2020. Vol. 242, p. 179-190. DOI: 10.31897/PMI.2020.2.179

8. Alsaba M., Al Dushaishi M.F., Nygaard R. et al. Updated criterion to select particle size distribution of lost circulation materials for an effective fracture sealing. *Journal of Petroleum Science and Engineering*. 2017. Vol. 149, p. 641-648. DOI: 10.1016/j.petrol.2016.10.027

9. Razavi O., Vajargah A.K., Van O.E., Aldin M. Comprehensive analysis of initiation and propagation pressures in drilling induced fractures. *Journal of Petroleum Science and Engineering*. 2017. Vol. 149, p. 228-243. DOI: 10.1016/j.petrol.2016.10.039

10. Elkatatny S., Gamal H., Ahmed A. et al. A Novel Solution for Severe Loss Prevention While Drilling Deep Wells. *Sustainability*. 2020. Vol. 12. Iss. 4. N 1339. DOI: 10.3390/su12041339

11. Miller M.L., Scorsone J.T., Whitfill D.L. et al. The Development of a Geopolymer-Based Pill as an Engineered Solution to Lost Circulation. SPE Annual Technical Conference and Exhibition, 30 September – 2 October 2013, New Orleans, LA, USA. OnePetro, 2013. N SPE-166123-MS. DOI: 10.2118/166123-MS

12. Alsaba M., Nygaard R., Hareland G., Contreras O. Review of Lost Circulation Materials and Treatments with an Updated Classification. AADE Fluids Technical Conference and Exhibition, 15-16 April 2014, Houston, TX, USA. 2014. № AADE-14-FTCE-25

13. Matanovic D., Gaurina-Medimurec N., Simon K. Risk Analysis for Prevention of Hazardous Situations in Petroleum and Natural Gas Engineering. Hershey: IGI Global, 2014, p. 433.

14. Savari S., Butcher J., Al-Hulail M. Managing Lost Circulation in Highly Fractured, Vugular Formations: Engineered Usage of High Fluid Loss Squeeze and Reticulated Foam Lost Circulation Materials. IADC/SPE International Drilling Conference and Exhibition, 3-5 March 2020, Galveston, TX, USA. OnePetro, 2020. N SPE-199635-MS. DOI: 10.2118/199635-MS

15. Whitfill D.L. Lost Circulation Material Selection, Particle Size Distribution and Fracture Modeling with Fracture Simulation Software. IADC/SPE Asia Pacific Drilling Technology Conference, 25-27 August 2008, Jakarta, Indonesia. OnePetro, 2008. N SPE-115039-MS. DOI: 10.2118/115039-MS

16. Budnikov V.F., Bulatov A.I., Peterson A.Ya., Shamanov S.A. Control and ways of improving well technical conditions. Moscow: Nedra, 2001, p. 305 (in Russian).

17. Ruzhnikov A. Theoretical Aspects and Practical Implementation of Study of Drilling Fluid Level in the Annulus While Drilling with Total Losses. Abu Dhabi International Petroleum Exhibition and Conference, 9-12 November 2020, Abu Dhabi, UAE. OnePetro, 2020. N SPE-203454-MS. DOI: 10.2118/203454-MS

18. Almetayev R., Hosani M.A., Ameri S.A. et al. First Nitrified Managed Pressure Drilling Application in United Arab Emirates. Abu Dhabi International Petroleum Exhibition and Conference, 12-15 November 2018, Abu Dhabi, UAE. OnePetro, 2018. N SPE-193025-MS. DOI: 10.2118/193025-MS

19. Ali A.S., Dosunmu A., Anyanwu C. et al. Optimizing the Drilling HPHT/Deep Offshore Wells Using Managed Pressure Drilling Techniques. SPE Nigeria Annual International Conference and Exhibition, 5-7 August 2014, Lagos, Nigeria. OnePetro, 2014. N SPE-172349-MS. DOI: 10.2118/172349-MS

20. Nugroho W.A., Hermawan S., Lazuardi B.H., Mirza R. Drilling Problems Mitigation in Geothermal Environment, Case Studies of Stuck Pipe and Lost Circulation. Asia Pacific Oil & Gas Conference and Exhibition, 17-19 October 2017, Jakarta, Indonesia. OnePetro, 2017. N SPE-186922-MS. DOI: 10.2118/186922-MS

21. Kamenskikh S.V. Experience of Fight Against Absorption of Boring and Grouting Solutions at Construction of Wells. *Scientific papers of donntu. Series: The Mining and Geology*. 2016. N 2 (25), p. 36-51.

22. Kang Y., Yu H., Xu C., Tang L. An optimal design for millimeter-wide facture plugging zone. *Natural Gas Industry B*. 2015. Vol. 2. Iss. 1, p. 113-119. DOI: 10.1016/j.ngib.2015.02.011

23. Scott P., Redburn M., Nesheim G., Phillips C. A Pragmatic approach to Lost Circulation Treatments: What every Drilling Engineer Should Know. AADE Fluids Technical Conference and Exhibition, 14-15 April 2020, Houston, TX, USA. 2020. N AADE-20-FTCE-062.

24. Liu H. Principles and Applications of Well Logging. Heidelberg: Springer, 2017, p. 356. DOI: 10.1007/978-3-662-54977-3

25. Saragi R., Husien M., Sinaga A.L.M. et al. Successful Approach in Curing Lost Circulation in Depleted Aquifer Formations by Utilizing a Combination of Swelling Polymer & a Shear-Rate Rheology-Dependent Cement System; Case Study in UAE Land Operation. Abu Dhabi International Petroleum Exhibition and Conference, 15-18 November 2021, Abu Dhabi, UAE. OnePetro, 2021. N SPE-207416-MS. DOI: 10.2118/207416-MS

26. Jadhav R., Patil S. Acid-Soluble Thixotropic Cement System for Lost Circulation Challenges. Abu Dhabi International Petroleum Exhibition and Conference, 12-15 November 2018, Abu Dhabi, UAE. OnePetro, 2018. N SPE-193168-MS. DOI: 10.2118/193168-MS

27. Fomenkov A., Pinigin I., Mikliayev M., Fedyanin A. Using Thixotropic Cement Slurry for Lost Circulation Control: Case History, Volga-Urals Region. SPE Russian Petroleum Technology Conference, 22-24 October 2019, Moscow, Russia. OnePetro, 2019. N SPE-196813-MS. DOI: 10.2118/196813-MS

28. Doutoum M.H.A., Alvarado R.F.B., Alaleeli A.R. et al. Advanced Light Weight Thixotropic Lost Circulation Cement Solution for Vugular and Natural Fractured Limestone Formations: UAE Offshore Case History. Abu Dhabi International Petroleum Exhibition and Conference, 15-18 November 2021, Abu Dhabi, UAE. OnePetro, 2021. N SPE-207264-MS. DOI: 10.2118/207264-MS

29. Yuan B., Yang Y., Tang X., Xie Y. A starting pressure prediction of thixotropic cement slurry: Theory, model and example. *Journal of Petroleum Science and Engineering*. 2015. Vol. 133, p. 108-113. DOI: 10.1016/j.petrol.2015.06.005

30. Yang J., Sun J. Status and Prospect of Drilling Fluid Loss and Lost Circulation Control Technology in Fractured Formation. *Gels*. 2022. Vol. 8. Iss. 5. N 260. DOI: 10.3390/gels8050260

31. Mokhtari M., Ozbayoglu E.M. Laboratory Investigation on Gelation Behavior of Xanthan Crosslinked With Borate Intended to Combat Lost Circulation. SPE Production and Operations Conference and Exhibition, 8-10 June 2010, Tunis, Tunisia. OnePetro, 2010. SPE-136094-MS. DOI: 10.2118/136094-MS

32. Jiang G., Deng Z., He Y. et al. Cross-linked polyacrylamide gel as loss circulation materials for combating lost circulation in high temperature well drilling operation. *Journal of Petroleum Science and Engineering*. 2019. Vol. 181. N 106250. DOI: 10.1016/j.petrol.2019.106250

33. Leusheva E., Morenov V. Research of Clayless Drilling Fluid Influence on the Rocks Destruction Efficiency. *International Journal of Applied Engineering Research*. 2017. Vol. 12. N 6, p. 945-949.

34. Ryltsev I.A., Ryltseva K.E., Shrager G.R. Kinematics of a Power-Law Fluid Flow in a Pipe with a Varying Cross Section. *Vestnik Tomskogo gosudarstvennogo universiteta. Matematika i mekhanika*. 2020. N 63, p. 125-138 (in Russian). DOI: 10.17223/19988621/63/11

35. Luzardo J., Oliveira E.P., Derks P.W.J., Nascimento R.V. Alternative Lost Circulation Material for Depleted Reservoirs. OTC Brasil, 27-29 October 2015, Rio de Janeiro, Brazil. OnePetro, 2015. N OTC-26188-MS. DOI: 10.4043/26188-MS

36. Bai Y., Liu C., Sun J. et al. High temperature resistant polymer gel as lost circulation material for fractured formation during drilling. *Colloids and Surfaces A: Physicochemical and Engineering Aspects*. 2022. Vol. 637. N 128244. DOI: 10.1016/j.colsurfa.2021.128244

37. Timkin N. Liquidation of Disastrous Acquisitions with the Use of Equipment Local Well Casing (OLKS-295C) During Construction of the Well N 71 of Kovykta Field. *Burenie & neft*. 2016. N 2, p. 36-37 (in Russian).

38. Park M., Teasdale P., Cowling M. Application of Uncemented Solid Expandable Liner for Combined Openhole Isolation and Casing Repair. SPE/IADC Drilling Conference and Exhibition, 17-19 March 2015, London, UK. OnePetro, 2015. N SPE-173134-MS. DOI: 10.2118/173134-MS

39. Cameron J.R., Cooper B.S., Gusevik R.T. Expandable Solid-Steel Liner Applications in the Marcellus. SPE Eastern Regional Meeting, 20-22 August 2013, Pittsburgh, PA, USA. OnePetro, 2013. N SPE-165671-MS. DOI: 10.2118/165671-MS

***Authors*: Andrei A. Predein,** *Deputy Director*, *Postgraduate Student*, *https://orcid.org/0000-0003-2415-1594* (*"PermNIPIneft" Branch of OOO "LUKOIL-Inzhiniring" in Perm*, *Perm, Russia*; *Perm National Research Polytechnic University, Perm, Russia*), **Olga V. Garshina,** *Candidate of Engineering Sciences, Head of Department*, *https://orcid.org/0000-0002-7188-3010* (*"PermNIPIneft" Branch of OOO "LUKOIL-Inzhiniring" in Perm*, *Perm, Russia*), **Aleksandr A. Melekhin,** *Candidate of Engineering Sciences*, *Associate Professor*, *melehin.sasha@mail.ru*, *https://orcid.org/0000-0002-0737-1360* (*Perm National Research Polytechnic University, Perm, Russia*).

The authors declare no conflict of interests.

ISSN 2411-3336; e-ISSN 2541-9404

JOURNAL OF MINING INSTITUTE
Zapiski Gornogo instituta
Journal homepage: pmi.spmi.ru

Research article

Comprehensive assessment of deformation of rigid reinforcing system during convergence of mine shaft lining in unstable rocks

Vladislav V. Tarasov[1]✉, **Valerii N. Aptukov**[1,2], **Oleg V. Ivanov**[1]
[1] *AO VNII Galurgii, Perm, Russia*
[2] *Perm State University, Perm, Russia*

How to cite this article: Tarasov V.V., Aptukov V.N., Ivanov O.V. Comprehensive assessment of deformation of rigid reinforcing system during convergence of mine shaft lining in unstable rocks. Journal of Mining Institute. 2024. Vol. 266, p. 305-315.

Abstract. Operation of vertical mine shafts in complex mining and geological conditions is associated with a number of features. One of them is a radial displacement of the concrete shaft lining, caused by the influence of mining pressure on the stress-strain state of the mine workings. A rigid reinforcing system with shaft buntons fixed in the concrete lining thus experiences elastoplastic deformations, their value increases with time. It results in deviation of conductors from design parameters, weakening of bolt connections, worsening of dynamic properties of geotechnical system "vehicle – reinforcing", increase of wear rate of reinforcing system elements, increase of risks for creating an emergency situation. The article offers a comprehensive assessment of displacements of characteristic points of the bunton system based on approximate engineering relations, numerical modeling of the deformation process of the bunton system and laser measurements of the convergence of the inner surface of the concrete shaft lining. The method was tested on the example of the reinforcing system of the skip-cage shaft of the potash mine. Displacement of the characteristic points of the reinforcing system is determined by the value of radial displacements of the surface of the concrete shaft lining. Evaluation of the radial displacements was made using monitoring measurements and profiling data. The results obtained make it possible to justify the need and timing of repair works. It is shown that the deterioration of the reinforcing system at different levels occurs at different rates, defined, among other things, by mechanical properties of the rock mass layers located at a given depth.

Keywords: mine shaft; concrete lining; rigid reinforcing; deformation assessment method; profiling

Received: 16.03.2023 ***Accepted: 27.12.2023*** ***Online: 28.02.2024*** ***Published: 25.04.2024***

Introduction. Vertical mine shafts are considered to be of the first class of importance, as their failure to operate properly can lead to shutdown of the entire company (SP 91.13330.2012). The main factor of reliable and accident-free operation of a mine shaft is the serviceability of its reinforcing system, consisting of a system of structures ensuring the movement of the vehicles under specified modes of operation of the lifting unit during the entire operating life of the shaft [1]. Calculation of rigid reinforcing is performed according to the conditions of dynamic stability of the movement of the vehicles in the conductors and is carried out at the stage of mine shaft design. Besides, the elements included in the reinforcing are calculated for compliance with the stiffness and strength characteristics [1-3]. The other loads are considered insignificant, so they are neglected in the calculation or some reserve coefficients are taken into account when determining the loads from the vehicles [4]. Simplifying the calculation scheme may lead to inaccurate determination of the parameters of rigid reinforcing of potash mine shafts, therefore, it is necessary to take into account the complex time-varying interaction of the geotechnical system "rigid reinforcing – shaft lining" [4].

It is known from field observations [5], that during the operation of potash mine shafts, corrosion and mechanical wear of buntons and guide conductors inevitably occurs. Wear of the reinforcing

elements results in changes in their geometric parameters – reduction of conductor and bunton wall thickness and reduction of stiffness of the entire reinforcing system. If the shaft is in complex mining and geological conditions (unstable rock mass, loading from additional excavations, etc.), then deformations of some sections of the lining and, consequently, of the reinforcing occur. Deformations in a concrete monolith can reach such a magnitude that at a certain point a situation arises, at which it is impossible for the vehicle to pass freely in the conductor track. It results in deterioration of dynamic properties of the system "vehicle – reinforcing" and reduction of operation parameters [5, 6]. To eliminate the failure, the deformed section of the bunton is replaced with a straight section of the bunton, whereby it is previously released by pressing the bunton end embedment out of the concrete lining [6]. Each bunton embedment point is opened to the size necessary to bring the conductor track to the base, design position. If necessary, not only the concrete lining is removed, but also the salt rock is stripped to sufficient length and width. A detailed description of the working conditions of the rigid shaft reinforcing with a list of the main load types and their effect on the reinforcing is presented in the papers [7-9].

Statement of problem. Studies by various authors have established that during the operation of a mine shaft in complex mining and geological conditions, deformation of the concrete lining is observed as a result of change of the rock mass containing the shaft [10-12]. Deformation of the concrete lining is transmitted to the rigid reinforcing, resulting in the disruption and design change of the buntons and conductors [13-15]. Various aspects of the effect of undermined areas on shaft geometry and performance are discussed in the papers [16, 17].

The following problems accumulate and occur during continuous operation of the mine shaft lining and reinforcing system [18-20]:

• changes in the track geometry of the guide conductors which can lead to out of track or jamming of the vehicles. It threatens to cause an emergency situation with severe consequences;

• due to intensive abrasion of the conductors and buntons, accumulation of fatigue stresses and corrosion wear, the service life of the reinforcing elements decreases;

• cost of operating the shafts, related to time-consuming regular inspections and labor-intensive repairs of the reinforcing fixing points, increases.

To solve these problems, it is necessary to perform a comprehensive assessment of the technical state of all the elements of the rigid reinforcing as a single frame structure, taking into account the convergence of the concrete lining.

Thus, the task of the research is to study the features of joint deformation of the geotechnical system "rigid reinforcing – shaft lining" followed by the assessment of critical deformations and their influence on the choice of structural and technological solutions for reinforcing vertical shafts.

Methods. To settle out the given problem both the engineering approach and numerical approach were used – finite element method (FEM) using ANSYS application program package. It is necessary to determine the relationships between the magnitude of the concrete lining convergence and the magnitude of deformation (displacements) of the rigid reinforcing by the example of the skip-cage mine shaft of the potash mine. In practice, instrumental methods of investigation and control of reinforcing systems and vehicles using modern measuring tools [21-23] and monitoring [24] are widely used. As calculation methods, primarily the engineering method is applied [25-27], based on approximate approaches of theoretical mechanics and resistance of materials [28, 29]. Approaches based on numerical solution of such problems by the finite element method are also developed [30-32]. Some of them consider box steel structures with corrosion taken into account [33-35]. Note that only individual elements of reinforcing systems have been considered by numerical modeling methods so far, although it seems to the authors that this method, combined with instrumental monitoring methods, has significant promise.

This paper offers a comprehensive approach to the study of joint deformation of the geotechnical system "rigid reinforcing – shaft lining", including engineering and numerical methods, as well as

instrumental measurements of the lining deformation. Approximate relations are presented and a 3D-numerical model has been developed to assess deformations of the rigid shaft reinforcing system with respect to the convergence of the concrete shaft lining. The stress-strain state and displacements of the reinforcing system were determined by the example of the skip-cage shaft of the potash mine. A predictive assessment of the reinforcing performance under the constant effect of the convergence factor of the concrete lining in salt rocks is presented.

Engineering problem statement. The main task for engineering evaluation of the reinforcing performance under the effect of the convergence factor of the inner diameter of the concrete lining is an analysis of the displacements of characteristic points for the complex bunton system over time. It is impossible to formulate equations for analytical determination of the displacements of the characteristic points for the complex bunton system with respect to all interfaces and fixing points. Here we shall take only approximate (engineering) estimates of the displacements within the framework of the following assumptions. All the fixing points of the reinforcing levels in the concrete lining are moved radially by the magnitude ΔR, determined by the lining convergence during salt rock creep under the effect of rock pressure and dependent on time.

Let us introduce the *OXY* coordinate system with the coordinate origin located in the centre of the shaft (Fig.1). Here letters *A*, *B*, …, *I*, *J* mark the points of fixing the shaft buntons R1-R8 to the concrete lining, and letter B_1 marks a new position of point *B* at radial convergence of the shaft lining. Based on the geometrical dimensions of the bunton system, for each fixing point we can determine the angle between radial direction (the segment connecting the shaft centre and the given point, the segment shown by the dotted line) and the axis *OX*. Figure 1 as an example shows an angle φ_B for the fixing point *B*. Through these angles, for each fixing point, we can find displacements of the corresponding point along the coordinate axes, e.g.

$$\Delta U_{BX} = -\Delta R\cos\varphi_B;\ \ \Delta U_{BY} = -\Delta R\sin\varphi_B. \qquad (1)$$

Based on the displacements of all the reinforcing fixing points, it is necessary to evaluate new positions of the junction points of longitudinal and transverse buntons (points *M*, *N*, *Q*, *S*, *V*, *W*). In general, it is a complex nonlinear problem that needs to take into account both the change of the angles in the points of fixing and junction of the buntons and their possible bending in the horizontal plane due to loss of stability. In case of bending, the central part of the bunton span receives additional displacement. Considering all these factors when obtaining engineering estimates requires additional assumptions.

Let us take the bunton R5 as an example. This bunton has junctions with the bunton R6 in the point *M* and the bunton R7 in the point *N* (Fig.1), with possible bending, resulting in maximum displacement along the *X* axis of the middle of the bunton at the connection point with the conductor P3.

The point *M* at the shaft lining convergence will turn to the point M_1, and the fixing points *B* and *C* – to the points B_1 and C_1. We assume that the bunton segments maintain their lengths $BM = B_1M_1$ and $CM = C_1M_1$ (in this case, the *BMC* junction angle may change). Therefore, the coordinates of the new fixing points

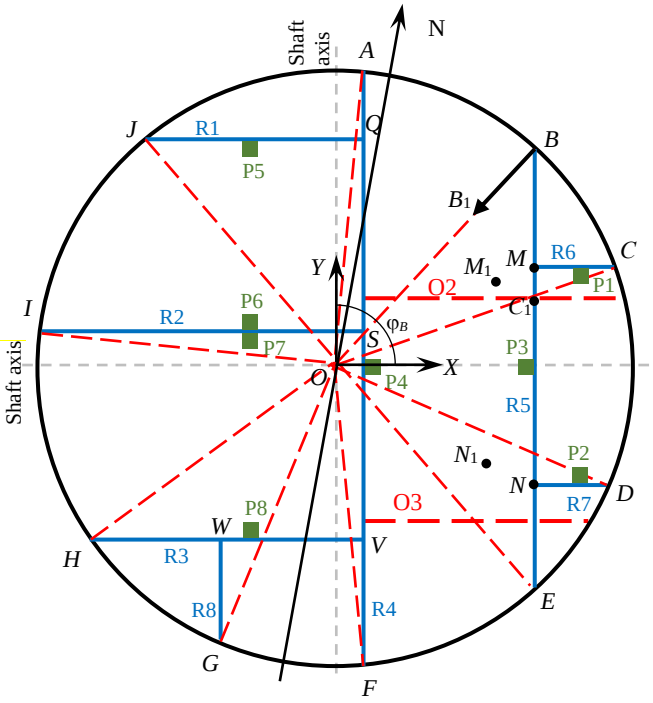

Fig.1. Scheme of buntons and conductors (by the example of the skip-cage shaft)

Journal of Mining Institute. 2024. Vol. 266. P. 305-315

$$X_{B_1} = X_B + \Delta U_{BX}; \quad Y_{B_1} = Y_B + \Delta U_{BY};$$

$$X_{C_1} = X_C + \Delta U_{CX}; \quad Y_{C_1} = Y_C + \Delta U_{CY}; \tag{2}$$

$$\Delta U_{CX} = -\Delta R\cos\varphi_C; \quad \Delta U_{CY} = -\Delta R\sin\varphi_C. \tag{3}$$

Let us say that

$$X_{M_1} \approx X_C + \Delta U_{XC}; \quad Y_{M_1} \approx Y_M + \Delta U_{YB}. \tag{4}$$

It should be noted that the position of the point M_1 will be also influenced by other displacements of the points *D*, *E*, as well as by the junction points of the buntons R5 and R7. In addition, large bunton spans between the fixing points and/or the junction points may bend in the horizontal plane.

We shall estimate the bending deflection of the bunton R5 in the section M_1N_1, assuming that there is a loss of stability of the bunton at its compression in the direction along its axis. As we know, when the critical compression force is reached, the beam loses stability and takes a new (in the special case, flat) sinusoidal shape [36]. The number (or fraction thereof) of sinusoidal waves depends on the boundary conditions of the beam fixation. In our case, the compressive forces do not act strictly coaxially, since for the considered cases the buntons are embedded in the concrete lining, which deforms radially over time, creating two projections of bunton end displacements: along and across its axis.

Following the article [36], we assume that the bending curve of the clamped beam at loss of stability represents a half-wave of the sinusoid shown in Fig.2, where half of the bent curve of the beam is shown, the dotted line shows its initial position.

The initial length of the bunton is *L*. The bunton bends with a bending deflection *C*, which should be estimated after displacement of one end of the beam along its axis relative to the other (fixed) end by the value of Δ. The condition for determining the bending deflection *C* is the equality of the initial length of the bunton half *L*/2 and its length *S* in a bent state. As we know* the length of the curve is defined by the integral [37]

$$S = \int_0^a \sqrt{1 + (y')^2}\, dx, \tag{5}$$

where *a* – integration length; *y*′– derivative of *x*.

In our case $y = 0.5C\sin(\pi x/a)$; $a = 0.5(L - \Delta)$. By entering a new variable $m = -(0.5C\pi/a)^2$, we link together the relation (1) and the full normal Legendre elliptic integral of the 2nd type $E_2(m)$, having no expression in quadrature*,

$$S = \left(\frac{2a}{\pi}\right)\int_0^{\frac{\pi}{2}} \sqrt{1 - m(\sin t)^2}\, dt = \left(\frac{2a}{\pi}\right) E_2(m). \tag{6}$$

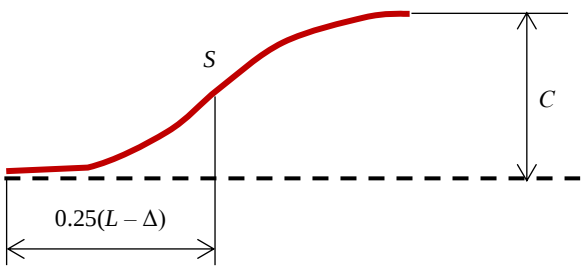

Fig.2. Bending scheme of the bunton beam

At small *m* (the bending deflection is significantly smaller than the bunton length), the function $E_2(m)$ decomposes as a rapidly descending power series

$$E_2(m) \approx \frac{\pi}{2} - \frac{\pi}{8}m - \frac{3\pi}{128}m^2 + O(m^3), \tag{7}$$

where $O(m^3)$ – a value (residue of the power series), which order does not exceed m^3.

* Akhiezer N.I. Elements of elliptic function theory. Moscow: Nauka, 1970, p. 304.

In this case $m \leq 0.1$, consequently, it is enough to use two members of the series in the decomposition (7) to obtain a reasonable engineering approximation.

Thus, in view of the requirement for the equality of the lengths of the bunton beam curves before and after deformation, the expressions for a, m and the decomposition (7), we obtain

$$S \approx a\left(1+\left(\frac{\pi C}{4a}\right)^2\right) = 0.5L\,. \qquad (8)$$

Relationship (8) allows us to get an analytical expression for the bending deflection

$$C \approx \left(2/\pi\right)\sqrt{\Delta\left(L-\Delta\right)}\,. \qquad (9)$$

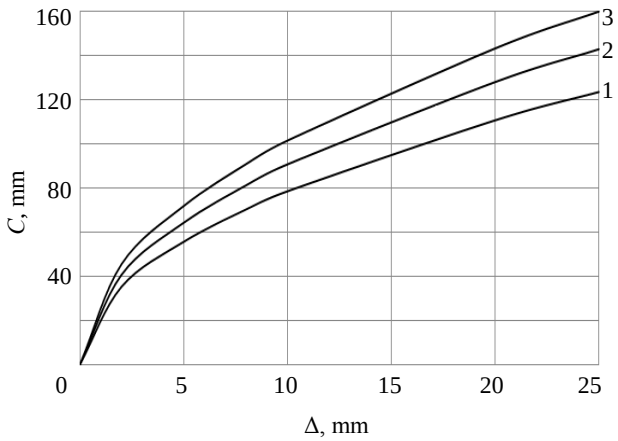

Fig.3. Dependence of the bending deflection on the magnitude Δ for different bunton lengths
1 – 1.5 m; 2 – 2.0 m; 3 – 2.5 m

Figure 3 shows a strong nonlinearity of the dependence on the magnitude of displacement of the bunton end along its axis Δ, especially at small values Δ: thus, at Δ = 5 mm, the bending deflection C = 55-72 mm in the presented range L. The obtained dependencies will be discussed when analyzing the bunton system by the example of the skip-cage shaft.

Estimation of displacements of the bunton characteristic points. From the perspective of accident-free operation of the reinforcing and the vehicles, first of all, it is important to assess the magnitude of displacements of the bunton points in the directions perpendicular to the bunton, in the places of conductor attachment, as they can cause the vehicle both to jam and to move out of the track of the guide conductors. The displacements of interest can be expressed through the corresponding displacements of the bunton fixing points and the value of ΔR, similarly to the formula (1):

$$\Delta U_{YP2} \approx \frac{1}{2}(\Delta U_{YE} + \Delta U_{YD}); \quad \Delta U_{YP5} \approx \frac{1}{2}(\Delta U_{YJ} + \Delta U_{YA});$$
$$\Delta U_{YP6} \approx \Delta U_{YP7} \approx 0; \quad \Delta U_{YP8} \approx \Delta U_{YG}; \qquad (10)$$
$$\Delta U_{XP4} \approx \Delta R + 0.2C(SV); \quad \Delta U_{XP3} \approx \Delta U_{XC} - C(MN),$$

where $C(SV)$, $C(MN)$ – the bending deflections of the bunton spans SV and MN, defined by means of graphical relationships.

Taking into account the dependences of the displacement of the bunton fixing points on the value of ΔR, similarly to the formula (1), we bring relations (10) to the form:

$$\Delta U_{YP1} \approx -0.548\Delta R; \quad \Delta U_{YP2} \approx 0.548\Delta R;$$
$$\Delta U_{YP5} \approx 0.906\Delta R; \quad \Delta U_{YP6} \approx \Delta U_{YP7} \approx 0; \quad \Delta U_{YP8} \approx -0.814\Delta R; \qquad (11)$$
$$\Delta U_{XP4} \approx \Delta R + 0.2C(SV); \quad \Delta U_{XP3} \approx -0.932\Delta R - C(MN).$$

Formulas (11) represent the final result of the approximate approach for estimating the displacements of the bunton points at the conductor fixing points. These formulas are valid for the bunton system (see Fig.1).

Thus, maximum displacements are realized on the conductor P4, further on the conductors P3, P5 and P8. Consequently, over time, problems will arise primarily for these conductors. It is these conductors that should be the subject of close attention during periodic inspections of the shaft reinforcing condition.

Numerical 3D-modeling. A quite promising method of mathematical modeling allows considering the reinforcing system as a single frame structure in combination with concrete lining. Application of numerical methods takes into account the change of many different factors of geometrical and physical state of the reinforcing, such as corrosion reduction of the profile wall thickness, mechanical characteristics of the used steel (modulus of elasticity, yield strength, ultimate strength) [33-35, 38], stress in the system "reinforcing – shaft lining", etc.

The geometric model and the model fragment with FE mesh are shown in Fig.4. The boundary conditions for the considered geometrical model of the reinforcing consist in specifying projections of the displacements along the axes of the *OXY* coordinate system for all points of attachment (end sections) of the shaft buntons R1-R8 to the concrete lining, similarly as it was done in the engineering approach (1). In practice, the buntons are inserted into the concrete lining and fixed in it by creating additional gaskets (wedges) and subsequent concreting of the "hole" created for the bunton. Such attachment cannot provide a "perfect embedment", during the operation the concrete in the hole may crack and the wedges may weaken. All this can result in the creation of an elastic hinge support instead of the "perfect embedment", as well as in "slippage" of the bunton under high axial loads inside the concrete lining.

To model these factors "false" volumes at least 30 cm long (that is how far the buntons enter the concrete) were formed at the ends of the bunton (Fig.4, *a*), then the displacement projections were set. The elastic hinge was modeled by specifying reduced (by a factor of 2) elastic properties of the "false" volumes compared to the bunton itself. The adopted design scheme simulates the concrete stiffness reduction in the "hole" of the bunton attachment and its partial "slippage" towards the rock massif. Thus, the developed numerical model can result in larger calculated bending displacements of the buntons than in reality, i.e., to some "reserve" in predicting the dangerous state of the reinforcing system.

Classical mathematical formulation of the problem of assessing the stress-strain state of an elastoplastic body [39, 40] includes: equations of equilibrium, boundary conditions in displacements and stresses, Cauchy equations, linear elasticity equations of an isotropic body, and plasticity equations. The present calculation scheme does not take into account volumetric forces; there are no surface loads. The boundary conditions are provided by the presence of the specified displacements at the ends of the buntons, an example of which is given in the relation (1).

The reinforcing material is steel 09g2s, yield strength is 325 MPa, ultimate strength is 470 MPa. The cross section of the buntons is a closed rectangular box with dimensions of 130×212 mm; wall thickness is 12 mm.

The tasks were solved by the finite element method in the ANSYS package [41] spatially. The following options were used: Rate Independent, Isotropic Hardening Plasticity, Mises Plasticity, Multilinear for plasticity calculations.

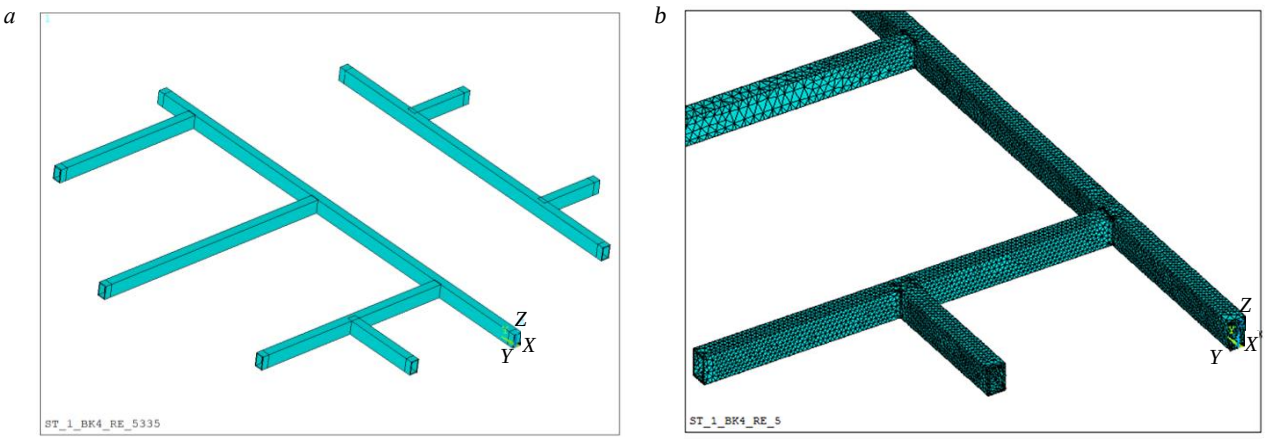

Fig.4. Geometric model of the bunton system with box profile (*a*) and model fragment with FE mesh (*b*)

Analysis of numerical results. A series of calculations of the reinforcing deformation at different values of the shaft lining convergence ΔR was carried out. The displacement field U_X at the value of the radial displacement of the lining ΔR = 30 mm is presented in Fig.5, where we can observe significant displacements of longitudinal bunton areas R4 and R5 located between the transverse buntons. There is a match of the directions of X axes in Fig.5 and 1. The displacement magnitude U_X reaches 192 mm (bunton R4) and –260 mm (bunton R5), which significantly exceeds the convergence value of the shaft lining diameter $2\Delta R$ = = 100 mm. This nonlinear effect is due to the strong bending of the parts of the longitudinal buntons.

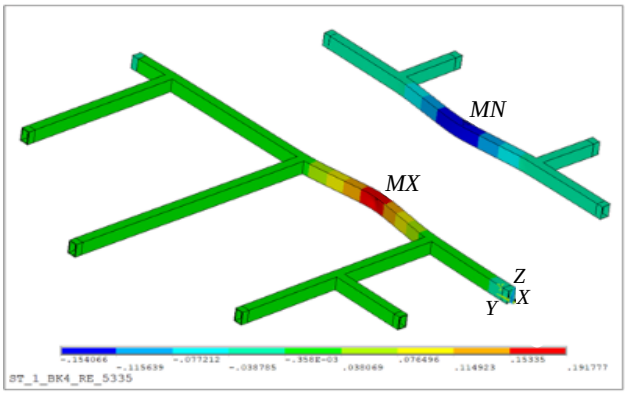

Fig.5. Displacement field U_X at ΔR = 30 mm (blue colour corresponds to the value +154 mm, red colour +192 mm)

It is well known that such deformations of the reinforcing cause failure in safe shaft operation much earlier, i.e., at lower values of the lining convergence. Besides, elastic-plastic deformations (and corresponding stress level) can lead to destruction of the welded box body of the bunton beams. In areas with developed plastic deformations, a so-called plastic hinge can occur. In practice, we are more interested in the displacements of the characteristic points of the reinforcing (e.g., at the conductor locations) as a function of the magnitude of the radial lining displacement ΔR.

Figure 6, *a* shows the dependence of the displacement U_X on ΔR for the fixing points of the conductors P3 and P4. Round markers indicate displacement values calculated by engineering formulas (11), which provide overestimated absolute displacements compared to the values obtained by the FEM. This is due to the fact that the numerical solution takes into account the influence of the entire bunton system as well as a possibility of plastic deformations. The sum of the absolute values of these displacements provides the value of the distance reduction between the conductors P3 and P4. It is obvious that already at the displacement of the lining ΔR is more than 15-20 mm, the displacements of the conductors P3 and P4 become unacceptable.

Figure 6, *b* shows dependences of the distance reduction along the *OY* axis between the conductors P5 and P6 (curve 1), P6 and P8 (2), P1 and P2 (3). Maximum changes of the distances here are observed for the conductors P1 and P2. In general, these values are less significant than the displacements along the axis *OX*. It means that maximum displacements of the bunton points, which determine accident-free operation of the reinforcing, occur in the horizontal plane perpendicular to the direction of the main buntons (the displacements in the fixing points of the conductors P3 and P4).

A similar series of calculations was performed for corrosion-prone reinforcing when the box section wall was reduced by 2.4 mm (up to 9.6 mm). Reduction of the wall results in the increased deformations of the bunton system, and quality changes of the deformation behavior of the main

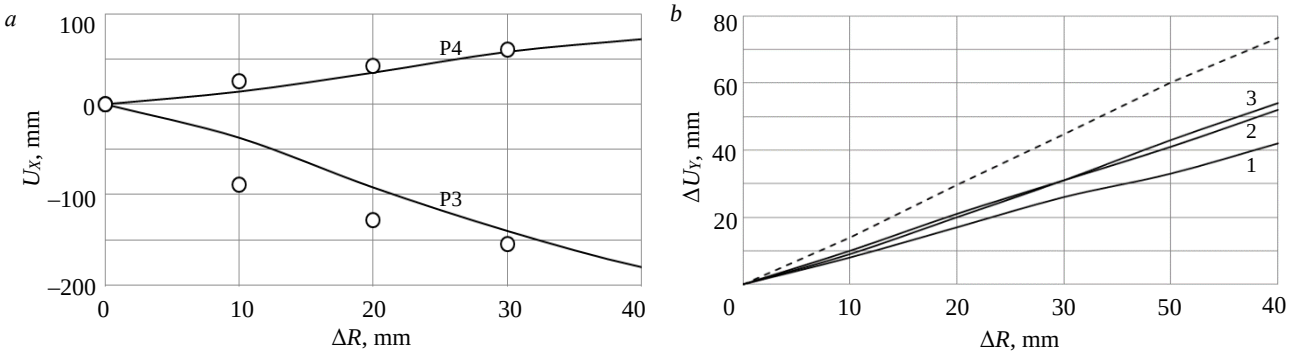

Fig.6. Displacements of the characteristic points of the bunton system

longitudinal bunton are possible. In Fig.6, *b* the dotted line indicates the dependence of the distance reduction along the *OY* axis between the conductors P6 and P8 at box section thickness of 9.6 mm.

Discussion of the results. Analysis and comparison of the modeling results, engineering calculations and in-situ observations were made based on the data of long-term studies on changes in the distances between the parallel buntons R4 and R5 performed in the interval of the levels N 95-140 of the skip-cage shaft of Berezniki mine. Measurements of the distance between the two buntons were carried out along bold red dotted lines drawn through the points of the plumb lines O2 and O3 (see Fig.1).

The value ΔR is taken from the data of the shaft laser scanning [8], conducted in 2021, with one "west-east" direction chosen for each level. We obtained an estimate of the average rate of diameter change at the intersection with carnallite layers at the site of stationary change in diameter 2.0 mm/year. Since the profiling was carried out in 2013, over 8 years the average diameter change could be about 16 mm. This value was subtracted from the laser scanning data. After the profiling before the end of 2013, the conductors were aligned. The results were taken into account when comparing the calculated and experimental data.

Figure 7 shows the dependences of calculated and experimental measurements of the distance reduction between the buntons for 2013. Maximum discrepancy between the calculated and the experimental data including the aligning is 30 %, the average discrepancy is 10.4 %. It should be noted a quality fit of the calculation data according to the proposed complex method and of the profiling measurements. Repairing and replacing the reinforcing is an extremely labor-intensive process, resulting in high financial costs associated with shaft shutdowns and a corresponding reduction in the productivity of part or the whole potash mine. In the first years of operation of the mine shaft reinforcing located in the salt massif, localized repairs (aligning) are done to correct the curvature of the conductors. Aligning of the reinforcing means adjustment of two reinforcing connection units (flange joints), with displacement of the longitudinal axis in each bunton unit by a certain length, allowing to bring the conductor track to the base value. In each specific case, the aligning time depends on the depth of the level *H* and on the geomechanical properties of the rock mass at this depth.

For example, mechanical properties of carnallitic rocks are significantly inferior to those of sylvinite or rock salt, so reaching the time *T* may occur earlier in the sylvinite-carnallite area rather than in the underlying rock salt area, which is much deeper. In addition, the area of the shaft junction with horizontal workings is also a weakened area. Estimation of the time *T* in this area is difficult, as it also depends (apart from the above factors) on the geometry (structural features) of the area of the shaft junction with horizontal workings [10].

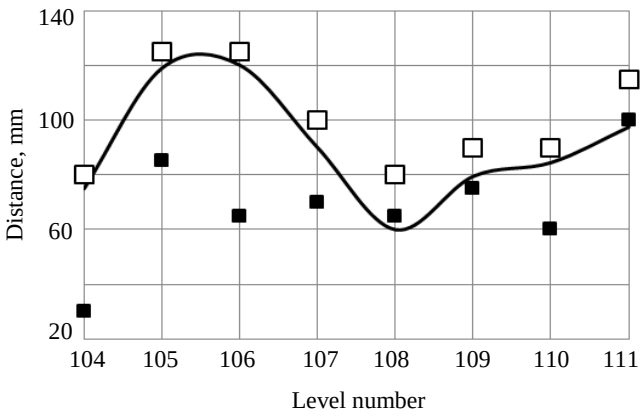

Fig.7. Change of the distance between the buntons: calculation (solid line) and experimental (squares) measurements. Average values of profiling data along the lines O2 and O3 exclusive of the aligning (black squares); including the aligning performed in 2013 (white squares)

Based on the specific rates of change of the shaft diameter obtained by laser scanning [8], results of research data and numerical modeling of the deformation process of the concrete lining as a result of salt mass creep [10], the following conclusions can be drawn:

• for the reinforcing levels located in carnallitic rocks with high rates of change in the shaft diameter, the first aligning should be carried out already in T = 4-5 years after the operation start, the second one – in 20 years (about 15 years after the first one), the third one – in 50 years (about 30 years after the second one);

• the first aligning for the levels with minimal rates of the diameter change (intersection with rock salt, sylvinite) is necessary after T = 20-25 years;

• aligning on the remaining levels is necessary in the time range between these two extreme cases.

The proposed integrated approach for each bunton system of a particular shaft needs to be performed anew: to carry out laser monitoring, profiling, to form a new calculation scheme and to perform numerical studies. Of course, the error of forecast calculations may be different for different shafts. The most difficult point is the application of the proposed method for the assessment of the bunton deformations after the performed aligning – it requires additional research.

Thus, practical application of the results of the calculations and the performed research consists in predicting the onset of critical deformations of the rigid reinforcing system with further substantiation of repair works.

Conclusion. This article considers the features and the problems of the rigid reinforcing operation in potash mine shafts, when concrete lining experiences significant deformations when interacting with rock massif. The authors offer the comprehensive assessment of displacements of the characteristic points of the bunton system based on approximate engineering relations, numerical modeling of the deformation process of the bunton system and laser measurements of convergence of the inner surface of the shaft concrete lining.

Numerical modeling of the complete bunton system of rigid reinforcing in 3D-setting at the convergence of the shaft concrete lining was carried out, specific features of the bunton deformation, maximum displacements of the characteristic points were revealed. The authors compared engineering and numerical estimates of the bunton system displacements at different levels with monitoring (profiling) data and laser measurements of the inner surface of the concrete lining of the skip-cage shaft of the potash mine. Based on the estimates of the convergence rates of the shaft concrete lining at the intersection of rock mass layers with different physical and mechanical properties, the forecast estimates of the limiting time of the reinforcing operation have been obtained, after which repair works will be required.

Thus, the comprehensive assessment of the rigid reinforcing deformation at the convergence of the shaft concrete lining allows making correct calculations for determining parameters of rational schemes of the reinforcing structures and the lining of the shafts located in salt massif.

REFERENCES

1. Manets I.G., Snegirev Yu.D., Parshintsev V.P. Maintenance and repair of mine shafts. Moscow: Nedra, 1987, p. 327 (in Russian).

2. Gerdemeli I., Candas A., Unalan M. Design of Mine Shaft Elevator. Scientific Proceedings IX International Congress “Machines, Technologies, Materials”, 19-21 September 2012, Varna, Bulgaria. Sofia, 2012. Vol. 2, p. 117-120.

3. Pleshko M.S., Nasonov A.A., Yagodkin F.I., Privalov A.A. Issues of improvement of vertical shaft planning, construction and reconstruction efficiency. *Mining Informational and Analytical Bulletin.* 2017. N 8, p. 179-186. DOI: 10.25018/0236-1493-2017-8-0-179-186

4. Stradanchenko S.G., Prokopov A.Y., Tkacheva K.E. Probabilistic approach to determination of the tempral loadings on reinforcement of vertical shafts. *Mining Informational and Analytical Bulletin.* 2012. N 8, p. 61-68.

5. Tarasov V.V., Pestrikova V.S., Rusakov M.I. Life cycles of the structure complex of mine shafts of Verkhnekamskoye deposit. Novosibirsk: Nauka, 2021, p. 230 (in Russian).

6. Yagodkin F.I., Prokopov A.Yu., Prokopova M.V. Repair of vertical mine shaft lining. *News of the Tula State University. Sciences of Earth*. 2017. Iss. 3, p. 195-208 (in Russian).

7. Samusya V.I., Ilin S.R., Ilina I.S., Ilina S.S. Instability factors of the vehicle-reinforcing system performance in complex mining and geological conditions of vertical shafts. *Vestnik Permskogo natsionalnogo issledovatelskogo politekhnicheskogo universiteta. Geologiya. Neftegazovoe i gornoe delo*. 2015. N 17, p. 72-80 (in Russian). DOI: 10.15593/2224-9923/2015.17.8

8. Tarasov V.V., Aptukov V.N. Deformation monitoring of mine shaft concrete lining by laser scanning. *Fiziko-tekhnicheskie problemy razrabotki poleznykh iskopaemykh*. 2022. N 5, p. 188-195 (in Russian). DOI: 10.15372/FTPRPI20220518

9. Trifanov G.D., Mikryukov A.Yu. Industrial development exploitation based monitoring system lifting vessels in the shafts. *Aktualnye problemy povysheniya effektivnosti i bezopasnosti ekspluatatsii gornoshakhtnogo i nefteprомyslovogo oborudovaniya*. 2016. Vol. 1, p. 49-54.

10. Tarasov V.V., Aptukov V.N., Pestrikova V.S. Deformation and failure of concrete lining in vertical shaft at intersections with horizontal tunnels. *Journal of Mining Science*. 2020. Vol. 56. Iss. 5, p. 726-731. DOI: 10.1134/S1062739120057056

11. Konstantinova S.A., Kramskov N.P., Solovev V.A. Some problems of rock mechanics as applied to the mining of diamond deposits in Yakutia. Novosibirsk: Nauka, 2011, p. 223 (in Russian).

12. Karasev M.A., Buslova M.A., Vilner M.A., Nguen T.T. Method for predicting the stress-strain state of the vertical shaft lining at the drift landing section in saliferous rocks. *Journal of Mining Institute*. 2019. Vol. 240, p. 628-637. DOI: 10.31897/PMI.2019.6.628

13. Dubinin M.V., Dvornikov B.I. Finite elemet modeling for stress-strain state of the mine trunks reinforcement that it has been made shaft skip. *Aktualnye problemy povysheniya effektivnosti i bezopasnosti ekspluatatsii gornoshakhtnogo i neftepromyslovogo oborudovaniya*. 2014. Vol. 1, p. 55-60.

14. Balek A.Y., Efremov E.Y. Stress-strain state investigation QF mine shaft and horizontal gallery crossing using surveying technique. *News of the Tula State University. Sciences of Earth.* 2019. Iss. 2, p. 267-279. DOI: 10.25635/IM.2019.29.37273

15. Prokopov A.Yu., Prokopova M.V. Engineering of vertical longhole shaft equipment on the basis of laws of functioning of system "an elevating vessel – reinforcement – a trunk". *Mining Informational and Analytical Bulletin.* 2012. N 7, p. 78-82.

16. Kopytov A.I., Pershin V.V., Voitov M.D., Wetti A.A. The Improvement of the Bunton Construction of Mine-shaft Equipment. The 8th Russian-Chinese Symposium. Coal in the 21st Century: Mining, Processing and Safety, 10-12 October 2016, Kemerovo, Russia. Atlantis Press, 2016, p. 108-110. DOI: 10.2991/coal-16.2016.21

17. Sentyabov S.V., Selin K.V., Karamnov D.V. Parameters refining and monitoring for vertical deformations of the axle of mine shaft on the worked space. *Problems of Subsoil Use.* 2020. N 2 (25), p. 108-115. DOI: 10.25635/2313-1586.2020.02.108

18. Ilin S.R., Samusia V.I., Ilina I.S., Ilina S.S. Influence of Dynamic Processes in Mine Hoists on Safety of Exploitation of Shafts with Broken Geometry. *Naukovyi visnyk Natsionalnoho hirnychoho universytetu.* 2016. N 3, p. 48-53.

19. Wolny S., Matachowski F. Analysis of Loads and Stresses in Structural Elements of Hoisting Installations in Mines. *Engineering Transaction*. 2010. Vol. 58. N 3-4, p. 153-174.

20. Kodnyanko E.V. Study of the wear of the profile of the mine shaft conductors. Innovations, Physical Studies and Digitalization in Mining Engineering 2021: Sbornik tezisov VIII Mezhdunarodnoi nauchno-prakticheskoi konferentsii, 22-23 April 2021, Saint Petersburg, Russia. Saint Petersburg: Saint Petersburg Mining University, 2021, p. 189-191.

21. Xiao Xing-ming, Li Zhan-fang, Zhang Jun. Study on fault mechanism of shaft hoist steelwork. The 6th International Conference on Mining Science & Technology, 18-20 October 2009, Xuzhou, China. Procedia Earth and Planetary Science, 2009. Vol. 1. Iss. 1, p. 1351-1356. DOI: 10.1016/j.proeps.2009.09.208

22. Trifanov G.D., Knyazev A.A., Filatov A.P., Lauk V.V. Experience of Operation of the Mine Winding Plants Equipped with Continuous Monitoring Systems. *Monthly Journal of Research and Production.* 2019. N 6, p. 52-58. DOI: 10.1016/j.proeps.2009.09.208

23. Hanna M., Lloyd A., Tikka T. Improving conveyance side slipper plate design to accommodate higher impact bunton force. Building Tomorrow's Society, 13-16 June 2018, Fredericton, Canada. Canadian Society for Civil Engineering, 2018, p. ST49-1 – ST49-10.

24. Zelenko A.V., Gorbach A.N. Continuous monitoring of safe movement of lifting vessels of shaft barks. Aktualnye problemy povysheniya effektivnosti i bezopasnosti ekspluatatsii gornoshakhtnogo i neftepromyslovogo oborudovaniya: Materialy VI Mezhdunarodnoi nauchno-prakticheskoi konferentsii "Gornaya i neftyanaya elektromekhanika-2019", 21-24 October 2019, Perm, Russia. Perm: Izd-vo Permskogo natsionalnogo issledovatelskogo politekhnicheskogo universiteta, 2019. Vol. 1, p. 37-43 (in Russian).

25. Nikolaitchik M. Determination of skip force effect on guides in mine shaft. Ukrainian School of Mining Engineering, 7-11 September 2020, Berdiansk, Ukraine. E3S Web of Conferences, 2020. Vol. 201. N 01017. DOI: 10.1051/e3sconf/202020101017

26. Mikryukov A.Y., Kamenskikh Y.V. Survey and evaluation of the technical condition of lifting vessels. Aktualnye problemy povysheniya effektivnosti i bezopasnosti ekspluatatsii gornoshakhtnogo i neftepromyslovogo oborudovaniya: Materialy VI Mezhdunarodnoi nauchno-prakticheskoi konferentsii "Gornaya i neftyanaya elektromekhanika-2019", 21-24 October 2019, Perm, Russia. Perm: Izd-vo Permskogo natsionalnogo issledovatelskogo politekhnicheskogo universiteta, 2019. Vol. 1, p. 69-75 (in Russian).

27. Pestrikova V.S. Algorithm for calculating the durability of rigid reinforcements of shaft operating under the conditions of Verkhnekamsky deposits of potassium salts. *News of the Tula State University. Sciences of Earth.* 2019. Iss. 4, p. 332-339.

28. Jiannan Yao, Xiaojie Deng, Chi Ma, Tong Xu. Investigation of Dynamic Load in Superdeep Mine Hoisting Systems Induced by Drum Winding. *Shock and Vibration*. 2021. Vol. 2021. N 4756813. DOI: 10.1155/2021/4756813

29. Kachurin N.M., Afanasiev I.A., Pestrikova V.S., Stas P.P. Interactions of vertical shafts with rock massifs by recovery of lining and fasteners and mine shaft equipment. *News of the Tula State University. Sciences of Earth.* 2020. Iss. 3, p. 290-303.

30. Zhuravkov M.A., Nikolaitchik M.A. Finite element modeling of the lifting vessel interaction with the mine shaft structural elements. *Mining Mechanical Engineering and Machine-Building.* 2021. N 4, p. 15-21.

31. Nikolaichik M.A., Zhuravkov M.I. Mathematical modeling of the state of critical elements of the mine hoisting complex. Problemy bezopasnosti na transporte: Materialy XII Mezhdunarodnoi nauchno-prakticheskoi konferentsii, posvyashchennoi 160-letiyu Belorusskoi zheleznoi dorogi, 24-25 noyabrya 2022 g.: v 2 ch. Gomel, Belarus. Belorusskii gosudarstvennyi universitet transporta, 2022. Part 2, p. 228-230 (in Russian).

32. Jakubowski J., Fiolek P. Evaluation of Stiffness and Dynamic Properties of a Mine Shaft Steelwork Structure through In Situ Tests and Numerical Simulations. *Energies*. 2021. Vol. 14. Iss. 3. N 664. DOI: 10.3390/en14030664

33. Fiolek P., Jakubowski J. Assessment of the Bending Moment Capacity of Naturally Corroded Box-Section Beams. *Materials*. 2021. Vol. 14. Iss. 19. N 5766. DOI: 10.3390/ma14195766

34. Fiolek P., Jakubowski J. Local buckling of highly corroded hot-rolled box-section beams. *Journal of Constructional Steel Research*. 2019. Vol. 157, p. 359-370. DOI: 10.1016/j.jcsr.2019.03.009

35. Jakubowski J., Fiołek P. Probabilistic structural reliability assessment of underground shaft steelwork. *Tunnelling and Underground Space Technology*. 2022. Vol. 130. N 104755. DOI: 10.1016/j.tust.2022.104755

36. Lalin V.V., Kushova D.A. Geometrically nonlinear deformation and stability problems of plane elastic rods with tension-compression, shear and bending stiffness taken into account. *International Journal for Computational Civil and Structural Engineering*. 2013. Vol. 9. Iss. 4, p. 178-185.

37. Prasolov V.V., Solovev Yu.P. Elliptic functions and algebraic equations. Moscow: Izd-vo Moskovskogo tsentra nepreryvnogo matematicheskogo obrazovaniya, 2022, p. 312 (in Russian).

38. Samusia V.I., Iliina I.S., Iliina S.S. Influence of parameters of roller guides on the contact load in the "vessel-reinforcement" for shafts with a broken geometry. *Bulletin of PNRPU. Geology. Oil & Gas Engineering & Mining*. 2016. Vol. 15. N 20, p. 277-285. DOI: 10.15593/2224-9923/2016.20.8

39. Tutyshkin N.D., Gvozdev A.E., Tregubov V.I. et al. Complex problems in plasticity theory. Tula: Tula State University Press, 2015, p. 408.

40. Brovko G.L. Approaches to formulation and methods of solving boundary value problems of solid mechanics. *Izvestiya MGTU MAMI*. 2013. Vol. 7. N 3-1, p. 46-65. DOI: 10.17816/2074-0530-67989

41. Morozov E.M., Muizemnek A.Yu., Shadskii A.S. ANSYS in engineer's hands: Fracture mechanics. Moscow: LENAND, 2014, p. 456 (in Russian).

Authors: **Vladislav V. Tarasov,** *Candidate of Engineering Sciences, Head of Laboratory, Vladislav.Tarasov@uralkali.com, https://orcid.org/0000-0002-3431-7028* (*AO VNII Galurgii, Perm, Russia*), **Valerii N. Aptukov,** *Doctor of Engineering Sciences, Chief Researcher, Head of Department, https://orcid.org/0000-0001-8048-3804* (*AO VNII Galurgii, Perm, Russia*; *Perm State University, Perm, Russia*), **Oleg V. Ivanov,** *Leading Engineer, https://orcid.org/0000-0001-6566-4375* (*AO VNII Galurgii, Perm, Russia*).

The authors declare no conflict of interests.

ISSN 2411-3336; e-ISSN 2541-9404

JOURNAL OF MINING INSTITUTE
Zapiski Gornogo instituta
Journal homepage: pmi.spmi.ru

Research article

Justification of the approaches to improve management strategy of the mining system based on the analysis of data on the mining of complex structural rock blocks

Mariya V. Tsupkina✉, Aleksei E. Kirkov, Dmitrii A. Klebanov, Dmitrii N. Radchenko
Institute of Comprehensive Exploitation of Mineral Resources RAS, Moscow, Russia

***How to cite this article*:** Tsupkina M.V., Kirkov A.E., Klebanov D.A., Radchenko D.N. Justification of the approaches to improve management strategy of the mining system based on the analysis of data on the mining of complex structural rock blocks. Journal of Mining Institute. 2024. Vol. 266, p. 316-325.

Abstract. Long-term activity of mining enterprises causes the necessity to substantiate the strategies of management of the mining and technical system functioning in terms of improvement of ore quality control, which is determined by its change in the course of field development due to the priority development of the main reserves and, as a consequence, forced transition to the mining of complex structural rock blocks with a decrease in the recovery percentage, which is typical in case the ore component meets the requirements of the feasibility study in terms of grade at substandard capacity. In this case, it is possible to identify the recovery percentage and the potential for its increase by analyzing the long-term activity of the mining and industrial enterprise, namely, by analyzing the data of mining complex structural rock blocks with the subsequent establishment of the relationship between the primary data on mining and geological conditions and information on the quality of the mineral obtained from the technological equipment. Therefore, the purpose of the research was to substantiate the necessity of improving the management strategy of the mining-technical system functioning, which consists in the fact that on the basis of analyzing the mining data of complex structural rock blocks it is possible to determine the ore mass losses and their quantity and to lay the basis for the development of decisions on its extraction. For this purpose, the collected data on the mining of complex structural rock blocks, accounting the geological and industrial type of extracted ores, were considered in modeling the conditions and studying the parameters of technological processes, the implementation of which provides additional products. It was revealed that the ore mass from substandard thickness layers is delivered to the dumps, and ore mass losses have been estimated at 25-40 % per year. It is proved that determination of ore mass losses based on the analysis of data on mining of complex structural rock blocks, as well as timely solution of this issue can significantly increase the production efficiency of mining and technical system. Taking into account for the results obtained, the options for optimizing the production of the mining and engineering system were proposed.

***Keywords*:** mining engineering; quality management; ore flow; complex structural rock blocks; big data; data analytics; production optimization

Acknowledgment. The study was funded by the Russian Science Foundation grant N 22-17-00142.

Received: 02.08.2023 ***Accepted: 27.12.2023*** ***Online: 29.02.2024*** ***Published: 25.04.2024***

Introduction. The continuous operation of mining enterprises with the priority of mining rich ores gradually leads to the fact that nowadays there is an increase in mining volumes with a simultaneous decrease in the quality characteristics of ore flow [1, 2]. This is one of the urgent problems reducing the production efficiency of the mining system [3, 4]. Since rational management of the qualitative characteristics of the extracted ore mass is the basis for ensuring the production performance of the mining and technical system [5, 6], the solution of this problem will increase the completeness of subsoil development and improve the production performance of mining enterprises as a whole.

The quality characteristics of ore streams are managed in all technological processes along the chain: stripping of the deposit or its parts – preparation for cleaning excavation – loading into vehicles – transportation – shipment and storage for processing – beneficiation. The effectiveness of quality management depends directly on the analysis of data from the rock mass [7, 8] and technological equipment [9].

According to the sources [10, 11], traditional methods and tools of quality management allow identifying problems and optimizing the decision-making process, but a significant disadvantage can be considered a delay in the implementation of corrective actions. In addition, prolonged development of mineral deposits introduces new complexities in technological processes, which is often associated with depletion of reserves or complication of mining and geological conditions and requires new approaches to quality management of ore mass. Information and communications technology make it possible to increase efficiency in quality management by integrating into technological processes various patterns obtained from data analysis and reflecting production efficiency [12, 13], as well as to manage the quality of ore mass in real time, while minimizing losses [11, 14, 15].

Currently, Industry 4.0* technologies such as the Internet of Things (IoT) [16], big data [17], cloud computing, 3D visualization, provide digital transformation of mining enterprises with a number of advantages in terms of production efficiency, product quality and cost reduction [18-20], as well as determination and prediction of various process parameters [21-23]. The authors of the article [24] believe that the key components for effective quality management are the processing of big data and improvement of prescriptive analytics.

The basis of the digital process control system capable of ensuring the required level of efficiency at a mining enterprise [25] is reliable and timely information at all levels of production [26, 27]. However, the highest efficiency indicators can be achieved only with the understanding of the target task, based on which the list of information sources and types of data generated during the implementation of technological processes should be determined. In terms of quality management such sources can be data on the material composition and technological properties of ores, geophysical and geochemical studies [28-30], as well as data from analytical information and automated systems [31], including the automated control system of the mining and transportation complex, automated control system of drilling and blasting control system, quality control system and other systems and types of data that include information on changes in the quality characteristics of the mineral at all stages of field development [32].

In terms of definition of sources of digital data and organization of their collection, the classification of data sources of mining-technical system based on the object of their obtaining, proposed in the paper, [33], is the most suitable, because this classification allows to justify the order of putting the source of information into operation at the design stage for each physical object, to determine the parameters of the received signals and the principles of their transformation into digital form and, if necessary, to establish the requirements for the frequency of the received data, as well as the format, suitable for the data collection. for processing, analysis, long-term storage and conditions for using the data.

Statement of problem. As the authors admit [34], the solution to improve the homogeneity of the quality characteristics of the formed ore streams is the reliable separation of ore deposits in the rock mass with their precise delineation and identification of technological types and grades of ores, ensuring their efficient mining and transportation in the appropriate modes of separation or quality averaging. However, the reliability of such allocation depends on the mining and geological conditions of the fields being developed, based on the analysis of which the industrial value and complexity group of the objects are determined with subsequent justification of the geotechnology of their development [35]. It should

* Industrial Development Report 2020: Industrializing in the digital age. Vienna: United Nations: Industrial Development Organization, 2019, p. 228.

be noted that the quality indicators of the extracted ore mass crucially depend on the mining and geological features of the mined deposits, so it is necessary to pay special attention to improving the reliability and processing of data on the rock mass and to interpret the obtained results accounting for the analysis of other data sources.

The problem of ensuring consistent quality is most relevant for mining companies engaged in the development of complex structural deposits of solid minerals [36, 37], where the total volume of the developed deposit has a significant proportion of low-power steeply dipping ore bodies, the effective excavation of which is complicated [38]. As a rule, the main difficulties in ensuring quality characteristics in this case are associated with the lower capacity of the working bodies of the excavation equipment compared to the thickness of ore layers, which results in the ore dilution, leading to a decrease in the quality characteristics of raw materials.

In addition, when developing deposits, mining companies are required to conduct their operations in accordance with the adopted feasibility report of the conditions, which may set limits on both the content of valuable components and the capacity of ore bodies. Thus, for example, the basic block model of the deposit, which is formed accounting for the compliance with the power specifications, is simplified by excluding ore layers whose thickness does not meet the accepted requirements, if within the developed deposit there are ore layers with a thickness of 4 to 5 m, and the specifications are focused on the development of layers with a thickness of more than 6 meters. As a result, the reliability of the real mining and geological situation is reduced, which subsequently leads to a decrease in the productivity of the enterprise due to the planning of mining operations based on an incomplete set of data, leading to significant losses of ore mass entering the dumping facilities. This allows us to formulate a hypothesis on the necessity of finding solutions aimed at identifying possible losses of ore mass and justifying the recommendations that will ensure increased efficiency in quality management in the course of deposit development.

Thus, due to the increasing probability of significant losses of the ore component, corresponding in content to the requirements of the feasibility study at substandard capacity, when mining complex structural rock blocks, a variant of improving the management strategy of the functioning of the mining and technical system is proposed, which differs in that the increase in the completeness of subsoil development can be provided on the basis of analyzing the data on the mining of complex structural rock blocks, namely by identifying the types of possible losses and their quantitative index, which as a result will contribute to the development of solutions aimed at additional extraction of ore mass. Justification of the proposed variant will determine the possibility of revision of the existing quality management systems or their supplementation accounting for the need to increase the productivity of the enterprise and obtain additional marketable products in the form of productive fraction, previously not extracted for objective reasons.

Justification of the improvement of the management strategy for the functioning of the mining and technical system in terms of quality management within mining and industrial enterprises is a considerable task, the solution of which can be realized by obtaining their long-term activity. The study is based on the analysis of big data generated during the functioning of the mining-technical system from each unit of mining equipment, which is the source of formation of data on the indicators of its operation and condition [9, 27, 39]. In this case, to solve the problem of ore flow quality management, special attention should be paid to analyzing data on the mining of complex structural rock blocks with the subsequent establishment of the relationship between the primary data on the mining and geological conditions of the deposit and data on the quality of the mineral obtained from the process equipment.

The aim of the paper is to substantiate the necessity and possibility of improving the management strategies of mining-technical systems based on more adequate block models and mechanisms of ore flow management using modern methods of predictive analytics.

Methodology. Since the highest efficiency indicators of mining system development processes can be achieved only by understanding the target task, it should be taken into consideration that the list of requested data is determined both depending on the availability of data at the enterprise and accounting for the geological and industrial deposit type. For example, when collecting information at an enterprise extracting iron ores*, data from both chemical sampling and geophysical methods for determining the quality of the mineral are mandatory.

In order to verify the proposed variant of improving the management strategy for the functioning of the mining-technical system at one of the iron ore mining-industrial enterprises of the country, an audit of the current quality management system was conducted, and retrospective data for the last three years of activity were requested, including information on the processing of complex structural rock blocks obtained from the mining mass and technological equipment.

Modeling of conditions and study of parameters of technological processes, implementation of which can provide extraction of additional marketable products, was carried out in several stages:

• collection and processing of all information received from the enterprise on the mining of complex structural rock blocks received from the mining massif and technological equipment;

• verification of the integrity of uploads from provided databases;

• preparation of initial data presented in the form of distribution of the rock mass structure indicators, elements of working processes of the mining and engineering system, tied to specific points of space and time;

• modeling of conditions and research of technological processes parameters based on the regularities identified at the first stage;

• preparation of conclusions based on the data analysis on possible scenarios for the development of complex structural rock blocks to determine the types of possible losses and their quantitative indicators.

Taking into account the data available to the enterprise, as well as the geological and industrial type of ores to be mined, the list of required data included:

• maps of magnetic iron content distribution by mined blocks, drawn up at the annual planning stage;

• maps of magnetic iron content distribution over mined blocks, based on drill and blast logging data;

• block layout on the pit plan;

• instructions adopted at the enterprise for determining, accounting and standardization of production losses;

• ore control station performance statistics;

• loss reports;

• data on ore types and their characteristics (study);

• data on wells of the exploration stage at the deposit, which are the basis for building the initial block model;

• current ore quality requirements at the beneficiation plant;

• list of attributes (magnetic iron content, sulfur content, enrichment, lithology);

• data on mining, loading and transportation means used;

• dispatching system data (number of machines sent to dump, ore stockpile, SMS with linkage to faces).

At the stage of initial data preparation for modeling, the integrity of database uploads was checked, which consisted in determining the presence of information on spatial position and hole parameters. In addition, a cross-check was performed to verify the consistency of the same information presented in different records of different database tables.

* Guidelines on the application of the Classification of reserves and forecast resources of deposits of solid minerals. Iron ore. Moscow: Gosudarstvennaya komissiya po zapasam poleznykh iskopaemykh, 2007, p. 40 (in Russian).

Journal of Mining Institute. 2024. Vol. 266. P. 316-325

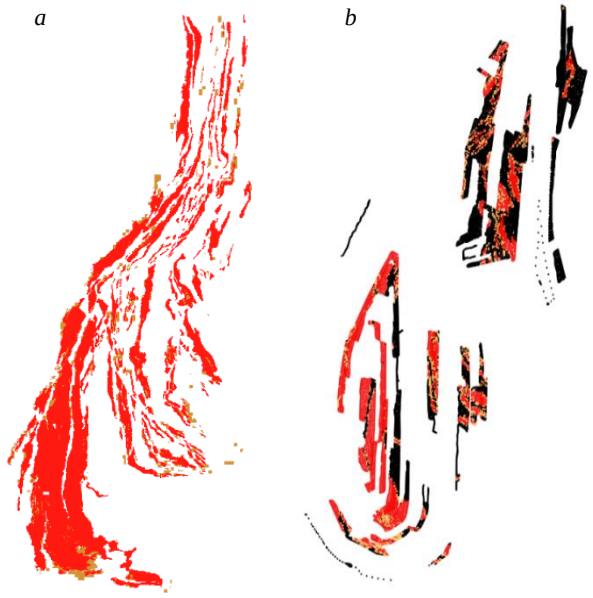

Fig.1. Results of comparing data of hole logs (*a*) and block model (*b*)

At the initial stage of resource model preparation, it was decided to use data from the enterprise's block model, however, during the analysis of the logging data by blocks, including the search for substandard thickness of interlayers, taking into account the peculiarities of ore depo-sits occurrence and annual mining decline, the discrepancy between the block model data and hole logging results was established (Fig.1). In the course of modeling, this may lead to a mismatch between the actual production volumes and the modeling results.

The second negative point affecting the quality of the final result is the use of interpolation models when building a block model, which increases the smoothness of contours and leads to increased resource costs for processing and analyzing the obtained information. Therefore, it was decided to use as initial information on the geological structure an analog of the block model built from hole logging data without using interpolation (Fig.2). The proposed model is based on A.K.Boldyrev's reserve calculation method and the concept of the nearest area (geometric area of influence of the hole)* (Fig.2, *b*).

At the stage of information processing the selection of initial data for modeling was carried out. Due to the lack of standardization of digital data collection and storage, as well as unstructured data from multiple technological processes, the obtained information on the functioning of the mining and technical system was multi-format, which made it difficult to analyze it using standard methods of mathematical analysis. Since geologic data are generated in the process of research and additional study of the massif under development (frequency of receipt and updating at least once a month), and dispatching data (discreteness – 1 s or more) – due to the operation of process equipment, there is a problem of linking the collected information into a single complementary complex or structure of spatial and temporal data sets. The problem is solved by synchronizing, structuring, transforming and bringing different datasets to a common format that allows the construction of a single spatio-temporal model processed using uniform methods and rules.

Analysis of the initial data at the stage of their preparation allowed us to identify two key sets of factors that have a major impact on the efficiency of the mining and technical system of this enterprise: factors related to the features of the geological structure, and factors related to the

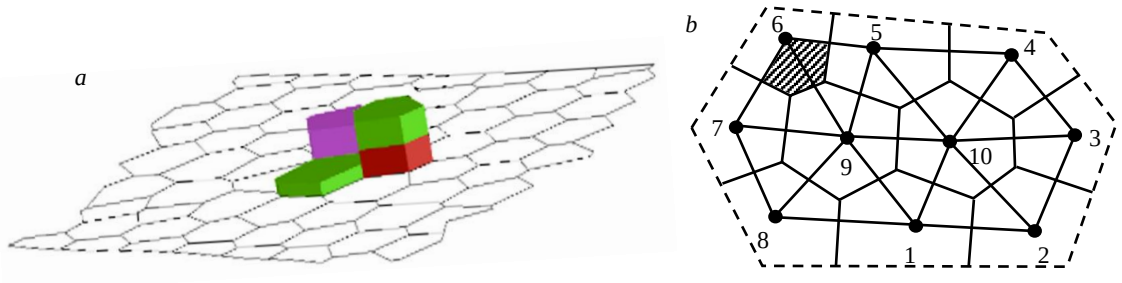

Fig.2. The principle of matching logging data with the nearest area (*a*) and the principle of constructing the nearest area (*b*) for holes

* Zamotin V.B., Koshkina L.B., Lyskov I.A. Calculation of solid mineral reserves. Perm: Perm National Research Polytechnic University, 2012, p. 33 (in Russian).

operation of the mining and transportation system, which forms the structure of the ore and overburden flow.

The geological component of the geospatial source data set in this case is represented by the description of geological information in the form of simple text and graphic files: graphical representation of the developed block in the form of nearest area sets for each hole in the block, logging data, hole data with areas of constructed nearest areas.

Information on the operation of mining and transportation equipment, including information on the volume of cargo transportation, is represented by a set of basic indicators of the automated dispatching system: average speeds of dump trucks, distances of their movement from blocks to unloading points, the model range of dump trucks by body volume, data on average intervals of loading of one dump truck taking into account the productivity of a particular excavator, data on bucket volumes of the used excavators. The specified set of data as constants and parameters is presented in the form of spreadsheets and was used to obtain different variants of models on the same set of geologic data.

The program part of the database generates output data based on the specified information in the form of sets of files: block card with stocks, dump truck flow with information on each machine, statistics on all generated dump trucks and total statistics on stock data in all blocks included in the model. This data set allows checking the correctness of resource generation for the model by means of simple comparison of data from different files.

Results. Comparison of the two approaches allowed us to draw the following conclusion: the quality of the information presented by the two methods is comparable, but the recommended modeling variant is less costly in terms of time and resources, also when applying various interpolation models smoothing the actual distribution of components, no additional distortion is introduced into the original information, so it is preferable. Figure 3 shows examples of graphical representation of modeled blocks.

In order to determine the necessary parameters of the quarry transport system operation, the analysis of the dispatching system data was performed. A total of 3548880 records were checked and processed according to the dispatching data. Corrections in coordinates were made in 391275 records, which is 11 % of the total volume.

Further, the average loading interval was calculated for the analysis and general data on excavator productivity was determined. During the calculations the data on loading time of each dump truck with reference to a specific excavator were analyzed. The analysis was performed for different intervals of statistics accumulation from a minute to a quarter. Figure 4 shows an example of building a graph of dump truck loading intensity.

Fig.3. Examples of graphical representation block model when creating a resource database

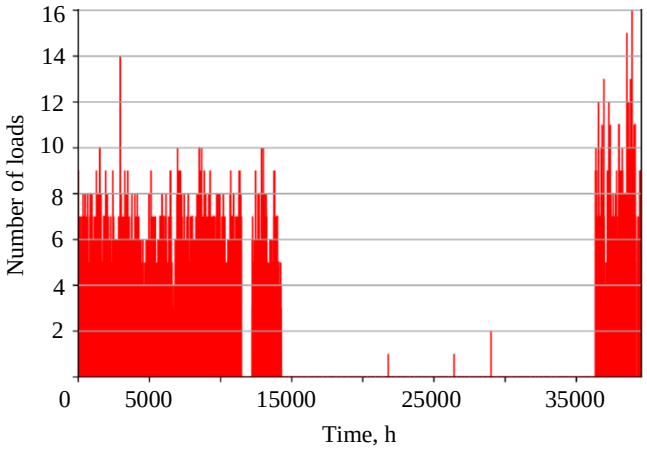

Fig.4. Excavator operation statistics 13 (maximum loadings – 16) during an hour

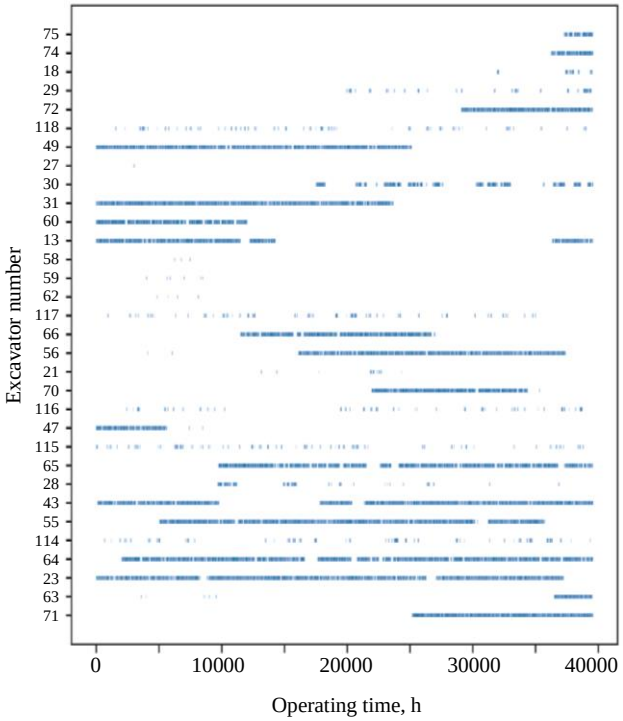

Fig.5. Chart of continuous operation duration for all excavators

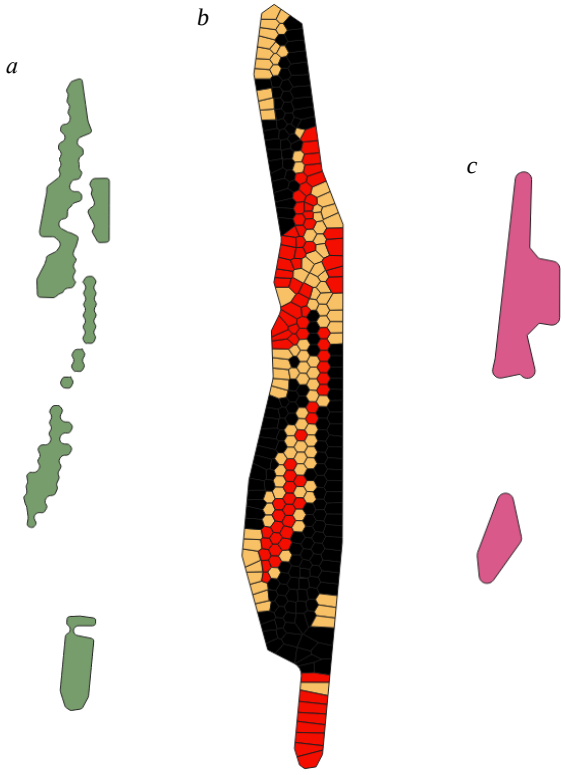

Fig.6. Result of modeling of loading processes and transportation of rock mass from complex structural rock blocks with and without power conditioning:
a – unit without power conditioning;
b – overview of the complex structural block considering balance (red) and off-balance (yellow) ores;
c – power conditioned unit

Analysis of the graphs allowed to determine the average length of intervals between dump truck loading, as well as fluctuations in the length of the interval depending on the intensity of excavator operation. The results of the intervals were compiled into a protocol file, the conclusion of which summarizes the downtime, number and intervals of loading. All information is presented in text with delimiters, which makes it easier to load into spreadsheet editors for further data analysis.

The second direction of the analysis was to estimate the number of simultaneously operating excavators. Analysis of the diagram of the duration of continuous operation for each excavator (Fig.5) allowed to establish that up to 13 excavators work simultaneously at the pit, and the average number of simultaneously working excavators is only seven units.

The obtained data on the operation intervals of mining and transportation equipment can be used as a basis for the ore flow management system to reduce downtime by redirecting transportation equipment. This will improve the strategy for managing the functioning of the mining and technical system by analyzing the data on the operation of mining and transportation equipment during the mining of complex structural rock blocks.

As a result, a resource database was created based on the results of statistical processing of data on the operation of the mining and industrial enterprise over the past few years. Thanks to the collected information it was possible to model the processes of loading and transportation of rock mass from complex structural rock blocks with and without power conditioning (Fig.6). Based on the modeling results, the volumes of ore mass were calculated with and without power conditioning. The difference in volumes determined further allowed us to determine the volumes of ore mass entering the overburden dumps, the values of which amounted to 25-40 % depending on the geological structure of the complex structural rock blocks being mined.

The model was further verified using two main facts – data from the beneficiation plant on the quality of ore flows entering the plant and

data on the quality of rock mass sent to the overburden dumps. Comparison of the data obtained in the modeling and the data used for verification confirmed the validity of the modeling.

As a result, the modeling allowed estimating the losses of quality-conditioned and substandard ore mass from 25 to 40 % per year, which confirms the need to improve the strategy of management of the mining and technical system based on the analysis of data on the mining of complex structural rock blocks.

Conclusion. The results of their integrity assessment obtained during the processing of databases available at the enterprise confirmed the need to standardize approaches to processing, collection and analysis of information [34]. The results of their integrity assessment obtained during the processing of databases available at the enterprise confirmed the need to standardize approaches to processing, collection and analysis of information. Standardized approach to the introduction of digital solutions will allow to expand the functionality more effectively and ensure the interface of information with related structural units in the management of mining and engineering system, which in support of the hypothesis will contribute to a rational assessment of possible options to improve the management strategy of the functioning of the mining and engineering system in terms of optimization of technological processes of a particular enterprise.

Comparison of the results of hole logs, which do not consider the minimum thickness of ore layers specified by the conditions feasibility report, and the data of the block model of the enterprise, created with account of all requirements, allowed to determine one of the types of losses: ore mass from low thickness layers of the required grade is delivered to the dumps, but the conditioned thickness of these layers is not provided in accordance with the requirements of the conditions feasibility report.

No doubt, the feasibility report of the conditions was developed considering the practicability and economic efficiency of the development of a certain mineral deposit, which implies regulatory and legal complexities in revising and changing the condition requirements, as well as changing the quality management system as a whole. Therefore, the possibility of adjusting the quality management system of mineral and raw material flows of the enterprise by optimizing the following areas has been determined:

• more detailed information on the structure of the blocks under preparation with the identification of ore bodies that are currently substandard in terms of thickness through the introduction of analytical platforms, which, based on the analysis of historical data and the search for patterns in them, will allow for increased reliability during subsequent sampling;

• improvement of selective ore extraction technologies at the excavation stage in the face to minimize ore dilution;

• in case it is impossible to improve selective excavation technologies, the option of introducing cyclic-flow technology is considered to separate previously unrecoverable ore mass on the conveyor; in this case, cyclic-flow technology will not only ensure optimization of ore mass transportation, but will also allow timely management of ore flow quality by identifying the ore component arriving on the conveyor from complex structural rock blocks and redirecting it to ore stockpiles rather than waste disposal facilities.

Management strategy improvement of the mining-technical system functioning against the background of the tendency of inevitable deterioration of mining-geological and mining-technical conditions of deposits development represents a highly relevant direction of optimization of subsoil development technological processes. Ensuring stable quality indicators of mined minerals is currently becoming an urgent problem of any mining enterprise and can be solved by analyzing the data on the development of complex-structural blocks obtained from the rock mass, environment, technological equipment, as well as automated systems of the mining and industrial enterprise.

REFERENCES

1. Kaplunov D.R., Rylnikova M.V., Yun A.B., Terenteva I.V. A new technological policy for integrated subsoil development in the conditions of depleting mineral reserves and resources. *Gornyi zhurnal*. 2019. N 4, p. 11-14 (in Russian). DOI: 10.17580/gzh.2019.04.02

2. Development of resource-saving and resource-replacing geotechnologies for integrated development of mineral deposits. Ed. by K.N.Trubetskoi. Moscow: Institut problem kompleksnogo osvoeniya nedr RAN, 2014, p. 196 (in Russian).

3. Yakovlev V.L. Methodological framework of the strategy for innovative development of mining systems for deep-seated mineral deposits. *Mining Informational and Analytical Bulletin.* 2021. N 5-1, p. 6-18 (in Russian). DOI: 10.25018/0236_1493_2021_51_0_6

4. Cohen M.W., Coelho V.N. Open-Pit Mining Operational Planning using Multi Agent Systems. *Procedia Computer Science*. 2021. Vol. 192, p. 1677-1686. DOI: 10.1016/j.procs.2021.08.172

5. Lomonosov G.G. Improving the quality of products of the mining production as a factor in increasing the effectiveness of the Russian mining and processing complex. *Mineral Mining & Conservation.* 2015. N 2, p. 51-61 (in Russian).

6. Turtygina N.A., Okhrimenko A.V., Tsygankova D.N. Factors affecting the level of variability of the quality of extracted ore raw. *Scientific bulletin of the Arctic.* 2022. N 13, p. 5-14 (in Russian). DOI: 10.52978/25421220_2022_13_5-14

7. Hadjigeorgiou J. Understanding, managing and communicating geomechanical mining risk. *Mining Technology*. 2020. Vol. 129. Iss. 3, p. 159-173. DOI: 10.1080/25726668.2020.1800909

8. Nimmagadda S.L., Murupindy V.V., Reiners V.T. On Digital Opencast Mining Ecosystems (DOME) and Knowledge Management – a Big Data Perspective. 1st Australasian Exploration Geoscience Conference, 18-21 February 2018, Sydney, Australia. ASEG Extended Abstracts, 2018. Vol. 2018. Iss. 1, p. 1-5. DOI: 10.1071/ASEG2018abP086

9. Deryabin S.A., Temkin I.O., Zykov S.V. About some issues of developing Digital Twins for the intelligent process control in quarries. *Procedia Computer Science*. 2020. Vol. 176, p. 3210-3216. DOI: 10.1016/j.procs.2020.09.128

10. Ruihan Zhao, Liang Luo, Pengzhong Li, Jinguang Wang. An industrial heterogeneous data based quality management KPI visualization system for product quality control. *Assembly Automation.* 2022. Vol. 42. Iss. 6, p. 796-808. DOI: 10.1108/AA-05-2022-0139

11. Aleksandrova S.V., Vasiliev V.A., Alexandrov M.N. Integration of Quality Management and Digital Technologies. 2019 International Conference "Quality Management, Transport and Information Security, Information Technologies", 23-27 September 2019, Sochi, Russia. IEEE, 2019, p. 20-22. DOI: 10.1109/ITQMIS.2019.8928426

12. Rylnikova M.V., Klebanov D.A., Knyazkin E.A. Data analysis as a basis for improving the efficiency of mining equipment in open pit operations. *Russian Mining Industry.* 2023. N 1, p. 52-56 (in Russian). DOI: 10.30686/1609-9192-2023-1-52-56

13. Cheskidov V.V., Manevich A.I., Lipina A.V. Obtaining and analyzing big data in the practice of monitoring the condition of mining structures. *Gornaya promyshlennost*. 2019. N 2 (144), p. 86-88 (in Russian). DOI: 10.30686/1609-9192-2019-2-144-86-88

14. Rylnikova M.V., Vlasov A.V., Makeev M.A. Justification of conditions for application of automated control systems for surface mining during construction of in pit crushing and conveying system using simulation modeling. *Russian Mining Industry*. 2021. N 4, p. 106-112 (in Russian). DOI: 10.30686/1609-9192-2021-4-106-112

15. Barnewold L., Lottermoser B.G. Identification of digital technologies and digitalization trends in the mining industry. *International Journal of Mining Science and Technology*. 2020. Vol. 30. Iss. 6, p. 747-757. DOI: 10.1016/j.ijmst.2020.07.003

16. Zhukovskiy Y., Batueva D., Buldysko A., Shabalov M. Motivation towards energy saving by means of IoT personal energy manager platform. *Journal of Physics: Conference Series*. 2019. Vol. 1333. Iss. 6. N 062033. DOI: 10.1088/1742-6596/1333/6/062033

17. Erkayaoglu M., Dessureault S. Improving mine-to-mill by data warehousing and data mining. *International Journal of Mining, Reclamation and Environment*. 2019. Vol. 33. Iss. 6, p. 409-424. DOI: 10.1080/17480930.2018.1496885

18. Reis M.S. A Systematic Framework for Assessing the Quality of Information in Data-Driven Applications for the Industry 4.0. *IFAC-PapersOnLine*. 2018. Vol. 51. Iss. 18, p. 43-48. DOI: 10.1016/j.ifacol.2018.09.244

19. Chong-chong Qi. Big data management in the mining industry. *International Journal of Minerals, Metallurgy and Materials.* 2020. Vol. 27. Iss. 2, p. 131-139. DOI: 10.1007/s12613-019-1937-z

20. Cicconi P., Raffaeli R. An Industry 4.0 Framework for the Quality Inspection in Gearboxes Production. *Computer-Aided Design & Applications*. 2020. Vol. 17. Iss. 4, p. 813-824. DOI: 10.14733/cadaps.2020.813-824

21. Zakharov L.A., Martyushev D.A., Ponomareva I.N. Predicting dynamic formation pressure using artificial intelligence methods. *Journal of Mining Institute.* 2022. Vol. 253, p. 23-32. DOI: 10.31897/PMI.2022.11

22. Trofimov A.V., Kirkin A.P., Rumyantsev A.E., Yavarov A.V. Use of numerical modelling to determine optimum overcoring parameters in rock stress-strain state analysis. *Tsvetnye Metally.* 2020. N 12, p. 22-27 (in Russian). DOI: 10.17580/tsm.2020.12.03

23. Zhukovskiy Y.L., Semenyuk A.V., Alieva L.Z., Arapova E.G. Blockchain-based digital platforms to reduce the carbon footprint of mining. *Mining Informational and Analytical Bulletin.* 2022. N 6-1, p. 361-378 (in Russian). DOI: 10.25018/0236_1493_2022_61_0_361

24. Sony M., Antony J., Douglas J.A. Essential ingredients for the implementation of Quality 4.0: A narrative review of literature and future directions for research. *The TQM Journal*. 2020. Vol. 32. Iss. 4, p. 779-793. DOI: 10.1108/TQM-12-2019-0275

25. Roberts F.S., Sheremet I.A. Resilience in the Digital Age. Cham: Springer, 2021, p. 199. DOI: 10.1007/978-3-030-70370-7

26. Upadhyay S.P., Askari-Nasab H. Simulation and optimization approach for uncertainty-based short-term planning in open pit mines. *International Journal of Mining Science and Technology*. 2018. Vol. 28. Iss. 2, p. 153-166. DOI: 10.1016/j.ijmst.2017.12.003

27. Rylnikova M.V., Klebanov D.A., Makeev M.A., Kadochnikov M.V. Application of artificial intelligence and the future of big data analytics in the mining industry. *Russian Mining Industry*. 2022. N 3, p. 89-92 (in Russian). DOI: 10.30686/1609-9192-2022-3-89-92

28. Luo Jian-ming, Zhang Qi, Song Bing-tian et al. Application of Integrated Geophysical and Geochemical Data Processing to Metallogenic Target Zone Quantitative Prediction and Optimization. *Bulletin of Mineralogy, Petrology and Geochemistry*. 2017. Vol. 36. N 6, p. 886-890. DOI: 10.3969/j.issn.1007-2802.2017.06.002

29. Cheskidov V.V., Lipina A.V., Melnichenko I.A. Integrated monitoring of engineering structures in mining. *Eurasian Mining.* 2018. N 2, p. 18-21. DOI: 10.17580/em.2018.02.05

30. Zhang Qi, Liu Xuelong. Big data: new methods and ideas in geological scientific research. *Big Earth Data*. 2019. Vol. 3. Iss. 1, p. 1-7. DOI: 10.1080/20964471.2018.1564478

31. Trubetskoi K.N., Pytalev I.A., Rylnikov A.G. Automated systems of ore flow quality control at mines. *Marksheiderskii vestnik*. 2013. N 6 (98), p. 9-14 (in Russian).

32. Rylnikova M.V., Tsupkina M.V., Kirkov A.E. Technologies of big data collection and processing – the basis for increasing the reliability of primary information about rock massifs in the development of mineral deposits and technogenic formations. *News of the Tula State University. Sciences of Earth.* 2023. Iss. 1, p. 308-327 (in Russian). DOI: 10.46689/2218-5194-2023-1-1-308-327

33. Zakharov V.N., Kaplunov D.R., Klebanov D.A., Radchenko D.N. Methodical approaches to standardization of data acquisition, storage and analysis in management of geotechnical systems. *Gornyi zhurnal.* 2022. N 12, p. 55-61 (in Russian). DOI: 10.17580/gzh.2022.12.10

34. Kaplunov D.R., Rylnikov A.G. Generalization of modern approaches to quality management technology a t opera ting mines. *News of the Tula State University. Sciences of Earth.* 2020. Iss. 4, p. 40-53 (in Russian).

35. Shvabenland E.E., Lapteva M.I. Principles of mineral raw material quality management in combined mining complex structural deposits. *News of the Tula state university. Sciences of Earth.* 2021. Iss. 3, p. 326-335 (in Russian). DOI: 10.46689/2218-5194-2021-3-1-320-329

36. Turtygina N.A., Okhrimenko A.V., Kovalchuk A.A., Kalashnikov K.A. Planning of mining works as organizational method of quality management for mineral raw materials in mining system. *Mining Informational and Analytical Bulletin.* 2018. N S17, p. 3-11 (in Russian). DOI: 10.25018/0236-1493-2018-5-17-3-11

37. Kantemirov V.D., Yakovlev A.M., Titov R.S., Timokhin A.V. Improvement of mineral processing methods in mining structurally-complex deposits. *Russian Mining Industry.* 2022. N 1S, p. 63-70 (in Russian). DOI: 10.30686/1609-9192-2022-1S-63-70

38. Teziev T.M., Dzhioeva A.K. The optimal block length when developing compound narrow pitching veins. *Vestnik Magnitogorskogo gosudarstvennogo tekhnicheskogo universiteta im. G.I.Nosova*. 2015. N 1 (49), p. 5-9 (in Russian).

39. Changbin Wang, Guangyao Si, Chengguo Zhang et al. Location error based seismic cluster analysis and its application to burst damage assessment in underground coal mines. *International Journal of Rock Mechanics and Mining Sciences*. 2021. Vol. 143. N 104784. DOI: 10.1016/j.ijrmm

***Authors*: Mariya V. Tsupkina,** *Junior Researcher, tsupkina_m@ipkonran.ru, https://orcid.org/0009-0003-6066-3084* (*Institute of Comprehensive Exploitation of Mineral Resources RAS, Moscow, Russia*), **Aleksei E. Kirkov,** *Researcher, https://orcid.org/0009-0003-1062-9857* (*Institute of Comprehensive Exploitation of Mineral Resources RAS, Moscow, Russia*), **Dmitrii A. Klebanov,** *Candidate of Engineering Sciences, Head of Laboratory, https://orcid.org/0000-0002-3289-9212* (*Institute of Comprehensive Exploitation of Mineral Resources RAS, Moscow, Russia*), **Dmitrii N. Radchenko,** *Candidate of Engineering Sciences, Head of Laboratory, https://orcid.org/0000-0003-1821-3840* (*Institute of Comprehensive Exploitation of Mineral Resources RAS, Moscow, Russia*).

The authors declare no conflict of interests.

ISSN 2411-3336; e-ISSN 2541-9404

JOURNAL OF MINING INSTITUTE
Zapiski Gornogo instituta
Journal homepage: pmi.spmi.ru

Research article

Study on the thin layer drying and diffusion mechanism of low rank coal in Inner Mongolia and Yunnan

Cheng Wang[1], Dan Wang[1], Zengqiang Chen[2], Chenlong Duan[2]✉, Chenyang Zhou[2]
[1] *China University of Mining and Technology School of Chemical Engineering, Xuzhou, China*
[2] *Key Laboratory of Coal Processing and Efficient Clean Utilization of Ministry of Education, China University of Mining and Technology, Xuzhou, China*

How to cite this article: Cheng Wang, Dan Wang, Zengqiang Chen, Chenlong Duan, Chenyang Zhou. Study on the thin layer drying and diffusion mechanism of low rank coal in Inner Mongolia and Yunnan. Journal of Mining Institute. 2024. Vol. 266, p. 326-338.

Abstract. Coal is one of the world's most important energy substances. China is rich in coal resources, accounting for more than 90 % of all ascertained fossil energy reserves. The consumption share of coal energy reaches 56.5 % in 2021. Due to the high moisture content of low-rank coal, it is easy to cause equipment blockage in the dry sorting process. This paper considers low-rank coal coming from Inner Mongolia (NM samples) and Yunnan (YN samples). The weight loss performance of the samples was analyzed using thermogravimetric experiments to determine the appropriate temperature for drying experiments. Thin-layer drying experiments were carried out at different temperature conditions. The drying characteristics of low-rank coal were that the higher the drying temperature, the shorter the drying completion time; the smaller the particle size, the shorter the drying completion time. The effective moisture diffusion coefficient was fitted using the Arrhenius equation. The effective water diffusion coefficient of NM samples was $5.07 \cdot 10^{-11}$-$9.58 \cdot 10^{-11}$ m^2/s. The effective water diffusion coefficients of the three different particle sizes of YN samples were $1.89 \cdot 10^{-11}$-$4.92 \cdot 10^{-11}$ (–1 mm), $1.38 \cdot 10^{-10}$-$4.13 \cdot 10^{-10}$ (1-3 mm), $5.26 \cdot 10^{-10}$-$1.49 \cdot 10^{-9}$ (3-6 mm). The activation energy of Inner Mongolia lignite was 10.97 kJ/mol (–1 mm). The activation energies of Yunnan lignite with different particle sizes were 17.97 kJ/mol (–1 mm), 33.52 kJ/mol (1-3 mm), and 38.64 kJ/mol (3-6 mm). The drying process was simulated using empirical and semi-empirical formulas. The optimal model for Inner Mongolia samples was the Two-term diffusion model, and Yunnan samples were the Hii equation was used.

Keywords: low-quality coal; thin-layer drying; drying characteristics; kinetic analysis; fitting simulation

Acknowledgments. The research work is financially supported by China National Funds for Distinguished Young Scientists (N 52125403), Natural Science Foundation of Jiangsu Province (N BK20200651), National Natural Science Foundation of China (N 52104276, N 52261135540, N 52220105008), International Postdoctoral Exchange Fellowship Program (N PC2021086), The Graduate Innovation Program of China University of Mining and Technology (N 2022WLJCRCZL057), The Postgraduate Research and Practice Innovation Program of Jiangsu Province (N SJCX22_1149).

Received: 16.01.2023 ***Accepted: 20.06.2023*** ***Online: 05.02.2024*** ***Published: 25.04.2024***

Introduction. Fossil energy is the fundamental material for economic and social development [1]. China is relatively abundant in coal resources, more than 90 % of the ascertained reserves of all fossil energy sources. The share of low-quality coal such as lignite occupies is about 40 % [2, 3]. The low-rank coal has characteristics of a low degree of coalification, high moisture content, abundant oxygen-containing functional groups, and easy weathering and spontaneous combustion have seriously hindered the development and utilization of low-rank coal powder [4]. The high moisture content not only limits the calorific value of the combustion of low-rank coal but also increases the transportation cost. In addition, low-rank coal below 6 mm is easy to cause equipment blockage in the process of dry coal preparation, which has become a technical problem in dry coal preparation [5]. Thus, the dewatering of low-rank coal is of great strategic importance [6].

Yong Jin et al. [7] research found that flow criteria showed that flowability decreased with increasing moisture content. The flowability and packing properties were different both above and below the critical moisture content. Xian Wu et al. [8] learned through low-temperature drying experiments that there is a time lag between volume shrinkage and water loss, and there are differences in their amounts. Rongtang Liu et al. [9] found by drying experiments of Yimin lignite at different temperatures that only H_2O and CO_2 are produced at low temperatures. Combustible gases, including CO and chemical gases, can be produced when the drying temperature exceeds 250 °C. B.A.Fu and M.Q.Chen [10] experimentally investigated the kinetics of thin lignite layers during forced convective drying of hot air. Experimental results show that the drying process of lignite presented a combination of the short warm-up period, the first falling rate period and the second falling rate period. H.Zhou et al. [11] investigated the effect of moisture content on high-pressure pulverized lignite dense-phase pneumatic conveying. When interparticle cohesion is strong, particles suffer from severe agglomeration problems, which make the resistance forces increase, leading to poor fluidization or even complete de-fluidization when particles are fluidized. P.Celen et al. [12] dried Turkish lignite using superheated steam and hot air at a temperature of 117 °C. The experiments showed that it took less time to heat the lignite samples with superheated steam compared to hot air. B.A.Fu et al. [13] studied the heat transfer in thin layers of lignite during convective drying with hot air. The effects of hot air temperature and velocity on the temperature of the thin layer were obtained.

In the existing studies, there is a lack of research on the drying mechanism and factor evaluation of low-rank coal below 6 mm. In this paper, the effects of temperature, particle size, organic composition and moisture content on the drying characteristics of low-rank coal will be studied, and the influence mechanism of different factors on the drying process will be analyzed by the kinetic analysis method. It provides data and practical guidance to solve the technical problems of low-rank coal drying that is difficult to screen below 6 mm [14].

Methods. To solve the above technical problems, this paper will use low-grade coal from Zhaotong, Yunnan and Shengli, Inner Mongolia, China to carry out drying experiments. We crushed and screened low-rank coal in Yunnan, and selected samples with particle sizes of –1, 1-3, and 3-6 mm for experiments. All samples with a particle size of –1mm were selected for experiments in Inner Mongolia low-grade coal. To understand the basic physical parameters and characteristics of the sample, the experimental samples were subjected to industrial and elemental analysis using the TGA701 automatic industrial analyzer produced by Deco in the United States and the Elementar Vario MACRO cube elemental analyzer produced by Elementar in Germany.

Before the drying experiment, a thermogravimetric analysis experiment is performed on the sample to determine the appropriate drying temperature for the sample. Thermogravimetric experiments were performed using a TG thermogravimetric (thermal) differential analyzer of NETZSCH, Germany, in this study. About 12 mg of the sample was weighed at a time, loaded into an empty crucible, and purged with air at a flow rate of 50 ml/min. The temperature rise was controlled at a rate of 10 °C/min and the absolute temperature was controlled at 800 °C.

In the isothermal thin-layer drying test a custom-made 27 × 20 × 2 cm aluminum tray was used to hold the samples. The samples were dried using an electric blast oven of model 101A-1ET produced by Shanghai Experimental Instrument Factory Co. Measurements were performed with the aid of an electronic balance, BSA 224S, manufactured by the Sartorius, Germany, accurate to 0.0001 g. To reduce test errors, cover the tray with tin foil to avoid extreme temperatures that cause low-rank coal to adhere or organic matter to corrode the tray. The sample on tin foil was placed in a tray, spread out in a thin layer and put place in a constant temperature drying box for drying. The drying time and the change in the quality of the sample were recorded until the sample is dried to a constant weight. The samples were dried at a drying wind speed of 0.6 m/s. A 10 g sample was taken for each test and dried to a constant weight. It was required to observe the change in the organic composition of the sample before and after drying. In this paper, infrared testing will be used to identify functional groups

of the sample [15]. The dry base moisture content and drying speed for each statistical time are calculated and the drying curve is plotted [16, 17]:

• dry base moisture content

$$M_d = \frac{m-n}{m};$$

• drying speed

$$v = \frac{dM_d}{dt},$$

where m is the mass of the sample for each test, g; n is the mass of the sample when dried to constant weight, g.

Porous media particles were mainly in the reduced drying stage during the skeletal bony thin layer of the isothermal drying process. The kinetic energy of water molecules was provided by the temperature gradient. The concentration gradient was the main driving force in the migration process of water molecules. The concentration of a substance depended on the time during the diffusion. Therefore, the drying process of low-rank coal can be described by Fick's second law [18-21]

$$\frac{\partial M_t}{\partial t} = D_{eff}\nabla^2 M_t, \quad (1)$$

where M_t is the water content of the test sample at time t, g/g; D_{eff} is the effective moisture diffusion coefficient, m^2/s.

A second-order approximation to the Fick second diffusion equation with an analytical solution was used to process the data [22, 23]

$$\ln M_R = \ln\left(\frac{8}{\pi^2}\right) - \frac{\pi^2 D_{eff}}{L^2},$$

where L is the thickness of the thin layer, into which the sample is laid flat in the tray, L = 0.002 m; M_R is the mass fraction of water content, %.

The mass fraction of water content can be calculated by the following formula [24]:

$$M_R = \frac{M_t - M_e}{M_0 - M_e}, \quad (2)$$

where M_0 is the initial moisture content, %; M_e is the water content at equilibrium, %.

M_e is negligible compared to M_0. The above equation (2) can be simplified to [25, 26]:

$$M_R = \frac{M_t}{M_0}.$$

The effective moisture diffusion coefficient of porous particles is related to the material composition of the particles, moisture, and the nature of the material itself. Its relationship with temperature obeys the Arrhenius equation [27]:

$$D_{eff} = D_0 \exp\left(-\frac{E_a}{R}\frac{1}{T}\right).$$

Taking the logarithm of both sides of the above equation yields [26]:

$$\ln D_{eff} = -\frac{E_a}{R}\frac{1}{T} + \ln D_0,$$

where D_0 determined by the material, m^2/s; E_a is the apparent activation energy, J/mol; R is the molar gas constant, J/(mol/k); T is the temperature of the drying medium, K.

In the field of drying characteristics, researchers generally believe that drying is an unsteady process of heat and mass transfer and heat and mass coupling, so they often use model-fitting methods to assist the research [28]. For low-rank coal drying, most of them are currently used in the theory and model of high reliability in the drying fields of food and materials [29, 30]. In this study, 16 classical drying models that are highly used in thin-layer drying research will be used for fitting, including theoretical models, empirical models, semi-empirical models, etc. The correlation coefficient is used as an evaluation index in model reliability discrimination to evaluate the fitting effect of different models. The closer the correlation coefficient R^2 is to 1, the better the fitting effect [31]:

$$R^2 = \frac{\sum_{i=1}^{n} y_i^{\,2}}{\sum_{i=1}^{n} y_i^{\,2} - \sum_{i=1}^{n} \left(y_i - Y_i\right)^2},$$

where y_i is the experimental value; Y_i is the theoretically calculated value of the fitted curve, and n represents the number of experimental values.

In this section, the 16 theoretical, empirical and semi-empirical drying models used in the fitting simulation are shown in Table 1. Among them, the theoretical model is derived from the drying-related theory (including the differential equation of moisture diffusion, thermal conductivity equation, etc.), while the semi-empirical model is established by combining the kinetic experimental data with high precision, and the empirical model constructed based on the experimental data can accurately describe the relationship between the moisture content of the material and the drying time during the experiment [32].

At present, researchers have carried out a lot of research work in low-rank coal drying fitting simulation, and the results show that the theoretical model is less applicable in low-order coal drying, and the applicability of empirical and semi-empirical models is stronger. However, empirical or semi-empirical models cannot theoretically analyze the mechanism of mass and heat transfer in the drying process. Therefore, this paper prefers the theoretical model as the best-fitting model and then reveals the drying mechanism from the basic theory.

Table 1

Drying mathematical models

Types	Name	Finder	Model formulas
Theoretical	Single diffusion	Henderson and Pabis	$M_R = a\exp(-k\tau)$
	Two-term diffusion	Sharaf-Eldeen	$M_R = a_1\exp(-k_1\tau) + a_2\exp(-k_2\tau)$
	Three-term diffusion	Karathanos	$M_R = a_1\exp(-k_1\tau) + a_2\exp(-k_2\tau) + a_3\exp(-k_3\tau)$
Semi-empirical equation	Lemus	Lemus	$M_R = \exp(a + k\tau)$
	Lewis	Lewis	$M_R = \exp(-k\tau)$
	Logarithmic	Togrul and Pehilvan	$M_R = a\exp(-k\tau) + c$
	Page	Page	$M_R = \exp(-k\tau^n)$
	Amendments Page I	Overhults	$M_R = \exp[-(k\tau^n)]$
	Amendments Page II	Wang	$M_R = a\exp(-k\tau^n)$
	Hii	Hii	$M_R = a_1\exp(-k_1\tau^n) + a_2\exp(-k_2\tau^n)$
	Approximate diffusion	Yaldiz	$M_R = a\exp(-ka\tau) + (1-a)\exp(-kb\tau)$
	Vema	Vema	$M_R = a\exp(-k_1\tau) + (1-a)\exp(-k_2\tau)$
Empirical equations	Chandra	Chandra	$M_R = a\tau^{-n}$
	Midilli	Midilli	$M_R = a\exp(-k\tau^n) + bt$
	Thompson	Thompson	$\tau = a\ln M_R + b(\ln M_R)^2$
	Wang	Wang	$M_R = 1 + a\tau + b\tau^2$

Results and discussion. The results in Table 2 are the physical property test results of Inner Mongolia and Yunnan samples. The moisture content of the samples from Inner Mongolia and Yunnan was 41.90 and 21.61 %, respectively. In addition, the carbon content of the Inner Mongolia sample was significantly higher than that of the Yunnan sample, which had more organic elements. It shows that the Yunnan sample has a lower degree of coalification and more organic composition.

Table 2

Industry and elemental analysis of Lignite coal in Inner Mongolia, %

Sample	Industrial analysis					Elemental analysis				
	M_{ad}	A_d	V_{ad}	A_{ad}	F_{cad}	C_{daf}	H_{daf}	O_{daf}	N_{daf}	S_{daf}
NM	41.90	32.11	37.55	27.27	20.12	56.41	4.56	37.44	0.83	0.76
YN	21.62	11.49	26.74	7.63	32.01	40.13	3.15	57.80	1.35	1.57

Note. M_{ad}, A_d, V_{ad}, A_{ad}, and F_{cad} refer to the moisture, volatile, fixed carbon and ash content on a received dried basis; H_{daf}, N_{daf}, O_{daf} and S_{daf} refer to the element content on a dry ash-free basis.

The differential thermogravimetric curves (DTG) and thermogravimetric curves (TG) of the samples fitted from the thermogravimetric experimental data were shown in Fig.1. TG and DTG curves of YN and NM samples could be divided into three stages. Among them, the water loss stages of NM samples were: 75-200 °C. The weight loss phase with the organic matter was 500-750 °C. The weight loss stage of spontaneous combustion was after 750 °C. The moisture weight-loss stage of YN samples was 85-220 °C. The weight loss phase with the organic matter was 450-750 °C and the weight loss phase with spontaneous combustion was after 750 °C. This was because evaporation of free and bound water in coal can be completed at 220 °C, most of this water evaporates at 100 °C. With a continued increase of temperature, volatilization of the organic matter in the coal occurs at 250 °C. Even the coal itself undergoes spontaneous combustion at 750 °C [33].

As shown in Fig.2, the experimental results of NM samples showed that the drying time of NM samples at 180 °C was 6 min; the drying time at 160 °C for 7 min; NM samples were dried at 140 °C for 9 min; the drying time at a temperature below 140 °C is more than 10 min. This was because the higher the temperature of the hot air, the higher the temperature of the sample, and the greater the kinetic energy of the water molecules inside the particles, which accelerates the water diffusion process. At the same time, the evaporation rate of water on the surface of the particles increases, which increases the concentration gradient between the surface and the internal water of the particles, since the liquid water migrates to the surface at a faster rate.

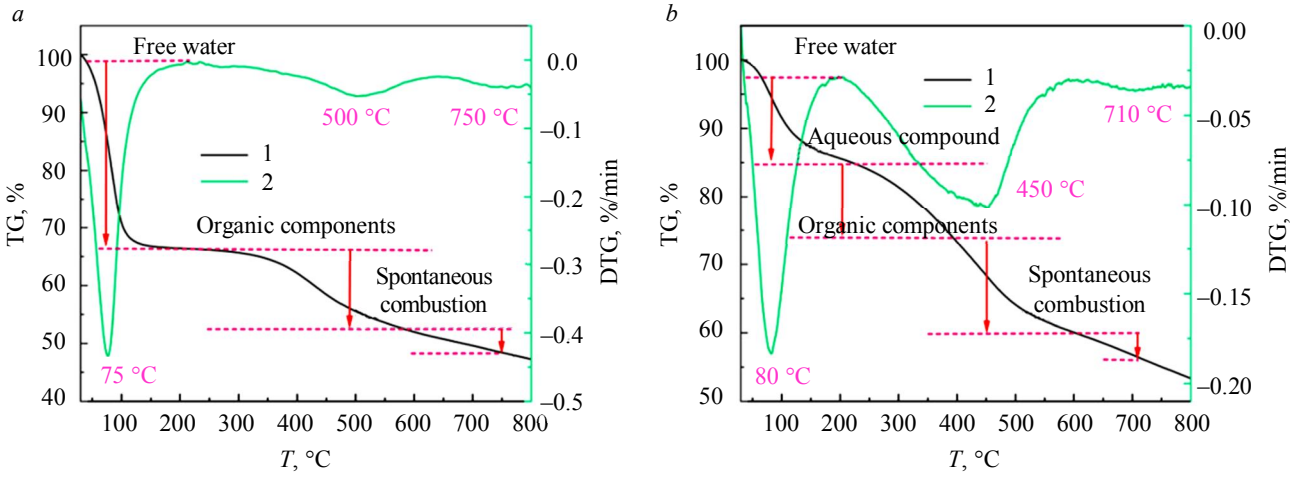

Fig.1. The thermogravimetric curves of NM (*a*) and YN (*b*) samples

1 – TG; 2 – DTG

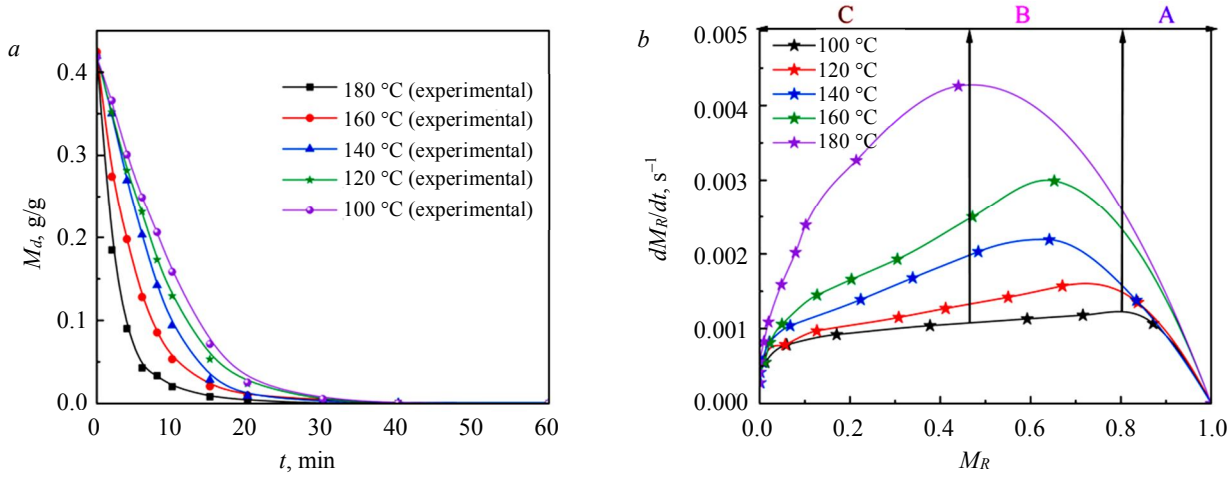

Fig.2. Drying (*a*) and drying rate (*b*) curves of –1 mm NM samples at different drying temperatures

When the drying temperature exceeds 160 °C, the effect of increasing the drying temperature on the drying effect was less than that of increasing the temperature below 160 °C. In addition, the higher the drying temperature, the greater the maximum drying rate, and the longer time in the slow-down drying stage.

At lower temperatures, the presence of a constant speed drying period was more pronounced. This was because the huge heat brought by high temperature makes free water evaporate quickly in a short time, and it takes a certain amount of time to absorb heat when drying at low temperatures, so the free water evaporation rate was in a more balanced state [34].

As shown in Fig.3, when the drying temperature is above 140 °C, the drying completion time of YN (–1 mm) samples is about 15 min. When the drying temperature is below 140 °C, the drying completion time of the YN (–1 mm) sample is about 20 min. When the organic composition is high, it will reduce the overall drying efficiency of the sample. When the temperature is less than 140 °C, the difference in the drying process of YN samples before drying is small. When the temperature exceeds 140 °C, the gap in the drying process in the first ten minutes increases. It shows that the organic components begin to significantly affect the drying process when the drying temperature exceeds 140 °C.

In the drying rate curves of different temperatures of YN samples, there are only ramp-up and slow-down stages. The increase speed phase can be thought of as a period in which the initial speed quickly reaches the highest rate. This was because initially, there was a large temperature difference between the sample and the dry hot air. As drying progresses, the temperature difference between the

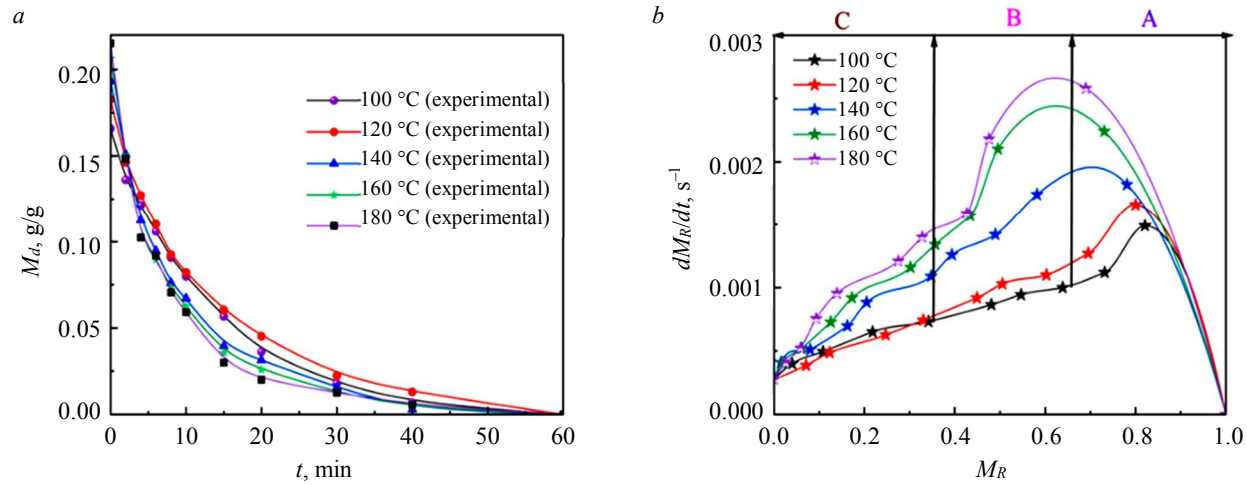

Fig.3. Drying (*a*) and drying rate (*b*) curves of –1 mm YN samples at different drying temperatures

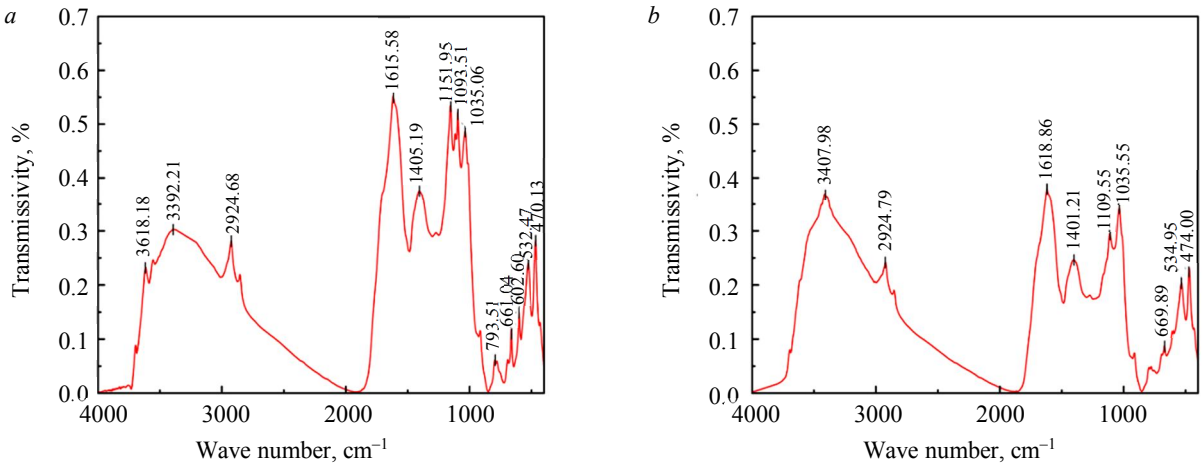

Fig.4. Drying and drying rate curves of YN samples is: before (*a*) and after (*b*) drying

sample temperature and the drying hot air becomes smaller and smaller, and the efficiency of heat transfer between the hot air to the inside of the material layer and the particle gradually decreases. At this time, the water content of the sample was also rapidly reduced due to the rapid evaporation of free water, and the remaining water to be evaporated was considered the internal water of the sample particles. This moisture must first be separated from the internal matter of the particles by heat and then transported to the surface of the particles. The descending drying stage in Fig.3, *b* illustrates the increase in mass transfer heat transfer resistance during the evaporation of combined water.

In the experimental results, the equilibrium moisture content difference was between 3-6 % when dried at different temperatures for 60 min. This was because the YN sample contains higher S, N and O elements and more organic matter, so the higher the drying temperature, the more volatilization of the components in the YN sample, and the more mass was lost. To demonstrate this, infrared analysis was performed on YN samples before and after drying (Fig.4).

Infrared analysis showed that the sample was rich in organic functional groups such as OH–, –C–O–, –C–H, –S–O–, –N=O before drying. However, after drying, organic functional groups such as OH–, C–O, C–H, S–O, N=0 are greatly reduced or even disappear. It shows that the organic components will not only reduce the drying efficiency, but also increase the error of the experiment due to thermal decomposition and volatilization.

The experimental results of different particle sizes show that the larger the particles, the slower the drying process. At the same time, when the drying temperature was lower than 140 °C, the drying

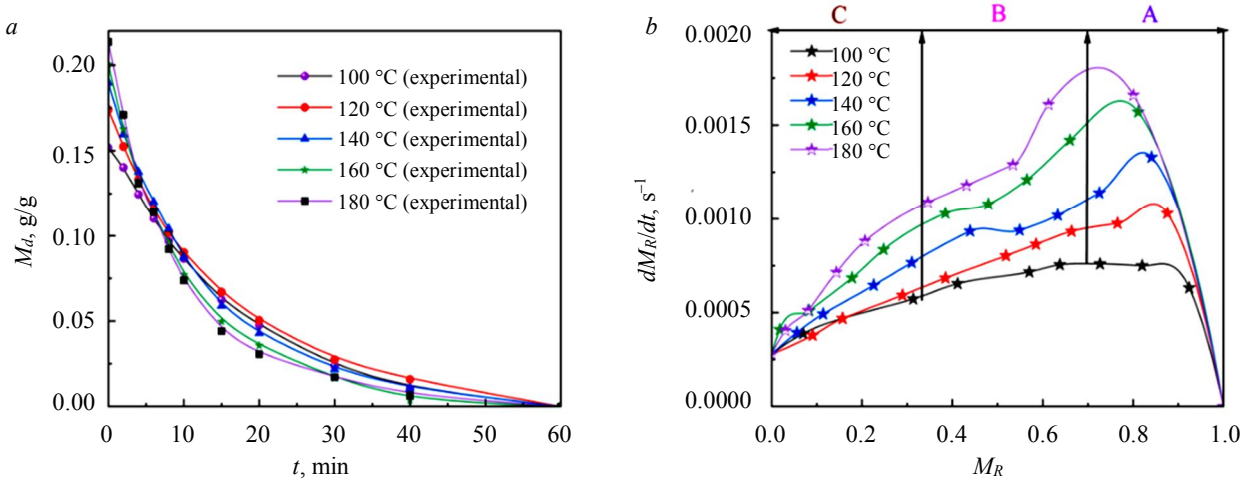

Fig.5. Drying (*a*) and drying rate (*b*) curve of 1-3 mm YN samples at different drying temperatures

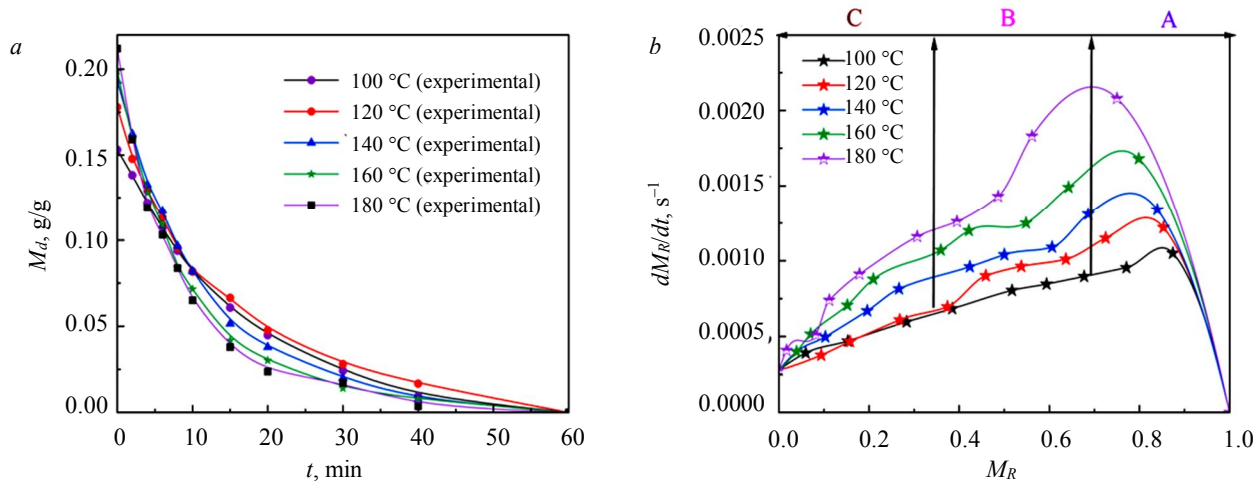

Fig.6. Drying (*a*) and drying rate (*b*) curve of 3-6 mm YN samples at different drying temperatures

completion time of –1 mm samples was significantly smaller than that of 1-3 (Fig.5) and 3-6 mm (Fig.6) samples, the difference in drying completion time between 1-3 and 3-6 mm samples was small. When the drying temperature was greater than 140 °C, the drying completion time of –1 mm samples was significantly faster than 1-3 mm, and the drying end time of 1-3 mm samples was significantly faster than 3-6 mm. This was because the smaller the particles, the easier it was for water molecules to absorb heat and evaporate. In the medium and low-temperature drying process, the driving force of water molecules was mainly determined by the concentration gradient, and the diffusion mechanism plays a leading role. When the drying temperature was higher, the temperature field could provide greater kinetic energy for water molecule migration, and the smaller the particle size, the faster the water evaporates and spreads.

To quantify the ease of drying completion of each sample, the results of the drying experiments were analyzed kinetically. The results of isothermal drying experiments were organized according to equation (1). The curve of low-order coal lnM_R at the corresponding temperature versus time t was obtained. The parameter D_{eff} at the corresponding temperature could be found from the slope of the curve (Table 3).

Table 3

Effective moisture diffusion coefficient D_{eff} at different drying temperatures, m^2/s

Sample	Drying temperature, °C				
	100	120	140	160	180
NM –1 mm	$5.07\cdot10^{-11}$	$6.19\cdot10^{-11}$	$7.56\cdot10^{-11}$	$8.14\cdot10^{-11}$	$9.58\cdot10^{-11}$
R^2	0.98647	0.98741	0.99101	0.99706	0.95812
YN –1 mm	$1.89\cdot10^{-11}$	$2.11\cdot10^{-11}$	$2.97\cdot10^{-11}$	$4.49\cdot10^{-11}$	$4.92\cdot10^{-11}$
R^2	0.99373	0.97746	0.96129	0.96738	0.98684
YN 1-3 mm	$1.38\cdot10^{-10}$	$1.76\cdot10^{-10}$	$2.53\cdot10^{-10}$	$3.08\cdot10^{-10}$	$4.13\cdot10^{-10}$
R^2	0.99324	0.97819	0.99200	0.98756	0.99626
YN 3-6 mm	$5.26\cdot10^{-10}$	$6.59\cdot10^{-10}$	$8.92\cdot10^{-10}$	$1.13\cdot10^{-9}$	$1.49\cdot10^{-9}$
R^2	0.96331	0.98591	0.99429	0.98304	0.98968

For the same millimeters particle size, the effective water diffusion coefficient of NM samples was $5.07\cdot10^{-11}$-$9.58\cdot10^{-11}$ m^2/s. The effective water diffusion coefficient of YN samples was small, $1.89\cdot10^{-11}$-$4.92\cdot10^{-11}$ m^2/s. Comparative analysis shows that the effective moisture diffusion coefficient increases with the increase in drying temperature. This is because, the higher the temperature, the greater the kinetic energy of water molecules, and the stronger the power to diffuse outward. At the same time, the larger the particle size, the greater the effective water diffusion coefficient, the

effective water diffusion coefficient of the YN (1-3 mm) sample was $1.38 \cdot 10^{-10}$-$4.13 \cdot 10^{-10}$ m^2/s, and the effective water diffusion coefficient of YN (3-6 mm) sample was $5.26 \cdot 10^{-10}$-$1.49 \cdot 10^{-9}$ m^2/s. This was because particle size was an important positive correlation parameter affecting the effective diffusion coefficient of moisture in the fitted equation. In addition, in the process of diffusion of water molecules, the larger the particle size, the more channels the water molecules diffuse to the outside world, and the more water evaporates per unit of time. However, the effective water diffusion coefficient per unit particle size will decrease, because the larger the particle size, the longer the path of water diffusion to the outside world, which will reduce the diffusion efficiency of water to the outside.

The apparent activation energy was an important parameter of drying kinetics, reflecting the difficulty of drying. This section analyzes the drying characteristics of low-rank coals by comparing the apparent activation energy of low-rank coals with different moisture content and particle sizes. The apparent activation energy was calculated by fitting the effective water diffusion coefficient, and the apparent activation energy of each sample was shown in Table 4 in detail. The apparent activation energy of NM was 10.97 kJ/mol, which was lower than YN's 17.97 kJ/mol. The apparent activation energy of YN samples was positively correlated with the particle size, and the activation energy of particles with particle sizes of 1-3 and 3-6 mm was 18.95 and 20.28 kJ/mol, respectively. From the fitting results, it can be seen that the higher the water content of the sample, the lower the apparent activation energy. This was because the higher the moisture content, the stronger the driving force provided by the moisture concentration gradient, the less energy required for internal moisture to diffuse outward, and the lower the apparent activation energy. The larger the particle size, the greater the apparent activation energy, because the larger the particle size, the longer the path of moisture diffusion to the outside, the more energy required to use, and the larger the particle and the more heat required for the particle to heat up, the apparent activation energy of the sample will increase [35-39].

Table 4

Apparent activation energy values of coal samples

Sample	E_a, kJ/mol	T, K	Size, mm	M_d, %
NM	10.97	373~453	–1	41.90
YN	17.97	373~453	–1	21.36
YN	18.95	373~453	1-3	21.36
YN	20.28	373~453	3-6	21.36

The experimental data of each sample were fitted using the 16 equations in the table to obtain the optimal drying kinematic model for each sample (Table 5). Meanwhile, the best model for each sample was fitted for five different working conditions, and the test data for each working condition was obtained by averaging six sets of the same tests. The best model for NM samples below –1 mm was two diffusion models, and the best model for YN samples with different particle sizes was the Hii equation. The parameters of the fitting results are shown in Table 5.

The experiments showed a high correlation of fitting results with the experiments: for the YN samples the correlation R^2 of –1 mm at 100, 120, 140, 160, 180 °C were 0.9984, 0.9994, 0.9987, 0.9976, 0.9971, respectively. The correlation R^2 of 1-3 mm at 100, 120, 140, 160, 180 °C were 0.9989, 0.9993, 0.9976, 0.9991, 0.9982, respectively. The correlation R^2 of 3-6 mm at 100, 120, 140, 160, 180 °C were 0.9989, 0.9993, 0.9976, 0.9991, 0.9982, respectively (Fig.7).

So, we could know that the two diffusion models were suitable for simulating samples with high moisture content. Hii models were suitable for simulating samples with low moisture content. A further step shows that the diffusion mechanism driven by concentration gradient plays a dominant role in samples with high water content. The two-dimensional diffusion model can well predict the isothermal thin-layer drying pattern of the high-water content samples. For samples with low water content, the concentration gradient was also one of the driving forces, but it was not the dominant role. Therefore, the diffusion model did not apply to samples with low water content.

Table 5

Fitting results of each sample

Samples	Model	Grain size, mm	Temperature, °C	R^2	a_1	a_2	k_1	k_2	n
YN	Hii	–1	100	0.9984	–0.2588	0.4186	0.1236	0.1075	0.8932
			120	0.9994	0.0148	0.1699	10.6822	0.0793	0.9502
			140	0.9976	–1.0517	1.2452	0.6375	0.5431	0.5707
			160	0.9987	–0.2042	0.4004	0.3874	0.7343	0.4558
			180	0.9971	–0.1303	0.3414	0.7614	0.3398	0.6853
YN	Hii	1-3	100	0.9989	–0.0061	0.1581	0.1257	0.0688	0.9843
			120	0.9993	0.0078	0.1701	0.3591	0.0661	10.0437
			140	0.9976	–0.1059	0.2992	0.6649	0.2652	0.7599
			160	0.9991	–0.0857	0.2847	10.0299	0.3042	0.6759
			180	0.9982	0.0218	0.1903	20.972	0.1006	10.0741
YN	Hii	3-6 mm	100	0.9992	0.0594	0.0915	0.0949	0.0422	1.1440
			120	0.9977	–3.1667	3.3309	0.3277	0.3126	0.7225
			140	0.9987	–0.0971	0.2748	0.3509	0.1531	0.8548
			160	0.9958	–0.1361	0.3264	0.9158	0.3228	0.6994
			180	0.9989	0.2184	–0.0048	0.1398	329.05	0.8481
NM	Two-term diffusion	–1	100	0.9986	–5.8756	6.2918	0.1955	0.1855	–
			120	0.9994	–18.929	19.345	0.2087	0.2055	–
			140	0.9976	–3.1762	30.5939	0.2474	0.2253	–
			160	0.9966	–6.9891	7.4073	0.2595	0.2517	–
			180	0.9994	0.3651	0.0582	0.4969	0.1226	–

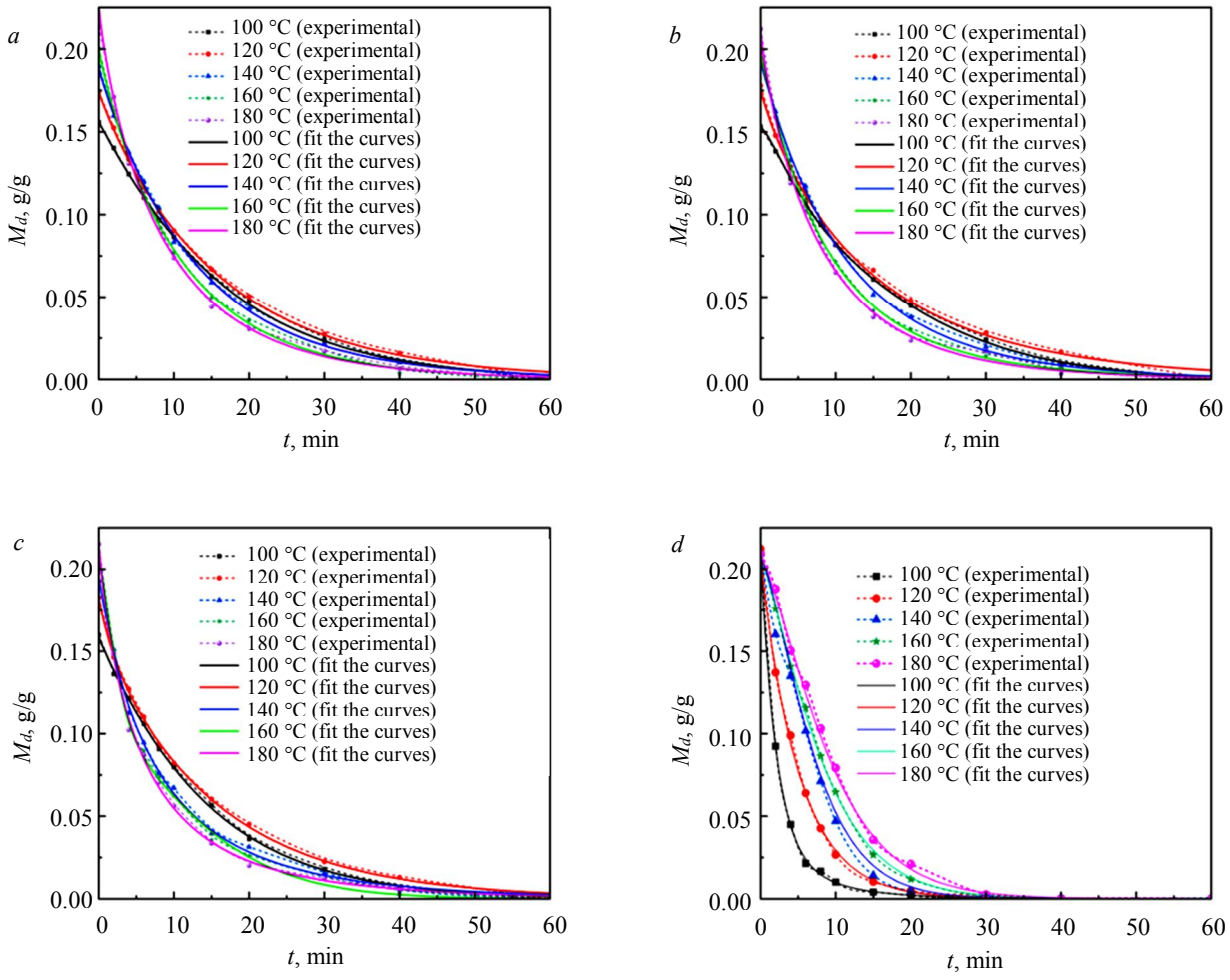

Fig.7. The fit of experimental results on samples at different drying temperatures: 3-6 mm YN samples (*a*); 1-3 mm YN samples (*b*); –1 mm YN samples (*c*); –1 mm NM samples (*d*)

Conclusions. In this article, thin-layer isothermal drying experiments were carried out on low-rank coal samples such as NM and YN, and the drying process and drying rate curves were drawn based on the data obtained by the experiments, and the effective water diffusion coefficient and apparent activation energy of each sample were calculated by combining the experimental data. Finally, the experimental data were fitted with 16 mathematical models of drying, and the best drying model for each sample was selected. The findings of this work show that:

• Moisture content and temperature are two of the most important factors affecting the drying process. For NM samples, when the temperature is less than 140 °C, the drying rate curve has three stages: increasing rate, constant speed and decreasing speed drying. When the temperature is greater than 140 °C, the drying curve has only two stages: increasing speed and decreasing speed drying. For samples with low moisture content, three different particle sizes there are only two drying stages at 100-180 °C drying: increasing and decreasing. When the temperature exceeds 160 °C, increasing the temperature no longer significantly improves the drying efficiency of YN samples. When the temperature exceeds 140 °C, increasing the temperature no longer significantly improves the drying efficiency of NM samples. In addition, the smaller the particle size, the higher the drying efficiency, and increasing the temperature will amplify the influence of particle size on drying efficiency. Organic components also reduce drying efficiency and volatilize at high temperatures in the later stages of drying.

• The higher the moisture content of the sample, the greater the effective water diffusion coefficient. The larger the particle size, the greater the effective moisture coefficient and the smaller the effective moisture coefficient per unit diameter. The higher the temperature, the greater the effective moisture diffusion coefficient. At the same time, the apparent activation energy of samples with low moisture content is higher and increases with particle size. In addition, NM samples are suitable for a double-diffusion theoretical model, and three YN samples with different particle sizes fit the Hii equation.

• This can be known through the analysis of the influencing factors. The moisture content has the greatest influence on the drying process. The second factor is the temperature. When the temperature exceeds a certain range, the increase in temperature will not be obvious to the improvement of drying efficiency. Then, there is the particle size. In low-rank coals below 6mm, the drying effect of the –1 mm sample was the best. Finally, there are organic components, which not only reduce drying efficiency but also increase mass loss when volatilized.

In the next step, this study will further reveal the drying mechanism of low-rank coal with the help of numerical simulation methods, and analyze the mass and heat transfer mechanism of the drying process in the mesoscopic scale.

REFERENCES

1. Aleksandrova T., Nikolaeva N., Kuznetsov V. Thermodynamic and Experimental Substantiation of the Possibility of Formation and Extraction of Organometallic Compounds as Indicators of Deep Naphthogenesis. *Energies*. 2023. Vol. 16. Iss. 9. N 3862. DOI: 10.3390/en16093862

2. Capellán-Pérez I., Mediavilla M., de Castro C. et al. Fossil fuel depletion and socio-economic scenarios: An integrated approach. *Energy*. 2014. Vol. 77, p. 641-666. DOI: 10.1016/j.energy.2014.09.063

3. Shunxuan Hu, Junguo Li, Xin Yang et al. Improvement on slurry ability and combustion dynamics of low quality coals with ultra-high ash content. *Chemical Engineering Research and Design*. 2020. Vol. 156, p. 391-401. DOI: 10.1016/j.cherd.2020.02.011

4. Aleksandrova T.N., Kuskov V.B., Afanasova A.V., Kuznetsov V.V. Improvement of the fine coking coal flotation technology. *Obogashchenie Rud*. 2021. N 3, p. 9-13 (in Russian). DOI: 10.17580/or.2021.03.02

5. Chenyang Zhou, Xuchen Fan, Chenlong Duan, Yuemin Zhao. A method to improve fluidization quality in gas–solid fluidized bed for fine coal beneficiation. *Particuology*. 2019. Vol. 43, p. 181-192. DOI: 10.1016/j.partic.2017.12.012

6. Daegi Kim, Seyong Park, Ki Young Park. Upgrading the fuel properties of sludge and low rank coal mixed fuel through hydrothermal carbonization. *Energy*. 2017. Vol. 141, p. 598-602. DOI: 10.1016/j.energy.2017.09.113

7. Yong Jin, Haifeng Lu, Xiaolei Guo, Xin Gong. Effect of water addition on flow properties of lignite particles. *Chemical Engineering Research and Design*. 2018. Vol. 132, p. 1020-1029. DOI: 10.1016/j.cherd.2017.11.012

8. Wu Xian, Dong Ziwen, Sun Lifeng, Jia Tinggui. Experimental Study of the Volume Drying Shrinkage Characteristics of Lignite under Low Temperatures. *ACS Omega*. 2022. Vol. 7. Iss. 12, p. 10029-10038. DOI: 10.1021/acsomega.1c05575

9. Rongtang Liu, Ming Liu, Xiaoqu Han, Junjie Yan. Drying characteristics and kinetics analyses for Yimin lignite at various temperatures. *Drying Technology*. 2021. Vol. 39. Iss. 7, p. 912-924. DOI: 10.1080/07373937.2020.1729174

10. Fu B.A., Chen M.Q. Thin-layer drying kinetics of lignite during hot air forced convection. *Chemical Engineering Research and Design*. 2015. Vol. 102, p. 416-428. DOI: 10.1016/j.cherd.2015.07.019

11. Haijun Zhou, Yuanquan Xiong, Yu Pei. Effect of moisture content on dense-phase pneumatic conveying of pulverized lignite under high pressure. *Powder Technology*. 2016. Vol. 287, p. 355-363. DOI: 10.1016/j.powtec.2015.10.026

12. Celen P., Erdem H.H. An experimental investigation of single lignite particle dried in superheated steam and hot air. *International Journal of Coal Preparation and Utilization*. 2018. Vol. 41. Iss. 12, p. 845-854. DOI: 10.1080/19392699.2018.1536047

13. Fu B.A., Chen M.Q., Huang Y.W. Heat transfer characteristics on lignite thin-layer during hot air forced convective drying. *Fuel*. 2015. Vol. 154, p. 132-139. DOI: 10.1016/j.fuel.2015.03.075

14. Hosseini T., Zhang L. Process modeling and techno-economic analysis of a solar thermal aided low-rank coal drying-pyrolysis process. *Fuel Processing Technology*. 2021. Vol. 220. N 106896. DOI: 10.1016/j.fuproc.2021.106896

15. Jinzhan Huang, Zhiqiang Li, Biao Chen et al. Rapid detection of coal ash based on machine learning and X-ray fluorescence. *Journal of Mining institute.* 2022. Vol. 256, p. 663-676. DOI: 10.31897/PMI.2022.89

16. Bojian Qi, Yong Yan, Wenbiao Zhang, Xueyao Wang. Measurement of biomass moisture content distribution in a fluidised bed dryer through electrostatic sensing and digital imaging. *Powder Technology*. 2021. Vol. 388, p. 380-392. DOI: 10.1016/j.powtec.2021.04.096

17. Ji Hyeon Park, Jung Hae Park, Soo Chul Kim. A Study on Application of Enzyme Additives to Improve Drying Speed of Urushi Lacquer. *Journal of the Korean Wood Science and Technology*. 2020. Vol. 48. N 3, p. 326-344. DOI: 10.5658/WOOD.2020.48.3.326

18. Huaigang Cheng, Lixiang Wu, Fangqin Cheng. Kinetics of static immersed leaching of low-grade sea-type evaporites based on theoretical and experimental investigation of unsteady-state mass transfer. *Journal of Cleaner Production*. 2020. Vol. 256. N 120501. DOI: 10.1016/j.jclepro.2020.120501

19. Yuwei Wei, Xishan Zhu, Chenquan Deng et al. Study on cracking process of hot pressed tee based on Fick's second law. *Engineering Failure Analysis*. 2022. Vol. 134. N 106014. DOI: 10.1016/j.engfailanal.2021.106014

20. Lingbo Kong, Xing Yang, Zhihao Hou, Jixian Dong. Mathematical Modeling of Drying Kinetics for Pulp Sheet Based on Fick's Second Law of Diffusion. *Journal of Korea TAPPI*. 2020. Vol. 52. N 2, p. 23-31. DOI: 10.7584/JKTAPPI.2020.04.52.2.23

21. Cheak Theng Ee, Ching Lik Hii, Sze Pheng Ong et al. Convective Air Drying of *Spondias Dulcis* and Product Quality. *International Journal of Food Engineering*. 2019. Vol. 15. Iss. 3-4. N 20180228. DOI: 10.1515/ijfe-2018-0228

22. Obradović B. Guidelines for general adsorption kinetics modeling. *Hemijska industrija*. 2020. Vol. 74. Iss. 1, p. 65-70. DOI: 10.2298/HEMIND2002010060

23. Yousuf M. A second-order efficient L-stable numerical method for space fractional reaction–diffusion equations. *International Journal of Computer Mathematics*. 2018. Vol. 95. Iss. 6-7, p. 1408-1422. DOI: 10.1080/00207160.2018.1435865

24. Pengbo Fu, Hao Yu, Qiqi Li et al. Cyclone rotational drying of lignite based on particle high-speed self-rotation: Lower carrier gas temperature and shorter residence time. *Energy*. 2022. Vol. 244. Part B. N 123005. DOI: 10.1016/j.energy.2021.123005

25. Ying Xu, Jiming Wang, Guojie Zhang et al. Evaluation of hydrothermal treatment on physicochemical properties and re-adsorption behaviors of lignite. *Energy*. 2022. Vol. 244. Part A. N 122597. DOI: 10.1016/j.energy.2021.122597

26. Crapse J., Pappireddi N., Gupta M. et al. Evaluating the Arrhenius equation for developmental processes. *Molecular Systems Biology*. 2021. Vol. 17. Iss. 8. N e9895. DOI: 10.15252/msb.20209895

27. Jaeho Cha, Sungho Yoon. Determination of shift factor for long-term life prediction of carbon/fiber epoxy composites using the time-temperature superposition principle. *Functional Composites and Structures*. 2022. Vol. 4. Iss. 1. N 015003. DOI: 10.1088/2631-6331/ac529e

28. Selimefendigil F., Coban S.O., Öztop H.F. An efficient method for optimizing the unsteady heat and mass transport features for convective drying of two porous moist objects in a channel. *International Journal of Mechanical Sciences*. 2021. Vol. 200. N 10644. DOI: 10.1016/j.ijmecsci.2021.106444

29. Joardder M.U.H., Karim M.A. Development of a porosity prediction model based on shrinkage velocity and glass transition temperature. *Drying Technology*. 2019. Vol. 37. Iss. 15, p. 1988-2004. DOI: 10.1080/07373937.2018.1555540

30. Ternes S., Börnhorst T., Schwenzer J.A. et al. Drying Dynamics of Solution-Processed Perovskite Thin-Film Photovoltaics: In Situ Characterization, Modeling, and Process Control. *Advanced Energy Materials*. 2019. Vol. 9. Iss. 39. N 1901581. DOI: 10.1002/aenm.201901581

31. Chicco D., Tötsch N., Jurman G. The Matthews correlation coefficient (MCC) is more reliable than balanced accuracy, bookmaker informedness, and markedness in two-class confusion matrix evaluation. *BioData Mining*. 2021. Vol. 14. N 13. DOI: 10.1186/s13040-021-00244-z

32. Jia-Qing Zhou, Hong-Bin Liu, Changdong Li. A semi-empirical model for water inflow into a tunnel in fractured-rock aquifers considering non-Darcian flow. *Journal of Hydrology*. 2021. Vol. 597. N 126149. DOI: 10.1016/j.jhydrol.2021.126149

33. Xun Zhang, Bin Zeng, Bing Lu et al. Experimental research on spontaneous combustion of coal oxidized by ultraviolet photocatalysis. *AIP Advances*. 2022. Vol. 12. Iss. 8. N 085226. DOI: 10.1063/5.0098407

34. Pengfei Zhao, Liping Zhong, Yuemin Zhao, Zhenfu Luo. Comparative studies on the effect of mineral matter on physicochemical properties, inherent moisture and drying kinetics of Chinese lignite. *Energy Conversion and Management*. 2015. Vol. 93, p. 197-204. DOI: 10.1016/j.enconman.2015.01.020

35. Jung J., Kobayashi C., Sugita Y. Optimal Temperature Evaluation in Molecular Dynamics Simulations with a Large Time Step. *Journal of Chemical Theory and Computation*. 2019. Vol. 15. Iss. 1, p. 84-94. DOI: 10.1021/acs.jctc.8b00874

36. Meng Liu, Jian Li, Yufeng Duan. Effects of solvent thermal treatment on the functional groups transformation and pyrolysis kinetics of Indonesian lignite. *Energy Conversion and Management*. 2015. Vol. 103, p. 66-72. DOI: 10.1016/j.enconman.2015.06.047

37. Liu Ming Qiang, Jian Zhong Liu, Yu Jie Yu et al. Investigation of Lignite Combustion Characteristics with Thermal Analysis. *Advanced Materials Research*. 2012. Vol. 614-615, p. 25-30. DOI: 10.4028/www.scientific.net/AMR.614-615.25

38. Yanyan Shi, Shuyuan Li, Haoquan Hu. Studies on pyrolysis characteristic of lignite and properties of its pyrolysates. *Journal of Analytical and Applied Pyrolysis*. 2012. Vol. 95, p. 75-78. DOI: 10.1016/j.jaap.2012.01.008

39. Lei Guo, Chenhui Liu, Srinivasakannan C., Gao Jiyun. Microwave upgradation of Yunnan lignite: dielectric properties, drying pattern and kinetics. *Journal of Microwave Power and Electromagnetic Energy*. 2021. Vol. 55. Iss. 3, p. 248-269. DOI: 10.1080/08327823.2021.1952834

***Authors*: Cheng Wang,** *Master, Master of Mineral Processing Engineering*, *https://orcid.org/0009-0002-6216-6631* (*China University of Mining and Technology School of Chemical Engineering, Xuzhou, China*), **Dan Wang,** *Doctor, PhD Candidate in Mineral Processing Engineering*, *https://orcid.org/0009-0002-3220-2152* (*China University of Mining and Technology School of Chemical Engineering, Xuzhou, China*), **Zengqiang Chen,** *Doctor, Associate Professor*, *https://orcid.org/0000-0002-0679-0993* (*Key Laboratory of Coal Processing and Efficient Clean Utilization of Ministry of Education, China University of Mining and Technology, Xuzhou, China*), **Chenlong Duan,** *Doctor, Professor*, *clduan@cumt.edu.cn*, *https://orcid.org/0000-0002-8093-6719* (*Key Laboratory of Coal Processing and Efficient Clean Utilization of Ministry of Education, China University of Mining and Technology, Xuzhou, China*), **Chenyang Zhou,** *Doctor, Associate Professor*, *https://orcid.org/0000-0002-5393-4240* (*Key Laboratory of Coal Processing and Efficient Clean Utilization of Ministry of Education, China University of Mining and Technology, Xuzhou, China*).

The authors declare no conflict of interests.